

Oxygen Electroreduction on Core-Shell Nanoparticle Catalysts Prepared by Selective Electrochemical Metal Dissolution of Pt-Cu and Pt-Co Alloys

vorgelegt von
Dipl. - Chem. Mehtap Özaslan
aus Berlin

Von der Fakultät II – Mathematik und Naturwissenschaften
der Technischen Universität Berlin
zum Erlangen des akademischen Grades

Doktorin der Naturwissenschaften
Dr. rer. Nat.

genehmigte Dissertation

Promotionsausschuss:

Vorsitzender: Prof. Dr. R. Süssmuth (TU Berlin)

Berichter: Prof. Dr. P. Strasser (TU Berlin)

Berichter: Prof. Dr. T. J. Schmidt (ETH Zürich)

Tag der wissenschaftlichen Aussprache: 08. Februar 2012

Berlin 2012

D83

Table of Contents

Table of Contents	2
List of Tables	7
List of Figures.....	9
1 Introduction and Background.....	22
1.1 Research Goals and Strategies	24
1.2 Acidic and Alkaline Hydrogen PEM Fuel Cell.....	26
1.3 Mechanism of the Oxygen Reduction Reaction (ORR).....	29
1.3.1 Pt Alloy Electrocatalyst Concepts	30
1.3.2 “Volcano” Plot	32
1.4 Platinum – Copper System.....	34
1.5 Platinum – Cobalt System.....	38
2 Experimental Methods.....	40
2.1 Synthesis of PtM (M = Cu, Co) Alloy Nanoparticle Precursor Electrocatalysts.....	40
2.2 Electrochemical Characterization	43
2.2.1 Preparation of Thin Catalytic Film Electrode.....	43
2.2.2 Rotating Disc Electrode (RDE) Technique.....	44
2.2.2.1 Cyclic Voltammetry	46
2.2.2.2 Linear Sweep Voltammetry (LSV).....	48
2.2.3 Rotating Ring Disk Electrode (RRDE) Technique	50
2.2.3.1 Determination of collection efficiency N	51
2.3 Structural and Compositional Characterization.....	53
2.3.1 High Temperature X-Ray Diffraction (HT-XRD) in Parallel Beam Geometry	53
2.3.1.1 Alignment and Calibration of the HT-XRD	55
2.3.2 X-Ray Diffraction (XRD) in Bragg-Brentano Geometry	58
2.3.2.1 XRD Profile Analysis.....	58
2.3.3 Energy-Dispersive X-Ray Spectroscopy (EDS)	60
2.3.4 Transmission Electron Microscopy (TEM)	60

2.3.5	Scanning Transmission Electron Microscopy with High Angle Annular Dark Field Detector (STEM-HAADF)	62
2.3.6	Electron Energy Loss (EEL) spectroscopy.....	62
3	In-situ HT-XRD Study of Alloy Formation and Particle Growth	66
3.1	Introduction	67
3.2	Preparation of Pt-Cu Precursor Material.....	69
3.3	Temperature – Time Protocols	70
3.4	Dynamic Behavior of the Alloy Formation and Size Growth during the “Synthesis Temperature Protocol”	72
3.5	Dynamic Behavior of Pt-Cu Alloy Formation during the “Stepped Heating Protocol”	76
3.6	Formation of Ordered Pt-Cu Alloys during the “Stepped Cooling Protocol”	80
3.7	Summary.....	82
4	Activation of Pt Bimetallic Nanoparticle Precursor Electrocatalysts	83
5	Pt-Cu Alloy Nanoparticle Electrocatalysts	85
5.1	Structural and Chemical Characterization of the As-Synthesized Pt-Cu Alloy Nanoparticle Electrocatalysts	86
5.2	Electrochemical Behavior of Pt-Cu Alloy Nanoparticle Electrocatalysts in Acidic and Alkaline Media.....	91
5.2.1	Comparison with pure Pt Nanoparticles.....	95
5.3	Platinum Electrochemical Active Surface Area (ECSA) and Chemical Composition of Pt-Cu Alloy Nanoparticles	97
5.4	ORR Performance of Pretreated Pt-Cu Alloy Nanoparticle Electrocatalysts in Acidic and Alkaline Media.....	99
5.5	Correlation of ECSA – Activity – Cu Alloy Composition in Dependence on Different Electrolyte Solutions and pH Values.....	102
5.6	Hydrogen Peroxide Production of Pretreated Pt-Cu Alloy Nanoparticle Electrocatalysts	105

5.7	Highly Active PtCu₃ Core-Shell Nanoparticles in Alkaline Media	106
5.8	Summary.....	109
6	Pt-Co Alloy Nanoparticle Electrocatalysts	111
6.1	Structural Characterization of the As-Synthesized Pt-Co Alloy Nanoparticle Electrocatalysts	112
6.2	Electrochemical Characterization of Pt-Co Alloy Nanoparticle Electrocatalysts in Alkaline and Acidic Media.....	116
6.2.1	Comparing with pure Pt Nanoparticles.....	120
6.3	Platinum Electrochemical Active Surface Area (ECSA) and Chemical Composition of Pt-Co Alloy Nanoparticles	122
6.4	ORR Activity of Voltammetric Pretreated Pt-Co Electrocatalysts in Acidic and Alkaline Electrolytes	124
6.5	Correlation of ECSA – Activity – Co Alloy Composition in Dependence on Different Electrolyte Solutions and pH Values.....	128
6.6	Hydrogen Peroxide Production of Pt-Co Alloy Nanoparticle Electrocatalysts.....	131
6.7	Highly Active PtCo₃ Core-Shell Nanoparticles in Alkaline Media	133
6.8	Summary.....	135
6.9	Effects of Annealing Conditions on the ORR Activity of PtCo₃ Alloy Nanoparticle Electrocatalysts	137
6.9.1	Effects of Annealing Temperature on the Structure of PtCo ₃ Alloy Nanoparticle Precursor Catalysts.....	138
6.9.2	Electrochemical Dealloying Behavior of PtCo ₃ Alloy Nanoparticles annealed at different Temperatures in Acidic Media	140
6.9.3	ORR Activity of Dealloyed PtCo ₃ Annealed at different Temperatures in Acidic Media.....	144
6.9.4	ORR Selectivity of Dealloyed PtCo ₃ compared with Dealloyed PtCu ₃ and pure Pt	146
6.9.5	Summary	152

7	Size-dependent Morphology of Dealloyed Bimetallic Catalysts: Linking the Nano to the Macro Scale	153
7.1	Introduction	154
7.2	Formation of Platinum-enriched Particle Shell by Dealloying 156	
7.3	Particle Morphology and Chemical Composition before and after Dealloying	158
7.4	Principle Nanoscale Particle Morphologies and Structures and their Size Dependence	160
7.4.1	“Single Core-Shell Nanoparticles” – Dealloyed Pt-Co and Pt-Cu Nanoparticles below 5 nm Diameter	160
7.4.2	“Multiple Cores-Shell Nanoparticles” – Dealloyed Pt-Co and Pt-Cu Particles up to 20 nm Diameters	163
7.4.3	“Nanoporous Multiple Cores-Shell Particles” – Dealloyed Pt-Co and Pt-Cu Particles up to 100 nm Diameter.....	167
7.5	Discussions.....	171
7.5.1	Size-dependent Morphology and Chemical Composition of Dealloyed Pt-Co and Pt-Cu Particles	171
7.6	Summary.....	176
8	Atomic-scale Structural and Element-Compositional Characterization of Dealloyed Pt-Co Core-Shell Nanoparticles 178	
8.1	Introduction	179
8.2	Compositional Particle Depth Profiles of Dealloyed Self- organized Pt-Co Core-shell Nanoparticles.....	181
8.3	Summary.....	190
9	Conclusions and Perspectives	191
9.1	Conclusions	191
9.2	Perspectives.....	195
10	Appendices.....	197
10.1	List of Chemicals	197
10.2	Criteria of Fit for XRD Profiles	198

Table of Contents

10.3	Abbreviations	199
11	References.....	202

List of Tables

<i>Table 1 Direct comparison of the acidic and alkaline PEMFCs.</i> ^{42, 43}	28
<i>Table 2 Proportioning the catalyst components for Pt-M alloy nanoparticle precursor electrocatalysts.</i>	42
<i>Table 3 Comparison of crystal structure, lattice parameter, Rietveld quantification, crystallite size, and stoichiometric composition for Pt-Cu alloy nanoparticle electrocatalysts.</i> ¹²⁶	88
<i>Table 4 Comparison of the as-synthesized mean particle size and chemical composition for the PtCu₃, PtCu and Pt₃Cu alloy nanoparticle catalysts and 28.2 wt. % Pt/HSAC catalyst before and after the electrochemical experiments (EC) in 0.1 M HClO₄ and 0.1 M KOH electrolytes.</i> ^{126, 127}	90
<i>Table 5 Pt electrochemical active surface area (ECSA), Pt mass based activity (<i>j</i>_{mass}) and Tafel slope at low current density (<i>I</i>_{cd}) for PtCu₃, PtCu and Pt₃Cu nanoparticle catalysts compared with 28.2 wt. % Pt/HSAC in 0.1 M HClO₄ and 0.1 M KOH electrolytes.</i> ^{126, 127}	98
<i>Table 6 Pt electrochemical active surface area (ECSA) and Pt mass based activity (<i>j</i>_{mass}) for activated PtCu₃ alloy nanoparticle electrocatalyst compared with 28.2 wt. % Pt/HSAC in 0.1 M HClO₄ and 0.1 M KOH electrolytes.</i> ¹²⁶	107
<i>Table 7 Crystal structure, space group, lattice parameter, crystallite size, Rietveld quantification, and stoichiometric composition of PtCo₃, PtCo and Pt₃Co alloy nanoparticle electrocatalysts.</i> ¹⁴⁰	114
<i>Table 8 Comparison of the initial mean particle size and chemical composition for the PtCo₃, PtCo and Pt₃Co alloy nanoparticle catalysts and 28.2 wt. % Pt/HSAC catalyst before and after the electrochemical experiments (EC) in acidic and alkaline electrolytes.</i> ^{127, 140}	115
<i>Table 9 Pt electrochemical active surface area (ECSA), Pt mass based activity (<i>j</i>_{mass}) and Tafel slope for low current density (<i>I</i>_{cd}) for PtCo₃, PtCo and Pt₃Co alloy nanoparticle catalysts compared with 28.2 wt. % Pt/HSAC in 0.1 M HClO₄ and 0.1 M KOH electrolytes.</i> ^{127, 140}	123

<i>Table 10 Pt electrochemical active surface area (ECSA) and Pt mass based activity (j_{mass}) for activated PtCo₃ alloy nanoparticle electrocatalyst compared with 28.2 wt. % Pt/HSAC in 0.1 M HClO₄ and 0.1 M KOH electrolytes.¹⁴⁰</i>	134
<i>Table 11 Crystal structure, lattice parameter, crystallite size, Rietveld quantification and stoichiometric composition of Co rich Pt-Co alloy system.⁹⁰</i>	140
<i>Table 12 Comparison of electrochemical active surface area (ECSA) and catalytic ORR activities for dealloyed PtCo₃ alloy nanoparticles catalysts annealed at 650 °C, 800 °C and 900 °C and commercial 28.2 wt. % Pt/HSAC catalyst.⁹⁰</i>	143
<i>Table 13 Changes in chemical composition of Pt-Co alloy nanoparticles, annealed at 650 °C, 800 °C and 900 °C after electrochemical (EC) experiments established by EDS technique.⁹⁰</i>	143
<i>Table 14 Criteria of fit using TOPAS. The observed and calculated data at data point are denoted with $Y_{o,m}$ and $Y_{c,m}$, respectively. M is the number of data points and P the number of parameters. w_m the weighting given to data point m which for counting statistics is given by $w_m = 1/\sigma(Y_{o,m})^2$ where $\sigma(Y_{o,m})$ is the error in $Y_{o,m}$ and $I_{o,k}$ and $I_{c,k}$ the “observed” and calculated intensities of the k^{th} reflection.</i>	198

List of Figures

<i>Figure 1 Structure –ORR activity relation.....</i>	<i>24</i>
<i>Figure 2 Schematics of an (a) acidic and (b) alkaline PEMFCs and the corresponding half cell reactions.</i>	<i>27</i>
<i>Figure 3 Mechanisms of the oxygen reduction reaction (ORR) in (a) acidic and (b) alkaline media.</i>	<i>29</i>
<i>Figure 4 Pt alloy electrocatalysts concepts and their fundamental mechanisms to tune the catalytic surface reactivity.</i>	<i>31</i>
<i>Figure 5 Volcano plots: trends in kinetic current density (symbolized the activity) plotted as a function of the calculated oxygen adsorption energy for the oxygen reduction reaction on Pt alloys. The calculation is in good agreement with the experimental data from different groups. The dashed lines indicate the theoretical predictions.¹⁹.....</i>	<i>33</i>
<i>Figure 6 Macroscopic thermodynamic stable phase diagram of Pt-Cu alloy system.⁵⁸.....</i>	<i>34</i>
<i>Figure 7 Collection of calculated segregation energies on the most close-packed surface of all binary combinations of transition metals.⁵⁷.....</i>	<i>35</i>
<i>Figure 8 Potential – pH equilibrium diagram for the systems (a) copper – water and (b) platinum – water at 25 °C.⁵⁹ The red dashed lines denote the voltage range cycling of 0.06 V and 1.00 V/RHE at pH 1 (0.1 M HClO₄) and pH 13 (0.1 M KOH).</i>	<i>37</i>
<i>Figure 9 Macroscopic thermodynamic stable phase diagram of Pt-Co alloy system.⁶⁰.....</i>	<i>38</i>
<i>Figure 10 Potential – pH equilibrium diagram for the systems cobalt – water at 25 °C.⁵⁹ The red dashed lines denote the voltage range cycling of 0.06 V and 1.00 V/RHE at pH 1 (0.1 M HClO₄) and pH 13 (0.1 M KOH).</i>	<i>39</i>
<i>Figure 11 Images of the synthesis of Pt-M alloy nanoparticle precursor electrocatalysts. (a) light viscous suspension after sonication, (b) frozen samples in liquid nitrogen, (c) samples in a freeze-drier, (d) quartz tray with a quartz plate in a alumina crucible, (e) impregnated powder in a quartz tube of the three-zone furnace, (f) opened three zone furnace.....</i>	<i>41</i>

- Figure 12 (a) Image of the electrochemical experimental RDE setup: (1) rotator, (2) working electrode coated with a thin catalytic film, (3) self-made three compartment electrochemical glass cell, (4) Pt mesh as counter electrode, (5) mercury-mercury sulfate electrode as reference electrode, (6) Luggin – Haber capillary for the reference electrode, (7) gas inlet for bubbling through the frit into the electrolyte and (8) gas inlet above the electrolyte solution. (b) Three glassy carbon (GC) disk working electrodes at 5 mm diameter: (1) rotating disk electrode, (2) rotating ring disk electrode with an outermost pure Pt ring electrode, (3) high temperature rotating disk electrode consisting of polyetheretherketone (PEEK). (c) Two catalyst ink suspensions. (d) GC electrode prepared with a thin catalytic film.....45
- Figure 13 Cyclic voltammograms (CVs) of carbon supported Pt nanoparticles in deaerated 0.1 M HClO₄ electrolyte solution at room temperature. The CV profile shows the characteristic features of a pure Pt catalyst corresponding to the hydrogen ad/desorption regime (0.06 – 0.40 V/RHE), the double layer regime (0.40 – 0.60 V/RHE), and the redox peak couple of Pt hydroxide/oxide (0.70 – 1.00 V/RHE).47
- Figure 14 (a) A typical polarization curve for oxygen reduction reaction (ORR) recorded by LSV. (b) Pt mass based Tafel slope of a commercial Pt/C. ...49
- Figure 15 a) Image of the RRDE setup. b) Ring current during the anodic disk potential sweep with a scan rate of 20 mV s⁻¹ to determine the collection efficiency N on a Pt/C thin-film RRDE electrode in 0.1 M HClO₄ with 10 mM K₃Fe(CN)₆ at room temperature.....52
- Figure 16 Experimental high temperature X-ray diffraction (HT-XRD) assembly in parallel beam geometry in (a) opened and (b) closed states. (a) HT-XRD with opened radiation heating chamber: (1) Cu X-ray source, (2) Goebel mirror, (3) external heating chamber positioned on the goniometer, (4) position-sensitive LynxEye detector (PSD). (c) (1) Sample in a white Al₂O₃ crucible, (2) thermocouple and (3) AlCr foil heater. (d) A white Al₂O₃ crucible of 14 mm diameter was filled with 6 – 10 mg black impregnated powder.54

- Figure 17 Alignment of the HT-XRD. a) Schematic sketch of the Z-drive. b) Series of XRD patterns at various values of Z height recorded by a direct beam and PSD fix scan. The optimal Z height is only achieved, when the intensity is the half of the maximum intensity. XRD parameters: $\Theta = -0.5 - +0.5^\circ$ for the X-ray tube, step size of 0.02° and holding time 1 s.56
- Figure 18 Calibration of the thermocouple by temperature-dependent XRD measurements from α -quartz (trigonal) to β -quartz (hexagonal). a) Series of XRD patterns at various temperatures in the range of 552°C to 595°C . b) Three-dimension representation of the phase transformation of α -quartz to β -quartz. XRD parameters: $2\Theta = 25.5 - 28^\circ$, step size of 0.01° and holding time of 2 s.57
- Figure 19 FEI TECNAI G² 20 S-TWIN transmission electron microscope (TEM) equipping a LaB₆ cathode, an energy-dispersive X-ray spectroscopy (EDS) detector and a GATAN MS794 P CCD camera.61
- Figure 20 probe-corrected FEI TITAN S 80-300 high-angle annular dark field scanning transmission electron microscopy (STEM-HAADF). (1) specimen port, (2) fluorescent screen, (3) binoculars, (4) high angle annular dark field (HAADF) detector and (5) cooling finger consisting of copper wires.....64
- Figure 21 Raw EEL spectra for Co L₃ and Pt M_{4,5}- edges at the measuring points #10, #14 and #17 along the dealloyed particle, shown in Figure 63a. The red curves show the original EEL spectra and the blue curves display background-subtracted data. The grey areas denote the integrated edges in the background-subtracted curves at 770 – 785 eV for Co and at 2155 – 2400 eV for Pt. The black curves indicate the background subtraction using a hyperbolic fit of the pre-edge spectrum at 580 – 765 eV for Co and at 1970 – 2130 eV for Pt.65
- Figure 22 Temperature – time profiles to anneal Pt-Cu precursor materials in reductive atmosphere. The individual XRD measurements are denoted with black circles. (a) temperature – time profile, referred to as a “synthesis protocol”; (b) temperature – time profile with temperature holds on the heating ramp, referred to as a “stepped heating protocol”; (c) temperature – time profile with temperature holds on the cooling ramp, referred to as a

<i>“stepped cooling protocol”</i> . Reprinted from ref 75 with permission of <i>Chemistry of Materials</i> , copyright (2011).	71
<i>Figure 23 Series of XRD patterns, recorded in parallel beam XRD setup during Pt-Cu alloy formation at 800 °C over 9 hours. Numbers indicate the first scan #6 (t = 0 h) and final #16 (t = 9 h) at 800°C. Symbols denote individual crystallographic phases for disordered fcc Pt-Cu alloy, pure Cu and pure Pt nanoparticles at 800 °C. Reprinted from ref 75 with permission of Chemistry of Materials, copyright (2011).</i>	72
<i>Figure 24 Lattice parameter of disordered Pt-Cu alloy and mean crystallite size normalized temperature time at 800 °C. The mean crystallite size was estimated from the (111) and (200) Pt-Cu alloy reflections. The normalized time (N-time) represents the first scan at 800 °C, in Figure 22a. a - lattice parameter error ± 0.001 Å. Reprinted from ref 75 with permission of Chemistry of Materials, copyright (2011).</i>	74
<i>Figure 25 Series of in-situ XRD patterns, recorded in parallel beam XRD setup during the “stepped heating protocol” of Figure 22b. Symbols denote individual crystallographic phases for disordered fcc Pt-Cu alloy, pure fcc Cu and Pt nanoparticles. Reprinted from ref 75 with permission of Chemistry of Materials, copyright (2011).</i>	77
<i>Figure 26 Lattice parameter composition relations of disordered Pt-Cu alloy nanoparticles at various temperatures (black squares for Pt-Cu alloys, blue circles for Pt, red triangle for Cu) extracted from Figure 25. Composition was estimated using a temperature-corrected Vegard’s rule. a - lattice parameter error ± 0.004 Å. Reprinted from ref 75 with permission of Chemistry of Materials, copyright (2011).</i>	78
<i>Figure 27 Series of in-situ HT-XRD profiles, recorded in parallel beam XRD setup in the neighborhood of the (100) PtCu₃ superlattice reflection during the “stepped cooling protocol” of Figure 22c. Ordered PtCu₃ alloy phase formed at temperatures below 600 °C. Reprinted from ref 75 with permission of Chemistry of Materials, copyright (2011).</i>	81

- Figure 28 Sketch of the formation of highly active bimetallic core-shell nanoparticle by selective electrochemical dealloying of less noble metal from a uniform Pt poor alloy precursor nanoparticle. Insert: STEM-HAADF micrographs of particles under Z contrast conditions before and after electrochemical dealloying to outline the changes in intraparticle composition and morphology.....84*
- Figure 29 XRD profiles of the as-synthesized Pt-Cu alloy nanoparticle electrocatalysts, displayed with y-offset. Rietveld profile fit of diffraction data for PtCu₃ ($R_{wp} = 2.80$, $R_{exp} = 0.55$, $GOF = 5.05$), for PtCu ($R_{wp} = 2.72$, $R_{exp} = 0.65$, $GOF = 4.19$) and for Pt₃Cu ($R_{wp} = 3.01$, $R_{exp} = 0.67$, $GOF = 4.50$). The fits are indicated by a red solid line. The superlattice reflections of the PtCu₃ (Pm3m) are denoted with “*”, the reflections of the Hongshiite PtCu (R-3m) are indicated with “^”, and the reflections of the pure fcc Cu (Fm3m) are denoted with “o”. Reproduced from ref ¹²⁶ by permission of The Electrochemical Society.....87*
- Figure 30 Histograms of particle size distributions with corresponding TEM images for the as-synthesized PtCu₃, PtCu, Pt₃Cu alloy nanoparticle and pure Pt nanoparticle electrocatalysts. The average particle size (d_{avg}) was determined from TEM images by counting of more than 400 particles. Reproduced from ref ¹²⁶ by permission of The Electrochemical Society....89*
- Figure 31 CV profiles of the PtCu₃ (a, b), PtCu (c, d), and Pt₃Cu (e, f) alloy nanoparticle electrocatalysts in deaerated 0.1 M HClO₄ (a, c, e; left side) and 0.1 M KOH (b, d, f; right side) electrolyte solutions. The first and final CV profiles denote with dashed and solid lines. The final CV was recorded after 200 voltage cycles with 500 mV s⁻¹. Cyclic voltammetry was performed from 0.06 to 1.00 V/RHE with 100 mV s⁻¹ at room temperature. Reproduced from ref ¹²⁶ by permission of The Electrochemical Society....92*
- Figure 32 CV profiles of pretreated PtCu₃, PtCu and Pt₃Cu catalysts compared with 28.2 wt. % Pt/HSAC after the voltage cycling in deaerated (a) 0.1 M HClO₄ and (b) 0.1 M KOH. Cyclic voltammetry was performed from 0.06 to 1.00 V/RHE with 100 mV s⁻¹ at room temperature. Reproduced from ref ¹²⁶ by permission of The Electrochemical Society.....95*

- Figure 33 Polarization curves of pretreated PtCu₃, PtCu and Pt₃Cu electrocatalysts in oxygen saturated (a) 0.1 M HClO₄ and (b) 0.1 M KOH. (c) Mass transport corrected Pt mass based Tafel plot of pretreated Pt-Cu catalysts in 0.1 M KOH and 0.1 M HClO₄ electrolyte solutions. LSV measurements were performed anodically from 0.06 – 1.00 V/RHE with 5 mV s⁻¹ and 1600 rpm (rotations per minute) at room temperature. Reproduced from ref ¹²⁶ by permission of The Electrochemical Society. .100*
- Figure 34 Illustration of morphological and chemical changes in bimetallic Pt-Cu alloy nanoparticles by voltage cycling in 0.1 M HClO₄ and 0.1 M KOH. Pt and Cu atoms are symbolized with light grey and red spheres, respectively. Reproduced from ref ¹²⁶ by permission of The Electrochemical Society. .102*
- Figure 35 a) ECSA versus initial Cu concentration and (b) Pt mass based activity (j_{mass}) versus initial Cu concentration established by EDS for Pt-Cu alloy nanoparticle electrocatalysts after voltage cycling in 0.1 M HClO₄ and 0.1 M KOH. Reproduced from ref ¹²⁶ by permission of The Electrochemical Society..... 103*
- Figure 36 Quantification of the hydrogen peroxide production at various applied disk voltages during oxygen reduction on pretreated PtCu₃, PtCu and Pt₃Cu alloy nanoparticle electrocatalysts. Reproduced from ref ¹²⁶ by permission of The Electrochemical Society..... 105*
- Figure 37 a) CV profiles of non-activated and activated PtCu₃ alloy nanoparticle electrocatalyst. b) Polarization curves of non-activated and activated PtCu₃ catalyst. Cyclic voltammetry was performed from 0.06 to 1.00 V/RHE with 100 mV s⁻¹ in 0.1 M KOH at room temperature. LSV measurements were performed anodically from 0.06 - 1.00 V/RHE with 5 mV s⁻¹ and 1600 rpm (rotations per minute) in 0.1 M KOH at room temperature. Reproduced from ref ¹²⁶ by permission of The Electrochemical Society. 107*

- Figure 38 XRD profiles of as-synthesized Pt-Co alloy nanoparticle electrocatalysts, displayed with y-offset. Rietveld profile fit of diffraction data for Pt₃Co ($R_{wp} = 3.56$, $R_{exp} = 0.62$, $GOF = 5.72$), for PtCo ($R_{wp} = 2.55$, $R_{exp} = 0.54$, $GOF = 4.73$), and for PtCo₃ ($R_{wp} = 1.53$, $R_{exp} = 0.43$, $GOF = 3.58$). The fits are indicated by a red solid line. The superlattice reflections of the Pt₃Co (Pm3m) are denoted with “*” and the reflections of the tetragonal PtCo (P4/mmm) are indicated with “x”. Reproduced from ref 140 by permission of The Electrochemical Society..... 113*
- Figure 39 Histograms of particle size distributions and corresponding TEM images for the as-synthesized PtCo₃, PtCo, Pt₃Co alloy and pure Pt nanoparticle electrocatalysts. The average particle size (d_{avg}) was determined from TEM images by counting of more than 400 particles. Reproduced from ref 140 by permission of The Electrochemical Society. 115*
- Figure 40 CV profiles of PtCo₃ (a, b), PtCo (c, d), and Pt₃Co (e, f) alloy nanoparticle electrocatalysts in deaerated 0.1 M HClO₄ (a, c, e; left side) and 0.1 M KOH (b, d, f; right side) electrolytes. The first and final CV profiles denote with dashed and solid lines. The final CV was recorded after 200 cycles with 500 mV s⁻¹. Cyclic voltammetry was performed from 0.06 to 1.00 V/RHE with 100 mV s⁻¹ at room temperature. Reproduced from ref 140 by permission of The Electrochemical Society..... 117*
- Figure 41 CV profiles of pretreated PtCo₃, PtCo and Pt₃Co alloy nanoparticle catalysts compared with 28.2 wt. % Pt/HSAC catalyst in deaerated (a) 0.1 M HClO₄ and (b) 0.1 M KOH. Cyclic voltammetry was performed from 0.06 to 1.00 V/RHE with 100 mV s⁻¹ at room temperature. Reproduced from ref 140 by permission of The Electrochemical Society..... 120*
- Figure 42 Polarization curves of the pretreated PtCo₃, PtCo and Pt₃Co alloy nanoparticle electrocatalysts in oxygen saturated (a) 0.1 M HClO₄ and (b) 0.1 M KOH. (c) Mass transport corrected Pt mass based Tafel plot of pretreated Pt-Co catalysts in both electrolytes. LSV measurements were performed anodically from 0.06 – 1.00 V/RHE with 5 mV s⁻¹ and 1600 rpm (rotations per minute) at room temperature. Reproduced from ref 140 by permission of The Electrochemical Society. 125*

- Figure 43 Illustration of morphological and chemical changes in bimetallic Pt-Co alloy nanoparticle electrocatalysts by voltage cycling in 0.1 M KOH and 0.1 M HClO₄. Pt atoms are symbolized with grey spheres and Co atoms are symbolized with blue spheres. Reproduced from ref 140 by permission of The Electrochemical Society..... 128
- Figure 44 a) ECSA versus initial Co concentration and (b) Pt mass based activity (j_{mass}) versus initial cobalt concentration established by EDS for as-synthesized Pt-Co alloy nanoparticle electrocatalysts after voltage cycling in 0.1 M HClO₄ and 0.1 M KOH. Reproduced from ref 140 by permission of The Electrochemical Society..... 129
- Figure 45 Hydrogen peroxide production versus the disk voltage during oxygen reduction on pretreated PtCo₃, PtCo and Pt₃Co alloy nanoparticle electrocatalysts. RRDE measurements were performed in oxygen saturated 0.1 M HClO₄ at room temperature. During the recording of the polarization curves for ORR on the disk electrode, the potential of pure Pt ring electrode was potentiostated at 1.20 V/RHE. The formation of hydrogen peroxide was independent of the rotating speed. Reproduced from ref 140 by permission of The Electrochemical Society. 131
- Figure 46 a) CV profiles of non-activated and activated PtCo₃ alloy nanoparticle electrocatalyst; b) Polarization curves of activated PtCo₃ catalyst in oxygen saturated acidic and alkaline electrolytes. Cyclic voltammetry was performed from 0.06 to 1.00 V/RHE with 100 mV s⁻¹ in nitrogen purged 0.1 M KOH at room temperature. LSV measurements were performed anodically from 0.06 - 1.00 V/RHE with 5 mV s⁻¹ and 1600 rpm (rotations per minute) at room temperature. Reproduced from ref 140 by permission of The Electrochemical Society..... 134
- Figure 47 XRD profiles of synthesized Pt-Co catalysts, displayed with y-offset. Rietveld profile fit of diffraction data for Pt-Co (650°C/7h) ($R_{wp} = 1.35$, $R_{exp} = 0.42$, $GOF = 3.18$); for Pt-Co (800°C/7h) ($R_{wp} = 1.51$, $R_{exp} = 0.41$, $GOF = 3.71$) and for Pt-Co (900°C/7h) ($R_{wp} = 1.89$, $R_{exp} = 0.43$, $GOF = 4.38$). The fits are indicated by a red solid line. Vertical dotted lines denote Pt, Co and Cu reference patterns. They are tabulated in the powder diffraction file (PDF) database of the international center for diffraction data (ICDD), in

- particular PDF(Pt)#00-004-0802, PDF(Co)#00-015-0806. Reprinted from ref 90 with permission of Elsevier, copyright (2011). 139
- Figure 48 a-c) Initial CV profiles of PtCo₃ alloy nanoparticle precursor electrocatalysts annealed at 650 °C, 800 °C and 900 °C for 7 hours. d) CV profiles of pretreated PtCo₃ catalysts compared with 28.2 wt. % Pt/HSAC after dealloying (200 scans with 500 mV s⁻¹). Cyclic voltammetry was conducted from 0.06 – 1.00 V/RHE with 100 mV s⁻¹ in deaerated 0.1 M HClO₄ at room temperature. Reprinted from ref 90 with permission of Elsevier, copyright (2011). 142
- Figure 49 a) Polarization curves of dealloyed PtCo₃, annealed at 650 °C, 800 °C and 900 °C for 7 hours. b) Pt surface area specific based Tafel plots and c) Pt mass based Tafel plots of dealloyed PtCo₃ catalysts compared with pure 28.2 wt. % Pt/HSAC. Linear sweep voltammetry was performed anodically from 0.06 – 1.05 V/RHE with 5 mV s⁻¹ and 1600 rpm in oxygen saturated 0.1 M HClO₄ at room temperature. Reprinted from ref 90 with permission of Elsevier, copyright (2011). 146
- Figure 50 RRDE measurements of the oxygen reduction reaction for dealloyed a) PtCo₃ and b) PtCu₃ catalysts. Insert: Koutecki-Levich plots of dealloyed PtCo₃ (800°C/7h) and PtCu₃ (800°C/7h) at various electrode potentials. Linear sweep voltammetry were conducted anodically from 0.06 – 1.05 V/RHE with 5 mV s⁻¹ in oxygenated 0.1 M HClO₄ at room temperature. Simultaneously recorded ring current at 1600 rpm for a ring potential of E_{ring} = 1.20 V/RHE. Reprinted from ref 90 with permission of Elsevier, copyright (2011). 148
- Figure 51 Hydrogen peroxide production with the disk potential during the O₂ reduction on dealloyed PtCo₃/HSAC (800°C/7h) with Pt loading of 11.4 μg cm_{geo}⁻², pretreated PtCu₃/HSAC (800°C/7h) with Pt loading of 11.4 μg cm_{geo}⁻², untreated 28.2 wt. % Pt/HSAC with Pt loading of 14.6 μg cm_{geo}⁻² and untreated pure HSAC with carbon loading of 51.0 μg cm_{geo}⁻² in oxygen saturated 0.1 M HClO₄ at room temperature. Calculated from the data in Figure 50 (at 1600 rpm) using the eq. (5) with N = 0.22 ± 0.01. Reprinted from ref 90 with permission of Elsevier, copyright (2011). 150

- Figure 52 CV profiles of (a) Pt-Cu and (b) Pt-Co alloy nanoparticle electrocatalysts before (dashed) and after (solid line) the electrochemical dealloying process. The broad hydrogen ad/desorption regime and redox peak couple of Pt (hydr-)oxide are indicated by red and blue areas. (a) Positions (1) and (2) signify the surface dissolution of pure bulk Cu and underpotentially deposited Cu. (b) Position (1) indicates the surface dissolution of underpotentially deposited Co from a Pt alloy particle surface. Reprinted from ref ¹⁵⁸ with permission of American Chemical Society, copyright (2012).*..... 157
- Figure 53 HAADF overview micrographs of Pt-Cu and Pt-Co particle ensembles; (a), (c) before and (b), (d) after dealloying. The white arrows exemplarily denote particles with non-trivial contrast features. Reprinted from ref ¹⁵⁸ with permission of American Chemical Society, copyright (2012).* 159
- Figure 54 a) HAADF micrograph of individual dealloyed Pt-Cu nanoparticles up to 5 nm with their according HAADF intensity line profiles; b) HAADF micrograph of a dealloyed Pt-Co nanoparticle at 3.6 nm with the according intensity line profile. The black arrows signify the scan direction of the intensity profiles and the dashed lines indicate the dark shaded particle regions. Reprinted from ref ¹⁵⁸ with permission of American Chemical Society, copyright (2012).* 161
- Figure 55 a) Illustration of the formation of core-shell bimetallic nanoparticle by electrochemical dealloying. Red and light grey spheres denote Cu atoms and Pt atoms, respectively. b) Simulated HAADF intensity profiles of a core-shell Pt-Co nanoparticle at ~3.5 nm with Pt shell thickness of ~0.8 nm. Solid line in the HAADF intensity profile denotes a sharp compositional transition between the core and shell, while dashed lines indicate a smoother profile with more continuous compositional transition at the core-shell interface. Reprinted from ref ¹⁵⁸ with permission of American Chemical Society, copyright (2012).* 162

- Figure 56 HAADF micrographs of individual dealloyed Pt-Co particles with various diameters of 8 - 15 nm. As guide to the eye, these contrast features are outlined by black dashed lines. Reprinted from ref ¹⁵⁸ with permission of American Chemical Society, copyright (2012). 164*
- Figure 57 EEL line scan profiles for Pt (black) and Co (red) concentration in dealloyed Pt-Co nanoparticles at (a) 11 nm and (b) 13 nm. Insert: The direction of the line scan is indicated with a black arrow. The red area highlights the contrast features in the HAADF micrograph. Reprinted from ref ¹⁵⁸ with permission of American Chemical Society, copyright (2012). 164*
- Figure 58 HAADF micrograph of individual dealloyed Pt-Cu particles in a size range of 10 - 22 nm. As guide to the eye, the black dashed lines in the HAADF image denotes the dark shaded regions. Reprinted from ref ¹⁵⁸ with permission of American Chemical Society, copyright (2012). 166*
- Figure 59 HAADF micrographs of dealloyed (a) Pt-Cu and (b) Pt-Co particles with diameters larger than 40 nm. As guide to the eye, the white arrows and black dashed lines denote the surface pits (nanopores) on the particle surface. Reprinted from ref ¹⁵⁸ with permission of American Chemical Society, copyright (2012). 168*
- Figure 60 TEM images and EDS measurements of single dealloyed Pt-Cu and Pt-Co particles larger than 30 nm diameter after dealloying. Reprinted from ref ¹⁵⁸ with permission of American Chemical Society, copyright (2012). 169*
- Figure 61 HAADF micrograph of dealloyed Pt-Cu particle at 100 x 150 nm with a clearly visible porous structure. The pores are on the order of 3 nm. Reprinted from ref ¹⁵⁸ with permission of American Chemical Society, copyright (2012). 170*
- Figure 62 Illustration of the evolution in size-dependent morphology and composition of dealloyed Pt-Cu and Pt-Co particle electrocatalysts. Reprinted from ref ¹⁵⁸ with permission of American Chemical Society, copyright (2012). 172*

- Figure 63 a, b, c) Atomic-scale resolution HAADF electron micrographs providing 'Z-contrast' conditions of three dealloyed Pt-Co bimetallic nanoparticle electrocatalysts. a) At the upper part of this nanoparticle, individual atomic columns are resolved. It is oriented along a (-110) zone axis of the face-centered-cubic structure. As guide to the eye, d, e and f highlight contrast features (hatched and red areas) of the corresponding micrograph. Black lines indicate the outlines of the nanoparticles and red areas signify Co-enriched dark shaded regions in the HAADF micrographs. Hatched red areas represent regions which show weak or no significant shading in the HAADF micrographs but clear Co signal in the EEL analysis. Dashed lines represent neighboring particles which are not in focus (d). Black arrows indicate the traces and direction of EEL line scans given in Figure 64..... 183*
- Figure 64 EEL intensity profiles across the dealloyed particles for Pt (black squares) and Co (red circles), respectively. The EEL profiles are normalized with the elemental scattering factor and hence represent thickness projected compositions. Insets on the top right depict sketches of the morphology and contrast features of the individual particles investigated. Black arrows across the sketches indicate the traces of the individual EEL line scans. Red arrows highlight shoulder/plateau and maxima features of the Co signal. 184*
- Figure 65 Co EEL scan of the particle in Figure 63c in comparison with the curve of an ideal ellipsoidal (or spherical) core with 4.6 nm diameter and a constant Co composition which shows no variation over the diameter of the core. The experimental curve has two local minima (2) within the core of the particle and clearly discriminates from the ideal curve (hatched area). The minima indicate a local depletion of Co. Outwards at the positions 3, the Co composition increases again and match the ideal curve of the ellipsoidal core of the particle. Outside of the core, i.e. in the shell region, the Co-composition decreases continuously. This observation suggests the existence of two 2 – 3 atoms thick adjacent bimetallic spherical shells just below the outer Pt shell, the inner showing a compositional minimum in Co, the outer a Co maximum..... 185*

Figure 66 a) Extraction of the actual atomic-scale Co composition within a specific shell (blue) from a representative Co EEL intensity profile (red). Shoulders and slight minima in the EEL intensity profile (2) correspond to strong depletions in the local Co composition. (b) and (c): Illustration of the formation mechanism of the unusual compositional multi-shell nanoparticle structure. A quarter of a spherical cross section through a dealloyed Pt-Co particle with a Co rich core (red color near origin) and Pt rich shell (grey color) is shown as background in both Figures. (b) The blue solid line schematically shows an early-stage Co composition profile (Co concentration on vertical axis, and distance from particle center on x axis) with monotonic negative slope as a consequence of rapid initial surface dealloying, Co bulk downhill diffusion (red arrow), and associated vacancy injection into the particle (black arrow). Prohibitively high surface energies of nanoscale voids prevent aggregation of the injected vacancies. (c) Instead, Pt surface diffusion acts as a vacancy sink and causes vacancy back migration toward the particle surface (inverse Kirkendall effect) followed by subsequent vacancy ejection/annihilation at the surface. The migration of vacancies is coupled to an opposite uphill Co diffusion (red arrow) inducing a sharp Co drop-off at position 4. The resulting Co non-monotonic single-maximum compositional profile (dashed blue curve) is consistent with the experimentally observed compositional multi-layer structure involving adjacent Co maxima and minima.....187

1 Introduction and Background

The polymer electrolyte membrane fuel cell (PEMFC) is a device that converts chemical energy directly into electrical energy and is one of the promising applications to solve the challenging problems relating to a clean energy production and conversion in the future. In particular, alkaline fuel cells have attracted great attention due to their improved durability and reduced material costs compared to acidic counterparts.¹ Furthermore, a renaissance in the alkaline fuel cells is recently occurring.^{2, 3} A long history of successful applications in the space program^{4, 5} shows, for example, the general importance of alkaline fuel cells. An additional advantage is thereby also the possibility⁶ of using non noble metal catalyst to substitute the costly platinum. Problems with corrosion, electrolyte carbonation and stability of membranes remain to date.

Currently, the most widely used electrocatalyst for PEMFC is carbon supported platinum nanoparticles. But, the critical issues should be addressed: the less catalytic efficiency for the oxygen reduction reaction (ORR) ($\text{O}_2 + 4 \text{H}^+ + 4 \text{e}^- \rightarrow 2 \text{H}_2\text{O}$), the high material cost and the gradual Pt degradation, such as Pt dissolution, Ostwald ripening, coalescence, carbon corrosion and Pt particle detachment. Under the operating conditions the kinetic limitation of ORR causes a cathodic overpotential loss of around 0.3 – 0.4 V, associated with the surface adsorption and reductive charge transfer process on the catalyst surface of the cathode side. Therefore, the development of novel highly active fuel cell electrocatalysts with reduced Pt loading for the electroreduction of oxygen still remains the important challenges in acidic and alkaline media. In particular, ORR studies in alkaline media are less frequently found in the literature, while Pt and Pt alloy nanoparticle electrocatalysts for ORR have been extensively studied in acid.

In the last decades Pt bimetallic nanoparticle catalysts (PtM with M = Co, Cu, Ni, etc.) have become more important due to the improved ORR activity, the decrease of Pt loading and therefore the resulting reduced material cost. All bimetallic particle concepts which show an activity improvement focus on the modification of the surface composition at the atomic scale.⁷⁻²⁴ The observed

surface reactivity induced by the neighborhood of two dissimilar metals in or near the particle surface is associated with ensemble effects, ligand effects²⁵⁻²⁷ and geometric effects^{25, 28}.

Core-shell nanoparticles as particular type of arrangement of binary metals have attracted much attention in electrochemical energy conversion²⁹⁻³⁵. They are distinguished by a particle shell of enriched or pure metal A surrounding a core with different composition (pure metal B^{36, 37} or alloys of metals A and B¹⁶). Dependent on the shell thickness, the improved surface catalytic reactivity is based on the short-range chemical ligand effects and/or long-range geometric effects such as lattice strain^{9, 10, 16, 38-40}.

The focus on this thesis is the design of novel highly active Pt alloy nanoparticle electrocatalysts and the structural and compositional characterization of the dealloyed Pt alloy core-shell nanoparticles in their most active state. This work provides a fundamental insight into the dynamic behavior of alloy formation and particle growth, the electrolyte-dependent ORR performance and the atomic processes occurring during the dealloying of nanoscale materials. New size-dependent morphological and compositional structures of dealloyed active Pt alloy are here uncovered and discussed. The aim of this thesis is the rational design of Pt bimetallic fuel cell nanoparticle catalysts with improved surface catalytic properties.

1.1 Research Goals and Strategies

Electrochemical dealloying of Pt alloys has emerged as a novel and important preparation process for highly active fuel cell electrocatalysts. The improved ORR activity is required to meet and exceed the activity targets of the U.S. Department of Energy⁴¹ for the technical application of PEM fuel cells. In particular, the dealloyed Pt bimetallic core-shell nanoparticles show clearly improved ORR activity. They are generated in-situ by selective electrochemical dissolution of less noble metal from the surface of alloy particle.

A better understanding of the structure – ORR activity relation provide a development of novel highly active catalysts. In this thesis, the experimentally determined ORR activities are correlated with initial and dealloyed active structures and compositions of Pt alloys, shown in Figure 1.

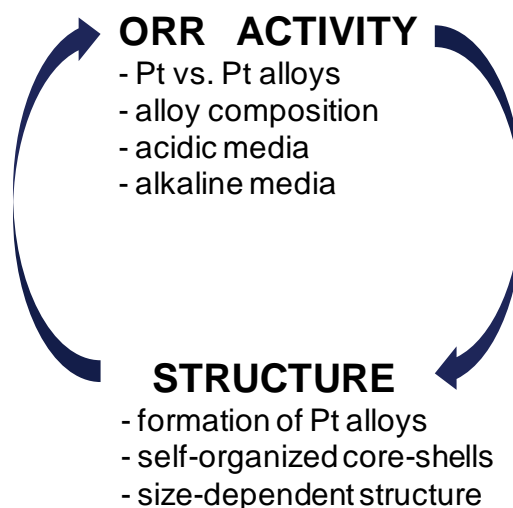


Figure 1 Structure –ORR activity relation.

The initial state of Pt alloy nanoparticles is a critical primary stage to obtain highly catalytically active dealloyed core-shell nanocatalysts. The catalytic performance is strongly influenced by the structure, composition and particle size of bimetallic nanoparticles. The clarification of the structure – ORR activity relation of thermally annealed Pt-M alloy nanoparticle catalysts is often limited by non-uniform alloy crystal phases (ordered, disordered, different compositions) and wide particle size distributions by sintering and coalescence. This issue is addressed in chapter 3. There involves in-situ HT-XRD studies of

the alloying process at the atomic level correlating microscopic alloy parameters such as lattice constant and crystallite size with experimental control parameters such as annealing temperature, heating rate and annealing time. The aim of this work is to design practical synthetic guidelines for the preparation of uniform disordered or ordered fcc PtM alloy electrocatalysts with desired particle size and composition.

The ORR activities of Pt alloys have been largely studied in acid, while it looks otherwise sparsely for ORR studies in alkaline media. Here, the changes of the composition of the outermost atomic layers of Pt-Co and Pt-Cu alloys are traced by surface-sensitive cyclic voltammetry technique. The background of this thesis is the better understanding of the electrochemical behavior and ORR performance for various Pt-Cu and Pt-Co alloy nanoparticle catalysts in different electrolyte solutions and pH values (chapters 5 and 6).

After dealloying the Pt alloys are subsequently analyzed to identify the active morphological and compositional structure. The single core-shell nanoparticles of a few nanometers diameter are the morphological basic type in dealloyed bimetallic nanoparticle ensembles. However, no particular emphasis is given to date how the size of dealloyed bimetallic particles is linked with their intraparticle structure and composition on an atomic scale. In this work, the size – structure – morphology relationships of dealloyed Pt bimetallic particles are presented in chapter 7. A detailed understanding of the size – structure – morphology relationships of the bimetallic particles spanning from the nano to the macro scale is, however, important for the rational design of improved electrocatalysts.

The conventional two-layer core-shell concept emerges as an insufficient structural description for dealloyed bimetallic nanoparticles of 10 – 20 nm. An atomic-scale structural and element-compositional investigation of a Pt-Co core-shell nanoparticle fuel cell catalyst reveals unusual self-organized compositional subsurface finestructure. Chapter 8 presents the new self-organized compositional motifs, such as off-center Co “satellite cores” and compositional depth profiles consisting of alternating layers with Co-depletion and Co-enrichment. The relevance of these observed features is discussed for the electrocatalysis.

1.2 Acidic and Alkaline Hydrogen PEM Fuel Cell

Fuel cells are electrochemical devices that convert chemical energy directly into electricity and offer one of the promising technologies for clean energy production and conversion in the future. The simple overall reaction is the conversion of hydrogen and oxygen to pure water. In 1849, William Grove invented the first fuel cell. Although at that time the research on fuel cells were minimally explored, since second half of the twentieth century fuel cells have extensively investigated. There are five major types of fuel cells which differentiate from one another on the basis of their electrolyte: phosphoric acid fuel cell (PAFC), polymer electrolyte membrane fuel cell (PEMFC), alkaline fuel cell (AFC), molten carbonate fuel cell (MCFC) and solid oxide fuel cell (SOFC).

This thesis focuses on the acidic and alkaline PEMFCs. Compared to the other fuel cell types, PEMFC provides the best fast-start and on-off cycling characteristics. PEMFC is suitable for portable applications due to the highest power density of all fuel cell types ($300 - 1000 \text{ mW/cm}^2$) and low operating temperature.^{42, 43}

Figure 2 illustrates schematics of an acidic and alkaline PEMFC. The differences of both PEMFC types are visible by the single half fuel cell reactions and by the diffusing electrolyte species through the membrane. In acidic PEMFC, the hydrogen as fuel is oxidized to protons on the anode side and the oxygen is reduced to water on the cathode side. The membrane serves as a separator of both half cell reactions and proton conductor. In contrast to the acidic PEMFC, where H^+ ions diffuse from the anode to cathode, in alkaline PEMFC OH^- ions are transmitted from the cathode to anode. Therefore, on the cathode side the oxygen is reduced to hydroxide ions, which diffuse through the anion-conductive membrane to the anode side and react with hydrogen to water. Despite the improved ORR performance in alkaline media compared to that in acid, the sluggish kinetic of oxygen reduction reaction (ORR) is still the rate-limiting reaction in the overall fuel cell. An additional advantage of alkaline PEMFCs is the possibility⁶ of using non noble metal catalyst such as metal oxide⁴⁴, ruthenium-based chalcogenides^{45, 46}, pyrolyzed porphyrins⁴⁷⁻⁵¹, and

cobalt/iron-polypyrrole-carbon^{52, 53}, to substitute the costly platinum. More details about acidic and alkaline PEMFC are described in Table 1.

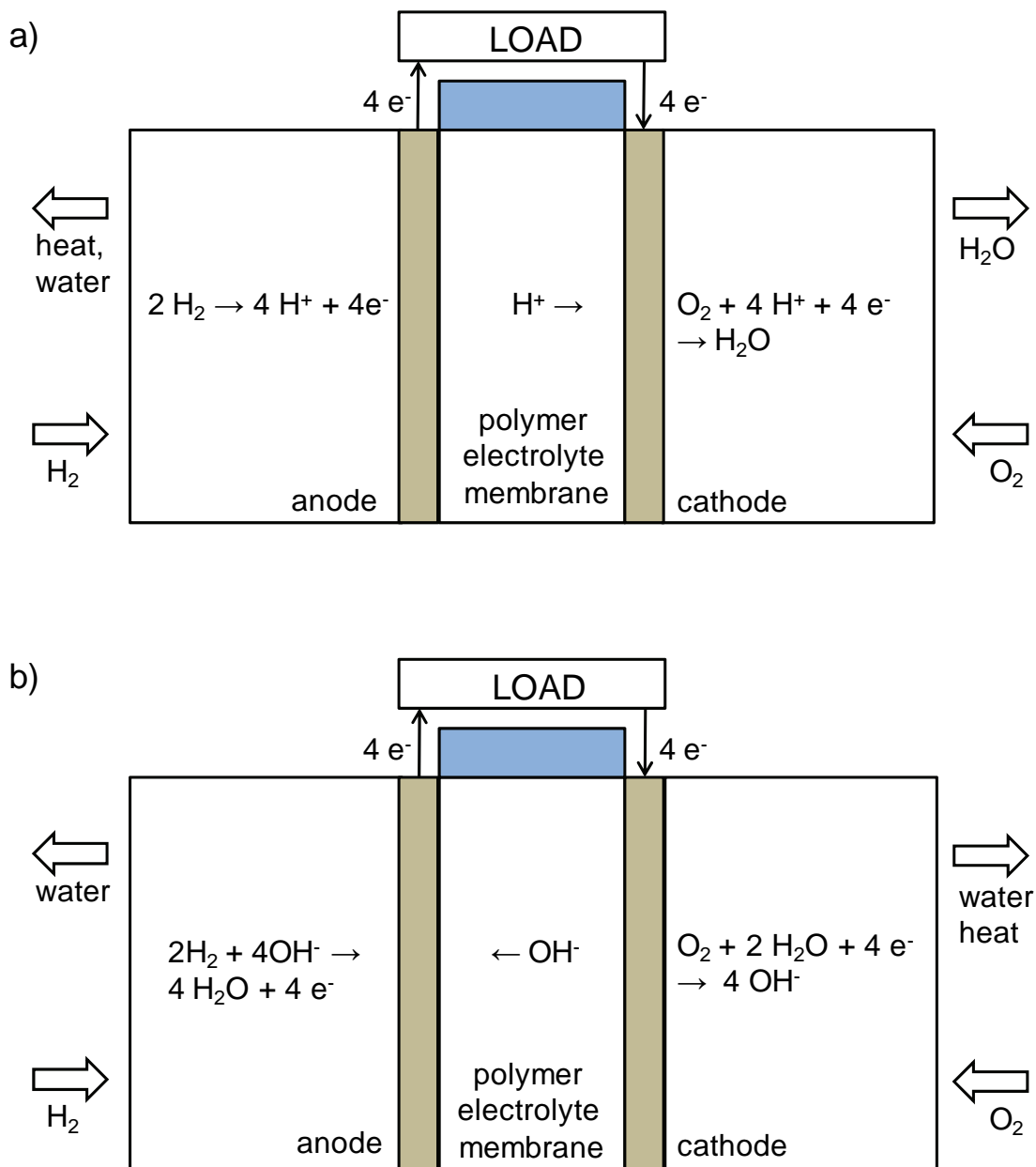


Figure 2 Schematics of an (a) acidic and (b) alkaline PEMFCs and the corresponding half cell reactions.

Table 1 Direct comparison of the acidic and alkaline PEMFCs.^{42, 43}

	acidic PEMFC	alkaline PEMFC
fuel	H ₂	H ₂
oxidizer	O ₂ , air	O ₂ , air
ion transferred	H ⁺	OH ⁻
most common catalyst	Pt	Pt or Ni
operating temperature	25 °C to 90 °C	25 °C to 90 °C
maximum efficiency	~ 58 %	~ 64 %
advantages	<ul style="list-style-type: none"> - commercially available polymer electrolyte membrane 	<ul style="list-style-type: none"> - improved cathode performance - improved conductivity - potential for non-precious metal catalysts
disadvantages	<ul style="list-style-type: none"> - insufficient contact (three boundary) - humidity dependence - very poor CO and S tolerance - expensive membrane - active water management is required 	<ul style="list-style-type: none"> - insufficient contact (three boundary) - high purification of H₂ and O₂ (air) - no commercially available anion exchange membrane - carbonate precipitates (electrolyte carbonation) - remove water from the anode

1.3 Mechanism of the Oxygen Reduction Reaction (ORR)

The mechanisms of the oxygen reduction reaction (ORR) in acidic and alkaline media are presented in Figure 3. It is obvious that the postulated mechanisms involve two parallel reaction paths. The main reaction paths are the direct reduction of oxygen to water and hydroxide ions in acidic and alkaline electrolytes, respectively. The second parallel reactions proceed via two-electron step to the formation of H_2O_2 and HO_2^- and subsequently another two-electron step to the final products, H_2O and OH^- .

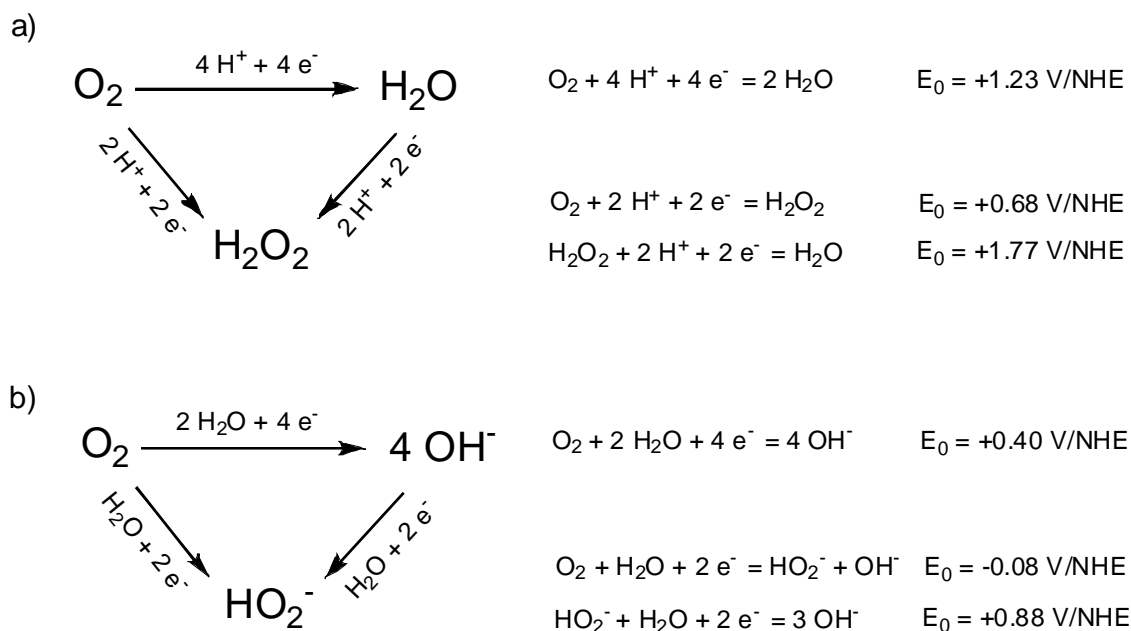


Figure 3 Mechanisms of the oxygen reduction reaction (ORR) in (a) acidic and (b) alkaline media.

The quantification of HO_2^- and H_2O_2 species which produce during the oxygen reduction can be determined by using of the Rotating Ring Disk Electrode (RRDE) technique. The serial reaction path reduces the overall fuel cell efficiency and their intermediate products (H_2O_2 and HO_2^-) destroy the membrane which leads to the additional reducing efficiency. Therefore, the electrocatalysts should reveal a high selectivity for the direct 4-electron-reaction path.

1.3.1 Pt Alloy Electrocatalyst Concepts

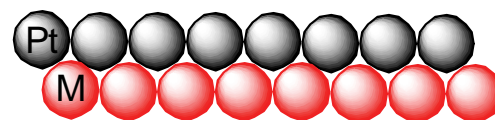
Figure 4 illustrates the different Pt alloy electrocatalyst concepts. All bimetallic concepts for the improved activity are related with the modification of the surface composition of the bimetallic particles in the atomic scale. The observed surface reactivity induced by the neighborhood of two dissimilar metals in or near the particle surface is addressed to ensemble effect, ligand effect and geometric effect. The following part described the difference of the effects.

Ensemble effect is caused by unequal surface atoms in terms of individual or cluster bimetallic groups, which offer different mechanistic functionalities.^{54, 55} A well known example is palladium atoms pairs on gold for the catalytic gas phase reaction.⁵⁶ Ligand effect arises by electronic charge transfer between direct dissimilar adjacent surface atoms and leads to a change of the electronic band structure.^{9, 10, 25-27, 38} Geometric effect is induced by the structural arrangement of the surface atoms.^{16, 25, 28, 39, 40} Thus, the mismatch of the lattice parameters induces a compressive or expansive interatomic distance at the outermost surface layer.²⁰ Mostly, the ligand and geometric effects appear together and simultaneously affect the surface reactivity. Currently, Pt₃Ni (111) with the special atomic arrangement, where Pt atoms form the outermost surface layer and Ni atoms the second atomic layer, is still the most active catalyst for ORR.¹⁴ Nevertheless, the geometric effect exhibits a surface reactivity over more than a few atomic layers compared to the ligand and ensemble effects.

ensemble effect
(bifunctional, uniform alloy)
e.g. PtRu



short-range ligand effect
(Pt top layer)
e.g. Pt monolayer, Pt₃Ni(111), Pt ML/Pd core



long-range geometric effect
(Pt top layer, base metal in 2-3rd layers)
e.g. Pt skin, dealloyed core-shell

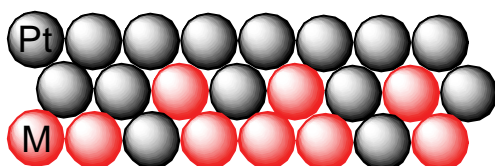


Figure 4 Pt alloy electrocatalysts concepts and their fundamental mechanisms to tune the catalytic surface reactivity.

1.3.2 “Volcano” Plot

The Butler-Volmer equation is the fundamental relationship between the kinetic current density j and potential E in the electrochemical kinetics. The rate expression for the oxygen reduction reaction (ORR) is

$$j = n F k_{\text{CO}_2} (1 - \theta_{\text{ad}}) \exp\left(-\frac{\alpha F E}{RT}\right) \exp\left(-\frac{\Delta G_{\text{ad}}}{RT}\right) \quad (\text{eq 1})$$

where c_{O_2} is the concentration of oxygen, θ_{ad} is the coverage of adsorbed species, n is the number of transferred electrons, F is the Faraday constant, R is the universal gas constant, T is the temperature, ΔG_{ad} is the Gibbs free energy and α is the symmetry factor. At a constant potential, the logarithm of the reaction rate should be a linear function of the Gibbs free energy of the adsorption of the rate-determining step intermediates. The reaction rate grows from positive (weak adsorption) to negative (strong adsorption) values of ΔG_{ad} . The preexponential term becomes dominate with increasing coverage of adsorbed intermediates θ_{ad} , which leads to a decrease of the reaction rate.

A simple relationship can be constructed from the theoretical calculations of a number of close packed metal surfaces and their binding energies of M-O for the oxygen reduction reaction, referred to as “Volcano” plot. Figure 5 illustrates the Volcano plot, which reflects the trends on different metal surfaces as a function of the calculated oxygen adsorption energy. The theoretical prediction is in good agreement with the experimental data. The Pt alloys on the left side of the top of the Volcano plot show strong binding energies, while on the right side the adsorbing energy becomes weaker.

Norskov et al.^{25-27, 57} reported a correlation of the catalytic activity of the metal with the state of the d-band center, referred to as “d-band model”. The increase or decrease of the reactivity can be achieved by the shift of the d-band center. It is based on the general principle of the formation of chemical bonds. A strong bonding is existent, if the antibonding is empty (a shift up through the Fermi level). In contrast, if the antibonding state is shifted down through the Fermi level (the antibonding become filled), the binding is weak. The position of the d-band center is influenced on the geometric and ligand effects such as alloy

formation of dissimilar metals. After the predictions^{25-27, 57}, the bindings of Pt-O and Pt-OH are too strong and affect a decrease of the ORR activity. To enhance the surface reactivity of metals, it is necessary to shift down the d-band center from the Fermi level. Kitchin et al.²⁵ have shown that a downshift of the d-band center causes a weakness of the adsorption binding of Pt-O for the reduction of oxygen and results in an improved activity.

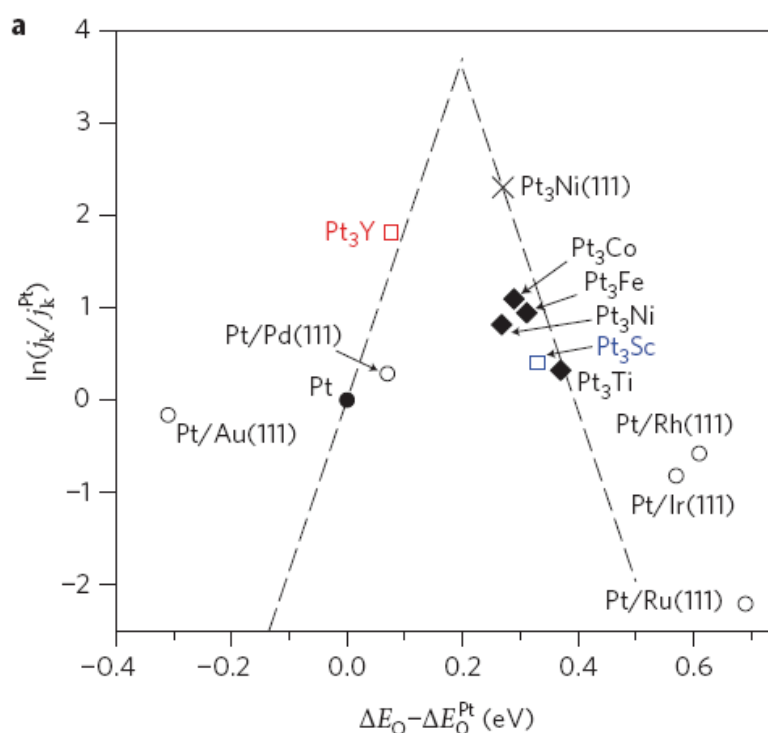


Figure 5 Volcano plots: trends in kinetic current density (symbolized the activity) plotted as a function of the calculated oxygen adsorption energy for the oxygen reduction reaction on Pt alloys. The calculation is in good agreement with the experimental data from different groups. The dashed lines indicate the theoretical predictions.¹⁹

1.4 Platinum – Copper System

Pt-Cu catalysts were synthesized by impregnation – freeze-drying – annealing method and subsequently electrochemically treated in 0.1 M KOH (pH 13) and 0.1 M HClO₄ (pH 1) between a voltage range of 0.06 and 1.00 V/RHE in this work. For the preparation of Pt-Cu alloys, the impregnated powder (see chapter 2.1 *Synthesis of PtM (M = Cu, Co) Alloy Nanoparticle Precursor Electrocatalysts*) was annealed at 800 °C for 7 hours under reductive atmosphere.

In the view to the macroscopic thermodynamic stable phase diagram of Pt-Cu alloy system (see Figure 6), Pt-Cu alloys form ordered structures in three different regions: PtCu₃, PtCu and Pt₃Cu. The ordered PtCu₃ and Pt₃Cu alloys exhibit a L1₂ structure (Pm3m) below 650 °C and 600 °C, respectively. In the case of ordered PtCu₃ L1₂ structure, Pt atoms take the positions at the eight edges of the cubic unit cell and Cu atoms occupy the face center positions. The Pt and Cu atoms of ordered Pt₃Cu are reversely occupied in the L1₂ unit cell. Below 816 °C, PtCu shows a rhombohedral structure with a space group of R3m, referred to as Hongshiite structure. During the annealing at 800 °C to form various compositional Pt-Cu alloys, these temperatures for the ordered Pt-Cu alloy structures were clearly passed. According to the crystal phase Rietveld refinement analysis, however, the Pt-Cu main components exist as substitutional disordered face-centered cubic (fcc) alloys.

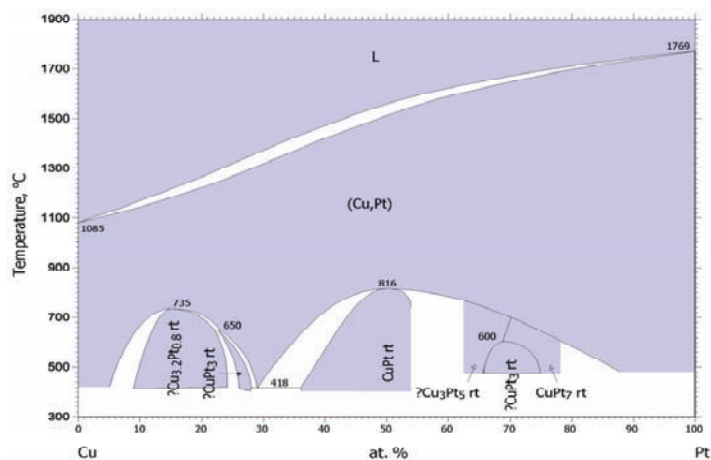


Figure 6 Macroscopic thermodynamic stable phase diagram of Pt-Cu alloy system.⁵⁸

Figure 7 shows a collection of DFT calculated surface segregation energies of all transition metals⁵⁷. There is predicted the effects of thermal-induced alloy formation on the surface segregation behavior for Pt-Cu. According to the DFT theoretical predictions, Cu rich Pt-Cu alloys reveal no significant segregation behavior, while a strong antisegregation tendency is to expect for Pt rich Pt-Cu alloys. Cu which solutes in a Pt host tends to segregate to the inside, while Pt diffuses in the contrary direction towards the surface. The resulting Pt skin prohibits the electrochemical dissolution of internal Cu.

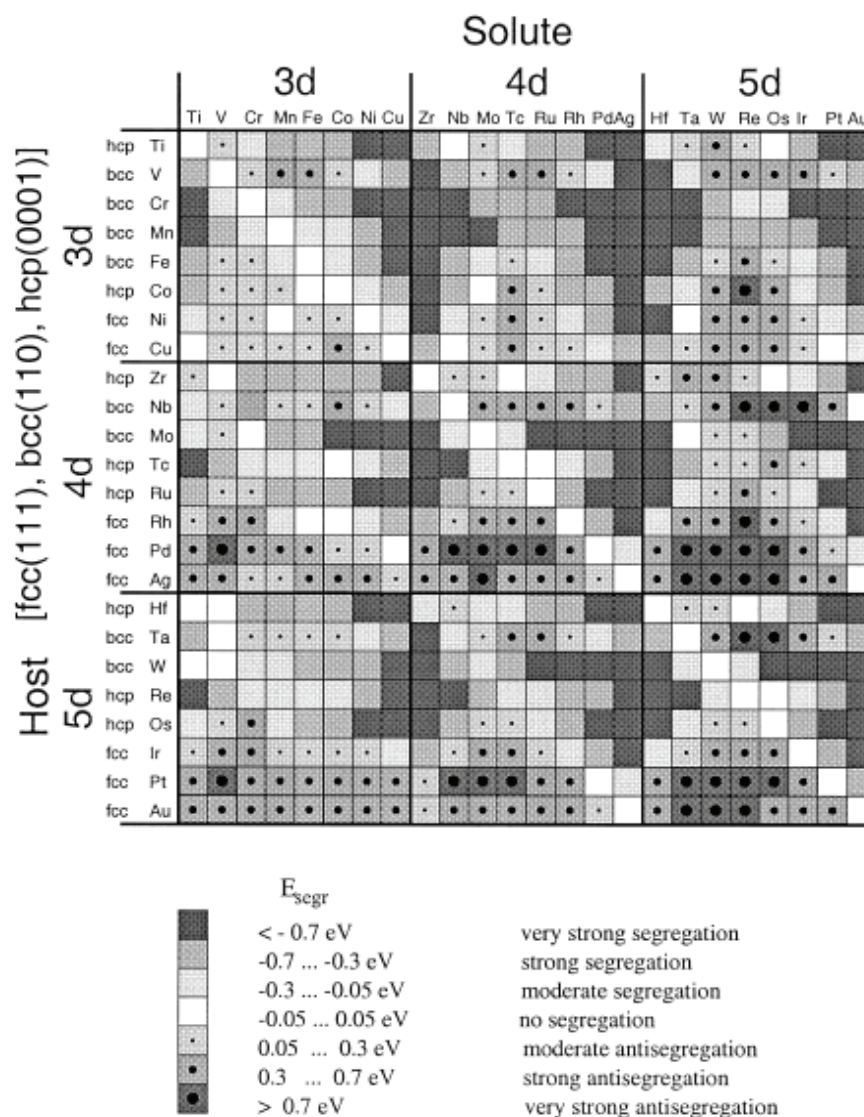


Figure 7 Collection of calculated segregation energies on the most close-packed surface of all binary combinations of transition metals.⁵⁷

The Pt-Cu alloys were electrochemically treated in the voltage range of 0.06 and 1.00 V/RHE in 0.1 M HClO₄ (pH 1) and 0.1 M KOH (pH 13). The conversion from NHE to RHE is $V/NHE = V/RHE - 0.058 \text{ V} \cdot \text{pH}$. The Pourbaix diagram⁵⁹ for the Cu – water system is shown in Figure 8a. At pH 1 Cu is stable between 0 and 0.34 V/NHE (0.06 – 0.40 V/RHE), while above this potential Cu oxidizes to Cu⁺² ions. At pH 13 and the same voltage range, copper can exist as: Cu₂O and HCuO₂⁻ as soluble species. Cu is relatively stable between -0.7 and -0.35 V/NHE (0.06 – 0.40 V/RHE). Above this potential, Cu oxidizes to Cu₂O. Cu₂O is stable in a narrow potential range from -0.35 /NHE to -0.2 V/NHE (0.4 – 0.55 V/RHE) and oxidizes further to soluble HCuO₂⁻ species. The dissolution of Cu₂O occurs in the following reaction: $\text{Cu}_2\text{O} + 3 \text{H}_2\text{O} \rightarrow 2 \text{HCuO}_2^- + 4 \text{H}^+ + 2 \text{e}^-$.

The Pourbaix diagram for the platinum – water system is shown in Figure 8b. At pH 1 and pH 13 under the chosen voltage conditions, Pt is stable from 0.06 V/RHE to about 0.95 V/RHE, where above this potential the oxidation from Pt to Pt(OH)₂ begins. During the voltage cycling this potential is passed for a short time. To avoid the formation of irreversible stable Pt oxide species, the upper limit of potential of 1.0 V/RHE was never exceeded in any experiment.

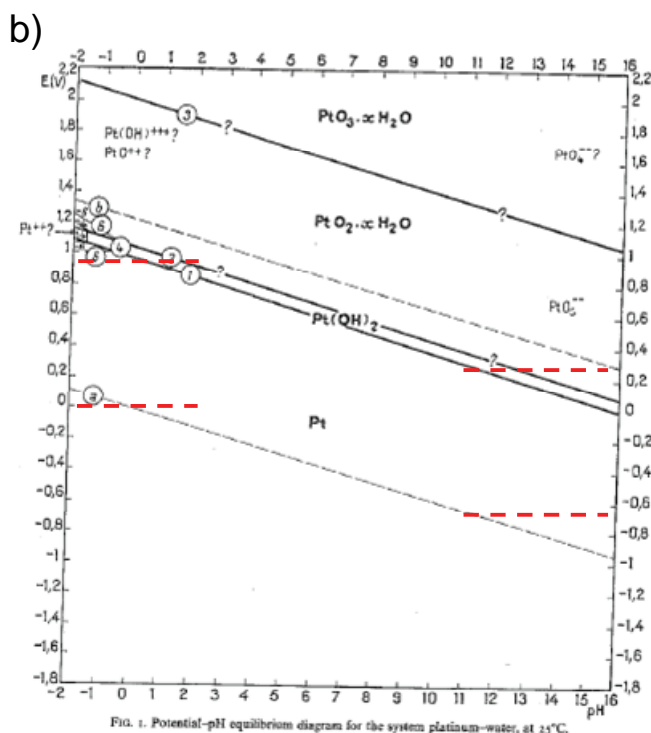
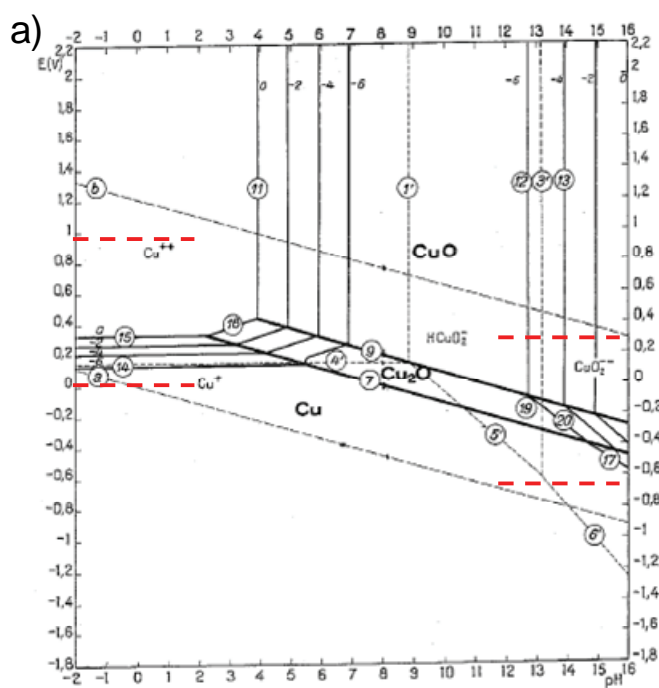


Figure 8 Potential – pH equilibrium diagram for the systems (a) copper – water and (b) platinum – water at 25 °C.⁵⁹ The red dashed lines denote the voltage range cycling of 0.06 V and 1.00 V/RHE at pH 1 (0.1 M HClO₄) and pH 13 (0.1 M KOH).

1.5 Platinum – Cobalt System

This thesis shows the synthesis and electrochemical behavior of various compositional Pt-Co catalysts in 0.1 M KOH (pH 13) and 0.1 M HClO₄ (pH 1) between 0.06 and 1.00 V/RHE. More details about the preparation of Pt-Co alloys are to find in chapter 2.1 *Synthesis of PtM (M = Cu, Co) Alloy Nanoparticle Precursor Electrocatalysts*. The annealing condition of the various Pt-Co alloys was 800 °C for 7 hours. Only for Co rich alloys, the maximum annealing temperatures were varied from 650 °C to 900 °C for 7 hours to drive the Pt-Co alloy formation and particle growth. Figure 9 shows the macroscopic thermodynamic stable phase diagram for Pt-Co system. Only two regions show ordered structures: PtCo and Pt₃Co. The tetragonal PtCo (P4/mmm) and cubic Pt₃Co (Pm3m) structures are formed below 825 °C and 750°C, respectively. For the Pt₃Co L1₂ structure (Pm3m), Co atoms take positions at the eight edges of the unit cell and Pt atoms occupy the six face center positions. During the annealing at 800 °C to form PtCo and Pt₃Co alloys, these temperatures were clearly passed. However, the evaluation of the Rietveld refinement for PtCo and Pt₃Co reveals that the main component for PtCo and Pt₃Co catalysts exist as substitutional disordered alloy crystal phase. In the view of the phase diagram to Co rich alloys, there shows no ordered structures.

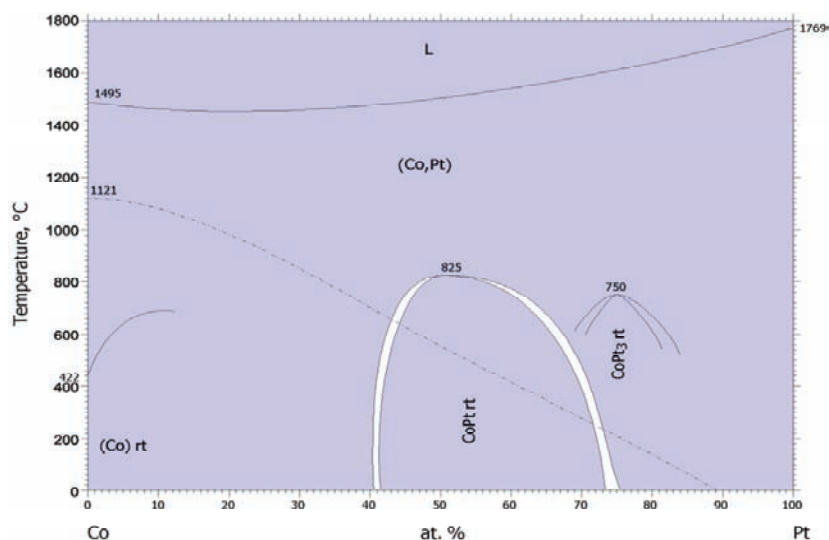


Figure 9 Macroscopic thermodynamic stable phase diagram of Pt-Co alloy system.⁶⁰

According to the predicted tendencies of surface segregation⁵⁷ shown in Figure 7, Co rich Pt-Co alloys show a strong segregation behavior. The solute Pt segregates towards the surface, while Co as host medium diffuses in the opposite direction. The trend of the strong surface segregation of Pt in Pt rich Pt-Co alloys is also evident and is in excellent agreement with the reported experimental observations.¹⁰

The Pt-Co alloys were electrochemically treated in the voltage range of 0.06 and 1.00 V/RHE in 0.1 M HClO₄ (pH 1) and 0.1 M KOH (pH 13). The Pourbaix diagram⁵⁹ for cobalt – water system is shown in Figure 10. Co is a non noble metal and dissolves in the chosen voltage range at pH 1. Meanwhile, at pH 13 under the same voltage range, Co can exist as: Co(OH)₂, Co₃O₄ and Co(OH)₃. The predominant species formed up to 1.0 V/RHE is Co(OH)₃ through the oxidation of Co(OH)₂ with the temporary stable Co₃O₄ as the intermediate specie due to its very narrow voltage range. The Pourbaix diagram for Pt – water system is described in chapter 1.4.

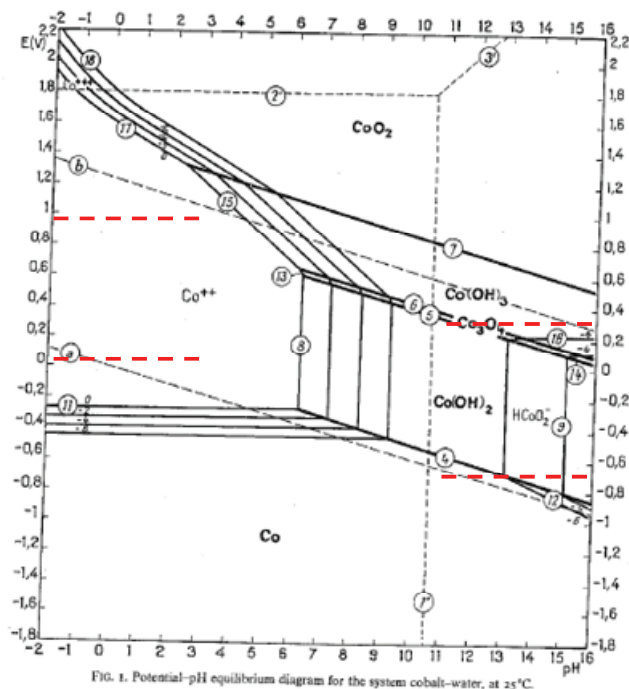


Figure 10 Potential – pH equilibrium diagram for the systems cobalt – water at 25 °C.⁵⁹ The red dashed lines denote the voltage range cycling of 0.06 V and 1.00 V/RHE at pH 1 (0.1 M HClO₄) and pH 13 (0.1 M KOH).

2 Experimental Methods

2.1 Synthesis of PtM (M = Cu, Co) Alloy Nanoparticle Precursor Electrocatalysts

The Pt-M (M = Cu, Co) alloy nanoparticle precursor electrocatalysts were prepared by a wet metal precursor impregnation – freeze-drying method, followed by annealing in a reductive atmosphere.

The following commercially available source materials were applied: high surface area carbon (HSAC) supported Pt nanoparticles (28.2 wt. %, part no. TEC10E30E, supplied by TKK, Japan), $\text{Cu}(\text{NO}_3)_2 \cdot 2.5 \text{H}_2\text{O}$ (Sigma Aldrich, #467855) and $\text{Co}(\text{NO}_3)_2 \cdot 6 \text{H}_2\text{O}$ (Alfa Aesar, #010694). All chemicals were used as received without further purification.

Table 2 summarizes the weighted amounts of Pt/HSAC and metal precursor salts for the synthesis of Pt-M (M = Cu, Co) alloy nanoparticle precursor electrocatalysts. Firstly, the metal precursor salt was dissolved in 3 – 4 ml of purified water. The Pt/HSAC was added to the metal precursor solution. The suspension was ultrasonicated for 5 min using a Branson Sonifier 150D with a power output of 7 – 8. The light viscous slurry was then frozen in liquid nitrogen for 15 min and freeze-dried (LABCONCO, Freezone 6) at 0.035 mbar for 2 – 3 days (see Figure 11 a-c). Finally, the dried, impregnated powder was annealed in a tube furnace at a maximum temperature of 800 °C for 7 hours in 4 vol% / 96 vol% hydrogen/ argon atmosphere (quality of 5.0, supplied by AirLiquide) with a flow rate of 100 ml min⁻¹. The impregnated powder was carefully given in a quartz tray and covered partially with a quartz plate for opened gas flow. Shown in Figure 11 e-f, the quartz tray prepared with impregnated powder was subsequently transferred in a quartz tube of the three zone furnace (supplied by Carbolite GmbH, Germany). The annealing protocol consisted of two temperature holds with a heating-ramp of 10 °C min⁻¹. Before the heating process started, the hydrogen/ argon had been previously flown through the quartz tube with 100 ml min⁻¹ at room temperature for 1 hour to remove oxygen. Firstly, the temperature was increased to 250 °C and held at 250 °C for 2 hours to decompose the precursor anions. After 2 hours at 250 °C,

the temperature was again increased with a heating rate of $10\text{ }^{\circ}\text{C min}^{-1}$ to the maximum annealing temperature of $800\text{ }^{\circ}\text{C}$ for 7 hours. Only for PtCo_3 catalysts the influence of the maximum annealing temperature on the Pt-Co alloy formation, crystal structure and particle growth was studied at $650\text{ }^{\circ}\text{C}$, $800\text{ }^{\circ}\text{C}$, and $900\text{ }^{\circ}\text{C}$ for 7 hours. After 7 hours at the maximum annealing temperature, the cooling process was rapidly reached by opening the furnace. When the room temperature had been achieved, the reductive gas flow was stopped and switched to 1 vol% O_2 / 99 vol% N_2 (quality of 5.0, supplied by AirLiquide) to prevent the carbon burning. The calculated platinum content of the Pt alloy nanoparticle precursor electrocatalysts is listed in Table 2.

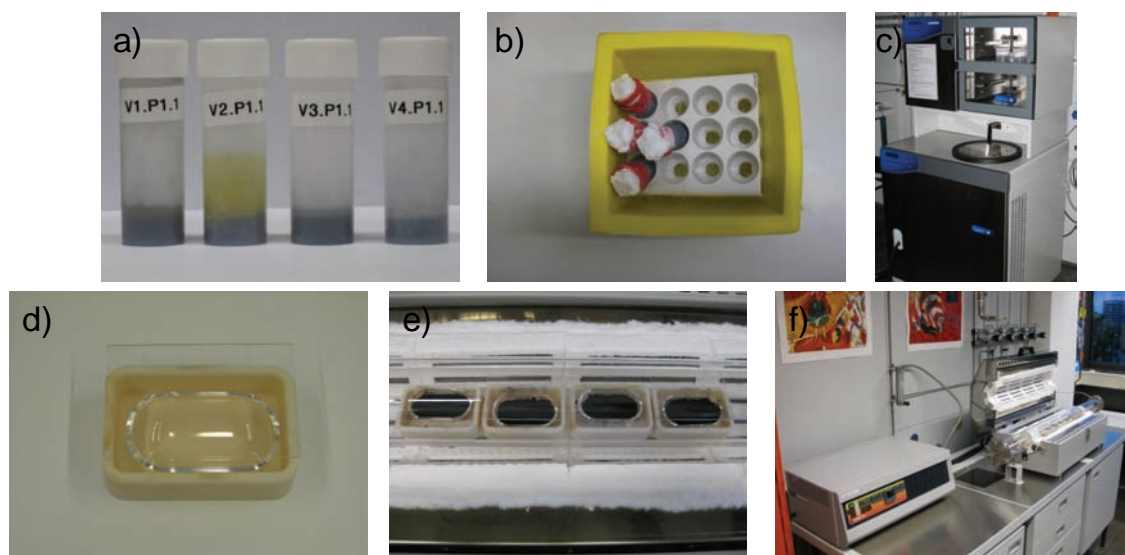


Figure 11 Images of the synthesis of Pt-M alloy nanoparticle precursor electrocatalysts. (a) light viscous suspension after sonication, (b) frozen samples in liquid nitrogen, (c) samples in a freeze-drier, (d) quartz tray with a quartz plate in an alumina crucible, (e) impregnated powder in a quartz tube of the three-zone furnace, (f) opened three zone furnace.

Experimental Methods

Table 2 Proportioning the catalyst components for Pt-M alloy nanoparticle precursor electrocatalysts.

	Mass of 28.2 wt. % Pt/HSAC [mg]	mass of $\text{Cu}(\text{NO}_3)_2 \cdot 2.5 \text{H}_2\text{O}$ [mg]	final calculated Pt content wt. %
PtCu ₃	250	251	22
PtCu	250	84	26
Pt ₃ Cu	250	28	27

	Mass of 28.2 wt. % Pt/HSAC [mg]	Mass of $\text{Co}(\text{NO}_3)_2 \cdot 6 \text{H}_2\text{O}$ [mg]	Final calculated Pt content wt. %
PtCo ₃	250	316	22
PtCo	250	105	26
Pt ₃ Co	250	35	27

2.2 Electrochemical Characterization

2.2.1 Preparation of Thin Catalytic Film Electrode

A commercial glassy carbon (GC) of a rotating disk electrode (RDE) (supplied by PINE Research Instrument, USA) (see Figure 12b) was firstly polished with alumina of 1.0 μm and nylon polishing cloth (Buehler Micropolish Alumina Alpha #1.5 μm , Buehler NYLON PSA 2 7/8") and subsequently polished with alumina of 0.5 μm and microcloth polishing cloth (Buehler Gamma Micropolish II Alumina #0.5 μm , Buehler MicroCloth PSA 2 7/8"). The GC electrode had a diameter of 5 mm and a geometric surface of 0.196 cm^2 . The polished GC electrode was cleaned and bath-sonicated in purified water for 5 min. To dissolve organic impurities, the GC electrode was cleaned with acetone (Sigma Aldrich, 99.5+%, A.C.S. reagent; 179124-2.5l) using a sonication bath and finally again in purified water. The GC electrode was dried under a nitrogen flux. Now, the GC electrode was ready for the preparation of the thin catalytic film.

About ~ 5 mg of the as synthesized Pt alloy nanoparticle precursor electrocatalyst powder was mixed in 3.98 ml of purified water, 1.00 ml of 2-propanol (Sigma-Aldrich, 99.5+%, A.C.S. reagent, #19076-4) and 20 μl of 5 wt.% Nafion solution (Sigma-Aldrich, 274704-25ml) (see Figure 12c). The suspension was ultrahorn-sonicated for 15 min using a Branson Sonifier 150D with a power output of 7 – 8. 10 μl of the catalyst suspension was pipetted onto the previously polished and cleaned GC electrode surface and dried in air at 60 $^{\circ}\text{C}$. Shown in Figure 12d, the resulting homogenous thin catalytic film was used as working electrode for the electrochemical experiments. The calculated Pt loading was in a range between 10 and 16 $\text{mg}_{\text{Pt}} \text{cm}_{\text{geo}}^{-2}$.

2.2.2 Rotating Disc Electrode (RDE) Technique

Rotating Disc Electrode (RDE) technique equipping with a commercial bipotentiostat (VSP-5, Biologic, France) and a rotator (PINE Research Instrument, USA) was used to perform the electrochemical experiments at room temperature, shown in Figure 12a. A self-made three compartment glass cell was used with a three electrode set-up: Pt gauze as counter electrode, reversible hydrogen electrode (RHE) (HydroFlex, supplied by Gaskatel) or mercury-mercury sulfate (MMS) electrode (Princeton Applied Research, AMETEK) as reference electrode and a rotating disk electrode (PINE Instrument) with a glassy carbon disk at 5 mm diameter as working electrode. The reference electrode was held in place by a Luggin – Haber capillary. The electrolyte solution was a 0.1 M perchloric acid solution and a 0.1 M potassium hydroxide solution for the acidic and alkaline experiments, respectively. 0.1 M HClO₄ electrolyte solution was prepared by diluting of 70 % redistilled perchloric acid (Sigma Aldrich, #311421) with purified water (18 MΩm at room temperature) (4.32 ml of 70 % redistilled perchloric acid in 500 ml of purified water), while 0.1 M KOH was prepared by dissolution of potassium hydroxide pellets (purity grade of 99,99%, Sigma-Aldrich, # 306568-100g) in purified water.

All given potentials were converted and reported in respect to the reversible hydrogen electrode (RHE) scale. Before the electrochemical measurements commenced, the working electrode had been immersed in the electrolyte under a potential control at 0.06 V/RHE.

The benchmark, commercially available 28.2 wt. % Pt/HSAC (part no. TEC10E30E, supplied by TKK, Japan) was taken for the comparison of the Pt mass and Pt surface area specific based activities for the oxygen reduction reaction (ORR) and the Pt electrochemical active surface area (ECSA).

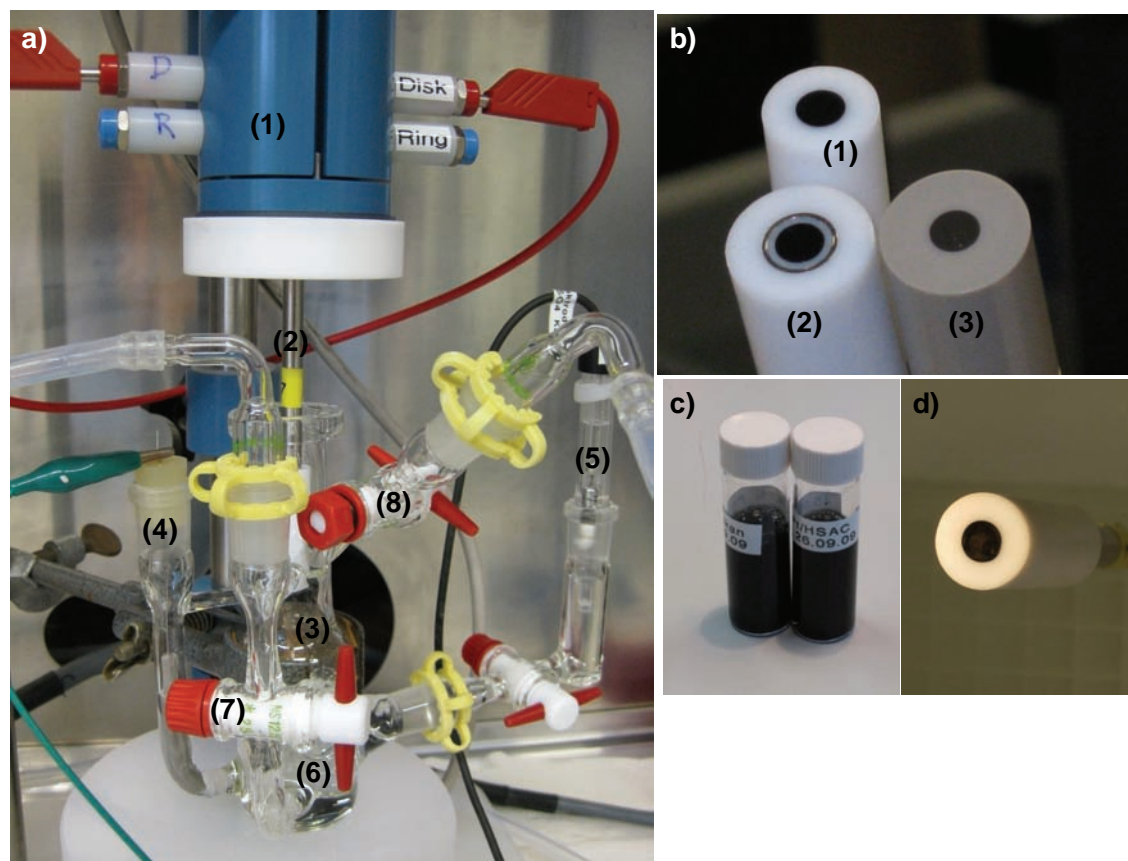


Figure 12 (a) Image of the electrochemical experimental RDE setup: (1) rotator, (2) working electrode coated with a thin catalytic film, (3) self-made three compartment electrochemical glass cell, (4) Pt mesh as counter electrode, (5) mercury-mercury sulfate electrode as reference electrode, (6) Luggin – Haber capillary for the reference electrode, (7) gas inlet for bubbling through the frit into the electrolyte and (8) gas inlet above the electrolyte solution. (b) Three glassy carbon (GC) disk working electrodes at 5 mm diameter: (1) rotating disk electrode, (2) rotating ring disk electrode with an outermost pure Pt ring electrode, (3) high temperature rotating disk electrode consisting of polyetheretherketone (PEEK). (c) Two catalyst ink suspensions. (d) GC electrode prepared with a thin catalytic film.

2.2.2.1 Cyclic Voltammetry

Cyclic voltammograms (CVs) were performed in a voltage range between 0.06 and 1.00 V/RHE (-0.65 and +0.290 V/MMS) in deaerated electrolyte solution under nitrogen at room temperature. Firstly, the Pt bimetallic nanoparticle catalysts were electrochemically treated to remove the less noble metal from the alloy particle surface. The dealloying protocol consisted of three cyclic voltammetric segments: three cycles with a scan rate of 100 mV s⁻¹, followed by 200 fast cycles with 500 mV s⁻¹ and finally three cycles with 100 mV s⁻¹. Only the final CV profile with a scan rate of 100 mV s⁻¹ was used to determine the platinum electrochemical active surface area (ECSA). The ECSA was estimated with the mean integrated charge of the underpotentially deposited hydrogen regime (H_{upd}) corrected with the double layer current corrected at 0.40 V/RHE, with the Pt pseudo-capacity of 210 $\mu\text{C cm}_{\text{Pt}}^{-2}$ and with the scan rate ν as follows:

$$ECSA = \frac{H_{\text{upd}}}{m_{\text{Pt}}} \quad H_{\text{upd}} = \frac{Q_{\text{ad/de}}}{210 \frac{\mu\text{C}}{\text{cm}^2} * \nu} \quad (\text{eq 2})$$

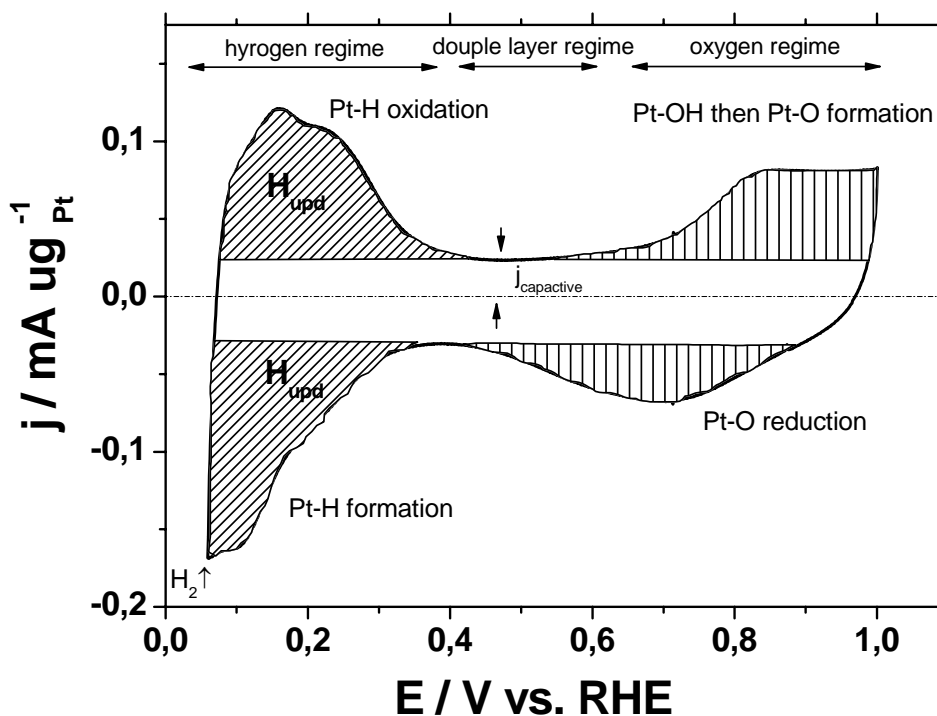


Figure 13 Cyclic voltammograms (CVs) of carbon supported Pt nanoparticles in deaerated 0.1 M HClO_4 electrolyte solution at room temperature. The CV profile shows the characteristic features of a pure Pt catalyst corresponding to the hydrogen ad/desorption regime (0.06 – 0.40 V/RHE), the double layer regime (0.40 – 0.60 V/RHE), and the redox peak couple of Pt hydroxide/oxide (0.70 – 1.00 V/RHE).

2.2.2.2 Linear Sweep Voltammetry (LSV)

Linear sweep voltammetry (LSV) measurements were carried out by anodic potential sweeping from 0.06 V/RHE (-0.66 V/MMS) to the open circuit potential (around 1.0 V/RHE; +0.31 V/MMS) at a scan rate of 5 mV s⁻¹ and a rotation speed of 1600 rpm (rotations per minute) at room temperature. The electrolyte solution was saturated with pure dioxygen by bubbling through a glass frit into the electrolyte at room temperature. The LSV experiments served to determine the Pt mass and Pt surface area specific based activities of catalysts for the electroreduction of dioxygen (oxygen reduction reaction, ORR). A typical course of the polarization curve obtained from the LSV measurements is shown in Figure 14a. The polarization curve exhibits a plateau behavior between 0.06 and 0.70 V/RHE, indicating the diffusion controlled regime. Within this voltage range, the oxygen diffusion to the catalytic reaction center is the rate limiting process and in consequence dependent on the rotation rotating rate.^{61, 62} The diffusion controlled regime turns into a mixed diffusion – kinetic controlled regime. Finally, from about 0.85 V/RHE the reaction rate is only kinetic controlled based on the independence of the rotating speeds. At the open circuit potential (around 1.0 V/RHE), eventually no electrocatalytic conversion of oxygen is observed.

The kinetic current density (j_{kin}) at 0.90 V/RHE is determined by

$$\frac{1}{j} = \frac{1}{j_{kin}} + \frac{1}{j_{dif}} \quad (\text{eq 3})$$

where j is the measured current density, j_{kin} and j_{dif} are the kinetic and mass transport limited current densities, respectively. The Pt mass based activity (j_{mass}) and the surface area specific based activity ($j_{specific}$) for ORR were established at 0.90 V/RHE by the following equations:

$$j_{mass} = \frac{j_{kin}}{m_{Pt}} \quad j_{specific} = \frac{j_{kin}}{H_{upd}} \quad (\text{eq 4})$$

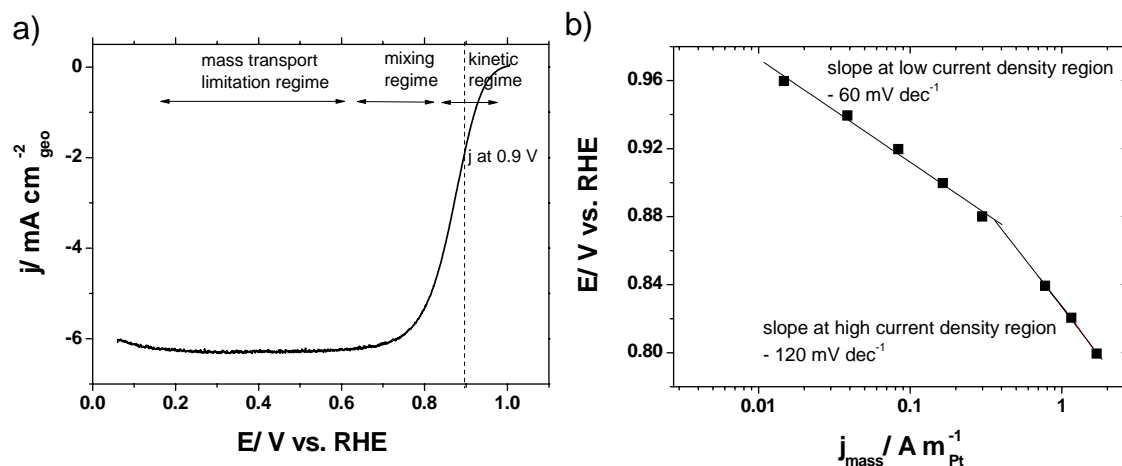


Figure 14 (a) A typical polarization curve for oxygen reduction reaction (ORR) recorded by LSV. (b) Pt mass based Tafel slope of a commercial Pt/C.

Figure 14b shows a Pt mass based Tafel plot of a commercial carbon supported Pt nanoparticle catalyst. The reported values in the literature of the Tafel slope for platinum as single crystal⁶³, polycrystalline⁶⁴, and carbon supported nanoparticles^{65, 66} are around $-2.3 RT/F$ at the low overpotentials ($E > 0.85$ V/RHE) and $-2 \times 2.3 RT/F$ at high overpotential ($E < 0.85$ V/RHE)⁶⁷. Typical values of the Tafel slopes at low and high current density region are -60 mV dec^{-1} and -120 mV dec^{-1} , respectively. The Tafel equation is a simplified electrode kinetics model deduced from the Butler-Volmer equation for electrode kinetics at large overpotentials η ($|\eta| \gg RT/nF = 25.7$ mV/n at 25°C).⁶¹ The Tafel equation is described as follows

$$j_D = -j_0 \cdot \exp\left[\frac{(1-\alpha)nF}{RT}\eta_D\right]$$

$$\eta_D = \frac{RT}{(1-\alpha)nF} 2.3\log j_0 - \frac{RT}{(1-\alpha)nF} 2.3\log|j_D| \quad (\text{eq 5})$$

$$\eta_D = A + B \cdot \log|j_D|$$

where j_D is the current density, j_0 is the exchange current density, n is the number of electrons, F is the Faraday constant, T is the temperature, R is the universal gas constant, α is the symmetry factor. The constant B is referred to as Tafel slope.

2.2.3 Rotating Ring Disk Electrode (RRDE) Technique

The hydrogen peroxide production of the voltammetric treated electrocatalysts was determined using the Rotating Ring Disk Electrode (RDE) technique. The experimental RRDE assembly included a self-made three compartment electrochemical glass cell, a commercial bipotentiostat (VSP-5, Biologic, France), a PINE rotator, a Pt gauze as counter electrode, a mercury - mercury sulfate electrode (Princeton Applied Research, AMETEK) as reference electrode and an replaceable 5 mm glassy carbon disk of rotating ring disk electrode (RRDE) with outermost pure Pt ring electrode (supplied by PINE Research Instrument, USA). 10 μ l of catalyst suspension was pipetted onto the replaceable, previously polished and cleaned glassy carbon disk of the RRDE electrode. The RRDE experiments were conducted in oxygen saturated 0.1 M HClO₄ solution at room temperature.

The hydrogen peroxide detection and its quantification occurred by measuring the Pt ring current in the RRDE experiments. The Pt ring electrode was potentiostated at 1.20 V/ RHE during the LSV measurements for ORR on the disk electrode. The experimentally established collection efficiency N was around 0.22 \pm 0.01. The collection efficiency of the ring disk electrode was previously measured in a [Fe(CN)₆]³⁻ / [Fe(CN)₆]⁴⁻ redox reaction system in a RRDE setup (see below).⁶⁸ It persists unchanged at N = 0.22 \pm 0.01 for a wide range of the rotating speed. The peroxide oxidation reaction proceeded under diffusion control. The ring background current was subtracted from the measured ring current. The total disk current, referred to as i_{disk} , is the sum of the oxygen reduction currents to water, $i_{\text{H}_2\text{O}}$ and to hydrogen peroxide, $i_{\text{H}_2\text{O}_2}$. using the collection efficiency N:

$$i_{\text{disk}} = i_{\text{H}_2\text{O}} + i_{\text{H}_2\text{O}_2} \text{ with } i_{\text{H}_2\text{O}_2} = i_{\text{ring}} * N^{-1} \quad (\text{eq 6})$$

The quantification of the peroxide production was calculated from the molar flux rates of O₂, $n(t)_{\text{O}_2(4e^-)}$ and H₂O₂, $n(t)_{\text{O}_2(2e^-)}$ according the following equation⁶⁹

$$\dot{n}_{\text{O}_2(4e^-)} = i_{\text{H}_2\text{O}} / 4F \text{ and } \dot{n}_{\text{O}_2(2e^-)} = i_{\text{H}_2\text{O}_2} / 2F \quad (\text{eq 7})$$

$$X_{H_2O_2} = \frac{\dot{n}_{O_2(2e^-)}}{\dot{n}_{O_2(2e^-)} + \dot{n}_{O_2(4e^-)}} = \frac{2 \cdot i_{ring}/N}{i_{disk} + (i_{ring}/N)} \quad (\text{eq 8})$$

2.2.3.1 Determination of collection efficiency N

The collection efficiency experiments are conducted in the following way: A carbon supported Pt nanoparticle catalyst was used for the RRDE experiments to determine the collection efficiency. 5 mg of Pt/C was mixed with 3.98 ml of purified water, 1.00 ml of 2-propanol and 20 μl of 5 wt.% Nafion solution. After sonication, 10 μl of the Pt catalyst suspension was pipetted onto the previously polished and cleaned GC surface of the RRDE electrode. The prepared RRDE electrode was dried at 60 $^\circ\text{C}$ in air. The calculated Pt loading of the catalytic thin film was around 12 – 14 $\mu\text{g}_{\text{Pt}} \text{cm}_{\text{geo}}^{-2}$. The determination of collection efficiency was performed in 10 mmol l^{-1} $\text{K}_3\text{Fe}(\text{CN})_6$ in 0.1 M HClO_4 as a typical reaction system⁷⁰. The electrolyte solution was purged with nitrogen for 20 min at room temperature. The disk potential of the catalytic thin film electrode was anodically swept from 0.40 V/RHE to 1.40 V/RHE with 20 mV s^{-1} , while the potential of the Pt ring electrode was retained at 1.55 V/ RHE. The oxidation of $[\text{Fe}(\text{CN})_6]^{4-}$ at a constant ring potential, which is generated at the disk electrode, to $[\text{Fe}(\text{CN})_6]^{3-}$ proceeds under pure diffusion control. The oxygen evolution reaction on the Pt ring electrode at the elevated potential can be neglected. Figure 15 shows the RRDE experiments for the determination of the collection efficiency in $[\text{Fe}(\text{CN})_6]^{3-} / [\text{Fe}(\text{CN})_6]^{4-}$ redox reaction system.

The ring current (i_{ring}) is related to the disk current (i_{disk}) by a quantity N, the collection efficiency. The collection efficiency is determined by different rotating speeds and remains unchanged within the chosen rotating speeds and examined potentials at $N = 0.22 \pm 0.01$ and is close to the theoretical collection efficiency of 0.25 specified by PINE research company.

$$N = - \frac{i_{ring}}{i_{disk}} \quad (\text{eq 9})$$

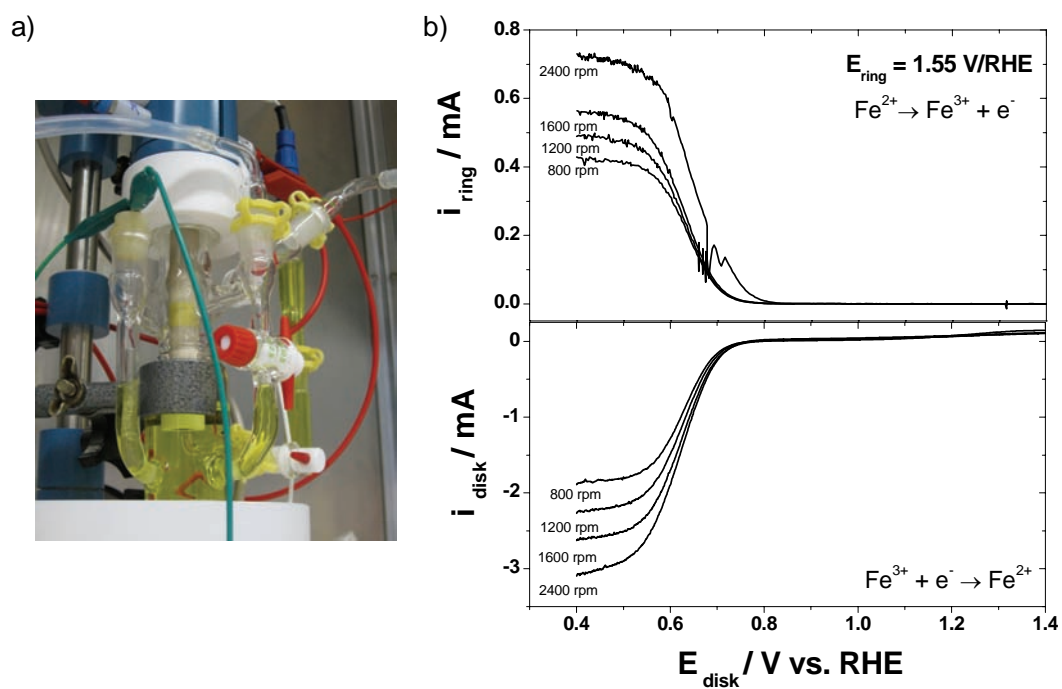


Figure 15 a) Image of the RRDE setup. b) Ring current during the anodic disk potential sweep with a scan rate of 20 mV s^{-1} to determine the collection efficiency N on a Pt/C thin-film RRDE electrode in 0.1 M HClO_4 with $10 \text{ mM K}_3\text{Fe}(\text{CN})_6$ at room temperature.

2.3 Structural and Compositional Characterization

2.3.1 High Temperature X-Ray Diffraction (HT-XRD) in Parallel Beam Geometry

For a high temperature X-ray diffraction (HT-XRD) study we used a laboratory standard D8 Advanced X-Ray Diffractometer (supplied by Bruker AXS, Germany) in parallel beam geometry. The experimental HT-XRD assembly is equipped with a Cu $K\alpha$ source, a Goebel mirror, a position-sensitive LynxEye detector (PSD), and an external radiation heating chamber (supplied by MRI Physikalische Geraete GmbH, Germany). The radiation heating chamber is positioned on the goniometer. Figure 16 shows the HT-XRD assembly in opened and closed states. The radiation heating chamber consisted of an AlCr foil as a radiation heater, a rotatable alumina crucible as a sample holder, a thermocouple, two gas lines and valves for gas inlet and outlet as well as a Kapton foil X-ray window. 6 – 10 mg of powder sample was given in the alumina crucible and carefully flattened to form a smooth surface.

The following acquisition parameters were adjusted in the WIZARD software: three different 2θ ranges ($23^\circ - 25^\circ$, $33.5^\circ - 35.5^\circ$ and $36.5^\circ - 51.5^\circ$), step size of 0.04° , holding time 3 s per step, fix divergence slit of 2 mm, and PSD Iris antiscattering slit setting of 13. The diffraction patterns were detected every time from the start to the end of the experiment at the hold temperature. The used temperature – time protocols are illustrated in the chapter 3.3.

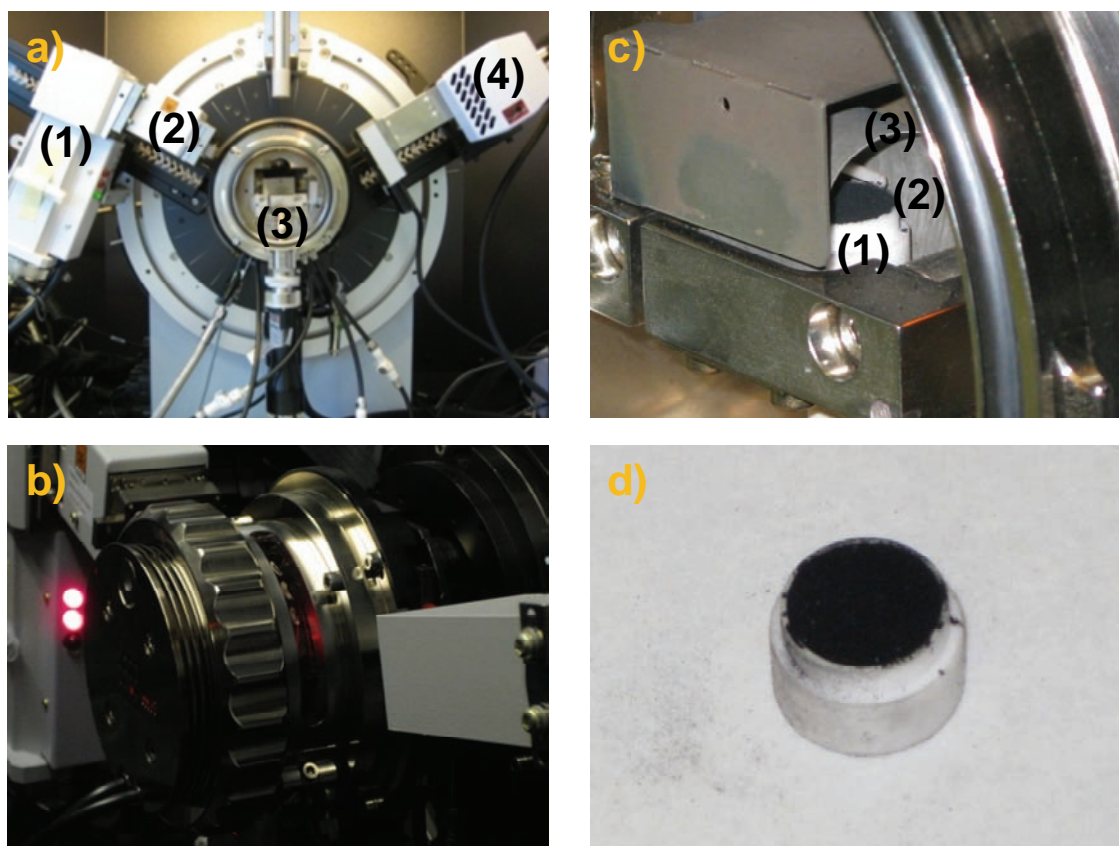


Figure 16 Experimental high temperature X-ray diffraction (HT-XRD) assembly in parallel beam geometry in (a) opened and (b) closed states. (a) HT-XRD with opened radiation heating chamber: (1) Cu X-ray source, (2) Goebel mirror, (3) external heating chamber positioned on the goniometer, (4) position-sensitive LynxEye detector (PSD). (c) (1) Sample in a white Al_2O_3 crucible, (2) thermocouple and (3) AlCr foil heater. (d) A white Al_2O_3 crucible of 14 mm diameter was filled with 6 – 10 mg black impregnated powder.

2.3.1.1 Alignment and Calibration of the HT-XRD

The alignment of the HT-XRD is to describe in the following way: The prepared sample holder is positioned on the automatic driven rotator of the radiation heating chamber. The X-ray source and the detector are positioned at $2\Theta = 0$. This adjustment is referred to as a direct alignment. Due to the very high intensity of X-ray source during the direct alignment, a slit of 1 mm and a Cu absorber filter are used at the primary (X-ray tube and Goebel mirror) and secondary (PSD detector) optics of the diffractometer, respectively. The chosen scan type is a PSD fix scan, where the X-ray source is only moved at a fix position of the PSD detector. The used parameters are $\Theta = -0.5$ and $+0.5$ for the X-ray tube, step size of 0.02° , $Z = 3 - 6$ and holding time 1 s. A Z drive test for each sample powder is essential to find out the optimal sample height for accurate $\Theta - \Theta$ XRD measurements (see Figure 17a). Therefore, the height of the sample holder is automatically changed using the Bruker software WIZARD, referred to as a “Z drive”. The series of XRD profiles are recorded by various Z heights (use the function “loop” in WIZARD) at a rotating sample to establish the course of the intensity in dependence on the Z position. Figure 17 illustrates a Z drive testing for the alignment on the HT-XRD. If the Z height of the sample is too low or too high, the detector records the full intensity or no intensity of the X-ray source, respectively. The optimal Z height is only achieved, when the intensity is the half of the maximum intensity. The effects of displacement can be neglected by an optimal Z height and parallel beam geometry.

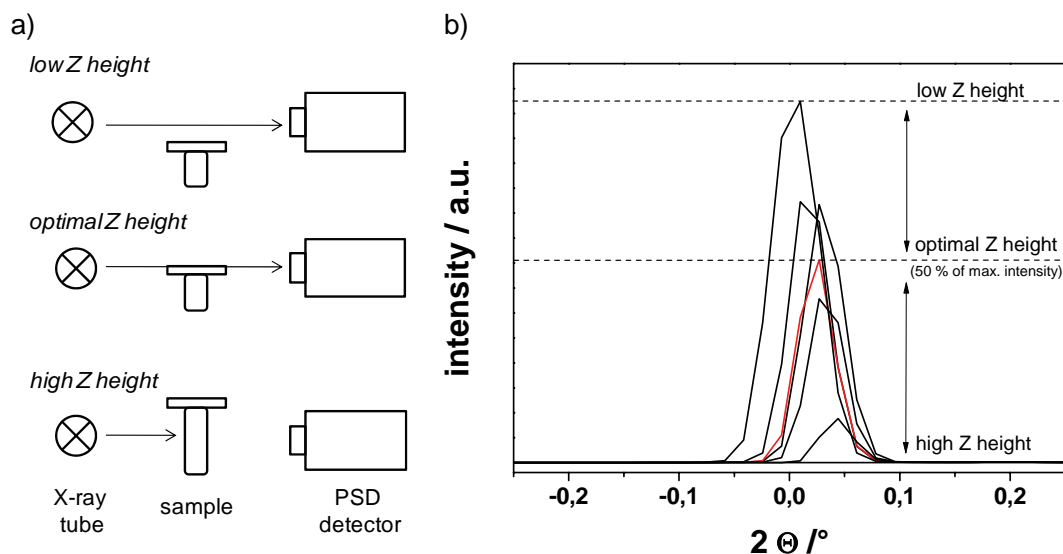


Figure 17 Alignment of the HT-XRD. a) Schematic sketch of the Z-drive. b) Series of XRD patterns at various values of Z height recorded by a direct beam and PSD fix scan. The optimal Z height is only achieved, when the intensity is the half of the maximum intensity. XRD parameters: $\Theta = -0.5 - +0.5^\circ$ for the X-ray tube, step size of 0.02° and holding time 1 s.

The calibration of the HT-XRD and the optimal distance between the thermocouple and sample occur by measuring of standard materials. The accurate temperature is to establish by standards to eliminate errors during the HT-XRD experiments. The important property of standard materials is the clear change of crystal structure (by melting or phase transformation) at a distinctly elevated temperature, which can be traced by recording of series of XRD profiles. The thermal phase transformation of α -quartz (trigonal) to β -quartz (hexagonal) in a 2Θ range of $25 - 27^\circ$ at 573°C , as an example, is shown in Figure 18. The shift of the reflection at various temperatures is clearly to observe in Figure 18a. Figure 18b illustrates the three-dimension illustration of the phase transformation of α -quartz (trigonal) to β -quartz (hexagonal) displayed using the Bruker EVA software. The experimentally observed difference of the temperature, where the phase transformation proceeds, can be reduced by the position change of the thermocouple. The value of ΔT should be in the range of $5 - 10^\circ\text{C}$. Further standard materials are aluminum (melting

point of 660 °C), copper (melting point of 1085 °C), KNO₃ (phase transformation from orthorhombic to trigonal at 128 °C).

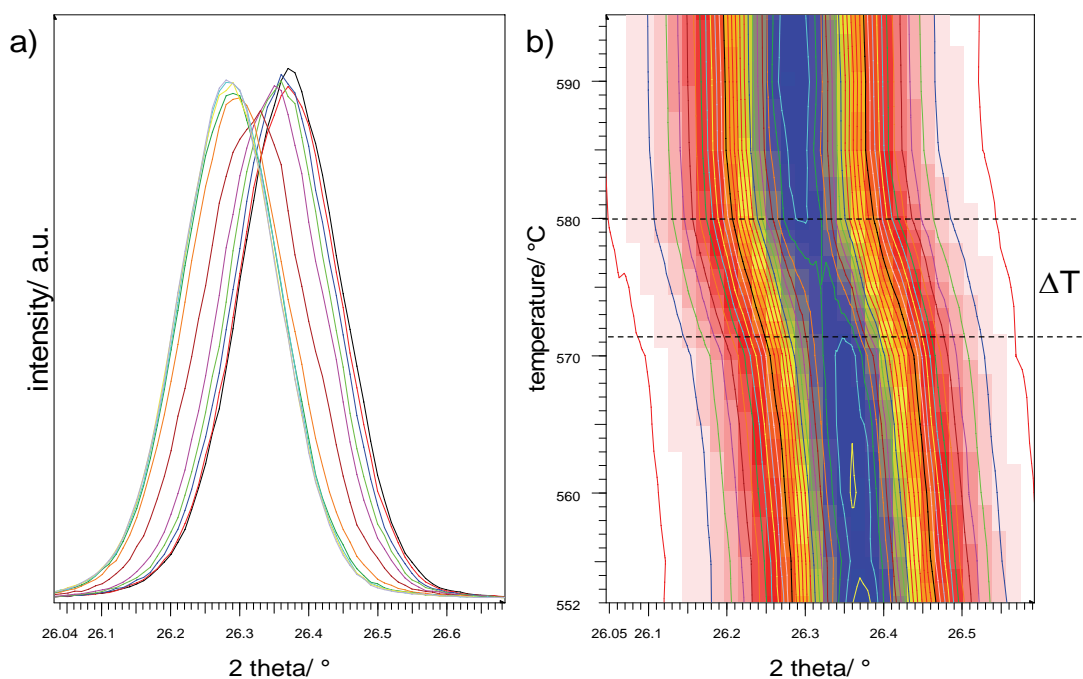


Figure 18 Calibration of the thermocouple by temperature-dependent XRD measurements from α -quartz (trigonal) to β -quartz (hexagonal). a) Series of XRD patterns at various temperatures in the range of 552 °C to 595 °C. b) Three-dimension representation of the phase transformation of α -quartz to β -quartz. XRD parameters: $2\theta = 25.5 - 28^\circ$, step size of 0.01° and holding time of 2 s.

2.3.2 X-Ray Diffraction (XRD) in Bragg-Brentano Geometry

The high-resolution XRD data were acquired using a laboratory standard D8 Advanced X-Ray Diffractometer in Bragg-Brentano Geometry (supplied by Bruker AXS, Germany) equipped with a Cu K α source, a position-sensitive LynxEye detector (PSD) and an automatic variable divergence aperture device. The XRD reflections recorded in Bragg-Brentano geometry are resolved better compared to those recorded in parallel beam geometry due to the focused beam. The verification of the instrument resolution was performed with a NIST corundum standard. The catalyst powder was positioned in a self made Plexiglas disk with a centered depth of 1 mm and a diameter of 10 mm. Before the XRD measurement commenced, the surface of the powder had previously been carefully flattened. The following XRD setting parameters were used: 2 Θ range between 15 and 80°, step size of 0.01°, holding time of 7 s per step, variable divergence slit of 4 mm, PSD Iris antiscattering slit setting of 13, and sample rotation of 15 rpm.

2.3.2.1 XRD Profile Analysis

The XRD profile analysis was performed with TOPAS (Bruker AXS, Version 4-2). The crystal phase quantification of the Pt alloy nanoparticle electrocatalysts was determined by Rietveld refinement. The following fit parameters were used during the refinements: background coefficients, displacement correction, peak shapes, and cell parameters. The quality of the refinement was evaluated with the resulting residual values, R – weighted pattern (R_{wp}), R – expected (R_{exp}), and goodness-of-fit (GOF) (see 10.2 Criteria of Fit for XRD Profiles).

The volume-averaged crystallite size of the alloy phases is a determination of the size of a coherently diffraction domain. Therefore, crystallite is equal to homogeneous domain giving rise to coherent diffraction. Here, the volume-averaged crystallite size β is estimated using the integral breadth method⁷¹ which is the ratio of the integrated intensity to the intensity at the maximum f_m :

$$\beta = \left[\int f(2\Theta)d(2\Theta) \right] / f_m \quad (\text{eq 10})$$

It is related to the crystallite size ε_β by the equation:

$$\varepsilon_\beta = \frac{\lambda}{\beta \cdot \cos \Theta} \quad (\text{eq 11})$$

where λ is the X-ray wavelength and Θ is Bragg angle. The advantage of the integral breadth method is the independence of the crystallite distribution in size and shape. The Scherrer constant can be assumed to be 1. According to the Scherrer equation^{72, 73}, the crystallite size is established by the full width at half maximum (FWHM). The Scherrer equation is:

$$\varepsilon_\omega = \frac{K_\omega \cdot \lambda}{\omega \cdot \cos \Theta} \quad (\text{eq 12})$$

Here, ε_ω is the crystallite size, λ is the X-ray wavelength, ω is the half width in angle which the intensity is equal to the half the maximal intensity, K_ω is the shape factor referred to as the Scherrer constant and Θ is the Bragg angle. However, the volume-average crystallite size is not to equalize with the particle size such as amorphous structure or dislocations of crystal structure.

Furthermore, the stoichiometric composition of the single crystal Pt alloy phase was determined from the lattice parameter using the Vegard's rule⁷⁴, which describes the linear dependence on the lattice parameters a of the disordered face centered cubic (fcc) Pt-M alloy crystal phase with those lattice parameters a of the constituent elements at the same temperature.

$$a_{Pt - M} = x \cdot a_{Pt} + (1 - x) \cdot a_M \quad (\text{eq 13})$$

2.3.3 Energy-Dispersive X-Ray Spectroscopy (EDS)

The overall chemical composition of Pt alloy nanoparticles was analyzed using the energy-dispersive X-ray spectroscopy (EDS). A high-resolution Hitachi S-4000 scanning electron microscope (SEM) is equipped with a cold field emitter and an energy-dispersive X-ray spectroscopy detector. The microscope was operated by an accelerating voltage of 20 kV, a beam current of 0.4 nA and a working distance of 20 mm. The as synthesized and electrochemically treated Pt alloy nanoparticles were prepared onto the carbon tabs of 1 cm diameter (supplied by PLANO, Germany). The powder was pressed onto the gluey carbon surface, while the electrochemically dealloyed catalytic film on the working electrode was transferred by pressing onto the carbon tabs.

The chemical composition was determined and averaged about a large range on different sample positions. The corresponding characteristic energy intensities of K – and M – line for Co/Cu and Pt were used for the quantification. The experimental precision was about 2 – 3 at. %.

2.3.4 Transmission Electron Microscopy (TEM)

The morphology and particle size distribution of the Pt alloy nanoparticles before and after the electrochemical experiments were investigated using a FEI TECNAI G² 20 S-TWIN transmission electron microscope (TEM) equipping a LaB₆ cathode, an energy-dispersive X-ray spectroscopy (EDS) detector and a GATAN MS794 P CCD camera. The microscope was operated by an accelerating voltage of 200 kV. EDS measurements were performed with a focused electron beam to establish the entire elemental composition of a single particle. The characteristic energy intensities of K – and L – line for Co/Cu and Pt were used for the quantification with the software TEM Imaging & Analysis. The as synthesized and dealloyed electrocatalyst powders were suspended in a 1:1 purified water/ 2-propanol solution. 10 µl of the well-dispersed sample was pipetted onto the holey carbon film coated Al grid and dried in air.



Figure 19 FEI TECNAI G² 20 S-TWIN transmission electron microscope (TEM) equipping a LaB₆ cathode, an energy-dispersive X-ray spectroscopy (EDS) detector and a GATAN MS794 P CCD camera.

The particle size distribution and number-averaged particle diameter for all catalysts was obtained from the evaluation of the TEM micrographs by counting of more than 400 particles using the analySIS FIVE software (SIS, Soft Imaging Systems, Olympus). For each distribution, the number-averaged diameter is estimated as follows:

$$\bar{d}_N = \frac{\sum_{i=1}^n n_i d_i}{\sum_{i=1}^n n_i} \quad (\text{eq 14})$$

where n_i is the number of particles having a diameter d_i .

2.3.5 Scanning Transmission Electron Microscopy with High Angle Annular Dark Field Detector (STEM-HAADF)

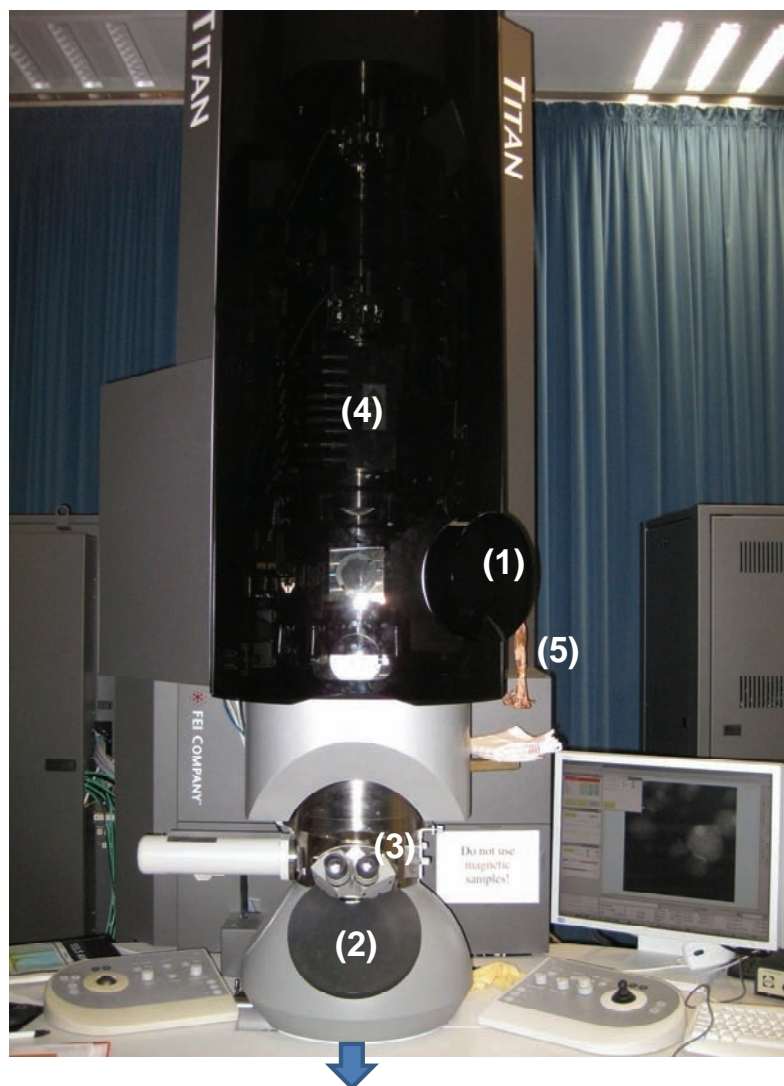
High-resolution structural investigations were carried out in a probe-corrected FEI TITAN S 80-300 high-angle annular dark field scanning transmission electron microscopy (STEM-HAADF). 'Z-Contrast' conditions were achieved using a probe semi-angle of 25 mrad and an inner collection angle of the detector of 70 mrad. The microscope was operated by an accelerating voltage of 300 kV. The as synthesized and dealloyed Pt alloy nanoparticle electrocatalysts were prepared for the high-resolution STEM-HAADF in the following way: The as synthesized and dealloyed particles were immersed in a 1:1 purified water/ 2-propanol solution and sonicated using a Branson Sonifier D150 at a power output of 1. Each sample was washed and centrifuged three times to reduce the particle agglomeration and to dissolve the residual Nafion polymer which was used in an earlier stage of the catalytic thin film preparation. Finally, the suspension was pipetted on an alumina grid with holey carbon film and dried in air. Before the transferring into the microscope, the sample was dried in vacuum at 90 °C for 5 hours.

2.3.6 Electron Energy Loss (EEL) spectroscopy

Electron energy loss (EEL) spectroscopy was performed using a probe-corrected FEI TITAN S 80-300 high-angle annular dark field scanning transmission electron microscopy (STEM-HAADF). EEL spectra were recorded using a Gatan image filter (GIF) Tridiem 866ERS with an energy resolution of 1 eV. Here, the energy resolution was established from the full width at half maximum of the zero loss peak. During the EEL line scan across the electrochemically treated bimetallic particle, 20 individual EEL spectra were collected and analyzed to establish the accurate chemical composition profiles.

Figure 21 shows examples of EEL spectra number 10 (a,b), 14 (c,d), and 17 (e,f) for the line profile (see Figure 64) and corresponds to the data at 8.1, 11.6 and 14.3 nm. We analyzed the Co L₃ and the Pt M_{4,5} – edges. The red curves show the original EEL spectra and the blue curves display background-subtracted data. The compositional data was obtained by integrating the

background-subtracted curves at 770 – 785 eV for Co and at 2155 – 2400 eV for Pt (grey areas in Figure 21). For the background subtraction, a hyperbolic curve was fitted to the pre-edge spectrum at 580 – 765 eV for Co and at 1970 – 2130 eV for Pt (black curves in Figure 21). The error bars for the compositional measurements were calculated according to standard deviation of the EEL data within the limit of integration in addition with the mismatch of the background fit curves (dashed curves in Figure 21).



EELS and CCD camera

Figure 20 probe-corrected FEI TITAN S 80-300 high-angle annular dark field scanning transmission electron microscopy (STEM-HAADF). (1) specimen port, (2) fluorescent screen, (3) binoculars, (4) high angle annular dark field (HAADF) detector and (5) cooling finger consisting of copper wires.

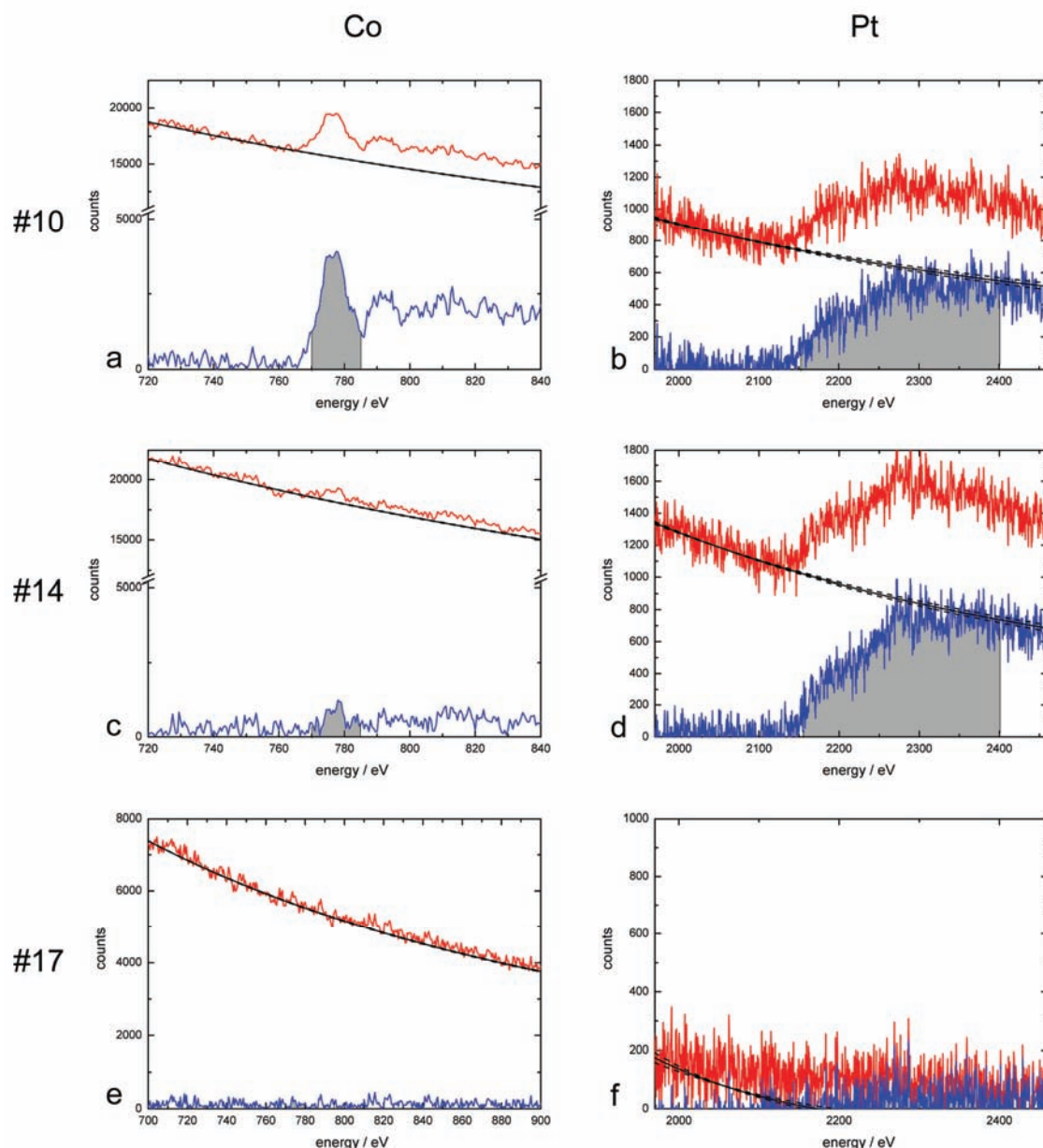


Figure 21 Raw EEL spectra for Co L_3 and Pt $M_{4,5}$ – edges at the measuring points #10, #14 and #17 along the dealloyed particle, shown in Figure 63a. The red curves show the original EEL spectra and the blue curves display background-subtracted data. The grey areas denote the integrated edges in the background-subtracted curves at 770 – 785 eV for Co and at 2155 – 2400 eV for Pt. The black curves indicate the background subtraction using a hyperbolic fit of the pre-edge spectrum at 580 – 765 eV for Co and at 1970 – 2130 eV for Pt.

3 In-situ HT-XRD Study of Alloy Formation and Particle Growth

Reprinted from ref 75 with permission of Chemistry of Materials, copyright (2011). <http://dx.doi.org/10.1021/cm103661q>

Bimetallic alloy nanoparticles exhibit a complex, for the most part poorly understood, crystallographic phase behavior, rarely following their macroscopic counterparts. Atomic-scale insight into the formation kinetics, the compositional and structural stability of nanoscale alloys are of great importance for the synthesis of functional bimetallic nanomaterials, such as catalysts with controlled microscopic ordering, composition or particle size. Here, we report in-situ XRD measurements of the formation dynamic behavior, compositional changes and the size evolution of Pt alloy nanoparticles.⁷⁵ We chose Pt-Cu system due to its combined technological importance as precursor for core-shell nanoparticle electrocatalysts (see below in the chapter 5). We provide correlation of annealing control parameters, such as heating rate, temperature and time, with microscopic alloy structure, composition and particle size, and clarify their distinctive roles and time-scales in the alloy formation process and size growth. We reveal that the annealing temperature essentially controls the Cu content of disordered Pt-Cu lattices during heating ramps, without formation of ordered $L1_2$ PtCu₃ phase. Annealing time, in contrast, leads to the particle growth. The phase ordering occurred only during cooling. Our insight offers practical synthetic guidelines toward single-phase ordered and disordered PtCu₃ alloy nanoparticles with optimized particle dispersion.

3.1 Introduction

Bimetallic alloy nanoparticles have attracted considerable attention in many areas of science and technology, because their optical, magnetic or catalytic properties differ significantly from those of their monometallic counterparts.⁷⁶ For instance, bimetallic nanoparticles often exhibit enhanced surface catalytic activity for different chemical reactions, which is attributed to the modifications in the surface electronic structure in combination with modified surface morphologies^{10, 15, 19, 34, 77-79} due to the atomic neighborhood of two dissimilar types of atoms.

Electrocatalytic activity of bimetallic nanoparticles is critically sensitive to the structure, composition and particle size of the alloy phases. The clarification of the structure – reactivity relationships of Pt-M alloy nanoparticle catalysts has been notoriously hampered by limited alloy crystal uniformity due to the presence of multiple alloy phases (ordered, disordered, different compositions) in the thermally annealed catalyst materials^{22, 80, 81}. Thermal annealing of bimetallic precursors is the most common synthetic step to form alloy nanoparticles⁸²⁻⁸⁵, yet rarely results in pure alloy phase, in particular for high molar ratios of M in Pt alloys^{21, 86}. Furthermore, macroscopic bulk alloys follow well-established thermodynamic phase diagrams, but alloys at the nanoscale do not typically ensue from those same structure – temperature relationships and phase stabilities.

Crystallographic phase uniformity of nanoparticle alloys was generally thought to improve using sufficiently high annealing temperatures and extended annealing times, which, however, resulted in undesired large (> 6 nm) nanoparticle diameters⁸⁷. Virtually, all published Pt-M alloy particle preparations involving thermal treatment were optimized empirically without any detailed knowledge of the relations between structural atomic parameters and annealing temperature and time. As a result of this, even the formation of single-phase Pt-M alloys with a desired nominal atomic ratio, with small (< 6 nm, preferably < 4 nm) particle size and controlled lattice order has remained a major challenge.^{21, 85, 88, 89}

We study the thermal preparation of nanoparticle alloys with controlled properties and clarify the insight into the alloy formation dynamic behavior. We report in-situ measurements of the alloy formation process of bimetallic Pt-Cu alloy nanoparticles using high temperature X-ray diffraction (HT-XRD). HT-XRD is a powerful technique to study in-situ the formation of ordered or disordered crystallographic phases combined with particle size. The Pt-Cu alloy system is of great technological interest, as single phase PtCu₃ alloy nanoparticles serve as precursors for core-shell nanoparticle electrocatalysts with significantly improved activity for the electroreduction of oxygen in realistic fuel cells^{16, 35, 90-96} (see below). We correlate annealing temperature and annealing time with atomic lattice parameters, alloy phase composition and particle size, and clarify their role and relative time-scales in the alloy formation process. In doing so, we map out entire Vegard-type structure – composition relations of the Pt-Cu nanoparticle system over a wide temperature range. Our work gives atomic-scale insight in the phase formation behavior of a nano scale bimetallic cubic Pt-Cu alloy system. We provide practical synthetic guidelines for the preparation of single-phase ordered and disordered bimetallic alloy nanoparticles.

3.2 Preparation of Pt-Cu Precursor Material

A Pt-Cu precursor material with a Pt:Cu atomic ratio of 1:3 was prepared by impregnation – freeze-drying method. The following commercial chemicals were applied: 28.2 wt. % Pt nanoparticles supported on high surface area carbon (HSAC) (part no. TEC10E30E, supplied by TKK, Japan) and copper nitrate as precursor salt ($\text{Cu}(\text{NO}_3)_2 \cdot 2.5 \text{H}_2\text{O}$, Sigma Aldrich, No. 467855, 50 g). All chemicals were used as received without purifications. The weighted amounts of Cu precursor salt, 28.2 wt. % Pt/HSAC and purified water were 1.0067 g, 1.0023 g and 67 ml, respectively. Firstly, the Cu nitrate salt was dissolved in purified water and added to a commercial 28.2 wt. % Pt/HSAC. After sonification, the light viscous slurry was frozen in liquid nitrogen for 20 min and freeze-dried in vacuum (Labconco Freezone 6) for 2 days. Finally, the dried impregnated powder was annealed in the heating chamber of the HT-XRD assembly in a reductive atmosphere.

3.3 Temperature – Time Protocols

For the in-situ HT-XRD study Figure 22 illustrates the three annealing protocols (temperature – time profiles) with a heating rate of 10 K min^{-1} under 4 vol% H_2 / 96vol % Ar flow of 100 ml min^{-1} . The “synthesis protocol” (shown in Figure 22a) was the commonly used standard annealing protocol for the preparation of Pt-Cu alloy nanoparticles. It consisted of two temperature holds: at $250 \text{ }^\circ\text{C}$ for 3 h to decompose the precursor anions and at a maximum temperature of $800 \text{ }^\circ\text{C}$ for 9 h to form an alloy and reduce the metals. Numerous HT-XRD profiles were recorded in parallel beam geometry during the “synthesis protocol”. The black circles along the temperature – time path in Figure 22 indicate the XRD measurements. After the controlled cooling process with $10 \text{ }^\circ\text{C min}^{-1}$ the reductive gas was switched to 1 vol% O_2 / 99 vol% N_2 at $30 \text{ }^\circ\text{C}$ for 2 h for the prevention of carbon burning.

Furthermore, the annealing protocol was extended and modified with additional temperature and cooling holds. The modified annealing temperature profile exhibited temperature holds at intervals of $100 \text{ }^\circ\text{C}$ for 90 min during the heating/ cooling process with a ramp of $10 \text{ }^\circ\text{C min}^{-1}$, shown in Figure 22b and c. The “stepped heating protocol” showed temperature holds during the heating between $300 \text{ }^\circ\text{C}$ and $800 \text{ }^\circ\text{C}$, while the “stepped cooling protocol” showed temperature holds during the cooling from $800 \text{ }^\circ\text{C}$ to $200 \text{ }^\circ\text{C}$. These modified annealing protocols served to uncover the formation of other alloy crystal phases, such as intermetallic, ordered Pt-Cu crystal phase structure (space group $\text{Pm}\bar{3}\text{m}$) and/or multiple disordered Pt-Cu alloy phase structures (space group $\text{Fm}\bar{3}\text{m}$).

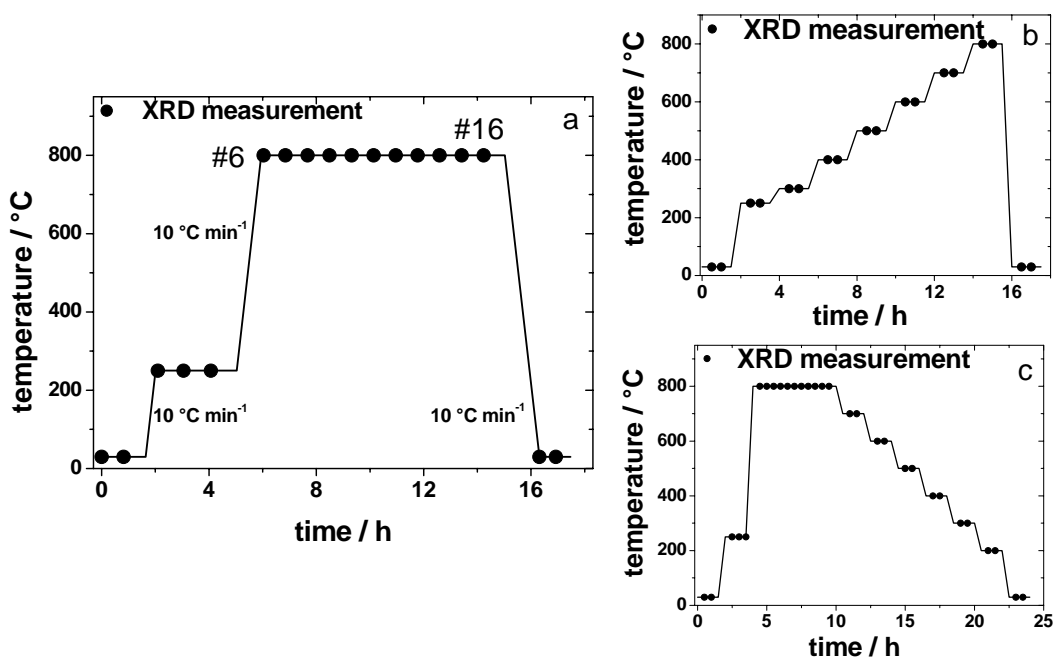


Figure 22 Temperature – time profiles to anneal Pt-Cu precursor materials in reductive atmosphere. The individual XRD measurements are denoted with black circles. (a) temperature – time profile, referred to as a “synthesis protocol”; (b) temperature – time profile with temperature holds on the heating ramp, referred to as a “stepped heating protocol”; (c) temperature – time profile with temperature holds on the cooling ramp, referred to as a “stepped cooling protocol”. Reprinted from ref 75 with permission of Chemistry of Materials, copyright (2011).

3.4 Dynamic Behavior of the Alloy Formation and Size Growth during the “Synthesis Temperature Protocol”

The time-resolved behavior of the alloy formation during the annealing at 800 °C over 9 hours was studied in-situ by measuring a number of HT-XRD patterns. The crystalline evolution of the Pt-Cu precursor material as the function of the holding time at 800 °C is shown in Figure 23.

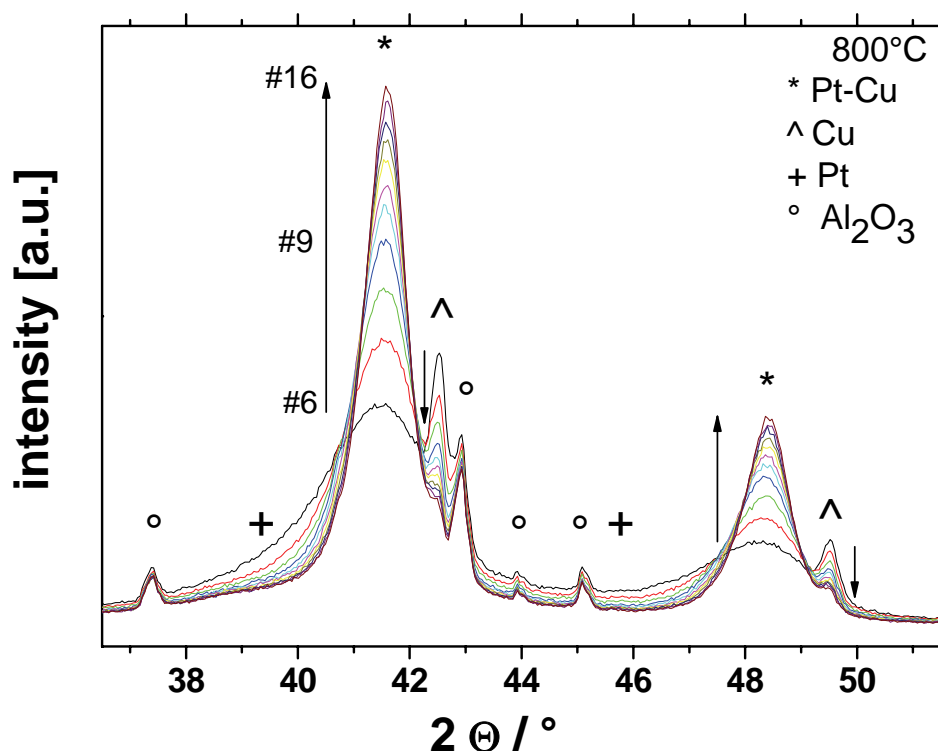


Figure 23 Series of XRD patterns, recorded in parallel beam XRD setup during Pt-Cu alloy formation at 800 °C over 9 hours. Numbers indicate the first scan #6 ($t = 0$ h) and final #16 ($t = 9$ h) at 800°C. Symbols denote individual crystallographic phases for disordered fcc Pt-Cu alloy, pure Cu and pure Pt nanoparticles at 800 °C. Reprinted from ref 75 with permission of Chemistry of Materials, copyright (2011).

The first experimental XRD profile at 800 °C shows reflections at $2\theta = \sim 41.8^\circ$ and $\sim 48.2^\circ$ for a Cu rich alloy phase, corresponding to the (111) and (200) lattice planes of a homogenous alloy. This indicates that the Pt-Cu alloy formation has, to a large extent, occurred during the heating up. Only, one

single disordered face-centered cubic (fcc) Pt-Cu alloy crystal phase was observed during the heating and annealing. The intensities of the sharp XRD reflections at $\sim 43^\circ$ and $\sim 49.7^\circ$ of pure fcc copper (symbolized by “^”) decreased gradually with the holding time, signified the continued Cu insertion into the disordered fcc Pt alloy lattice. At the same time, the (111) and (200) reflections of Pt-Cu alloy (symbolized by “*”) shifted very slightly to more positive 2θ values, indicated the contraction of Pt alloy lattice by increasing Cu content. In addition, over the 9 hours at 800°C the reflection of Pt-Cu alloy crystal phase became more sharply and intensely, associated with an increasing particle growth.

Figure 24 shows the quantitative analysis of the alloy dynamic behavior and particle growth and illustrates the evolution of lattice parameters and compositions during the annealing process at 800°C over 9 hours, obtained from the accurate reflex positions and sample peak broadings of the Pt-Cu alloy. The composition of the disordered fcc Pt-Cu alloy was estimated from the lattice parameter using the temperature-corrected Vegard's law⁷⁴. The mean particle (crystallite) size of fcc Pt-Cu alloy was determined from the (111) and (200) reflections using the integral breadth method⁷¹. The reflections of alumina oxide (sample holder) were used as internal standard for all HT-XRD measurements. The internal standard served to track out the displacement effects by sample sintering and deformation. Lattice parameters of fcc pure Pt and Cu crystal phases at 800°C were determined from independent HT-XRD experiments as reference profiles of carbon supported Pt and Cu nanoparticles of 3 – 4 nm diameter. The experimental lattice parameters were the result of a balance between thermal lattice expansion effects and size-dependent lattice compression effects⁹⁷, which contributed likely minor for particles of 3 – 4 nm size. The compressive lattice strain increases generally by decreasing particle size. Nanoparticles below 2 nm in size exhibit compressive lattice strain of up to few percent of the bulk lattice parameter, whereas the compressive lattice strain for particles of 3 – 4 nm and larger can be neglected.⁹⁷

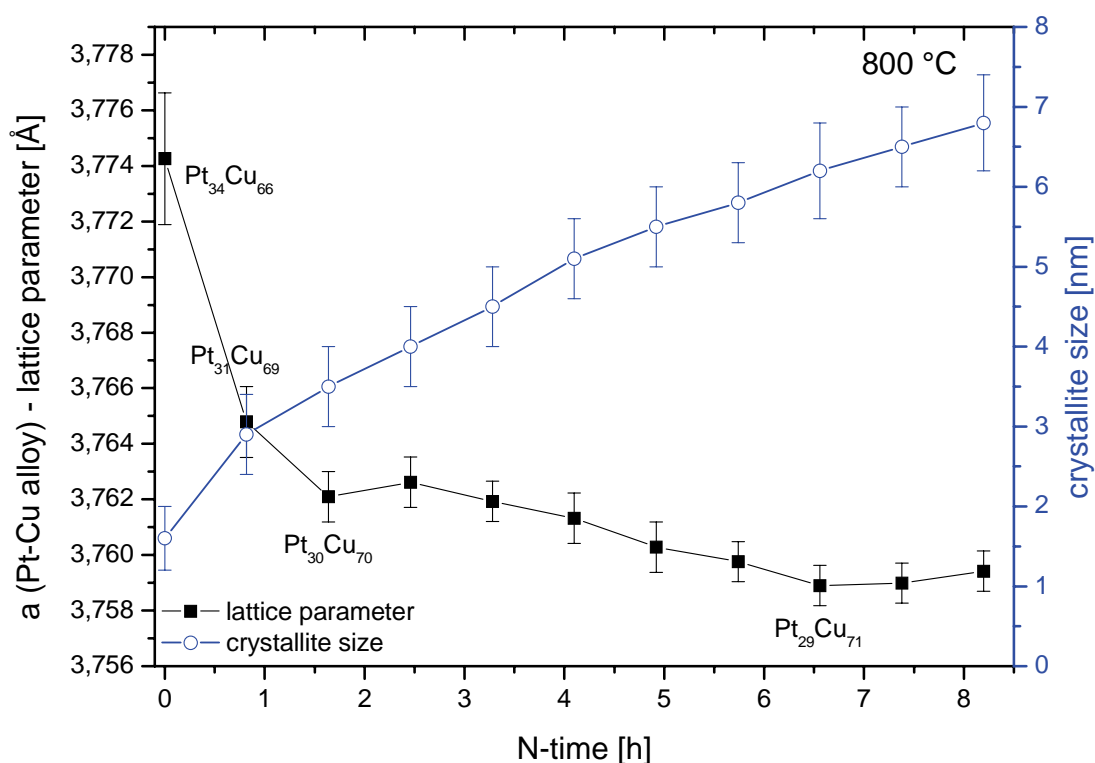


Figure 24 Lattice parameter of disordered Pt-Cu alloy and mean crystallite size normalized temperature time at 800 °C. The mean crystallite size was estimated from the (111) and (200) Pt-Cu alloy reflections. The normalized time (N-time) represents the first scan at 800 °C, in Figure 22a. *a* - lattice parameter error ± 0.001 Å. Reprinted from ref 75 with permission of Chemistry of Materials, copyright (2011).

In Figure 24, the first XRD measurement at 800 °C revealed a uniform Cu rich alloy crystal phase. In the view of the composition – size relationship, two separate temporal regimes for Cu insertion and particle growth were pointed out. The first regime is the continuous insertion of copper atoms into the Pt-Cu alloy lattice in the first two hours at 800 °C (denoted as “Cu insertion regime”). Here, the chemical composition changed from $\text{Pt}_{34-35}\text{Cu}_{66-65}$ to $\text{Pt}_{29-30}\text{Cu}_{71-70}$, while the mean crystallite size grew slightly from 2.2 ± 0.4 nm to 3.8 ± 0.4 nm. Nevertheless, the alloying process was gradual at 800 °C for the first few hours compared with that which had already been occurred during the heating ramp up to 800 °C. The second regime was distinguished by almost unaltered composition (from $\text{Pt}_{29-30}\text{Cu}_{71-70}$ to $\text{Pt}_{28-29}\text{Cu}_{72-71}$), however, strong increased

particle size (from 3.8 ± 0.4 nm to 7.2 ± 0.5 nm) over the residual annealing time (denoted as "*particle growth regime*").

Referred to Figure 23 and Figure 24, only the disordered fcc Pt-Cu alloy crystal phase was formed during the heating and annealing process. The superlattice reflections of the ordered PtCu₃ phase were not observed until now. Furthermore, the annealing time mainly controls the particle size. Only with extended increasing holding time, the particle size increases dramatically.

3.5 Dynamic Behavior of Pt-Cu Alloy Formation during the “Stepped Heating Protocol”

During the heating ramp, the largest content of copper was reduced and incorporated into the already existing Pt lattice. Disordered fcc Pt-Cu alloy crystal phase has formed preferentially compared to the ordered intermetallic Pt-Cu phase. To provide an insight into the temperature behavior of the alloy formation, XRD profiles were recorded during the modified temperature - time protocol with additional heating ramps and temperature holds of each 90 min (“stepped heating protocol”, Figure 22b) under reductive atmosphere. A series of corresponding XRD patterns at various temperatures is shown in Figure 25. Below 300 °C Cu ions were mostly reduced to fcc metallic copper of a large crystallite size. The (111) and (200) Cu reflections shifted to smaller 2θ values based on the thermal cubic lattice expansion. This evidences, that the formation of pure metallic copper occurred more rapidly compared to the alloy formation and alloy particle growth, as is explained in the following.

The calibration and extraction of the temperature-dependent lattice parameters were conducted with carbon supported pure platinum and copper nanoparticles to determine lattice parameter – composition relations over a wide temperature range. As shown in Figure 26, the calibration measurements offered a linear lattice expansion of pure metal nanoparticles 3 – 4 nm in size over a wide temperature range. It can be viewed as a family of Vegard's relations⁷⁴ at given temperature for Pt-Cu alloys at the nano scale.

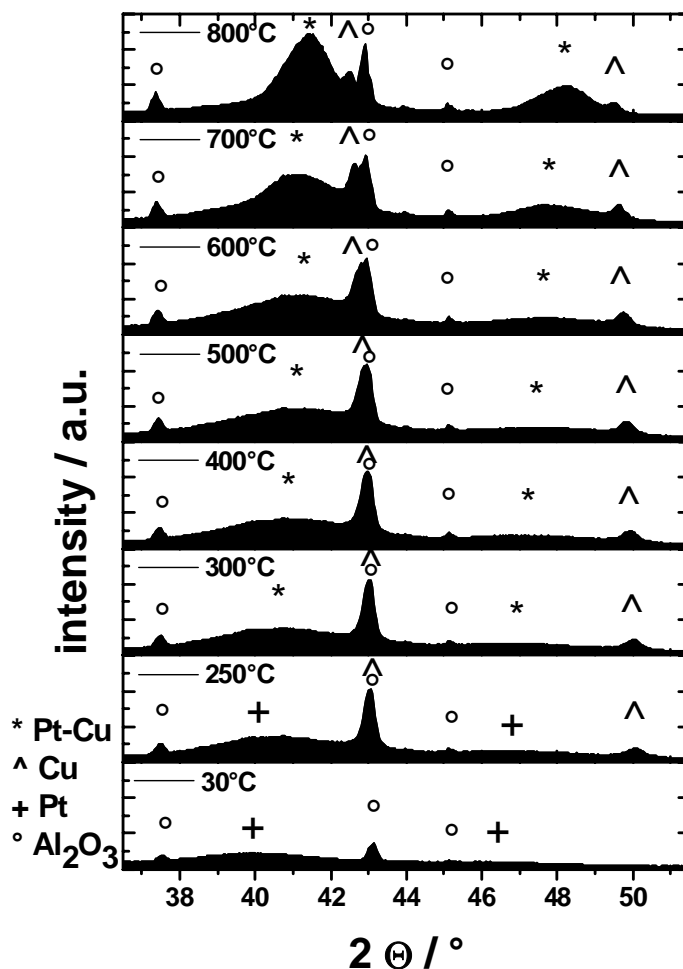


Figure 25 Series of in-situ XRD patterns, recorded in parallel beam XRD setup during the “stepped heating protocol” of Figure 22b. Symbols denote individual crystallographic phases for disordered fcc Pt-Cu alloy, pure fcc Cu and Pt nanoparticles. Reprinted from ref 75 with permission of Chemistry of Materials, copyright (2011).

This calibration allows us an accurate data analysis about the dynamic behavior of alloy formation in dependence on the elevated temperature and time. The Pt content in the alloy nanoparticles decreased gradually with increasing temperature up to 500 °C due to the insertion of Cu into the Pt lattice. During the temperature holds of each 90 min, only a slight positive shift in 2θ of fcc disordered Pt-Cu alloy reflections was observed, associated with an almost stable alloy composition. In conclusion, the Cu insertion process into

the Pt lattice is essentially controlled by temperature not by annealing time. At 500 °C the composition changed from pure Pt to Pt₄₆₋₅₁Cu₅₄₋₄₉. With increasing temperature, the Pt-Cu lattice parameters and compositions showed an almost plateau behavior in Figure 26. However, the change of the alloy composition was clearly significant from Pt₄₃₋₄₅Cu₅₇₋₅₅ at 700 °C to Pt₃₃₋₃₄Cu₆₇₋₆₆ at 800 °C.

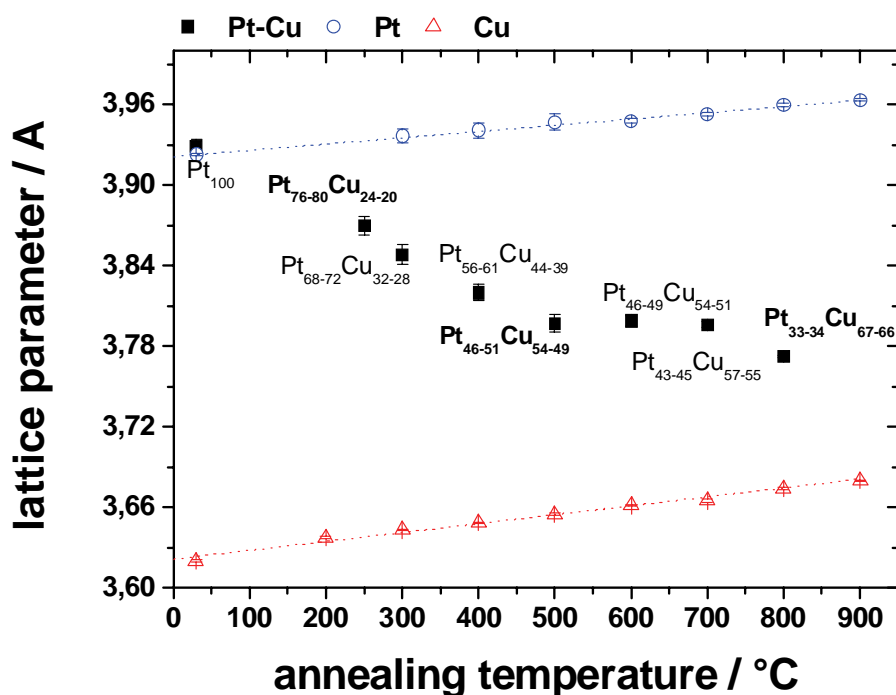


Figure 26 Lattice parameter composition relations of disordered Pt-Cu alloy nanoparticles at various temperatures (black squares for Pt-Cu alloys, blue circles for Pt, red triangle for Cu) extracted from Figure 25. Composition was estimated using a temperature-corrected Vegard's rule. a - lattice parameter error ± 0.004 Å. Reprinted from ref 75 with permission of Chemistry of Materials, copyright (2011).

Only, a disordered Pt-Cu alloy crystal phase was observed during heating by the “stepped heating protocol”. Contrary to expectations from the bulk phase diagram, the thermodynamic stable ordered L1₂ PtCu₃ phase structure was not formed at and below 600 °C in the Pt-Cu alloy nanoparticles. It is suggested that a combination of kinetic effects and thermodynamic size effects may be responsible for this. The diffusion coefficients of Cu and Pt lattice atoms may not be sufficient to mix enough Cu and Pt atoms over the 90 min. The thermodynamic size and composition – dependent segregation effects of

copper, which favor surface segregation of Cu with increasing Cu content^{57, 98}, may contribute and limit Cu alloying into the bulk of Pt particles.

3.6 Formation of Ordered Pt-Cu Alloys during the “Stepped Cooling Protocol”

Only during the cooling process (“stepped cooling protocol”, in Figure 22c), XRD data revealed the partial phase transformation from the disordered fcc Pt-Cu alloy to the thermodynamic stable ordered $L1_2$ PtCu₃ crystal phase. According to the macroscopic thermodynamic phase diagram, the phase transformation occurs at 650 °C.⁵⁸

Figure 7 shows the formation and stability of the superlattice reflection with decreasing temperature. This superlattice reflection peak at $\sim 24^\circ$ corresponds to the (100) lattice plane of the ordered $L1_2$ PtCu₃ structure. The partial phase transformation leads to a decrease of the fcc unit cell symmetry with randomly distributed Cu and Pt atoms to the ordered structure with Cu atoms in the center of each face of the cube and Pt atoms in the edges. The (100) superlattice reflection shifted to higher 2θ values with decreasing temperature because of the thermally caused lattice contraction. Other 2θ reflections at higher angles, which indicated an ordered alloy, overlapped with reflections of disordered fcc Pt-Cu alloy and Al₂O₃ materials. After the prediction of the macroscopic bulk alloy phase diagram, the formation of the ordered PtCu₃ phase occurs at and below 600 °C during the cooling process. This matches our results.

Nevertheless, we have shown that the disordered PtCu₃ alloy phase was a major fraction. The disordered phase was clearly kinetically preferred and stabilized under our synthetic conditions compared with the thermodynamic favorable ordered phase structure.

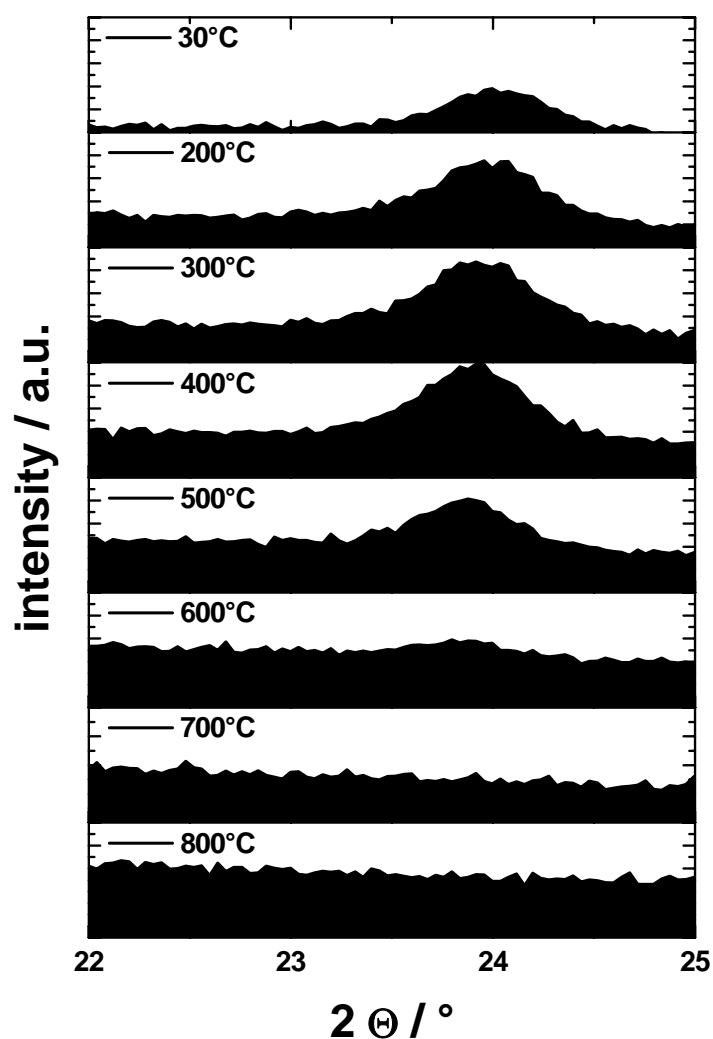


Figure 27 Series of in-situ HT-XRD profiles, recorded in parallel beam XRD setup in the neighborhood of the (100) PtCu_3 superlattice reflection during the “stepped cooling protocol” of Figure 22c. Ordered PtCu_3 alloy phase formed at temperatures below 600 °C. Reprinted from ref 75 with permission of Chemistry of Materials, copyright (2011).

3.7 Summary

The formation kinetics, time-resolved mechanisms, and particle growth of PtCu₃ alloy nanoparticles were studied using the in-situ HT-XRD. The influence of the annealing temperature and time on the alloy formation process was clarified. The lattice parameter – composition relationships over a wide temperature range was also shown using the temperature – corrected Vegard's law.

Based on the experiential results, we concluded:

- The maximum temperature during heating ramps largely determines the composition of the fcc Pt-Cu alloy phase, that is, the extent of Cu insertion into a Pt lattice for bimetallic nanoparticles.
- The annealing time at constant temperature only results in minor additional Cu insertion for ~1.5 h, which, however, causes sustained particle growth and therefore controls the particle size of the resulting alloy material. Annealing times can substantially be shortened without compromising composition.
- The Cu reduction and formation of large pure Cu crystallites was more rapid than the Pt alloy formation and the particle growth, being essentially completed at merely 250 °C on the initial heating ramp.
- The disordered PtCu₃ alloys are preferred during heating ramps, even at prolonged temperature holds.
- The ordered PtCu₃ structure only forms on cooling ramps, with maximum order being achieved at ~400 °C.

This work provides practical synthetic guidelines toward to obtain disordered or ordered highly dispersed PtCu₃ alloy electrocatalysts with desired size.

4 Activation of Pt Bimetallic Nanoparticle Precursor Electrocatalysts

Bimetallic alloy nanoparticles are of great importance in diverse areas, such as magnetic, optical and catalytic applications, due to the clearly altered properties compared with monometallic nanoparticles.⁹⁹⁻¹⁰³ They offer a wide range of compositional (e.g. overall, surface and bulk ratios of metal A and B) and morphological (e.g. particle size, shape and crystal facets) configurations, which sensitively control their surface properties. For instance, dissimilar metals in or near the surface of homogeneously alloyed bimetallic particle catalysts can lead to coexisting surface functionalities and affect the surface reaction kinetics.¹⁰⁴⁻¹⁰⁹

Shown in Figure 28, core-shell nanoparticles as particular type of arrangement of binary metals have attracted much attention in electrochemical energy conversion.²⁹⁻³⁵ They are distinguished by a particle shell of enriched Pt surrounding a Pt poor alloy core. The dealloyed Pt bimetallic core-shell nanoparticle is generated in-situ by selective electrochemical leaching (dealloying) of less noble metal from the surface of a uniform Pt poor bimetallic nanoparticle, as shown in Figure 28. Dependent on the shell thickness, the improved surface catalytic reactivity is based on short-range chemical ligand effects and/or long-range geometric effects such as lattice strain.^{9, 10, 16, 38-40}

Chemical dealloying has emerged as a novel and important synthesis process to obtain catalytically active core-shell bimetallic particles. Historically, dealloying was used for depletion gilding in ancient societies.^{110, 111} In 1927 Raney invented the well-known Raney nickel, which is used as a heterogeneous catalyst for hydrogenation reactions.¹¹² In this century, the selective dissolution of less noble metal from bimetallic alloy system has been mostly studied in the corrosion realm to produce nanoporous materials and highly active dealloyed catalysts for catalytic and sensory applications.¹¹³⁻¹²³ In particular, dealloyed Pt alloy core-shell nanoparticles, formed in-situ by the selective surface dissolution of the less noble component from a uniform binary alloy precursor, have shown very promising catalytic reactivities for the electroreduction of dioxygen (oxygen reduction reaction, ORR) to water in

polymer electrolyte membrane fuel cells (PEMFCs).^{81, 89, 91, 92, 124} More precisely, the dealloyed PtCu₃ is currently the alloy nanoparticle electrocatalyst which meets and exceeds the cathode catalyst activity targets in RDE and real MEA experiments for automotive applications.^{75, 81, 90, 93, 94, 125} The significantly improved performance is due to the lattice strain in the Pt rich shell. The strain significantly changes¹⁶ the chemisorption energies of oxygenated reactive intermediates and effects a 4 – 6 fold activity enhancement of the oxygen reduction.

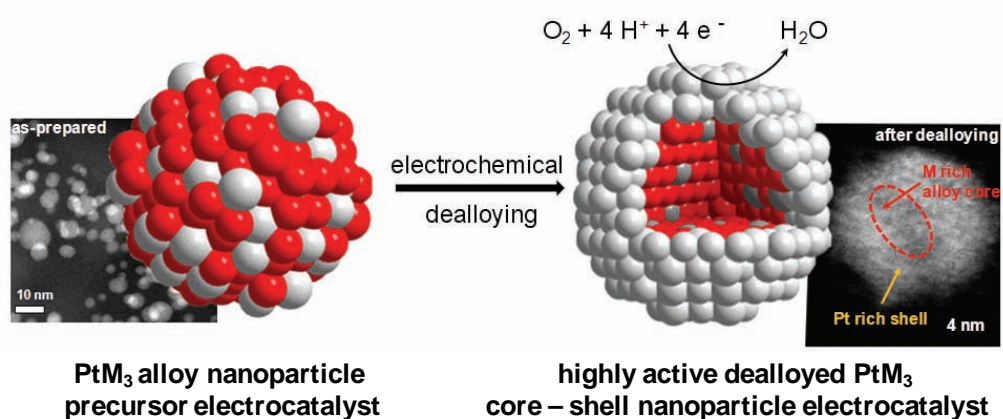


Figure 28 Sketch of the formation of highly active bimetallic core-shell nanoparticle by selective electrochemical dealloying of less noble metal from a uniform Pt poor alloy precursor nanoparticle. Insert: STEM-HAADF micrographs of particles under Z contrast conditions before and after electrochemical dealloying to outline the changes in intraparticle composition and morphology.

In the following chapters, this dealloyed catalyst concept is examined on Pt-Cu and Pt-Co alloy nanoparticles for the electroreduction of oxygen in acidic and alkaline media.

5 Pt-Cu Alloy Nanoparticle Electrocatalysts

Reprinted from ref 126 with permission of The Electrochemical Society, copyright (2012). <http://dx.doi.org/10.1149/2.106204jes>

Dealloying of Pt bimetallic nanoparticles is a promising synthesis method to prepare highly active electrocatalysts for oxygen reduction reaction (ORR) in fuel cells. We present here a structural, compositional and electrochemical characterization linked with ORR activity for carbon supported PtCu₃, PtCu, and Pt₃Cu alloy nanoparticles in different electrolytes and pH values.^{90, 91, 127} The effects of electrolyte and pH are systematically examined on the ECSA and Pt mass based activity (j_{mass}) at different Cu contents in Pt alloys. Our study shows that during voltage cycling in 0.1 M KOH the Cu atoms partially form oxide species on the particle surface, while the residual Cu atoms are electrochemically redissolved/redeposited. In 0.1 M HClO₄, in contrast, the voltage cycling immediately causes the surface dissolution of Cu. We have correlated the ECSA and mass activity with the initial composition in dependence on both electrolytes. In summary, after voltage cycling in 0.1 M HClO₄ the values of j_{mass} increase according: Pt₃Cu < PtCu < PtCu₃. However, after voltage cycling in 0.1 M KOH the values of j_{mass} increase in the following trend: PtCu₃ < PtCu < Pt₃Cu. Only after activation process, PtCu₃ core-shell catalyst shows enhanced ORR activity in 0.1 M KOH compared to pure Pt.

5.1 Structural and Chemical Characterization of the As-Synthesized Pt-Cu Alloy Nanoparticle Electrocatalysts

The PtCu₃, PtCu, and Pt₃Cu alloy nanoparticle electrocatalysts supported on high surface area carbon (HSAC) annealed at 800 °C for 7 h were analyzed by XRD. All XRD profiles of as-synthesized Pt-Cu catalysts are shown in Figure 29. The XRD profile of PtCu₃ catalyst shows multiple face-centered cubic (fcc) crystal phases. The large broad XRD reflections at ~41° and ~49° correspond to the (111) and (200) lattice planes of a disordered fcc Pt-Cu alloy crystal structure with a space group of Fm3m. The XRD reflections of the fcc Pt-Cu phase are located between those of pure fcc platinum and copper crystal phases, indicating the alloy formation by inserting of Cu atoms in the Pt lattice. The sharp XRD reflections at 43.3° and 50.4° signify the presence of pure fcc copper phase (Fm3m) with a large crystallite size of about 35 nm (symbolized by “o” in Figure 29), whereas the ordered L1₂ PtCu₃ phase (Pm3m) is here identified by small superlattice reflections at 24.1°, 34.3° and 55.7° (symbolized by “*” in Figure 29). Table 3 sums up the space groups, lattice parameters, Rietveld crystal phase quantification, crystallite sizes and stoichiometric composition established by Vegard’s rule⁷⁴ for all as-synthesized Pt-Cu alloy nanoparticle electrocatalysts. The integral breadth method⁷¹ was used to determine the mean crystallite size from all XRD reflections. According to Vegard’s law, the stoichiometric composition of the disordered Pt-Cu alloy phase was estimated from the resulting lattice parameter.

The Rietveld analysis for PtCu₃ catalyst revealed that the disordered fcc Pt-Cu alloy phase is the main component with 85.2 ± 1.1 wt. % and a crystallite size of 3.1 ± 0.1 nm. The stoichiometric composition of the main component of the Pt-Cu alloy phase is Pt₃₈Cu₆₂, which is close to the nominal atomic ratio of 1:3. The ordered PtCu₃ crystal phase as minor component is only determined with 5.9 ± 1.0 wt. % and a crystallite size of 9.6 ± 1.9 nm, whereas the pure copper phase at large crystallite size (> 35 nm) exists with 8.9 ± 0.7 wt. %.

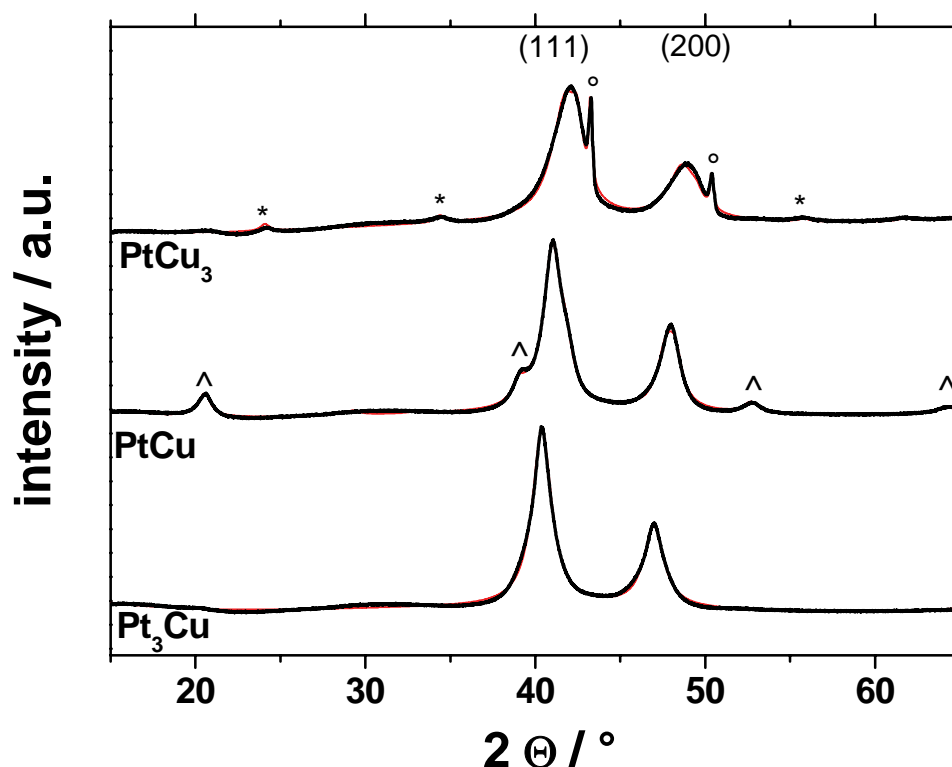


Figure 29 XRD profiles of the as-synthesized Pt-Cu alloy nanoparticle electrocatalysts, displayed with y-offset. Rietveld profile fit of diffraction data for PtCu_3 ($R_{wp} = 2.80$, $R_{exp} = 0.55$, $GOF = 5.05$), for PtCu ($R_{wp} = 2.72$, $R_{exp} = 0.65$, $GOF = 4.19$) and for Pt_3Cu ($R_{wp} = 3.01$, $R_{exp} = 0.67$, $GOF = 4.50$). The fits are indicated by a red solid line. The superlattice reflections of the PtCu_3 ($Pm3m$) are denoted with “*”, the reflections of the Hongshiite PtCu ($R-3m$) are indicated with “^”, and the reflections of the pure fcc Cu ($Fm3m$) are denoted with “o”. Reproduced from ref ¹²⁶ by permission of The Electrochemical Society.

Unlike to the PtCu_3 catalyst, crystalline pure platinum and copper were not detected in the XRD profiles for PtCu and Pt_3Cu alloy catalysts. All reflections shifted here to higher 2θ values with respect to pure platinum, indicating the alloy formation by inserting of Cu in the Pt lattice. The XRD profile of PtCu catalyst only exhibits two crystal phases. The reflections at $\sim 41^\circ$ and $\sim 46^\circ$ correspond to the (111) and (200) lattice planes of a disordered fcc Pt-Cu phase

with a space group of Fm3m. In addition, the reflections at 20.4°, 39.2°, 52.6°, and 62.3° are identified as a rhombohedral PtCu Hongshiite crystallite phase (R3m) (symbolized by “^” in Figure 29). A detailed crystal phase Rietveld analysis could not be performed for this Pt-Cu powder due to the insufficient information about the accurate atom positions of the Hongshiite crystal structure. First estimation shows that the disordered fcc Pt-Cu alloy phase is the main component of ~80 wt. % as Pt₆₀Cu₄₀ and with a crystallite size of 5.0 ± 0.1 nm, while the rhombohedral PtCu Hongshiite crystal phase exists up to ~20 wt. % and with a crystallite size of 7.1 ± 0.5 nm.

Only in the case of Pt₃Cu catalyst, the XRD pattern showed clearly a uniformly alloyed single disordered fcc Pt-Cu crystal phase. The single fcc Pt-Cu alloy crystal phase exhibits a crystallite size of 4.1 ± 0.1 nm and a stoichiometric composition of Pt₈₃Cu₁₇, which confirms almost with a Pt:Cu atomic ratio of 3:1

*Table 3 Comparison of crystal structure, lattice parameter, Rietveld quantification, crystallite size, and stoichiometric composition for Pt-Cu alloy nanoparticle electrocatalysts.*¹²⁶

catalyst	space group	lattice parameter [Å]	Rietveld quantification [wt. %]	crystallite size [nm]	composition via Vegard'
PtCu ₃	Fm3m	3.733 ± 0.001	85.2 ± 1.1	3.1 ± 0.1	Pt ₃₈ Cu ₆₂
	Pm3m	3.676 ± 0.001	5.9 ± 1.0	9.6 ± 1.9	Pt ₂₅ Cu ₇₅
	Fm3m (Cu)	3.614 ± 0.001	8.9 ± 0.7	40.0 ± 6.5	
PtCu	Fm3m	3.808 ± 0.001	~ 80	5.0 ± 0.1	Pt ₆₀ Cu ₄₀
	R3m	10.532 ± 0.005			
	(Hongshiite)	13.363 ± 0.008	~ 20	7.1 ± 0.5	Pt ₅₀ Cu ₅₀
Pt ₃ Cu	Fm3m	3.880 ± 0.001	100 ± 0	4.1 ± 0.1	Pt ₈₃ Cu ₁₇

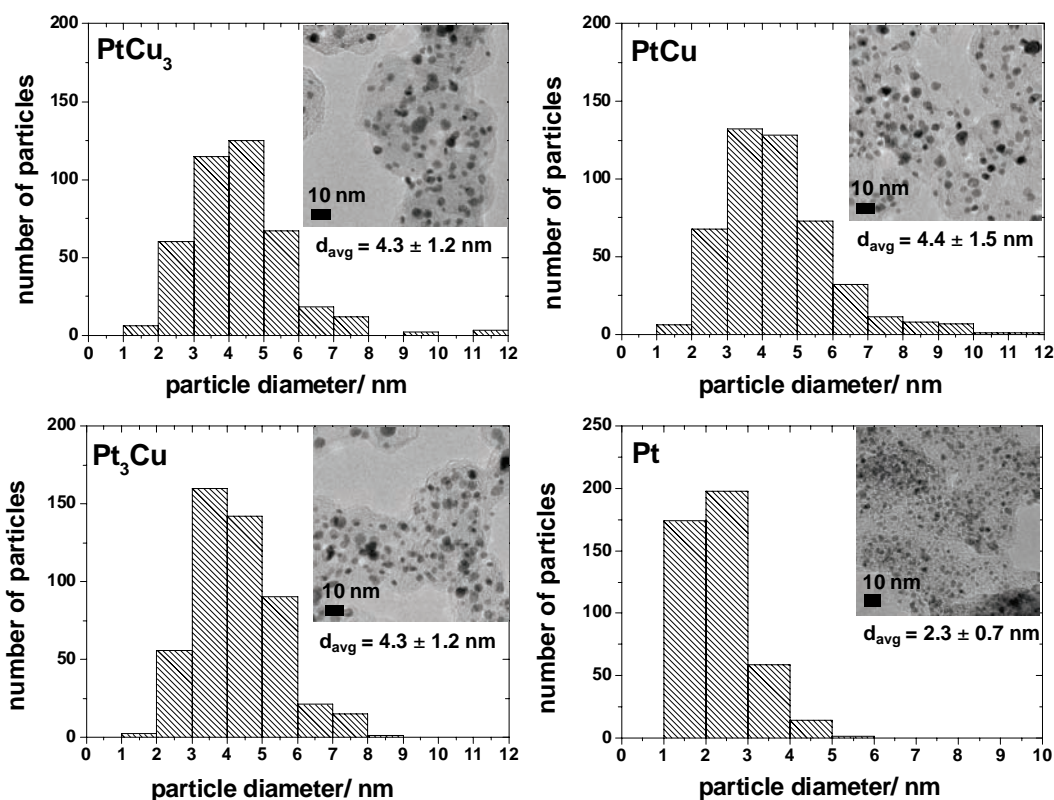


Figure 30 Histograms of particle size distributions with corresponding TEM images for the as-synthesized PtCu₃, PtCu, Pt₃Cu alloy nanoparticle and pure Pt nanoparticle electrocatalysts. The average particle size (d_{avg}) was determined from TEM images by counting of more than 400 particles. Reproduced from ref ¹²⁶ by permission of The Electrochemical Society.

The overall chemical composition and mean particle size established by EDS and TEM techniques for the as-synthesized PtCu₃, PtCu, Pt₃Cu, and 28.2 wt. % Pt/HSAC catalysts are presented in Table 4. Shown in Figure 30, the TEM images were evaluated to determine the mean particle size by counting of more than 400 particles. In results, the as-synthesized PtCu₃, PtCu and Pt₃Cu alloy electrocatalysts exhibit a mean particle sizes of 4.3 ± 1.2 nm, 4.4 ± 1.5 nm, and 4.3 ± 1.2 nm, respectively. The direct comparison of the mean crystallite size and mean particle size for all Pt-Cu catalysts shows an excellent agreement. Therefore, a size-dependent activity benefit can be here ruled out. The overall chemical compositions for PtCu₃, PtCu, and Pt₃Cu alloy nanoparticle electrocatalysts are Pt₃₅Cu₆₅, Pt₆₀Cu₄₀ and Pt₈₂Cu₁₈ which confirm

almost with the Pt:Cu atomic ratios of 1:3, 1:1 and 3:1. Amorphous phases in the Pt-Cu samples can be determined by direct comparing the as-synthesized chemical compositions established by XRD and EDS techniques. Based on the compositional and crystallographic results, we concluded that all Pt-Cu catalysts existed completely as crystalline phases. Despite the differences in the established atomic ratios with the mentioned ratios, we will denote the various Pt-Cu alloys with the original normalized used weighted contents of Pt and Cu precursor materials throughout this paper.

Table 4 Comparison of the as-synthesized mean particle size and chemical composition for the PtCu₃, PtCu and Pt₃Cu alloy nanoparticle catalysts and 28.2 wt. % Pt/HSAC catalyst before and after the electrochemical experiments (EC) in 0.1 M HClO₄ and 0.1 M KOH electrolytes.^{126, 127}

catalyst	mean particle size [nm]	composition initial [at. %]	composition after EC in 0.1 M HClO ₄ [at. %]	composition after EC in 0.1 M KOH [at. %]
PtCu ₃	4.3 ± 1.2	Pt ₃₅ Cu ₆₅	Pt ₆₅ Cu ₃₅	Pt ₅₂ Cu ₄₈
PtCu	4.4 ± 1.5	Pt ₆₀ Cu ₄₀	Pt ₇₅ Cu ₂₅	Pt ₇₀ Cu ₃₀
Pt ₃ Cu	4.3 ± 1.2	Pt ₈₂ Cu ₁₈	Pt ₈₅ Cu ₁₅	Pt ₈₇ Cu ₁₃
Pt	2.3 ± 0.7	Pt ₁₀₀	Pt ₁₀₀	Pt ₁₀₀

5.2 Electrochemical Behavior of Pt-Cu Alloy Nanoparticle Electrocatalysts in Acidic and Alkaline Media

The electrochemical behavior of PtCu₃, PtCu and Pt₃Cu alloy nanoparticle electrocatalysts was examined in different electrolyte solutions at pH 1 and pH 13. Figure 31 illustrates the changes in the shape of cyclic voltammograms (CVs) for Pt-Cu catalysts before and after the fast voltage cycling (200 voltage cycles with 500 mV s⁻¹) in nitrogen-purged 0.1 M HClO₄ (left side) and 0.1 M KOH (right side) electrolyte solutions at room temperature. It is now widely accepted that ClO₄⁻ anions are weakly absorbed on the catalytically active surface and therefore influence slightly the ORR activity. In contrast, the non-covalent interactions between hydrated K⁺ cations and adsorbed OH in alkaline solution affect stronger the ORR activity.^{128, 129} The chosen electrochemical conditions are consistent with our previously published works, where Pt alloys have demonstrated an activity enhancement after activation by electrochemical dealloying.^{75, 81, 82, 90, 130}

Strong differences are evident in the first (dashed lines) and final (solid line) CV profiles of PtCu₃ catalyst recorded in acidic and alkaline media. Unlike to the Pt₃Cu and PtCu catalysts, only the first CV profile for PtCu₃ catalyst measured in 0.1 M HClO₄ shows no presence of underpotentially deposited hydrogen ad/desorption between 0.06 and 0.30 V/RHE (dashed lines, Figure 31a), indicating the complete covering of Cu on the particle surface. The surface segregation of Cu is consistent with DFT theoretical predictions.^{57, 98} The first CV profile exhibits the leaching of copper in two distinct faradic current peaks corresponding to the Cu bulk dissolution at 0.35 V/RHE and the dissolution of underpotentially deposited Cu at 0.75 V/RHE. A small current peak at ~-0.35 V/RHE in the cathodic scan signifies the deposition from soluble Cu species in electrolyte solution. After 200 voltage cycles with 500 mV s⁻¹ in 0.1 M HClO₄, the final CV profile reached a temporarily stable shape. It shows clearly the characteristic features of a pure Pt surface consistent with the hydrogen ad/desorption regime (0.06 – 0.40 V/RHE), the double layer regime (0.40 – 0.60 V/RHE) and the redox peak couple of Pt hydroxide/oxide species at 0.75 and 0.83 V/RHE.

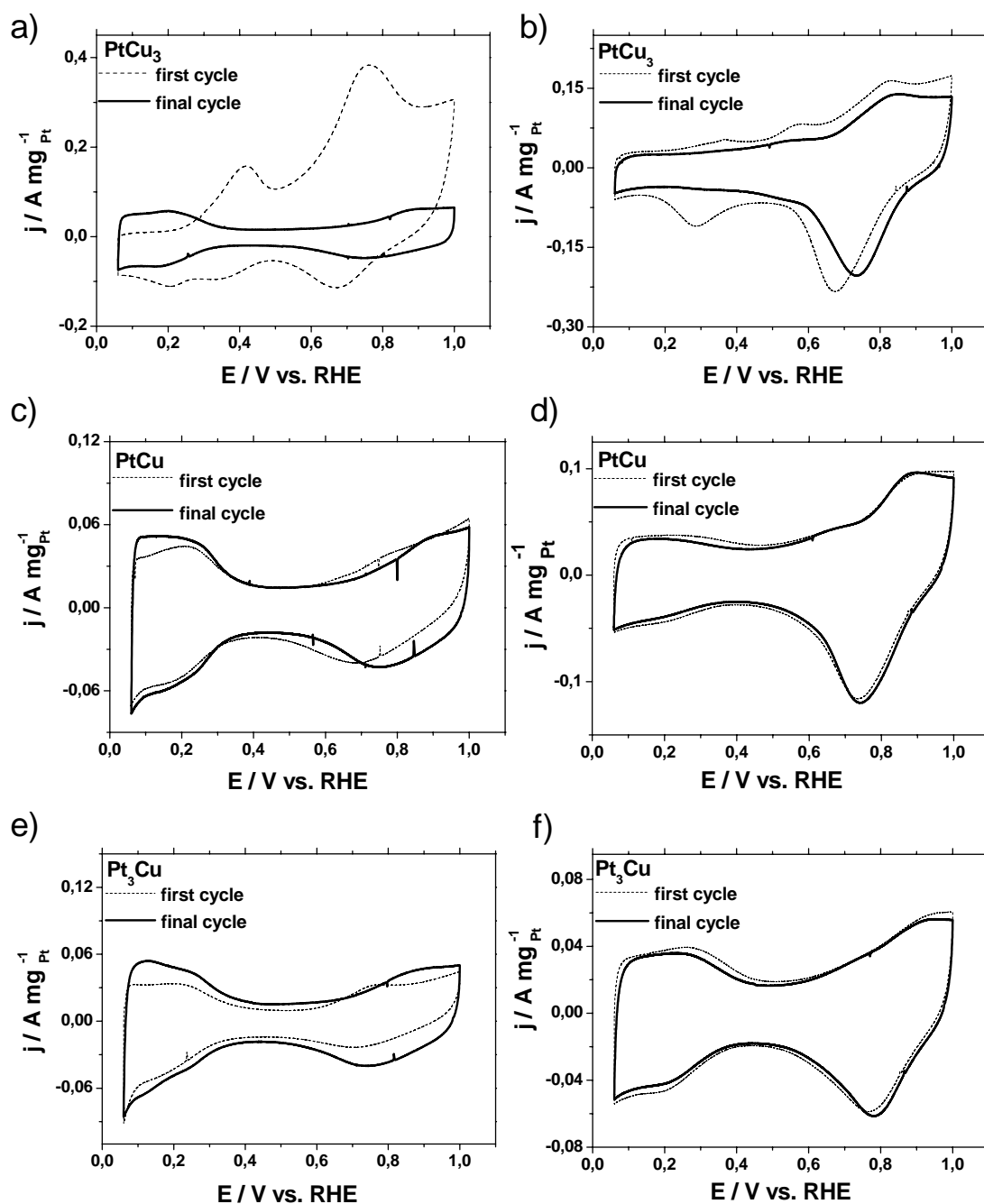


Figure 31 CV profiles of the PtCu_3 (a, b), PtCu (c, d), and Pt_3Cu (e, f) alloy nanoparticle electrocatalysts in deaerated 0.1 M HClO_4 (a, c, e; left side) and 0.1 M KOH (b, d, f; right side) electrolyte solutions. The first and final CV profiles denote with dashed and solid lines. The final CV was recorded after 200 voltage cycles with 500 mV s^{-1} . Cyclic voltammetry was performed from 0.06 to 1.00 V/RHE with 100 mV s^{-1} at room temperature. Reproduced from ref ¹²⁶ by permission of The Electrochemical Society.

The complete coverage of Cu on the particle surface was also evident in the first anodic CV scan in 0.1 M KOH (dashed lines, Figure 31b). According to the Pourbaix diagram⁵⁹, it is shown that at pH 13 in a voltage range from 0.06 to 1.00 V/RHE, copper can exist as: Cu, Cu₂O and HCuO₂⁻ as soluble species. The redox peak couples can be associated with the changes in the oxidation state of Cu atoms from 0 to + I and from + I and + II. Under this condition the oxidation of Cu proceeds in the following pathway: $2 \text{Cu} + \text{H}_2\text{O} \rightarrow \text{Cu}_2\text{O} + 2 \text{H}^+ + 2 \text{e}^-$.¹³¹ Subsequently, Cu₂O can be dissolved in the following pathway: $\text{Cu}_2\text{O} + 3 \text{H}_2\text{O} \rightarrow 2 \text{HCuO}_2^- + 4 \text{H}^+ + 2 \text{e}^-$, which can be deposited during the cathodic scan.¹³¹ In the first anodic scan two distinct faradic current peaks emerged at ~0.58 V/RHE, and ~0.82 V/RHE. We suggest that the two anodic peaks related to the formation of Cu oxide species and surface dissolution of Cu oxide species. The current peak at ~0.32 V/RHE seems to be an experimental artifact. In the first cathodic scan, two current peaks at 0.28 V/RHE and 0.68 V/RHE appeared in alkaline media. During the cathodic scan the main current peak at 0.68 V/RHE corresponded to the deposition from soluble Cu oxide species on a Pt-Cu alloy surface, whereas the small cathodic current peak indicated the further reduction of Cu oxide species to pure Cu. Obviously, the voltage cycling (200 voltage cycles with 500 mV s⁻¹) in alkaline media effects clearly a change in shape of the CV profile of PtCu₃. The final CV profile (solid line, Figure 31b) shows now a broad main redox peak couple at 0.75 and 0.82 V/RHE. The absence of Pt atoms on the particle surface, however, remains. The observed redox peak couples implied the formation of Cu oxide and subsequently the dissolution/deposition of Cu oxide species. In addition, the large current peak in the cathodic scan shifted significantly to more positive potentials, signifying that the redox process became more reversible.

Recorded in 0.1 M HClO₄, the first CV profile (dashed lines, Figure 31c) of PtCu catalyst shows initially a hydrogen ad/desorption regime between 0.06 and 0.40 V/RHE, implying the presence of Pt atoms on the particle surface. Only a very broad current peak at 0.60 – 0.80 V/RHE indicates the dissolution of underpotentially deposited copper. A deposition of Cu during the cathodic scan was not observed. After 200 voltage cycles with 500 mV s⁻¹ in 0.1 M HClO₄, the final quasi stable CV profile (solid line, Figure 31c) of PtCu catalyst

shows clearly the characteristic features of a pure Pt surface. The comparison of the first and final CV profiles recorded in acidic media exhibits an increase of the underpotentially deposited hydrogen regime, indicating a gradual enrichment and rearrangement of Pt atoms on the particle surface. In 0.1 M KOH, the first CV profile (dashed lines, Figure 31d) for PtCu catalyst shows also the presence of Pt atoms on the particle surface and it is consistent with the voltammetric observation in 0.1 M HClO₄. In addition, a very broad current peak in the range of 0.5 and 0.75 V/RHE of the first anodic scan signifies the presence of Cu oxide species. The cathodic peak at 0.75 V/RHE overlapped likely with the reduction peak of Pt oxide and deposition peak of Cu species on the alloy surface. After the voltage cycling in alkaline media, the shape of the final CV profile seems to be temporary stable.

In the case of the Pt₃Cu catalyst, the first CV profile (dashed lines, in Figure 31e) recorded in acidic media resembles initially the typical characteristic features of a pure Pt surface, indicating a very high covering of platinum atoms on the particle surface. The hydrogen ad/desorption regime increases significantly during the voltage cycling due to the rearrangement of Pt atoms and the removal of carbonous catalyst surface poisons. The Pt-enriched particle surface is also to identify in the first and final CV profiles recorded in 0.1 M KOH, as shown in Figure 31f. The shape of the CV profiles of Pt₃Cu in alkaline media is quasi stable after voltage cycling. Referred to the voltammetric results in alkaline and acidic media, the surface segregation of Pt atoms in Pt rich alloys is completely reached by thermal annealing.

5.2.1 Comparison with pure Pt Nanoparticles

The final CV profiles of the Pt-Cu alloy catalysts are compared with a commercially available 28.2 wt. % Pt/HSAC after voltage cycling (200 voltage cycles with 500 mV s^{-1}) in 0.1 M HClO_4 and 0.1 M KOH electrolyte solutions. In acidic media (see Figure 32a) the CV profiles of the voltammetric pretreated PtCu_3 , PtCu and Pt_3Cu catalysts evidence the typical characteristic features of a pure Pt surface corresponding to the hydrogen ad/desorption regime, the double layer regime, and the redox peak couple of Pt hydroxide/oxide. It is noted that the voltage cycling in 0.1 M HClO_4 effects strongly the dissolution of Cu atoms from the surface of alloy particles. The final CV profiles of Pt-Cu reveal an anodic onset shift of the anodic current peaks of Pt oxide species between 0.8 and 0.9 V/RHE compared to that for pure Pt. This indicates an improved activation for Pt-Cu catalysts and the reduction of the oxygen chemisorption energy.^{67, 132}

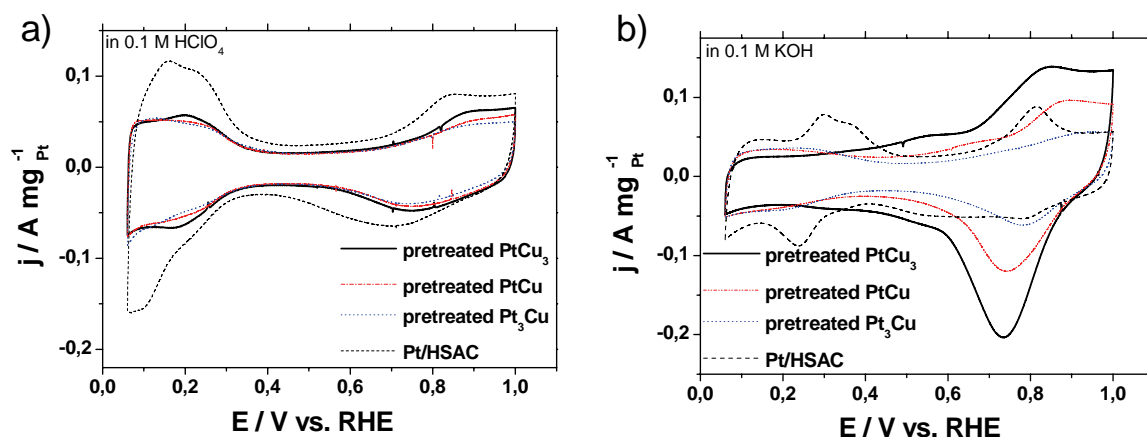


Figure 32 CV profiles of pretreated PtCu_3 , PtCu and Pt_3Cu catalysts compared with 28.2 wt. % Pt/HSAC after the voltage cycling in deaerated (a) 0.1 M HClO_4 and (b) 0.1 M KOH. Cyclic voltammetry was performed from 0.06 to 1.00 V/RHE with 100 mV s^{-1} at room temperature. Reproduced from ref ¹²⁶ by permission of The Electrochemical Society.

Figure 32b shows the temporarily stable shape of the cyclic voltammograms for PtCu₃, PtCu and Pt₃Cu catalysts compared with that for pure Pt catalyst after voltage cycling in 0.1 M KOH. Only the CV profiles for pretreated PtCu and Pt₃Cu exhibit clearly the characteristic features of a Pt-enriched surface. With a careful view on the CV profile for PtCu catalyst, the broad anodic current peak in the voltage range of 0.5 and 0.7 V/RHE indicates the presence of Cu oxide species on the particle surface. In the case of PtCu₃ catalyst, the CV profile shows clearly the absence of Pt atoms and therefore the complete coverage of Cu on the surface. It is noted, that the current peak at ~0.75 V/RHE in the cathodic scan increases with increasing Cu content in Pt alloys and shifted to more negative potentials. We pointed out that during alkaline voltage cycling copper formed relatively stable oxide species, which subsequently were redissolved/ redeposited. The observed loss of Cu established by EDS (see column 3 and 5 of Table 4) is associated with the incomplete deposition from soluble Cu species in electrolyte solution during the cathodic scan.

5.3 Platinum Electrochemical Active Surface Area (ECSA) and Chemical Composition of Pt-Cu Alloy Nanoparticles

The platinum electrochemical active surface areas (ECSAs) and the changes in chemical composition for PtCu₃, PtCu, and Pt₃Cu alloy nanoparticle electrocatalysts are determined before and after the electrochemical experiments in both deaerated 0.1 M HClO₄ and 0.1 M KOH electrolyte solutions, shown in Table 4 and Table 5. Despite the changes in initial chemical composition we will denote now the voltammetric pretreated Pt-Cu alloy catalysts as “pretreated PtCu₃”, “pretreated PtCu” and “pretreated Pt₃Cu” in this paper.

The ECSA estimated from the mean integral charge of the underpotentially deposited hydrogen ad/desorption regime implies the electrochemically active platinum atoms on the particle surface for electrocatalysis. Referred to Table 5, the values of ECSA for all pretreated Pt-Cu catalysts are smaller than those for 28.2 wt. % Pt/HSAC in acidic and alkaline media. The low values of ECSA are caused by the growth of alloy particles after annealing. This can be explained by the relationship between ECSA and particle size. In general, the ECSA decreases with increasing particle size.¹³³⁻¹³⁷ In addition, the values of the ECSA for pretreated Pt-Cu catalysts are significantly higher in 0.1 M HClO₄ compared with those in 0.1 M KOH. After the same electrochemical conditions in acidic media the values of ECSA increase in the following trend: Pt₃Cu < PtCu < PtCu₃. So, the increasing ECSA is deduced with the increasing surface roughness due to the rapid electrochemical dissolution of Cu. In contrast, after the voltage cycling in 0.1 M KOH the values of ECSA increase according: PtCu₃ < PtCu < Pt₃Cu. In this case, the increased ECSA is related to the surface coverage and rearrangement of Pt atoms. Cu atoms partially form surface oxide species, while the residual Cu atoms are electrochemically redissolved/redeposited during voltage cycling in alkaline media. The relatively stable Cu atoms on the particle surface reduce the electrochemical active Pt surface area.

Table 4 shows the changes in overall chemical composition established by EDS after the electrochemical experiments in both 0.1 M HClO₄ and 0.1 M KOH solutions. In alkaline media the composition for PtCu₃ catalyst changed from initial Pt₃₅Cu₆₅ to final Pt₅₂Cu₄₈, indicating that soluble Cu species are formed during voltage cycling. A complete deposition from soluble Cu species in the electrolyte was not attained during the cathodic scan. However, the loss of Cu in acidic media is higher with a final composition of Pt₆₅Cu₃₅. Unlike to the results for PtCu₃ catalyst, the final concentration of Pt₃Cu catalyst changed very slightly in acidic and alkaline media. The thermal induced segregation of Pt atoms towards the particle surface hampers the dissolution of internal copper. Finally, the EDS results show for PtCu catalyst that the loss of Cu is slightly higher after the same electrochemical treatment in acidic media than that in alkaline media.

Table 5 Pt electrochemical active surface area (ECSA), Pt mass based activity (j_{mass}) and Tafel slope at low current density (lcd) for PtCu₃, PtCu and Pt₃Cu nanoparticle catalysts compared with 28.2 wt. % Pt/HSAC in 0.1 M HClO₄ and 0.1 M KOH electrolytes.^{126, 127}

catalyst	ECSA in acidic [m ² g _{Pt} ⁻¹]	ECSA in alkaline [m ² g _{Pt} ⁻¹]	j_{mass} at 0.9 V/RHE in acidic [A mg _{Pt} ⁻¹]	j_{mass} at 0.9 V/RHE in alkaline [A mg _{Pt} ⁻¹]	Tafel slope at lcd in acidic / alkaline [mV dec ⁻¹]
PtCu ₃	58 ± 6	8 ± 3	0.45 ± 0.04	0.01 ± 0.01	68 / 21
PtCu	45 ± 6	15 ± 1	0.38 ± 0.06	0.05 ± 0.01	71 / 47
Pt ₃ Cu	40 ± 2	24 ± 3	0.23 ± 0.02	0.12 ± 0.01	64 / 68
Pt	73 ± 3	49 ± 3	0.13 ± 0.01	0.16 ± 0.01	61 / 64

5.4 ORR Performance of Pretreated Pt-Cu Alloy Nanoparticle Electrocatalysts in Acidic and Alkaline Media

The pretreated PtCu₃, PtCu and Pt₃Cu alloy nanoparticle electrocatalysts were subsequently tested for the oxygen reduction reaction (ORR) in both electrolyte solutions. The polarization curves were performed by anodic sweeping with 5 mV s⁻¹ and 1600 rpm (rotations per minute) in oxygen saturated 0.1 M HClO₄ and 0.1 M KOH at room temperature, shown in Figure 33. A plateau behavior at 0.06 – 0.60 V/RHE in the polarization curves of each Pt-Cu catalyst was observed, indicated the diffusion-limited regime for the oxygen reduction. Here, the diffusion-limited current density is in the range between -5 and -6 mA cm_{geo}⁻². The different diffusion-limited current densities in acidic and alkaline media are based on the differences in oxygen solubility, diffusivity and kinematic viscosity of the electrolyte solution. The differences of experimental diffusion-limited current densities and the discrepancy to the theoretical value for the four-electron ORR pathway¹³⁸ in one solution likely cause the unequal electrode coverage with catalyst as experimental artifact. The change from a mixed kinetic-diffusion control to a diffusion-limiting regime takes place at 0.6 V/RHE in 0.1 M KOH and at 0.7 V/RHE in 0.1 M HClO₄. With a careful view on the polarization curves in 0.1 M KOH (see Figure 33b), a positive potential shift at the mixed region occurred with increasing Pt content. In contrast, in 0.1 M HClO₄ the positive potential shift was observable with decreasing Pt content (see Figure 33a). It reveals that this positive potential shift indicates a strong ORR activity improvement.

Figure 33c shows the mass transport corrected Pt mass based Tafel plot for all pretreated Pt-Cu catalysts obtained from the polarization curves in both electrolyte solutions. In the view of the Pt mass based Tafel plot, it evidences that the pretreated Pt-Cu catalysts in acidic media show a significantly improvement of ORR activity than those in alkaline media. The reported values in the literature of the Tafel slope for platinum as single crystal⁶³, polycrystalline⁶⁴, and carbon supported nanoparticles^{65, 66} are around -2.3 RT/F at the low overpotentials ($E > 0.85$ V/RHE) and -2 x 2.3 RT/F at high

overpotentials ($E < 0.85$ V/RHE)⁶⁷. The estimated values of the Pt mass based Tafel slopes for Pt-Cu at low current density (lcd) region are compared with those of 28.2 wt. % Pt/HSAC (not shown). The results are summarized in column 4-6 of Table 5. In 0.1 M KOH the value of the Tafel slope for pretreated Pt₃Cu catalyst is in good agreement with the Tafel slope value of 60 mV dec⁻¹ obtained from the experimental and literature data for bulk and single platinum crystals^{63, 64}. Only the pretreated PtCu₃ and PtCu catalysts show here low values of Tafel slope in the alkaline media compared to that for supported pure Pt nanoparticles due to the high coverage of Cu atoms on the particle surface. In contrast, we found similar values of Tafel slope (see Figure 33c and column 6 in Table 5) for PtCu₃ and Pt₃Cu at lcd in acidic media, which is close to the experimental and literature data for pure Pt⁶³⁻⁶⁵. The slope for the pretreated PtCu is slightly higher compared to that of pure Pt. The difference in the Tafel slopes can be explained by the changed adsorption behavior of oxide species at increasing presence of Cu atoms on the particle surface.¹⁷

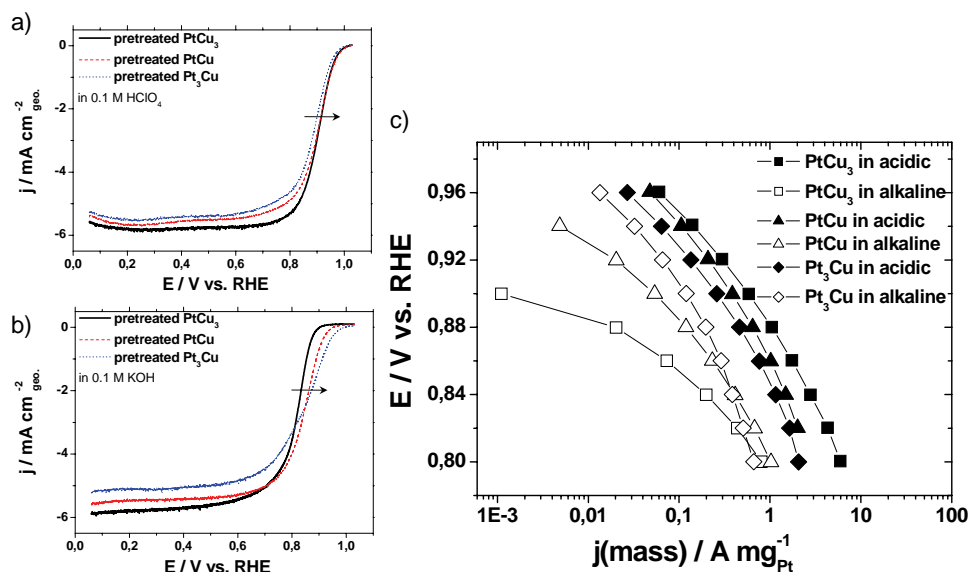


Figure 33 Polarization curves of pretreated PtCu₃, PtCu and Pt₃Cu electrocatalysts in oxygen saturated (a) 0.1 M HClO₄ and (b) 0.1 M KOH. (c) Mass transport corrected Pt mass based Tafel plot of pretreated Pt-Cu catalysts in 0.1 M KOH and 0.1 M HClO₄ electrolyte solutions. LSV measurements were performed anodically from 0.06 – 1.00 V/RHE with 5 mV s⁻¹ and 1600 rpm (rotations per minute) at room temperature. Reproduced from ref ¹²⁶ by permission of The Electrochemical Society.

Table 5 summarizes the Pt mass based activities (j_{mass}) of pretreated PtCu₃, PtCu, and Pt₃Cu alloy nanoparticle electrocatalysts for ORR after the electrochemical treatment in 0.1 M HClO₄ and 0.1 M KOH. Here, 28.2 wt. % Pt/HSAC was taken as benchmark catalyst. In results, in alkaline media the pretreated Pt₃Cu electrocatalyst exhibits the highest j_{mass} compared with PtCu and PtCu₃ catalysts; while pretreated PtCu₃ catalyst shows the highest j_{mass} than PtCu and Pt₃Cu catalysts in acidic media. After the voltage cycling in 0.1 M KOH the values of j_{mass} increase in the following trend: PtCu₃ < PtCu < Pt₃Cu. However, the pretreated Pt₃Cu catalyst is slightly less active than the commercial pure Pt/HSAC catalyst. The decreasing activity in alkaline media can be explained by increasing surface coverage of Cu. By voltage cycling in alkaline media copper forms relatively stable surface oxide as well as soluble species which can be only partially deposited during the cathodic scan. The improved activity in alkaline media can be associated with the Cu concentration in the subsurface layers of a Pt-enriched shell and the level of coordination of Pt surface atoms. The thermal segregation-induced Pt skin on Pt₃Cu catalyst leads to a slight positive shift in the potential for the formation of oxygen adsorbed species on Pt and causes to an increase of active Pt surface atoms for the oxygen reduction.

After voltage cycling in 0.1 M HClO₄, in contrast, the values of j_{mass} increase according: Pt₃Cu < PtCu < PtCu₃. The pretreated PtCu₃ exhibits clearly 3-4 fold increase in j_{mass} compared to the pure Pt nanoparticles.^{90, 91, 130} The clear activity improvement of the pretreated PtCu₃ catalyst in acidic media is due to the rapid electrochemical dissolution of Cu atoms and the formation of a Pt-enriched particle shell. The resulting lattice strain in the Pt-enriched shell¹⁶ for pretreated PtCu₃ is uncovered and addressed for the significantly improved activity. The comprehensive strain results in a shift of the electronic Pt band structure and weakens the chemisorptions of the oxygen species. In the case of PtCu catalyst, after voltage cycling in 0.1 M HClO₄ j_{mass} is 2-3 times higher than that for pure Pt. Finally, the Pt₃Cu catalyst shows only 2 fold increase in j_{mass} compared to commercial Pt in acidic media. The effects of electrolyte and pH become noticeable for Pt-Cu nanoparticle catalysts.

5.5 Correlation of ECSA – Activity – Cu Alloy Composition in Dependence on Different Electrolyte Solutions and pH Values

The ECSA and the Pt mass based ORR activity were correlated here with the initial alloy composition of Pt-Cu after similar electrochemical treatment (200 voltage cycles with 500 mV s^{-1}) in 0.1 M HClO_4 (pH 1) and 0.1 M KOH (pH 13). Obviously, the morphology and chemical composition of Pt-Cu alloys exhibit strong effects of electrolyte and pH during voltage cycling. The surface-sensitive cyclic voltammetry was used to investigate the change of composition of the outermost atomic layers of Pt-Cu alloys.

Based on our results, the sketch in Figure 34 illustrates the chemical and morphological changes of Pt-Cu alloys initiated by voltage cycling in 0.1 M HClO_4 and 0.1 M KOH . After the rapid electrochemical dissolution of copper atoms in acidic media, the particles exhibit a Pt-enriched shell surrounding by an alloy particle core. The picture of the particle structure changes in alkaline electrolyte solution. The voltage cycling up to 1.0 V/RHE in alkaline media causes the formation of surface Cu oxide species and subsequently the dissolution of Cu oxide species. The soluble Cu species can be partially deposited during the cathodic scan.

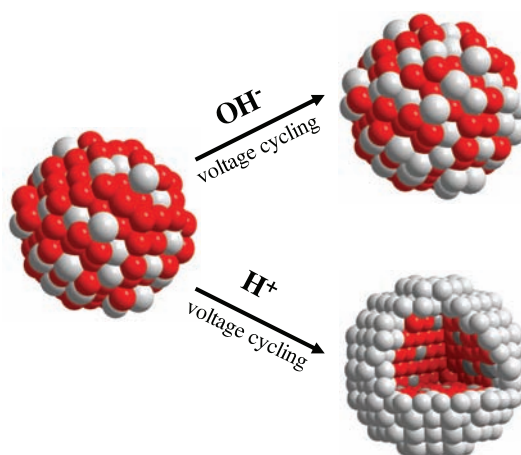


Figure 34 Illustration of morphological and chemical changes in bimetallic Pt-Cu alloy nanoparticles by voltage cycling in 0.1 M HClO_4 and 0.1 M KOH . Pt and Cu atoms are symbolized with light grey and red spheres, respectively. Reproduced from ref ¹²⁶ by permission of The Electrochemical Society.

Due to the similar mean particle sizes, ECSA and activity benefits can be ruled out. The established values of ECSA and Pt mass based activity are related to the initial alloy composition and electrolyte solutions at pH 1 and pH 13. Figure 35a correlates the ECSA established after the same voltage procedure in different electrolyte solutions with the initial Cu concentration in the alloys. A strong difference is evident in the courses of ECSA in acidic and alkaline media. In 0.1 M KOH the ECSA decreases clearly with increasing Cu contents in the alloys due to the relative stability of Cu atoms by forming of oxide species and deposition from soluble species. The relatively stable Cu atoms cause a decrease of Pt surface area or number of electrochemically active Pt surface atoms. Apparently, we observed here an opposite trend in acidic media. Here, Cu atoms are immediately removed from the particle surface and the Pt atoms remain and enrich successively the particle surface. In acidic media the ECSA increases with increasing Cu contents in alloys due to the resulting surface roughness.

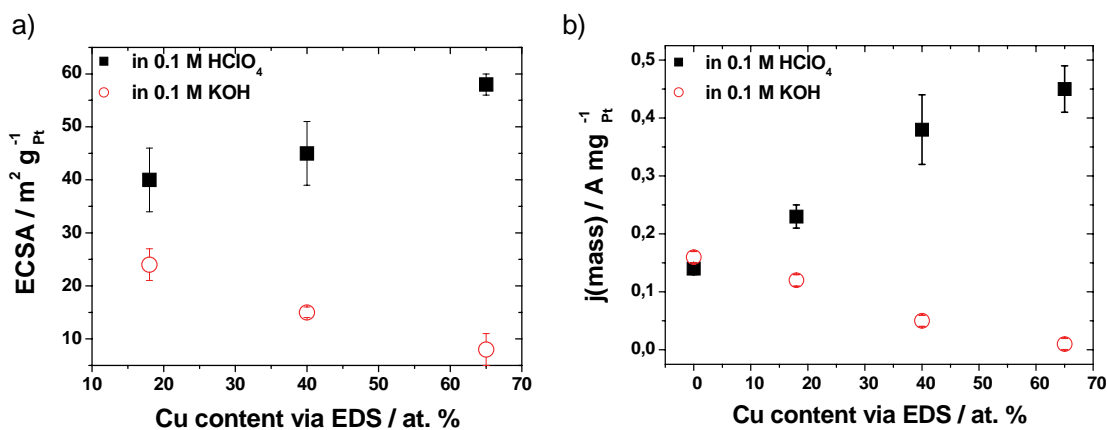


Figure 35 a) ECSA versus initial Cu concentration and (b) Pt mass based activity (j_{mass}) versus initial Cu concentration established by EDS for Pt-Cu alloy nanoparticle electrocatalysts after voltage cycling in 0.1 M HClO₄ and 0.1 M KOH. Reproduced from ref ¹²⁶ by permission of The Electrochemical Society.

The composition – activity – electrolyte relationship is clearly shown in Figure 35b. In 0.1 M KOH j_{mass} decreases drastically with increasing initial Cu concentration in the Pt alloys. The strong decrease of j_{mass} can be explained by the increasing covering of Cu atoms on the particle surface. Cu atoms on the surface are relatively stable in 0.1 M KOH due to the formation of surface Cu oxide species and deposition of Cu. We did not observe an activity enhancement by the presence of Cu atoms in the surface and in particular in the subsurface in alkaline media. Copper possesses a less oxophilic character than cobalt. We suggest that the less oxophilic Cu atoms at the neighborhood of Pt atoms reduce insufficiently the coverage of OH_{ads} species on the platinum atoms. Thus, in alkaline media the Pt_3Cu catalyst shows slightly less j_{mass} for ORR than the commercial supported Pt catalyst. In the view of the course on j_{mass} in 0.1 M HClO_4 , however, the ORR activity increases significantly with increasing initial Cu concentration. The improved activity is here caused by the Cu content in the subsurface layers and the level of coordination of Pt surface atoms. Due to the depletion of Cu, Pt atoms enrich the particle surface. In addition, the electrochemical dealloying procedure in acid leads also to a rough particle surface. The surface roughness may also contribute in an improved Pt mass based activities. In results, the PtCu_3 catalyst shows the highest ORR activity in the family of Pt-Cu alloy electrocatalysts due to the formation of highly active alloy rich core – Pt rich shell structure. The improved activity is caused by the resulting lattice strain in the Pt-enriched shell.¹⁶ In the case of Pt_3Cu catalyst, the Pt skin surface induced by thermal annealing shows only a slight increase of j_{mass} .

5.6 Hydrogen Peroxide Production of Pretreated Pt-Cu Alloy Nanoparticle Electrocatalysts

The selectivity of the oxygen reduction for pretreated PtCu₃, PtCu and Pt₃Cu alloy nanoparticle electrocatalysts was examined in 0.1 M HClO₄ electrolyte using a RRDE technique. The formation of hydrogen peroxide was determined with the well-known standard method described in the literature.^{62, 90, 139} The production of hydrogen peroxide for Pt-Cu with the elevated disk potential during the recording of the polarization curves are shown in Figure 36.

The established hydrogen peroxide for each Pt-Cu catalyst is clearly below 0.5 %. It is noted, that the course of the hydrogen peroxide decreased continuously with increasing disk potential. The values of hydrogen peroxide were close to zero at the kinetic diffusion regime. Only the highest concentration of peroxide was detected in a disk potential range of 0.06 and 0.20 V/RHE. The enhancement of peroxide formation in the H_{upd} regime is due to co-adsorption of H_{upd} and oxygen. Nevertheless, due to the very low production of hydrogen peroxide, we highlighted, that the PtCu₃, PtCu, and Pt₃Cu alloy nanoparticle electrocatalysts are suitable for the direct four electron transfer as the main mechanism for oxygen reduction in 0.1 M HClO₄.

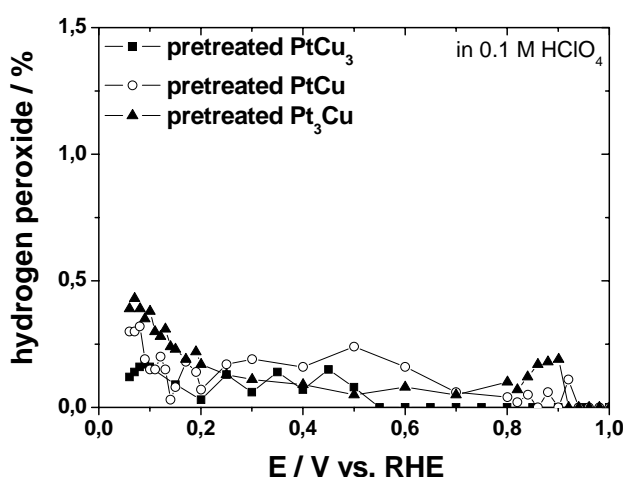


Figure 36 Quantification of the hydrogen peroxide production at various applied disk voltages during oxygen reduction on pretreated PtCu₃, PtCu and Pt₃Cu alloy nanoparticle electrocatalysts. Reproduced from ref ¹²⁶ by permission of The Electrochemical Society.

5.7 Highly Active PtCu₃ Core-Shell Nanoparticles in Alkaline Media

An improvement of ORR performance for PtCu₃ alloy nanoparticle catalyst can be attained by an optimal pretreatment in alkaline media. The highly active PtCu₃ core-shell catalyst cannot be formed in alkaline media by voltage cycling due to the relatively stable Cu oxide and deposition from soluble Cu oxide species. Only the voltage cycling in 0.1 M HClO₄ effects the irreversible rapid dissolution of Cu and thus the enrichment of Pt on the particle surface. It results in highly catalytically active PtCu₃ core-shell arrangement.

The cyclic voltammograms recorded in 0.1 M KOH for PtCu₃ catalyst are shown before and after the activation process in Figure 37a. The activation occurred by electrochemical dealloying (200 voltage cycles with 500 mV s⁻¹) in 0.1 M HClO₄ to change the surface chemical composition of Cu rich alloy particles. It is noted that a strong differences are evident in the shape of CV profiles before and after the activation process. In 0.1 M KOH the first CV profile of PtCu₃ catalyst shows clearly the absence of Pt atoms (between the voltage ranges from 0.06 to 0.30 V/RHE) and therefore the complete coverage of Cu atoms on the particle surface. Meanwhile, after activation by electrochemical dealloying in 0.1 M HClO₄ the CV profile reveals the typical characteristic features of a pure Pt surface corresponding to the hydrogen ad/desorption peaks, capacitive double layer regime, and redox peak couple of Pt hydroxide/oxide. The arrangement of Pt rich shell – Pt poor alloy rich particle core was subsequently tested for ORR in 0.1 M KOH.

The polarization curves of the non-activated and activated PtCu₃ catalyst are compared in Figure 37b. In 0.1 M KOH both polarization curves show a plateau behavior at 0.06 – 0.60 V/RHE, indicating the diffusion-limited regime for the oxygen reduction. Here, the diffusion-limited current density of the activated PtCu₃ electrocatalyst is a range of -5 and -6 mA cm_{geo}⁻². It is noticed, that the mixed region of the polarization curve for activated PtCu₃ shifted strongly to more positive potentials compared to that for non-activated PtCu₃ catalyst. We highlighted that this significantly positive shift indicates a strong enhancement of the ORR activity in 0.1 M KOH.

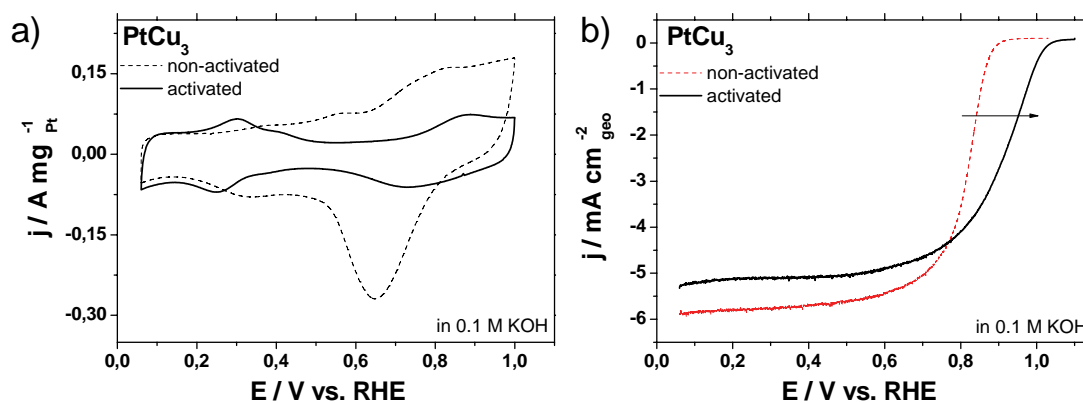


Figure 37 a) CV profiles of non-activated and activated $PtCu_3$ alloy nanoparticle electrocatalyst. b) Polarization curves of non-activated and activated $PtCu_3$ catalyst. Cyclic voltammetry was performed from 0.06 to 1.00 V/RHE with 100 mV s^{-1} in 0.1 M KOH at room temperature. LSV measurements were performed anodically from 0.06 - 1.00 V/RHE with 5 mV s^{-1} and 1600 rpm (rotations per minute) in 0.1 M KOH at room temperature. Reproduced from ref ¹²⁶ by permission of The Electrochemical Society.

Table 6 Pt electrochemical active surface area (ECSA) and Pt mass based activity (j_{mass}) for activated $PtCu_3$ alloy nanoparticle electrocatalyst compared with 28.2 wt. % Pt/HSAC in 0.1 M $HClO_4$ and 0.1 M KOH electrolytes.¹²⁶

catalyst	ECSA in acid [$\text{m}^2 \text{g}_{\text{Pt}}^{-1}$]	ECSA in alkaline [$\text{m}^2 \text{g}_{\text{Pt}}^{-1}$]	j_{mass} at 0.9 V/RHE in 0.1 M $HClO_4$ [$\text{A mg}_{\text{Pt}}^{-1}$]	j_{mass} at 0.9 V/RHE in 0.1 M KOH [$\text{A mg}_{\text{Pt}}^{-1}$]
activated $PtCu_3$	40 ± 5	22 ± 6	0.50 ± 0.06	0.43 ± 0.08
non-activated $PtCu_3$	49 ± 8	8 ± 3	0.50 ± 0.06	0.01 ± 0.01
Pt	74 ± 4	49 ± 3	0.14 ± 0.01	0.16 ± 0.01

Table 6 sums up the resulting ECSA and Pt mass based activities at 0.9 V/RHE for the activated $PtCu_3$, non-activated $PtCu_3$ and pure Pt catalysts in both electrolytes. The direct comparison of the non-activated and activated $PtCu_3$ points out the strong increase of the ECSA and in particular of the Pt mass based activity. The strong difference in activity is based on the structural and compositional change. The non-activated $PtCu_3$ shows no ORR activity due

to the high coverage and stability of Cu on the particle surface in alkaline media. Now, the significantly improved Pt mass based activity is caused by the formation of a Pt-enriched shell surrounding by alloy particle core. So, in KOH the activated PtCu₃ core-shell nanoparticles exhibit clearly a 3 fold increase in j_{mass} compared to pure benchmark Pt and a 43 fold increase in j_{mass} compared to the non-activated PtCu₃ catalyst. The Pt mass based activity of PtCu₃ core-shell catalyst is slightly higher in acid compared to that in alkaline media. This can be likely explained by non-covalent interactions between hydrated K⁺ and adsorbed OH species and the very weak anion adsorption strength of ClO₄⁻.

We concluded that the PtCu₃ core-shell arrangement is a highly active ORR electrocatalyst for acidic and in particular for alkaline PEM fuel cells.

5.8 Summary

Our study has shown a comprehensive characterization of the structure, composition and electrochemical behavior linked with the resulting ORR activity for PtCu₃, PtCu and Pt₃Cu alloy nanoparticle electrocatalysts in acidic and alkaline electrolyte solutions. The effects of electrolyte and pH on the morphology and chemical composition of Pt-Cu alloy particles initiated by voltage cycling were uncovered. We have established the ECSA – activity – alloy composition relationship in dependence on HClO₄ and KOH electrolyte solutions. Based on the electrochemical, compositional and structural results, we concluded that

- According to the crystal phase Rietveld quantification, the main component (above 80 wt.%) for PtCu₃ and PtCu catalysts is the disordered fcc alloy crystal phase with a crystallite size in range of 3 - 5 nm. The crystallite sizes are in excellent agreement with the mean particle sizes of 4 nm established by TEM. Only, the Pt₃Cu catalyst shows clearly a uniformly alloyed single disordered fcc crystal phase (100 wt. %) with a size of 4 nm established by XRD and TEM. The initial chemical compositions are Pt₃₅Cu₆₅, Pt₆₀Cu₄₀, and Pt₈₂Cu₁₈ established by EDS.
- During the voltage cycling in 0.1 M KOH copper forms surface oxide species and then soluble Cu oxide species, which can be partially deposited. In addition, the EDS results reveal a gradual loss of Cu after the electrochemical treatment in alkaline media due to the incomplete deposition from soluble Cu species.
- In contrast, the voltage cycling in 0.1 M HClO₄ causes a rapid surface dissolution of Cu atoms and therefore the enrichment of Pt on the particle surface. The dealloyed particles exhibit a Pt-enriched shell surrounding by an alloy core.
- After voltage cycling in 0.1 M KOH the Pt mass based activities increase according: PtCu₃ < PtCu < Pt₃Cu. Here, the pretreated Pt₃Cu catalyst is slightly less active for ORR than commercial pure Pt.

- In contrast, after the voltage cycling in 0.1 M HClO₄ the Pt mass based activities increase in the following trend: Pt₃Cu < PtCu < PtCu₃. The Pt mass based activity for pretreated PtCu₃ catalyst increases by 3-4 times compared to the benchmark pure Pt.
- The activated PtCu₃ catalyst exhibits 3 fold increase in Pt mass based activity in 0.1 M KOH than the benchmark pure Pt and 43 fold increase in j_{mass} compared to the non-activated PtCu₃ catalyst. The formed PtCu₃ core-shell structure is the highly catalytically active species. The established enhanced j_{mass} of PtCu₃ core-shell nanoparticles for ORR in alkaline media is comparable with that in 0.1 M HClO₄.

We provide the suitability of PtCu₃ core-shell nanoparticles as highly active ORR electrocatalyst for acidic and in particular for alkaline PEM fuel cells.

6 Pt-Co Alloy Nanoparticle Electrocatalysts

Reprinted from ref 140 with permission of The Electrochemical Society, copyright (2012). <http://dx.doi.org/10.1149/2.075204jes>

Pt-Co alloy nanoparticles have emerged as one of the most promising electrocatalysts for the oxygen reduction reaction (ORR) in hydrogen fuel cells. Our study presents a comprehensive structural, chemical and electrochemical characterization linked with ORR activity for carbon supported PtCo₃, PtCo, and Pt₃Co alloy nanoparticle catalysts in electrolytes at different pH values.^{90, 91, 127} Surface-sensitive cyclic voltammetry was used to investigate the change of composition of the outermost atomic layers of Pt-Co alloys. Our electrochemical results in 0.1 M KOH show clearly a stability and voltage-induced accumulation of Co on the surface of alloyed Pt particles, whereas in 0.1 M HClO₄ the voltage cycling initiates a rapid dissolution of Co atoms to form a Pt-enriched surface surrounding by alloy core. We correlated the ECSA and ORR activity with the initial chemical composition of Pt-Co alloys. In results, after electrochemical treatment in 0.1 M HClO₄ the Pt mass based activities (j_{mass}) increase according: PtCo < Pt₃Co < PtCo₃. In contrast, after the electrochemical treatment in 0.1 M KOH j_{mass} increase according: PtCo₃ < PtCo < Pt₃Co. Particularly, however, PtCo₃ catalyst shows after the activation by electrochemical dealloying in acid outstanding mass activity compared to pure Pt in 0.1 M KOH, an increase by 4 times.

6.1 Structural Characterization of the As-Synthesized Pt-Co Alloy Nanoparticle Electrocatalysts

The high surface area carbon (HSAC) supported PtCo₃, PtCo, and Pt₃Co nanoparticle electrocatalysts were structurally characterized by XRD. Figure 38 shows all XRD profiles of as-synthesized Pt-Co catalysts. The XRD pattern for PtCo₃ catalyst shows two disordered face-centered cubic (fcc) crystal phases. The 2 Θ reflections at $\sim 43^\circ$, $\sim 48^\circ$, and $\sim 68^\circ$ correspond to the (111), (200), and (220) lattice planes of the fcc lattice cell with a space group of Fm3m. It is noted, that all reflections shifted to higher 2 Θ values with respect to pure platinum, indicated the lattice contraction by inserting of Co atoms in the Pt lattice. Crystalline cobalt and platinum were not observed in all XRD profiles. Table 7 summarizes space groups, lattice parameters, Rietveld crystal phase quantification, crystallite sizes and stoichiometric compositions established by Vegard's rule⁷⁴ for all as-synthesized Pt-Co electrocatalysts. The crystallite size was estimated from the complete XRD profile using the integral breadth method⁷¹, which is independent of the crystallite distribution in size and shape. The Rietveld analysis for PtCo₃ powder revealed that the disordered Pt-Co alloy phase is the main component: 74.8 ± 2.2 wt. % with a crystallite size of 2.1 ± 0.1 nm. The minor component is a disordered fcc Co rich alloy phase with 25.2 ± 2.1 wt. % and a crystallite size of 20.8 ± 1.0 nm. The stoichiometric composition was estimated from the lattice parameter of the disordered fcc Pt-Co phases using the Vegard's rule. According to the Vegard's rule, the main and minor Pt-Co crystal phases are composed of Pt₄₇Co₅₃ and Pt₅Co₉₅.

In the case of the PtCo catalyst, the XRD profile shows clearly multiple crystal phases. The XRD analysis revealed, that the main component of the disordered fcc Pt-Co alloy phase (84.5 ± 2.1 wt. % with a crystallite size of 2.5 ± 0.1 nm) exhibited a composition of Pt₆₅Co₃₅. Small sharp reflections at 24.2° , 33.4° , 54.4° , and 61.1° indicated the presence of a tetragonal PtCo crystal structure (P4/mmm) (symbolized by "x" in Figure 38). The tetragonal PtCo crystal phase exists with 14.5 ± 2.0 wt. % and a crystallite size of 12.4 ± 1.4 nm. Only traces of a third disordered fcc Pt rich alloy phase was detected with around 0.6 wt. %.

Finally, the XRD pattern for Pt₃Co catalyst shows clearly a disordered fcc alloy crystal phase (Fm3m) and an ordered Pt₃Co crystal phase (Pm3m). The ordered Pt₃Co crystal phase (Pm3m) (symbolized by “*” in Figure 38) was identified by superlattice reflections at 23.1°, 32.8°, and 53.1°. However, the disordered fcc Pt-Co alloy crystal phase with a composition of Pt₈₅Co₁₅ is still the main component (95.3 ± 2.1 wt. % and a crystallite size of 2.8 ± 0.1 nm). The ordered Pt₃Co phase only exists with 4.8 ± 1.2 wt. % and a crystallite size of 9.0 ± 2.4 nm.

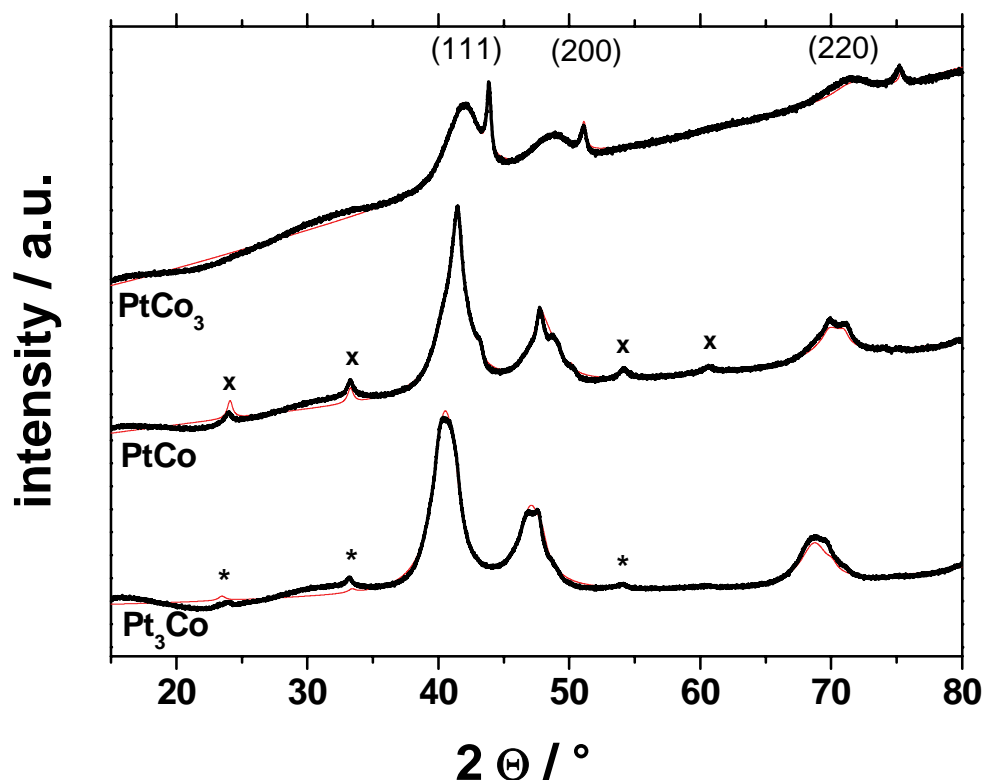


Figure 38 XRD profiles of as-synthesized Pt-Co alloy nanoparticle electrocatalysts, displayed with y-offset. Rietveld profile fit of diffraction data for Pt₃Co ($R_{wp} = 3.56$, $R_{exp} = 0.62$, $GOF = 5.72$), for PtCo ($R_{wp} = 2.55$, $R_{exp} = 0.54$, $GOF = 4.73$), and for PtCo₃ ($R_{wp} = 1.53$, $R_{exp} = 0.43$, $GOF = 3.58$). The fits are indicated by a red solid line. The superlattice reflections of the Pt₃Co (Pm3m) are denoted with “*” and the reflections of the tetragonal PtCo (P4/mmm) are indicated with “x”. Reproduced from ref 140 by permission of The Electrochemical Society.

Table 7 Crystal structure, space group, lattice parameter, crystallite size, Rietveld quantification, and stoichiometric composition of PtCo₃, PtCo and Pt₃Co alloy nanoparticle electrocatalysts.¹⁴⁰

catalyst	space group	lattice parameter [Å]	Rietveld quantification [wt. %]	crystallite size [nm]	composition via Vegard
PtCo ₃	Fm3m	3.728 ± 0.001	74.8 ± 2.2	2.1 ± 0.1	Pt ₄₇ Co ₅₃
	Fm3m	3.566 ± 0.001	25.2 ± 2.1	20.8 ± 1.0	Pt ₅ Co ₉₅
PtCo	Fm3m	3.797 ± 0.001	84.5 ± 2.1	2.5 ± 0.1	Pt ₆₅ Co ₃₅
	P4/mmm	3.814 ± 0.001	14.5 ± 2.0	12.4 ± 1.4	Pt ₅₀ Co ₅₀
		3.704 ± 0.001			
	Fm3m	3.641 ± 0.002	0.6 ± 0.3	----	---
Pt ₃ Co	Fm3m	3.867 ± 0.001	95.3 ± 2.1	2.8 ± 0.1	Pt ₈₅ Co ₁₅
	Pm3m	3.803 ± 0.001	4.8 ± 1.2	9.0 ± 2.4	Pt ₇₅ Co ₂₅

Table 8 summarizes the chemical composition and the mean particle size of the as-synthesized PtCo₃, PtCo, Pt₃Co, and commercially available 28.2 wt. % Pt/HSAC catalysts obtained from the EDS and TEM analysis. The mean particle size was determined from the evaluation of TEM images by counting of more than 400 particles, shown in Figure 39. In results, the mean particle sizes for the as-synthesized PtCo₃, PtCo and Pt₃Co electrocatalysts are 3.6 ± 1.0 nm, 3.8 ± 1.1 nm, and 4.0 ± 1.1 nm. Referred to Table 7, the average crystallite sizes of all Pt-Co catalysts extracted from the XRD profile are slightly smaller than those established by TEM, however, the values are still in the error range of the mean particle size. Due to the similar initial mean particle sizes, a size-dependent activity benefit can be here ruled out. From the EDS analysis the initial chemical compositions for PtCo₃, PtCo, and Pt₃Co nanoparticle electrocatalyst are Pt₃₆Co₆₄, Pt₅₉Co₄₁, and Pt₈₃Co₁₇ and confirmed almost with the desired Pt:Co atomic ratios of 1:3, 1:1 and 3:1. The comparison of the as-synthesized chemical compositions established by XRD and EDS techniques can be used to determine amorphous phases in Pt-Co alloy catalysts. Based on our compositional and crystallographic results, we concluded that the PtCo and Pt₃Co catalysts exist completely as crystalline phases, while PtCo₃ revealed the presence of an amorphous phase of below 15 wt%.

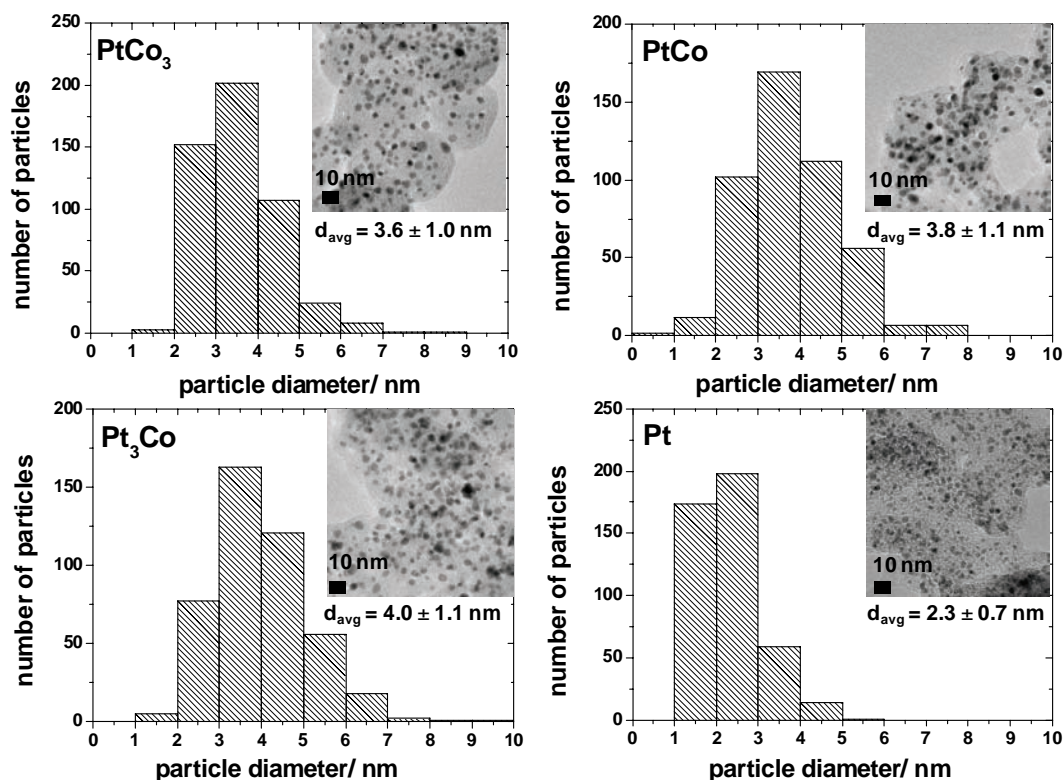


Figure 39 Histograms of particle size distributions and corresponding TEM images for the as-synthesized PtCo₃, PtCo, Pt₃Co alloy and pure Pt nanoparticle electrocatalysts. The average particle size (d_{avg}) was determined from TEM images by counting of more than 400 particles. Reproduced from ref 140 by permission of The Electrochemical Society.

Table 8 Comparison of the initial mean particle size and chemical composition for the PtCo₃, PtCo and Pt₃Co alloy nanoparticle catalysts and 28.2 wt. % Pt/HSAC catalyst before and after the electrochemical experiments (EC) in acidic and alkaline electrolytes.^{127, 140}

catalyst	mean particle size [nm]	initial composition [at. %]	composition after EC in 0.1 M HClO ₄ [at. %]	composition after EC in 0.1 M KOH [at. %]
PtCo ₃	3.6 ± 1.0	Pt ₃₆ Co ₆₄	Pt ₇₈ Co ₂₀	Pt ₃₂ Co ₆₈
PtCo	3.8 ± 1.1	Pt ₅₉ Co ₄₁	Pt ₇₇ Co ₂₃	Pt ₇₁ Co ₃₉
Pt ₃ Co	4.0 ± 1.1	Pt ₈₃ Co ₁₇	Pt ₈₇ Co ₁₃	Pt ₈₄ Co ₁₆
Pt	2.3 ± 0.7	Pt ₁₀₀	Pt ₁₀₀	Pt ₁₀₀

6.2 Electrochemical Characterization of Pt-Co Alloy Nanoparticle Electrocatalysts in Alkaline and Acidic Media

The effects of electrolyte and pH values on the electrochemical behavior of PtCo₃, PtCo and Pt₃Co alloy nanoparticle catalysts were studied by recording cyclic voltammograms (CVs). Perchloric acid and potassium hydroxide were used to clarify the role of supporting electrolyte on the electrochemical behavior and ORR activity for Pt alloys. Figure 40 illustrates the changes of the cyclic voltammograms (CVs) for PtCo₃, PtCo, and Pt₃Co electrocatalysts before and after the fast voltage cycling (200 voltage cycles with 500 mV s⁻¹) in nitrogen-purged 0.1 M HClO₄ (left side) and 0.1 M KOH (right side) electrolyte solutions at room temperature. We chose these conditions due to the previously published works, which an activity improvement for PtCu₃ and PtCo₃ alloys has shown after the electrochemical dealloying in 0.1 M HClO₄.^{16, 81, 90, 91, 130}

In the case of PtCo₃ catalyst, the initial CV profile (dashed lines, Figure 40a) in acidic media showed a very broad anodic peak in a voltage range between 0.40 and 0.75 V/RHE, indicated the dissolution of underpotentially deposited Co atoms from the particle surface. The Co leaching is generally a very rapid process in acidic and electrochemical environment. In addition, the first CV profile showed also the characteristic features of the underpotential deposited hydrogen regime between 0.06 and 0.30 V/RHE, associated with the presence of platinum on the surface of alloy particles. After fast 200 voltage cycles the final CV profile clearly exhibited the typical characteristic features of a pure platinum surface, corresponding to the hydrogen ad/desorption regime (0.06 – 0.40 V/RHE), the double layer regime (0.40 – 0.60 V/RHE), and the current peak couple of Pt hydroxide / oxide at ~0.75 and ~0.83 V/RHE on the cathodic and anodic CV scan^{90, 91}.

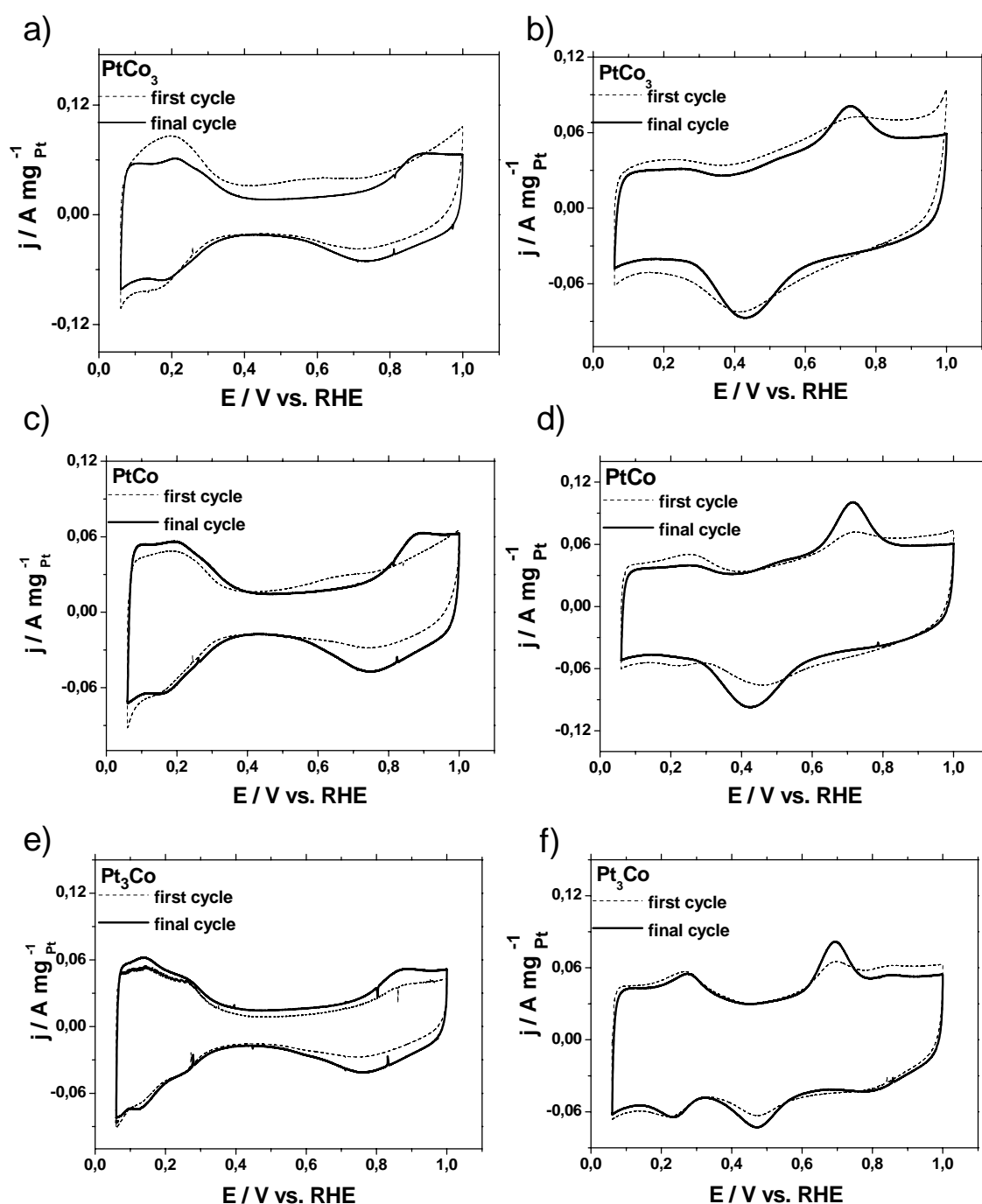


Figure 40 CV profiles of $PtCo_3$ (a, b), $PtCo$ (c, d), and Pt_3Co (e, f) alloy nanoparticle electrocatalysts in deaerated 0.1 M $HClO_4$ (a, c, e; left side) and 0.1 M KOH (b, d, f; right side) electrolytes. The first and final CV profiles denote with dashed and solid lines. The final CV was recorded after 200 cycles with 500 mV s^{-1} . Cyclic voltammetry was performed from 0.06 to 1.00 V/RHE with 100 mV s^{-1} at room temperature. Reproduced from ref 140 by permission of The Electrochemical Society.

In 0.1 M KOH the initial CV profile (dashed lines in Figure 40b) for PtCo₃ showed also slight hydrogen desorption regime at 0.06 – 0.35 V/RHE, indicated a low covering of Pt atoms on the particle surface. In addition, very broad peaks emerged between 0.20 – 0.60 V/RHE and 0.40 – 0.90 V/RHE in the cathodic and anodic scan, respectively. In the view of the Pourbaix diagram of Co, it is shown that at pH 13 and in a voltage range from 0.06 to 1.0 V/RHE, Co can exist as: Co(OH)₂, Co₃O₄ and Co(OH)₃. The predominant species from up to 1.0 V/RHE in the anodic scan might be Co(OH)₃ through the oxidation of Co(OH)₂ with the temporary stable Co₃O₄ as the intermediate specie. Thus, this redox peak couple can be associated with the change in the surface oxidation state of Co atoms from +2 to +3.⁵⁹ After the voltage cycling in alkaline media, the hydrogen desorption regime grew very slightly, while the well-defined current peaks of Co oxide species emerged clearly stronger at 0.42 and 0.72 V/RHE. In addition, the current peak at 0.42 V/RHE in the cathodic scan shifted to more positive potentials, implying that the redox process of Co became more reversible. The comparison of the final CV profiles in acidic and alkaline media shows that in 0.1 M KOH cobalt atoms on the particle surface are stable by forming of oxide species. Duong et al. reported that the XPS analysis reveals the stability of Co for Pt₃Co catalyst in alkaline media.¹⁴¹ The experimentally observed increased redox peak couple of Co oxide species indicates a successive enrichment of additional Co atoms on the particle surface. These phenomena can be explained by the surface rearrangement and/or surface segregation of Co.¹⁴² Cobalt possesses a strong oxophilic character. The voltage cycling causes a surface roughness and formation of oxygen adsorbed species on the particle surface, which initiates an accumulation process of Co.

In the case of PtCo catalyst, in 0.1 M HClO₄ the first CV profile (dashed lines, Figure 40c) showed from the beginning the typical characteristic features of a Pt-enriched particle surface. Only a very broad anodic peak at 0.50 – 0.80 V/RHE signified the surface dissolution of underpotentially deposited Co atoms. By comparing the first and final CV profiles in acidic media, the slightly increased hydrogen ad/desorption regime indicated a gradual enrichment and rearrangement of Pt atoms on the surface of PtCo alloy particles. In 0.1 M KOH shown Figure 40d, the first CV profile showed also hydrogen desorption regime

and additional broad redox peak couple of cobalt oxide species at ~ 0.45 and ~ 0.71 V/RHE. However, after the voltage cycling in alkaline media the final CV profile exhibited a slight decrease of the hydrogen desorption peak and simultaneously a significant growth of redox peak couple of Co oxide species, indicated a successive accumulation of cobalt atoms and thus a gradual displacement of outermost Pt surface atoms. In addition, the shift of the current peak at 0.45 V/RHE to more negative potentials in the cathodic scan implied slightly more irreversible redox process of Co. It evidences that the redox peak couple of Co oxide species increased significantly after the voltage cycling. We suggest that the gradual enrichment of Co atoms on the particle surface is caused by the adsorbed oxygen surface species and surface rearrangement induced by voltage cycling.

Shown in Figure 40e, in 0.1 M HClO_4 the first CV profile for Pt_3Co catalyst clearly resembled the typical characteristic features of a pure Pt surface, and signified a complete covering of platinum atoms on the particle surface. After voltage cycling the hydroxide ad/desorption regime increased slightly and the redox peak couple of Pt oxide emerged pronounced, associated with a recrystallization of Pt on the particle surface. The Pt-enriched particle surface is also to identify in the first and final CV profiles recorded in 0.1 M KOH (see Figure 40f). But, the redox peak couple of Co oxide species at 0.47 V/RHE and 0.70 V/RHE increased by additional voltage cycling, indicated clearly a successive accumulation of Co atoms on the particle surface. At the same time the hydrogen desorption peak decreased slightly, associated with a reduced Pt surface area or a reduced number of electrochemically active Pt atoms. No shift of the redox peak couple of Co oxide species was observed after the voltage cycling. The features of Co can be described by a surface rearrangement process and/or surface segregation by forming of oxygen adsorbed species induced by voltage cycling. By comparing of the first CV profiles in the acidic and alkaline media, it revealed that the surface segregation of Pt atoms is not attained completely by thermal annealing. The first CV profile in alkaline media showed current peaks at ~ 0.47 and ~ 0.70 V/RHE, associated with the presence of Co atoms on the particle surface in alkaline media.

6.2.1 Comparing with pure Pt Nanoparticles.

Figure 41 compares the final CV profiles of the Pt-Co alloy catalysts with 28.2 wt. % Pt/HSAC after the voltage cycling (200 voltage cycles with 500 mV s^{-1}) in 0.1 M HClO_4 and 0.1 M KOH electrolytes at room temperature. Shown Figure 41a, in acidic media the CV profiles of the electrochemically pretreated PtCo_3 , PtCo and Pt_3Co reveals typical characteristic features of a pure Pt surface corresponding to the hydrogen ad/desorption regime, double layer regime, and the redox peak couple of Pt hydroxide/oxide. Here, the Co atoms were completely removed from the particle surface. In addition, the onset of the platinum oxide peak for each pretreated Pt-Co catalysts at 0.80 – 0.90 V/RHE shifted to higher voltage compared to that of pure 28.2 wt. % Pt/HSAC. This positive voltage shift relates to a reduced formation of oxygenated surface species on the Pt-enriched particle surface. This increased anodic onset shift causes likely decreasing surface oxide coverage and may lead to a reduction in oxygen chemisorptions energy on dealloyed Pt-enriched surfaces. The decreasing surface coverage of oxide may result in activity enhancements.^{67, 132}

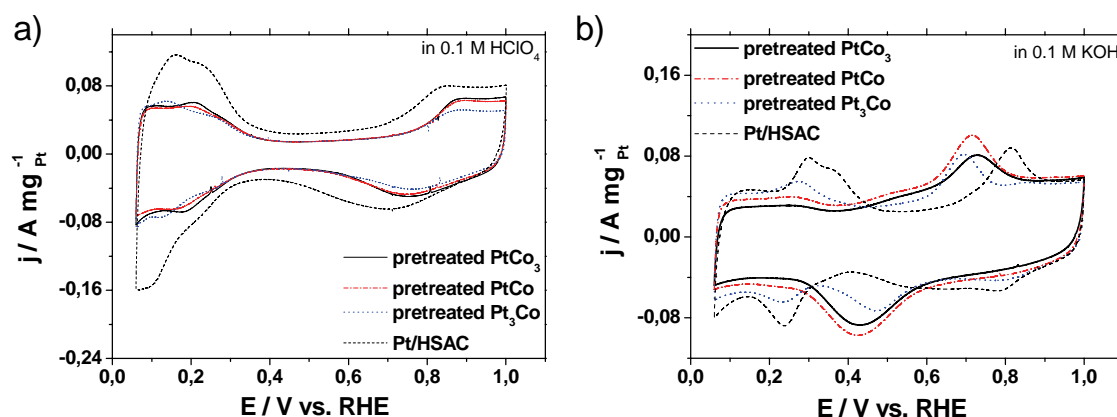


Figure 41 CV profiles of pretreated PtCo_3 , PtCo and Pt_3Co alloy nanoparticle catalysts compared with 28.2 wt. % Pt/HSAC catalyst in deaerated (a) 0.1 M HClO_4 and (b) 0.1 M KOH. Cyclic voltammetry was performed from 0.06 to 1.00 V/RHE with 100 mV s^{-1} at room temperature. Reproduced from ref 140 by permission of The Electrochemical Society.

Figure 41b shows the features of PtCo₃, PtCo and Pt₃Co catalysts after the voltage cycling in 0.1 M KOH. The well-defined redox peak couple of Co oxide species located at ~0.40 and ~0.70 V/RHE appeared dominantly compared to the redox peak couple of Pt oxide. It is noted, that the current peak at 0.47 V/RHE in the cathodic scan for Pt₃Co catalyst is located to more positive potentials compared to those for PtCo₃ and PtCo catalysts. We observed that the surface covering of Co grew significantly based on the surface rearrangement and/or the Co segregation induced by voltage cycling. In addition, the typical double layer regime for a pure Pt surface appeared ambiguously due to the strengthened presence of Co oxide species in this voltage range. Only the hydrogen desorption regime indicated still the existence of Pt atoms on the surface of Pt-Co alloy particles.

The voltammetric pretreated Pt-Co alloy catalysts will be denoted as “pretreated Pt₃Co”, “pretreated PtCo”, and “pretreated PtCo₃”, implying that their final overall atomic Pt:Co ratio during the voltage cycling step changed from the initial.

6.3 Platinum Electrochemical Active Surface Area (ECSA) and Chemical Composition of Pt-Co Alloy Nanoparticles

The ECSA was established from the final quasi stable CV profile by integrating of the underpotentially deposited hydrogen regime regarding the Pt mass. Table 8 and Table 9 sum up the changes in chemical composition and the platinum electrochemical active surface area (ECSA) for PtCo₃, PtCo, and Pt₃Co nanoparticle electrocatalysts before and after the electrochemical measurements in deaerated 0.1 M HClO₄ and 0.1 M KOH electrolytes. The resulting values of the ECSA for all Pt-Co catalysts are generally smaller in acidic and alkaline electrolytes than those for 28.2 wt. % Pt/HSAC. The TEM results (see Table 8) show the growth of alloy particles after annealing at 800 °C for 7 hours. It is well-known that the ECSA decreases with increasing particle size.¹³³⁻¹³⁷ In addition, in 0.1 M KOH the values of the ECSA for PtCo₃, PtCo and Pt₃Co catalysts are significantly smaller compared with those in acidic media. This observation can be explained due to the effects of electrolyte and pH on the surface composition for all Pt-Co alloy nanoparticle electrocatalysts. The voltage cycling in acidic media removes immediately Co atoms from the surface and results in a Pt-enriched particle shell surrounding an alloy core. In contrast in alkaline media, cobalt atoms form stable oxide species on the particle surface. Obviously, the CV profiles show successive accumulation of Co atoms induced by voltage cycling and at the same time the observed decreasing hydrogen desorption regime indicates a reduced Pt surface area.

Referred to Table 8, the EDS results reveal a slight change in Co concentrations for Pt-Co alloy nanoparticles in 0.1 M KOH, which is in agreement from stable Co atoms in the cyclic voltammetric measurements. In particular, in 0.1 M KOH the composition for PtCo₃ catalyst altered from initial Pt₃₆Co₆₄ to final Pt₃₂Co₆₈ after voltage cycling compared with the resulting final composition of Pt₇₈Co₂₀ in acidic media. Unlike to the chemical results for PtCo₃, the final concentration of Pt₃Co catalysts changed only very slightly in acidic and alkaline media due to the high covering of Pt atoms on the particle surface which inhibited the dissolution of Co. In the case of PtCo, the EDS

results showed slightly higher loss of Co atoms after the same voltage cycling conditions in acidic media compared with that in alkaline.

Table 9 Pt electrochemical active surface area (ECSA), Pt mass based activity (j_{mass}) and Tafel slope for low current density (lcd) for PtCo₃, PtCo and Pt₃Co alloy nanoparticle catalysts compared with 28.2 wt. % Pt/HSAC in 0.1 M HClO₄ and 0.1 M KOH electrolytes.^{127, 140}

catalyst	ECSA in acid [m ² g _{Pt} ⁻¹]	ECSA in alkaline [m ² g _{Pt} ⁻¹]	j_{mass} at 0.9 V/RHE in acid [A mg _{Pt} ⁻¹]	j_{mass} at 0.9 V/RHE in alkaline [A mg _{Pt} ⁻¹]	Tafel slope at lcd in acid / alkaline [mV dec ⁻¹]
PtCo ₃	50 ± 3	5 ± 2	0.38 ± 0.06	0.15 ± 0.07	80 / 75
PtCo	45 ± 4	8 ± 1	0.25 ± 0.07	0.19 ± 0.04	88 / 65
Pt ₃ Co	44 ± 2	17 ± 4	0.35 ± 0.08	0.35 ± 0.03	59 / 64
Pt	74 ± 7	49 ± 3	0.14 ± 0.01	0.16 ± 0.01	61 / 64

6.4 ORR Activity of Voltammetric Pretreated Pt-Co Electrocatalysts in Acidic and Alkaline Electrolytes

The ORR activity of voltammetric pretreated PtCo₃, PtCo and Pt₃Co electrocatalysts was established by RDE in oxygen saturated 0.1 M HClO₄ and 0.1 M KOH at room temperature. The polarization curves for Pt-Co catalysts in both electrolytes are shown in Figure 42. It is noticed that all polarization curves show a plateau behavior at 0.06 – 0.60 V/RHE, indicating the diffusion-limited regime for the oxygen reduction. The diffusion-limited current density is in the range between -5 and -6 mA cm_{geo}⁻² in acidic and alkaline media. The different diffusion-limited current densities in acidic and alkaline media are based on the differences in oxygen solubility, diffusivity and kinematic viscosity of the electrolyte solution. The differences of experimental diffusion-limited current densities and the discrepancy to the theoretical value for the four-electron ORR pathway¹³⁸ in one solution likely cause the unequal electrode coverage with catalyst as experimental artifact. Here, the onset potential of all pretreated Pt-Co catalysts from a mixed kinetic-diffusion control to a diffusion-limiting regime occurs at around 0.70 V/RHE. It is noted, that in 0.1 M KOH the mixed region of the polarization curves moved to more positive potentials with increasing Pt content in the Pt-Co alloys, shown in Figure 42b. The observed positive shift indicates a strong enhancement of the ORR activity. The intrinsic kinetic current density at 0.90 V/RHE was corrected in respect to the mass transport diffusion limiting current and normalized with the used platinum mass.

Figure 42c shows the mass transport corrected Pt mass based Tafel plot for all pretreated PtCo₃, PtCo and Pt₃Co alloy nanoparticle electrocatalysts obtained from the polarization curves in alkaline and acidic media. It evidences, that the pretreated Pt₃Co catalyst exhibits a similar course of Pt mass based Tafel plot in both electrolytes. The reported values in the literature of the Tafel slope for platinum as single crystal⁶³, polycrystalline⁶⁴, and carbon supported nanoparticles^{65, 66} are around -2.3 RT/F at the low overpotentials ($E > 0.85$ V/RHE) and -2×2.3 RT/F at high overpotentials ($E < 0.85$ V/RHE)⁶⁷. Table 9 sums up the estimated values of the Pt mass normalized Tafel slopes for pretreated Pt-Co catalysts at low current density (lcd) region compared with

28.2 wt. % Pt/HSAC (not shown). In 0.1 M KOH the values of the Tafel slope for pretreated Pt₃Co and PtCo catalysts are in good agreement with the Tafel slope value of 60 mV dec⁻¹ obtained from the experimental and literature data for bulk and single platinum crystals. Only the pretreated PtCo₃ shows a slightly higher Tafel slope in alkaline media compared to that for pure Pt nanoparticles. We found also similar results of Tafel slopes (Figure 42c) in 0.1 M HClO₄. The slope for the pretreated Pt₃Co catalyst at low overpotentials in acid is in excellent agreement with the experimental and literature values for pure Pt; while the slopes for the pretreated PtCo and PtCo₃ catalysts are still slightly higher. The difference in the Tafel slopes at low overpotentials can be explained by the changed adsorption behavior of oxide species particularly by the increased presence of Co atoms on the Pt-Co surface of alloy particles.¹⁷

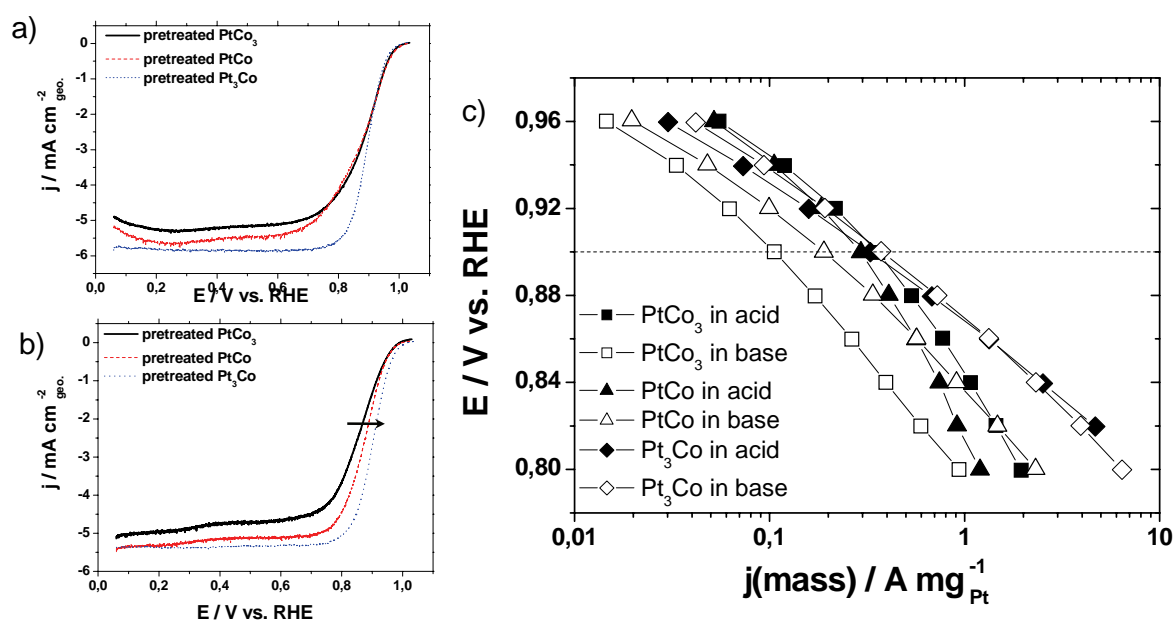


Figure 42 Polarization curves of the pretreated PtCo₃, PtCo and Pt₃Co alloy nanoparticle electrocatalysts in oxygen saturated (a) 0.1 M HClO₄ and (b) 0.1 M KOH. (c) Mass transport corrected Pt mass based Tafel plot of pretreated Pt-Co catalysts in both electrolytes. LSV measurements were performed anodically from 0.06 – 1.00 V/RHE with 5 mV s⁻¹ and 1600 rpm (rotations per minute) at room temperature. Reproduced from ref 140 by permission of The Electrochemical Society.

We pointed out that the effects of electrolyte and pH values become noticeable with increasing Co concentration. Table 9 sums up the Pt mass based activities (j_{mass}) of pretreated PtCo₃, PtCo and Pt₃Co nanoparticle electrocatalysts for ORR after the voltage cycling in 0.1 M HClO₄ and 0.1 M KOH. Commercially available 28.2 wt. % Pt/HSAC catalyst was taken as benchmark catalyst for the comparison of the ORR activities in both electrolytes. In summary, in 0.1 M KOH the pretreated Pt₃Co electrocatalyst shows clearly the highest j_{mass} compared with PtCo and PtCo₃ catalysts; while in 0.1 M HClO₄ the pretreated PtCo₃ catalyst exhibits the highest j_{mass} compared to Pt₃Co and PtCo catalysts. After the voltage cycling in 0.1 M KOH the Pt mass normalized activities increase according: PtCo₃ < PtCo < Pt₃Co. The pretreated Pt₃Co catalyst shows 2-3 times higher j_{mass} than commercial pure Pt/HSAC. In contrast, after voltage cycling in 0.1 M HClO₄ the Pt mass based activities increase according: PtCo < Pt₃Co < PtCo₃. The pretreated PtCo₃ exhibits clearly 3 fold increase in j_{mass} compared to pure Pt.^{90, 91} In addition, the mass activities for Pt₃Co electrocatalyst are similar after the voltage cycling in the different electrolyte solutions. Thus, the effects of electrolyte and pH are negligible for Pt₃Co catalyst due to the already existing high covering of Pt atoms on the particle surface. The improved activity can be attributed to the Co concentration in the subsurface layers and the level of coordination of Pt surface atoms. The thermal induced Pt skin on Pt₃Co nanoparticle catalyst leads to a positive shift in the potential for the formation of oxygen adsorbed species on Pt. This indicates an increase of active Pt surface atoms for the oxygen reduction.^{10, 143-145} In addition, Co atoms as oxophilic metal decrease the surface coverage of OH_{ads} species on Pt. Lima et al. reported lower oxide coverage on Pt-Co catalysts and a slight reduction of the Pt-Pt distance compared to pure Pt in alkaline media using XANES and EXAFS measurements.^{146, 147}

After the voltage cycling in 0.1 M HClO₄, PtCo₃ catalyst exhibits clearly 3 fold increase in j_{mass} compared to pure Pt, however, in 0.1 M KOH j_{mass} resembles almost pure Pt/HSAC. The ORR activity of PtCo₃ catalyst is influenced unambiguously on the electrolyte due to the high coverage of Co on the particle surface in alkaline media. The strong activity enhancement of

pretreated PtCo₃ catalyst in acidic media is due to the rapid dissolution of Co atoms and formation of Pt-enriched particle shell surrounding by alloy core. We suggest that the resulting lattice strain in the Pt-enriched shell, similar to that found in dealloyed PtCu₃^{16, 98}, is responsible for the significantly improved activity. The comprehensive strain results in a shift of the electronic Pt band structure and weakens the chemisorptions of the oxygen species. In 0.1 M KOH we observed a low coverage of Pt atoms and a successive enrichment of cobalt on the surface of alloy particles which reduces significantly the Pt mass based activity for ORR and ECSA.

In the case of PtCo catalyst, in 0.1 M HClO₄ j_{mass} is almost 2 times higher after voltage cycling than that for Pt/HSAC; while j_{mass} in 0.1 M KOH is only slightly higher compared to Pt/HSAC.

6.5 Correlation of ECSA – Activity – Co Alloy Composition in Dependence on Different Electrolyte Solutions and pH Values

We correlated the ECSA and the ORR performance with the initial chemical composition of Pt-Co alloy nanoparticle electrocatalysts after the same voltage cycling conditions (200 voltage cycles with 500 mV s^{-1}) in different electrolyte solutions at pH 1 and pH 13. In Figure 43, the sketch illustrates the changes in compositions and morphology for Pt-Co alloy nanoparticles induced by voltage cycling in 0.1 M KOH and 0.1 M HClO₄. The Pt-enriched shell surrounding an alloy core structure is formed by electrochemical dealloying in acid; whereas Co atoms enrich the particle surface induced by voltage cycling in alkaline media.

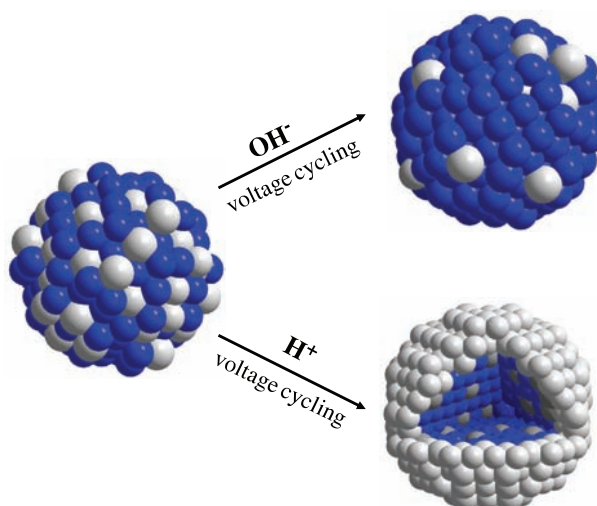


Figure 43 Illustration of morphological and chemical changes in bimetallic Pt-Co alloy nanoparticle electrocatalysts by voltage cycling in 0.1 M KOH and 0.1 M HClO₄. Pt atoms are symbolized with grey spheres and Co atoms are symbolized with blue spheres. Reproduced from ref 140 by permission of The Electrochemical Society.

Figure 44 shows the relationship between ECSA, Pt mass based activities (j_{mass}) and initial bulk cobalt concentration for Pt-Co alloys in 0.1 M KOH and 0.1 M HClO₄. Based on the similar particle size, an activity benefit for Pt-Co can be here ruled out. The established values of ECSA and Pt mass based activity are

related to the initial chemical composition and electrolyte solutions. In 0.1 M KOH the values of ECSA decrease with increasing Co content in the alloys due to the formation of stable oxide species on Co atoms on the particle surface. Furthermore, the observed enrichment of Co reduces gradually the Pt surface area or number of electrochemically active Pt surface atoms. The mechanism of the Co accumulation is likely based on the surface rearrangement and/or the oxygen adsorbate-induced segregation initiated by voltage cycling. In contrast, Co atoms are leached electrochemically off from the particle surface in 0.1 M HClO₄. The increasing ECSA with increasing Co content can be explained by the resulting surface roughness by dealloying which forms a large number of electrochemically active Pt surface atoms.

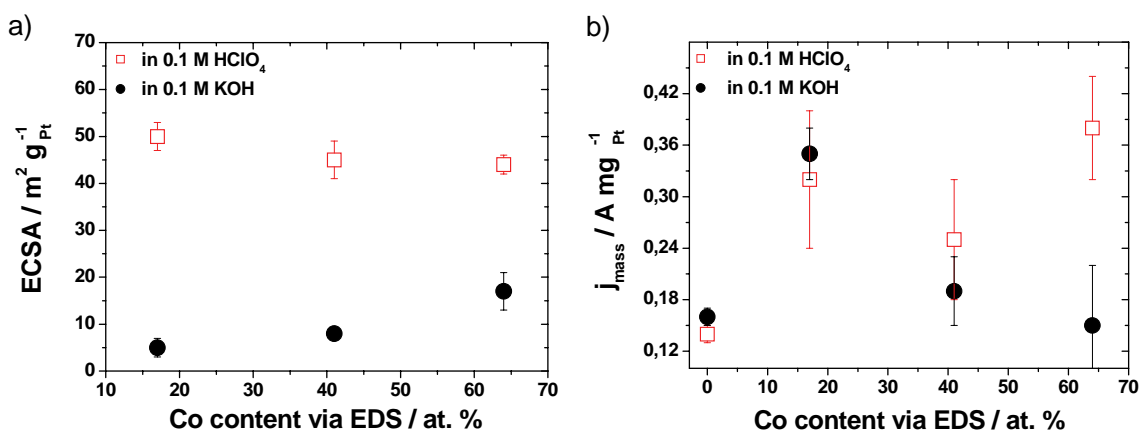


Figure 44 a) ECSA versus initial Co concentration and (b) Pt mass based activity (j_{mass}) versus initial cobalt concentration established by EDS for as-synthesized Pt-Co alloy nanoparticle electrocatalysts after voltage cycling in 0.1 M HClO₄ and 0.1 M KOH. Reproduced from ref 140 by permission of The Electrochemical Society.

In 0.1 M KOH the course of j_{mass} shows a maximum at initial cobalt content of 17 at. %. Beyond this content, the values of j_{mass} decrease dramatically with increasing Co concentration in the alloy particles and approximate more and more the value of pure Pt. The negative trend of j_{mass} in alkaline media can be explained by the increasing coverage of Co atoms on the particle surface. The activity enhancement is caused by the Co concentration in the surface and

subsurface, which modify the electronic and geometric structure of Pt-enriched surface. The presence of Co atoms at the neighboring Pt atoms on the particle surface reduces the coverage of OH_{ads} species on platinum.

However, with increasing Co contents in the alloys Co atoms blocks the surface and therefore reduces Pt surface area or number of electrochemically active Pt surface atoms. In view of the course of j_{mass} in 0.1 M HClO_4 , the improved activity is caused by the Co concentration in the subsurface layers and the level of coordination of Pt surface atoms. The cobalt atoms are dissolved immediately from the particle surface in an electrochemical, acidic environment and results in a rough particle surface. The surface roughness may also contribute in an improved Pt mass based activities. The pretreated PtCo_3 shows the highest ORR activity in the family of Pt-Co alloy electrocatalysts due to the formation of highly active alloy rich core – Pt rich shell structure. The improved activity may be related to the resulting lattice strain in the Pt-enriched shell, which weakens the chemisorptions of the oxygen species on catalytically active Pt atoms. The pretreated Pt_3Co catalyst shows significantly improved activity compared to the pretreated PtCo catalyst. The formed Pt skin surface induced by thermal annealing for Pt_3Co catalyst is attributed the improved activity. A clear activity trend in dependence on Co concentration of Pt-Co alloys in acid is not to identify, unlike to the observed results in j_{mass} in 0.1 M KOH.

6.6 Hydrogen Peroxide Production of Pt-Co Alloy Nanoparticle Electrocatalysts

RRDE experiments were performed to establish the selectivity of voltammetric pretreated PtCo_3 , PtCo and Pt_3Co alloy nanoparticle electrocatalysts for the oxygen reduction in 0.1 M HClO_4 electrolyte solution at room temperature. The quantification of hydrogen peroxide was established by the standard RRDE method described in the literature.^{62, 90, 139} Figure 45 shows the resulting hydrogen peroxide production for pretreated Pt-Co catalysts with the elevated disk potential during the recording of polarization curves in acidic media.

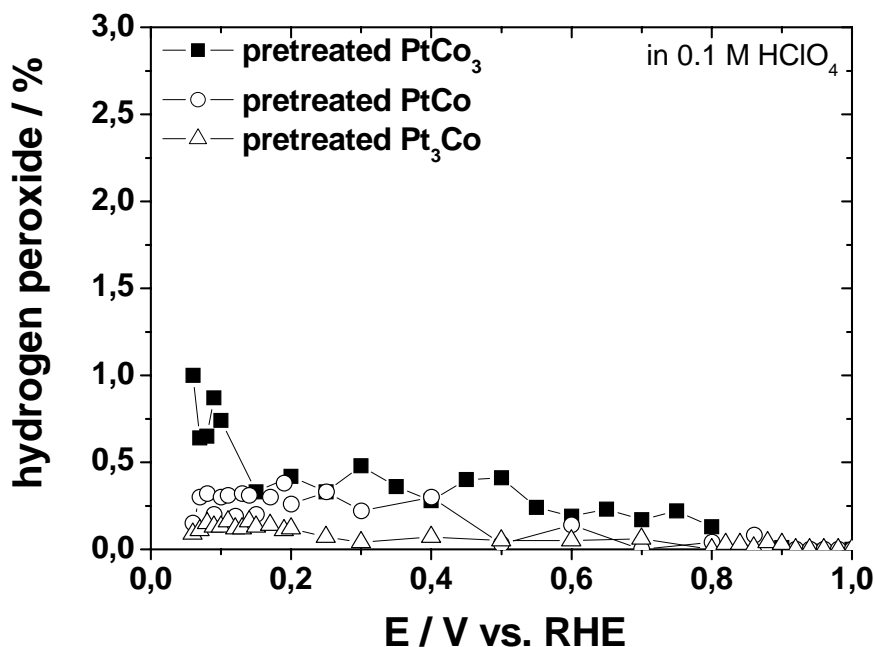


Figure 45 Hydrogen peroxide production versus the disk voltage during oxygen reduction on pretreated PtCo_3 , PtCo and Pt_3Co alloy nanoparticle electrocatalysts. RRDE measurements were performed in oxygen saturated 0.1 M HClO_4 at room temperature. During the recording of the polarization curves for ORR on the disk electrode, the potential of pure Pt ring electrode was potentiostated at 1.20 V/RHE. The formation of hydrogen peroxide was independent of the rotating speed. Reproduced from ref 140 by permission of The Electrochemical Society.

The formed hydrogen peroxide for all Pt-Co catalysts is clearly below 1 %. In addition, the course of the hydrogen peroxide decreased continuously with increasing disk potential and was close to zero at the kinetic diffusion regime. The highest values of peroxide were detected in a disk potential range of 0.06 and 0.40 V/RHE due. The enhancement of peroxide formation in the H_{upd} regime is due to co-adsorption of H_{upd} and oxygen. Nevertheless, all pretreated Pt-Co catalysts reveal a very low production of hydrogen peroxide. This evidences, that the direct four electron transfer is the main mechanism for oxygen reduction on voltammetric pretreated PtCo_3 , PtCo , and Pt_3Co alloy nanoparticle electrocatalysts in 0.1 M HClO_4 .

6.7 Highly Active PtCo₃ Core-Shell Nanoparticles in Alkaline Media

The pretreatment of PtCo₃ alloy nanoparticle catalyst is a critical step for an improved ORR performance. The highly active core-shell arrangement of PtCo₃ catalyst only formed by voltage cycling in 0.1 M HClO₄ because of the relatively high stability of Co surface atoms in strong alkaline media.

Figure 46a shows the CV profiles in 0.1 M KOH for PtCo₃ electrocatalyst before and after the activation. The activation occurs by voltage cycling (200 voltage cycles with 500 mV s⁻¹) in 0.1 M HClO₄ to remove immediately Co atoms from the particle surface. In 0.1 M KOH the initial CV profile of PtCo₃ catalyst shows clearly the slight covering of Pt atoms on the particle surface. After the electrochemical activation in acidic media, the CV profile reveals the typical characteristic features of a pure Pt surface corresponding to the hydrogen ad/desorption regime, capacitive double layer regime, and Pt hydroxide/oxide peaks. The ORR activity of activated PtCo₃ core-shell nanoparticles was subsequently established by RDE in oxygen saturated 0.1 M KOH at room temperature.

The polarization curves of the activated PtCo₃ core-shell nanoparticle catalyst recorded in both electrolytes are compared in Figure 46b. The polarization curves show a plateau behavior at 0.06 - 0.60 V/RHE, indicating the diffusion-limited regime for the oxygen reduction. Here, the diffusion-limited current density of the activated PtCo₃ electrocatalyst is around -5 mA cm_{geo}⁻². The onset potential from a mixed kinetic-diffusion control to the diffusion-limiting regime occurs at around 0.70 V/RHE. It is noticed, that the mixed region of the polarization curves for activated PtCo₃ catalyst in alkaline media shifted clearly to more positive potentials compared with that in acid. The observed positive shift indicates an enhancement of the ORR activity in 0.1 M KOH.

Table 10 sums up the resulting ECSA and Pt mass based activities for the activated PtCo₃ nanoparticle catalyst in both electrolytes. In 0.1 M KOH the mass activity enhances significantly due to the formation of PtCo₃ core-shell nanoparticle catalyst.

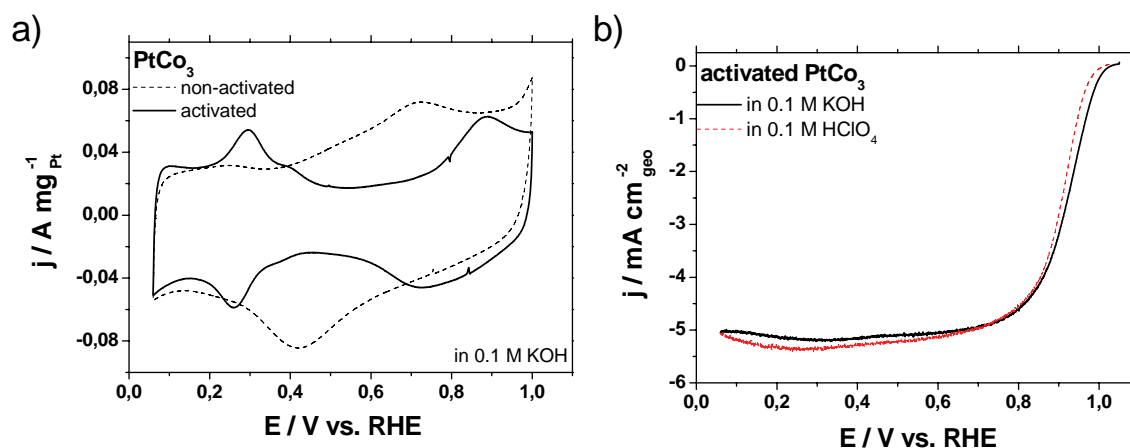


Figure 46 a) CV profiles of non-activated and activated PtCo_3 alloy nanoparticle electrocatalyst; b) Polarization curves of activated PtCo_3 catalyst in oxygen saturated acidic and alkaline electrolytes. Cyclic voltammetry was performed from 0.06 to 1.00 V/RHE with 100 mV s^{-1} in nitrogen purged 0.1 M KOH at room temperature. LSV measurements were performed anodically from 0.06 - 1.00 V/RHE with 5 mV s^{-1} and 1600 rpm (rotations per minute) at room temperature. Reproduced from ref 140 by permission of The Electrochemical Society.

Table 10 Pt electrochemical active surface area (ECSA) and Pt mass based activity (j_{mass}) for activated PtCo_3 alloy nanoparticle electrocatalyst compared with 28.2 wt. % Pt/HSAC in 0.1 M HClO_4 and 0.1 M KOH electrolytes.¹⁴⁰

catalyst	ECSA in acid [$\text{m}^2 \text{g}_{\text{Pt}}^{-1}$]	ECSA in alkaline [$\text{m}^2 \text{g}_{\text{Pt}}^{-1}$]	j_{mass} at 0.9 V/RHE in 0.1 M HClO_4 [$\text{A mg}_{\text{Pt}}^{-1}$]	j_{mass} at 0.9 V/RHE in 0.1 M KOH [$\text{A mg}_{\text{Pt}}^{-1}$]
activated PtCo_3	43 ± 4	20 ± 2	0.40 ± 0.03	0.63 ± 0.09
non-activated PtCo_3	50 ± 3	5 ± 2	0.38 ± 0.06	0.15 ± 0.07
Pt	74 ± 4	49 ± 3	0.14 ± 0.01	0.16 ± 0.01

More precisely, the activated PtCo_3 core-shell structure exhibits clearly 4 fold increase in j_{mass} in alkaline media compared to state-of-the-art pure Pt nanoparticles and non-activated PtCo_3 ; whereas j_{mass} is still 3 times higher in acid than that of pure Pt/HSAC. We concluded that the PtCo_3 core-shell rearrangement is a highly active ORR electrocatalyst for acidic and in particular for alkaline PEM fuel cells.

6.8 Summary

In this work, we have presented a comprehensive structural, chemical and electrochemical characterization linked with the ORR performance for PtCo₃, PtCo and Pt₃Co alloy nanoparticle electrocatalysts in different electrolyte solutions and pH values. We clarified the effects of electrolyte and pH for Pt-Co alloy particles during the voltage cycling. Based on the results, we correlated the ECSA and the Pt mass based activity with the initial chemical composition of Pt-Co alloys in acidic and alkaline media. From the electrochemical, structural and chemical results, we concluded that

- The Rietveld crystal phase quantification revealed, that after the annealing at 800 °C for 7 hours the main component (about 75 wt.%) for PtCo₃, PtCo and Pt₃Co catalysts exhibits a disordered fcc alloy crystal phase with a crystallite size in range of 2-3 nm (3-4 nm established by TEM). From the EDS results, the overall chemical compositions for PtCo₃, PtCo and Pt₃Co are Pt₃₆Co₆₄, Pt₅₉Co₄₁, and Pt₈₃Co₁₇.
- In 0.1 M KOH a strong surface enrichment of Co atoms is identified in Pt alloy nanoparticles induced by adsorption of oxygen species and surface rearrangement during voltage cycling; whereas in 0.1 M HClO₄ the voltage cycling removes immediately cobalt atoms from the surface for the formation of a Pt-enriched shell surrounding alloy particle core.
- The observed stability of Co on the particle surface during the voltage cycling in 0.1 M KOH is in line with the final chemical compositions after the electrochemical experiments established by EDS. Here, the PtCo₃ catalyst shows an unchanged Co concentration after the voltage cycling in alkaline media, in contrast to the cycling in acid.
- The values of ECSA in alkaline media for voltage pretreated Pt-Co catalysts are generally smaller than those in acid. In 0.1 M KOH the observed successive accumulation of Co atoms on the surface reduces gradually the Pt surface area or number of electrochemically active Pt atoms.

- After voltage cycling in 0.1 M HClO₄ the Pt mass based activities increase according: PtCo < Pt₃Co < PtCo₃. The pretreated PtCo₃ catalyst exhibits clearly 3 fold increase in j_{mass} compared to pure Pt.
- In contrast, after the voltage cycling in 0.1 M KOH the mass activities increase according: PtCo₃ < PtCo < Pt₃Co. The pretreated Pt₃Co catalyst shows 2-3 times higher j_{mass} than the benchmark pure Pt.
- The PtCo₃ core-shell structure can only form by voltage cycling in acid and not in alkaline media. After the electrochemical dealloying in 0.1 M HClO₄ PtCo₃ core-shell nanoparticles show an outstanding ORR mass activity for alkaline PEM fuel cells, an increase by 4 times compared to pure Pt/HSAC.

6.9 Effects of Annealing Conditions on the ORR Activity of PtCo₃ Alloy Nanoparticle Electrocatalysts

Reprinted from ref 90 with permission of Elsevier, copyright (2011).

<http://dx.doi.org/10.1016/j.jpowsour.2010.11.016>

The effects of annealing conditions on the alloy formation and the particle growth of the Pt-Co precursor electrocatalyst and the resulting ORR activity are studied. Here, we have varied the maximum annealing temperature in range of 650 °C and 900 °C for 7 hours (referred to as PtCo₃ (650°C/7h), PtCo₃ (800°C/7h) and PtCo₃ (900°C/7h)) to investigate the Pt-Co alloy structure and crystallite size using XRD and EDS techniques. According to the quantitative crystal phase Rietveld refinement, the structure and size of Pt-Co precursor alloys are correlated with the Pt mass and Pt surface area specific activities for ORR. The ORR activities were established by RDE technique. Our study highlighted that with increasing annealing temperature, the Co content in the Pt alloys did not increase. However, the particle size grew with increasing annealing temperature. We concluded that the PtCo₃ catalyst (800°C/7h) shows after the activation by electrochemical dealloying the most favorable balance between mass and specific ORR activities. The Pt mass based activities increase for PtCo₃ according: 650 °C/1.8 nm \approx 900 °C/3.2 nm < 800 °C/2.2 nm. In contrast, the Pt surface area specific activities increase for Pt-Co in the following trend: 650°C/1.8 nm < 800°C/2.2 nm < 900°C/3.2 nm. The dealloyed PtCo₃ (800°C/7h) electrocatalyst shows 3 times higher in terms of Pt mass based activity and 4 - 5 times higher in terms of Pt surface area specific based activity than the state-of-the-art Pt/C.

6.9.1 Effects of Annealing Temperature on the Structure of PtCo₃ Alloy Nanoparticle Precursor Catalysts

The high surface area carbon (HSAC) supported PtCo₃ alloy nanoparticle precursor electrocatalysts were synthesized and annealed at 650 °C, 800 °C and 900 °C for 7 hours to drive the Pt-Co alloy formation and the particle growth. The XRD profiles of various Pt-Co alloys are shown in Figure 47. The vertical dotted lines denote the face-centered cubic (fcc) pure Pt and Co reference patterns with a space group of Fm3m. All XRD patterns of Pt-Co alloys show multiple cubic crystal phase structures. The broad XRD reflections indicate small crystallite sizes of Pt-Co alloys, whereas the sharp reflections imply the presence of Co rich alloys of large crystallite size. The absence of additional superlattice reflections of the ordered Pt-Co alloy phase structures (Pm3m) signify that all Pt-Co catalysts show a substitutional disordered fcc lattice type structures. Crystalline cobalt and platinum were not observed in all XRD profiles. The shift of the XRD reflections to higher 2θ values with respect to pure Pt indicates the contraction of the lattice by the alloy formation after annealing. The XRD reflections of the Pt-Co samples relate to the diffraction from (111), (200) and (220) lattice planes of the disordered fcc crystal structure with Fm3m. Table 11 sums up the crystal phase, lattice parameter, crystallite size, Rietveld quantification and stoichiometric alloy composition established by Vegard's rule⁷⁴ for all Pt-Co alloys annealed at 650 °C, 800 °C and 950 °C for 7 hours. The average crystallite size was calculated from the complete XRD profile using the integral breadth method⁷¹, which is independent of the distribution in size and shape of crystal domains.

The XRD profile of Pt-Co sample (650°C/7h) shows multiple disordered fcc crystal phases. According to the Rietveld refinement and Vegard's rule, the main component (65.6 ± 2.4 wt. %, referred to as fcc 1) of Pt-Co alloy (650°C/7h) exhibits a stoichiometric composition of Pt₅₄Co₄₆ and a crystallite size of 1.8 ± 0.1 nm, while the minor Pt-Co component (34.4 ± 2.4 wt. %, referred to as fcc 2) shows a composition of Pt₂₁Co₇₉ with a crystallite size of 10.9 ± 0.9 nm. With a careful observation on the XRD reflections of Pt-Co (650 °C/7h), the slight left shoulder indicates probably a third minor fraction of below

1 wt. % with lower alloy degree of Co content. The XRD profile of Pt-Co (800 °C/7h) shows clearly two disordered fcc alloy crystal phases. Here, the main component (fcc 1) of Pt-Co (800°C/7h) exists up to 75.8 ± 1.9 wt. % as $\text{Pt}_{48}\text{Co}_{52}$ and with a crystallite size of 2.2 ± 0.1 nm. Meanwhile, the minor component of 24.2 ± 1.9 wt. % (fcc 2) shows a composition of $\text{Pt}_{11}\text{Co}_{89}$ with a large crystallite size of about 18 nm. Finally, the XRD profile of Pt-Co (900 °C/7h) shows also two disordered fcc alloy crystal phases. The main component (62.0 ± 2.8 wt. %; fcc 1) of Pt-Co sample (900°C/7h) as $\text{Pt}_{46}\text{Co}_{54}$ shows a crystallite size of 3.2 ± 0.1 nm, while the minor component (38.0 ± 2.8 wt. %; fcc 2) exists as $\text{Pt}_{21}\text{Co}_{79}$ with a large crystallite size of about 11 nm.

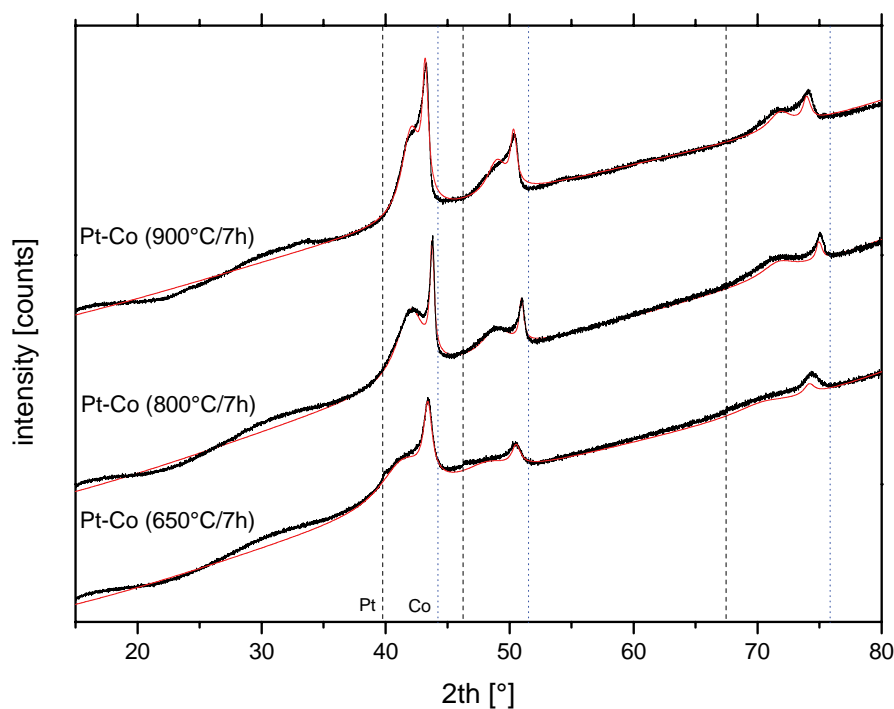


Figure 47 XRD profiles of synthesized Pt-Co catalysts, displayed with y-offset. Rietveld profile fit of diffraction data for Pt-Co (650°C/7h) ($R_{wp} = 1.35$, $R_{exp} = 0.42$, $GOF = 3.18$); for Pt-Co (800°C/7h) ($R_{wp} = 1.51$, $R_{exp} = 0.41$, $GOF = 3.71$) and for Pt-Co (900°C/7h) ($R_{wp} = 1.89$, $R_{exp} = 0.43$, $GOF = 4.38$). The fits are indicated by a red solid line. Vertical dotted lines denote Pt, Co and Cu reference patterns. They are tabulated in the powder diffraction file (PDF) database of the international center for diffraction data (ICDD), in particular PDF(Pt)#00-004-0802, PDF(Co)#00-015-0806. Reprinted from ref 90 with permission of Elsevier, copyright (2011).

Table 11 Crystal structure, lattice parameter, crystallite size, Rietveld quantification and stoichiometric composition of Co rich Pt-Co alloy system.⁹⁰

catalyst	crystal phase	lattice parameter [Å]	Rietveld quantification [wt. %]	crystallite size [nm]	composition via Vegard
PtCo ₃ (650°C/7h)	fcc 1	3.749 ± 0.001	65.9 ± 2.4	1.8 ± 0.1	Pt ₅₄ Co ₄₆
	fcc 2	3.624 ± 0.001	34.4 ± 2.4	10.9 ± 0.9	Pt ₂₁ Co ₇₉
PtCo ₃ (800°C/7h)	fcc 1	3.726 ± 0.001	75.8 ± 1.9	2.5 ± 0.1	Pt ₄₈ Co ₅₂
	fcc 2	3.585 ± 0.002	24.2 ± 1.9	17.5 ± 1.9	Pt ₁₁ Co ₈₉
PtCo ₃ (900°C/7h)	fcc 1	3.717 ± 0.001	62.0 ± 2.8	3.2 ± 0.1	Pt ₄₆ Co ₅₄
	fcc 2	3.623 ± 0.001	38.0 ± 2.8	11.6 ± 1.1	Pt ₂₁ Co ₇₉

Referred to Table 11, an increase of the annealing temperature at same annealing time only caused to a particle size growth for Pt-Co alloys and very low decrease of the alloy lattice parameter by inserting of Co atoms in the existing Pt lattice. Thus, more Co insertion in the Pt lattice was not released with increase of annealing temperature.

6.9.2 Electrochemical Dealloying Behavior of PtCo₃ Alloy Nanoparticles annealed at different Temperatures in Acidic Media

The electrochemical dealloying behavior of PtCo₃ alloy nanoparticle precursor catalysts annealed at 650 °C, 800 °C and 900 °C for 7 hours was examined by recording of cyclic voltammograms (CVs) in 0.1 M HClO₄. The initial CV profiles of Pt-Co catalysts are shown in Figure 48a-c. All Pt-Co alloy catalysts reveal similar electrochemical characteristic features. The initial CV profile exhibits a broad maximum current peak between 0.25 and 0.75 V/RHE for all Pt-Co alloys during the anodic scan, signifying the dissolution of underpotentially deposited Co atoms from the surface of Pt alloy nanoparticles. In addition, the first CV profile shows the presence of the underpotentially deposited hydrogen (H_{upd}) in the potential range between 0.06 and 0.30 V/RHE, indicating also the presence of Pt atoms on the particle surface. The hydrogen desorption regime overlaid here partially with the dissolution current of

underpotentially deposited Co in the anodic scan. The features of the first CV profile implies that the segregation of Pt on the particle surface for Co rich Pt-Co alloy systems was not completely reached by thermal treatment to form a Pt particle skin. In addition, the second and third CV profiles show that the dissolution of Co continued slightly in higher voltage range between 0.50 and 0.80 V/RHE. The cathodic scan exhibits any deposition of Co from the electrolyte. It is evident, that the large loss of Co occurs in the first anodic scan. Furthermore, the hydrogen ad/desorption regime increases during the fast voltage cycling (200 scans with 500 mV s^{-1}) due to the enrichment and reconstruction of Pt atoms on the particle surface.

The voltammetric pretreated Pt-Co alloy nanoparticles will be denoted as “dealloyed PtCo₃”, implying that their final overall atomic Pt:Co ratio during the voltage cycling step changed from the initial.

Figure 48d presents the temporary stable CV profiles of dealloyed PtCo₃ (650°C/7h), PtCo₃ (800°C/7h) and PtCo₃ (900°C/7h) electrocatalysts compared to that of a commercial 28.2 wt. % Pt/HSAC after the voltage cycling (200 scans with 500 mV s^{-1}). It is clearly observed, that each CV profile exhibits the characteristic features of a pure Pt surface, corresponding to a hydrogen ad/desorption regime (0.06 – 0.40 V/RHE), a double layer regime (0.40 – 0.60 V/RHE) and a redox peak couple of Pt hydroxide/oxide (0.7 – 1.0 V/RHE). The dealloyed PtCo₃ catalysts reveal also an onset shift to higher potentials around 50 – 60 mV, which is to relate to the activation of water and decreased surface coverage of oxygenated species on the Pt rich particle surface. A decreasing surface coverage can enhance the activity of molecular oxygen chemisorption rate.

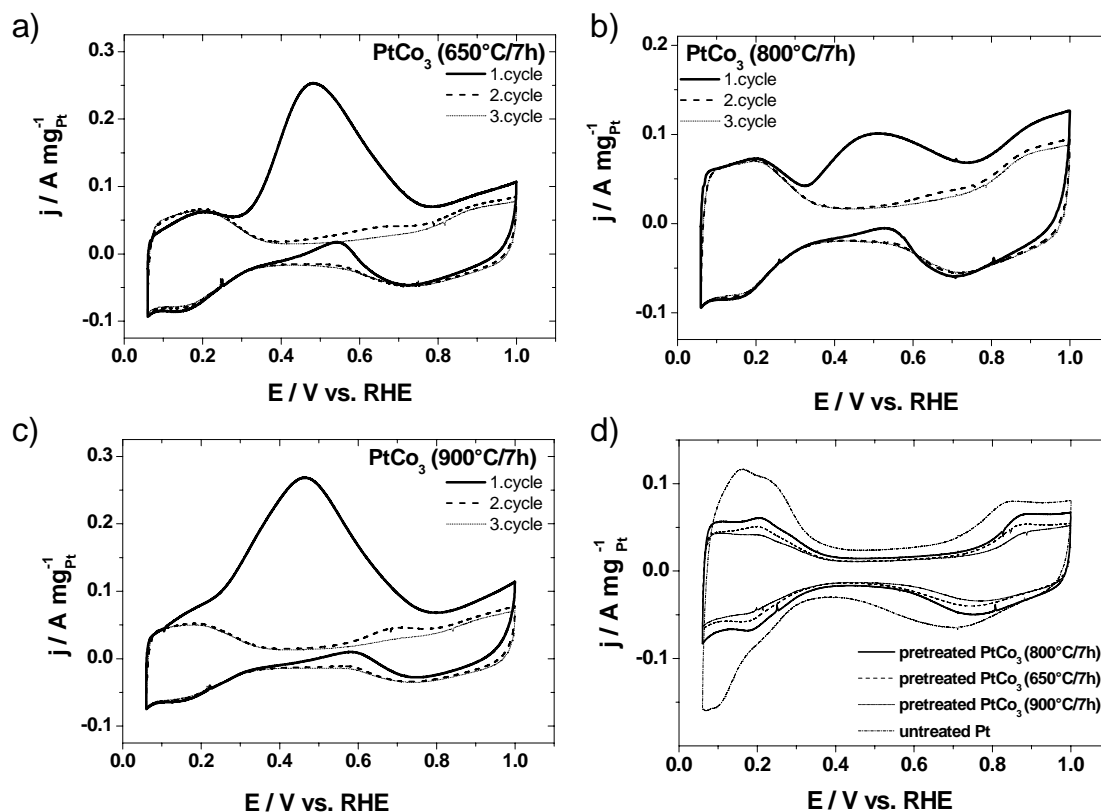


Figure 48 a-c) Initial CV profiles of PtCo_3 alloy nanoparticle precursor electrocatalysts annealed at 650 °C, 800 °C and 900 °C for 7 hours. d) CV profiles of pretreated PtCo_3 catalysts compared with 28.2 wt. % Pt/HSAC after dealloying (200 scans with 500 mV s^{-1}). Cyclic voltammetry was conducted from 0.06 – 1.00 V/RHE with 100 mV s^{-1} in deaerated 0.1 M HClO_4 at room temperature. Reprinted from ref 90 with permission of Elsevier, copyright (2011).

Table 12 sums up the ECSA of dealloyed PtCo_3 (650°C/7h), PtCo_3 (800°C/7h) and PtCo_3 (900°C/7h) alloy nanoparticle electrocatalysts compared with a commercial carbon supported Pt nanoparticle catalyst. It is clearly noticed, that the values of ECSA for dealloyed Pt-Co samples are smaller than that of supported Pt/C. The reduced ECSA values are caused by the increased particle size after annealing. However, the voltammetric dealloying leads to an increased surface roughness and results in an increased Pt active electrochemical surface area.

Table 12 Comparison of electrochemical active surface area (ECSA) and catalytic ORR activities for dealloyed PtCo₃ alloy nanoparticles catalysts annealed at 650 °C, 800 °C and 900 °C and commercial 28.2 wt. % Pt/HSAC catalyst.⁹⁰

catalyst	ECSA [m ² g _{Pt} ⁻¹]	j _{mass} at 0.9 V/RHE [A mg _{Pt} ⁻¹]	j _{specific} at 0.9 V/RHE [A mg _{Pt} ⁻¹]	Tafel slope at lcd [mV dec ⁻¹]
PtCo ₃ (650°C/7h)	40 ± 4	0.28 ± 0.05	701 ± 68	75
PtCo ₃ (800°C/7h)	45 ± 4	0.38 ± 0.05	804 ± 146	80
PtCo ₃ (900°C/7h)	36 ± 2	0.29 ± 0.04	811 ± 99	85
Pt	73 ± 3	0.13 ± 0.01	179 ± 4	61

The loss of cobalt in alloy nanoparticles is investigated before and after voltammetric treatment established by EDS. Table 13 shows the changes in chemical composition. So, the initial chemical compositions for Pt-Co are close to the Pt:Co atomic ratio of 1:3. The chemical composition of Pt-Co alloy catalysts changed from initial Pt₂₈Co₇₂ (650°C/7h) to final Pt₈₂Co₁₈, from initial Pt₃₇Co₆₃ (800°C/7h) to final Pt₈₀Co₂₀ and finally from initial Pt₂₇Co₇₃ (900°C/7h) to final Pt₇₃Co₂₇. It reveals that the Co loss of each Pt-Co catalyst is consistent with the observed dissolution current in the cyclic voltammetric experiments. The Co loss for Pt-Co annealed at 650 °C is higher than those of Pt-Co annealed at 800 °C and 900 °C. This can be explained by the increased content of amorphous Co due to insufficient annealing temperature for the alloy formation.

Table 13 Changes in chemical composition of Pt-Co alloy nanoparticles, annealed at 650 °C, 800 °C and 900 °C after electrochemical (EC) experiments established by EDS technique.⁹⁰

catalyst	chemical composition initial [at. %]	chemical composition after EC [at. %]
PtCo ₃ (650°C/7h)	Pt ₂₈ Co ₇₂	Pt ₈₂ Co ₁₈
PtCo ₃ (800°C/7h)	Pt ₃₇ Co ₆₃	Pt ₈₀ Co ₂₀
PtCo ₃ (900°C/7h)	Pt ₂₇ Co ₇₃	Pt ₇₃ Co ₂₇

6.9.3 ORR Activity of Dealloyed PtCo₃ Annealed at different Temperatures in Acidic Media

Figure 49a shows the polarization curves of dealloyed PtCo₃ alloy electrocatalysts for ORR and compared with that of commercial 28.2 wt. % Pt/HSAC. It is observed, that each electrocatalyst exhibits a plateau behavior in the potential range between 0.06 – 0.70 V/RHE, indicating the diffusion-limited current regime. The diffusion-limited current density for Pt-Co and Pt catalysts is in range of -5 and -5.5 mA cm_{geo}⁻². The discrepancy to the theoretical value of diffusion-limited current density for the four-electron ORR pathway¹³⁸ likely causes the unequal electrode coverage with catalyst as experimental artifact. The onset potentials of each Pt-Co catalysts from a mixed kinetic-diffusion control to a diffusion-limiting region occurred at around 0.70 V/RHE. The open circuit potential for dealloyed Pt-Co catalysts is around 1.02 V/RHE.

Figure 49b and c presents the Pt surface area specific and Pt mass based Tafel plots, obtained from the kinetic current j_{kin} for dealloyed PtCo₃ catalysts and compared to those of 28.2 wt. % Pt/HSAC. The Tafel plots reveal a significant improvement of intrinsic activities for all Pt-Co alloy catalysts. The Tafel slope for ORR changes continuously in the examined potential range. The experimental data exhibits two Tafel slopes at low current density (lcd) and high current density (hcd) region. The results of the Tafel slope at the low current region are summarized in column 5 of Table 12. The previously reported values of the Tafel slope for a single crystal Pt⁶³, polycrystalline Pt⁶⁴ and carbon supported Pt nanoparticle⁶⁵ are around -2.3 RT/F at low overpotentials ($E > 0.85$ V/RHE) and $-2 * 2.3$ RT/F ($E < 0.80$ V/RHE) at high overpotentials. The values of the Tafel slope for all pretreated PtCo₃ electrocatalysts at the low current density (lcd) region are slightly higher compared to the experimental value of Pt nanoparticles and to the Tafel slope of 60 mV dec⁻¹ for bulk and single Pt crystals described in the literature. The Tafel slopes at the high current density region for PtCo₃ samples are clearly higher than the experimentally observed and reported values for Pt in literature^{64, 65}. Gasteiger et al. and Paulus et al. explained that the difference of the Tafel slope can be attributed with the change of oxide species adsorption on the Pt-Co alloy surface.^{17, 138}

Referring to Figure 49 and Table 12, the Pt mass (j_{mass}) and Pt surface area specific (j_{specific}) based ORR activities of Pt-Co alloy electrocatalysts after voltammetric activation by dealloying exhibit a considerable performance compared to those of pure Pt/C. We hypothesized, that geometric strain effects of the dealloyed Pt-Co nanoparticles, similar to those found out for dealloyed PtCu₃ nanoparticles, are responsible for the improvement in ORR activity.¹⁶ The dealloyed PtCo₃ (800°C/7h) electrocatalyst shows 3 times higher in terms of j_{mass} and 4 - 5 times higher in terms of j_{specific} than the commercially available pure 28.2 wt. % Pt/HSAC. Meanwhile, the dealloyed PtCo₃ (650°C/7h) and PtCo₃ (900°C/7h) show two folds for the mass activity increase compared to Pt/HSAC. This result indicates that further increase of the annealing temperature affects no mass activity benefit. It is well-known, that the surface area specific activity of Pt-Co electrocatalysts increase with the particle size.^{133, 137, 148} Therefore, the specific activities increase for PtCo₃ catalysts according to the increasing annealing temperature (650°C/1.8 nm < 800°C/2.2 nm < 900°C/3.2 nm). We concluded that the dealloyed Pt-Co catalyst, annealed at 800°C shows the most favorable balance between mass and specific ORR activity with a particle size of 2.2 ± 0.1 nm. The increased improvement for ORR activity can be associated with the uniformity of the crystal phase. The disordered fcc crystal phase structure of PtCo₃ (800°C/7h) (fcc 1) exists up to 75.8 ± 1.9 wt. % and is more uniform than PtCo₃ (650°C/7h) and PtCo₃ (900°C/7h). According to the Rietveld analysis, the Pt-Co systems consisting of numerous alloy phases do not emerge as a very active class of electrocatalysts. The increasing uniformity of alloy phase leads to an improved ORR activity for Co rich Pt-Co system and a better understanding of structure – activity relationship.

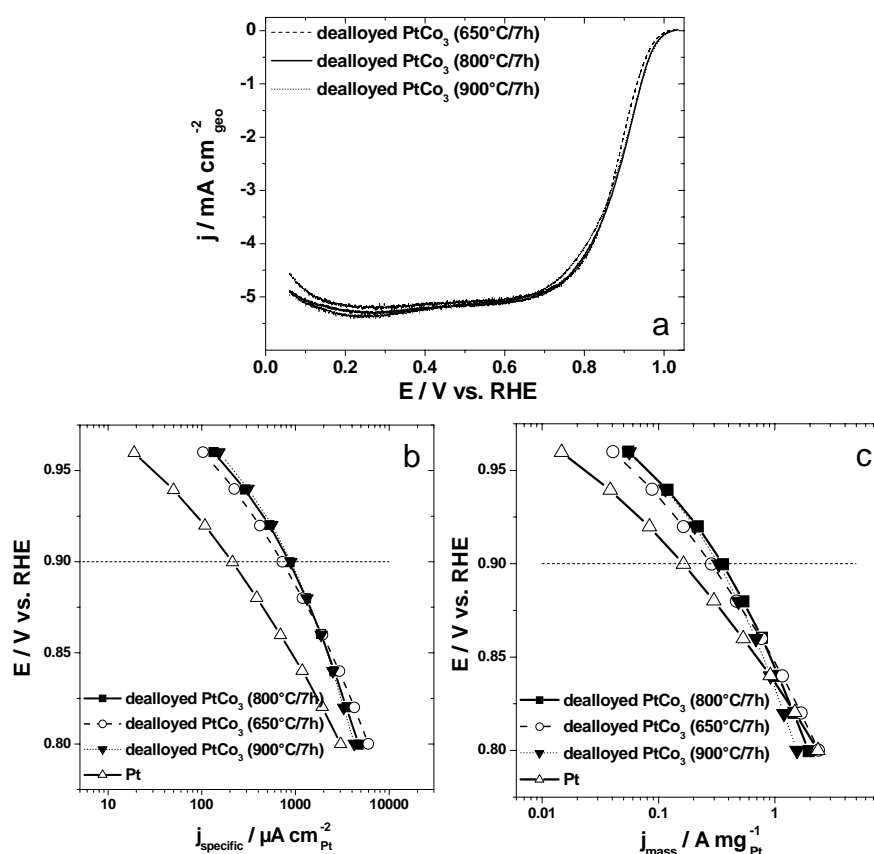


Figure 49 a) Polarization curves of dealloyed PtCo_3 , annealed at 650 °C, 800 °C and 900 °C for 7 hours. b) Pt surface area specific based Tafel plots and c) Pt mass based Tafel plots of dealloyed PtCo_3 catalysts compared with pure 28.2 wt. % Pt/HSAC. Linear sweep voltammetry was performed anodically from 0.06 – 1.05 V/RHE with 5 mV s^{-1} and 1600 rpm in oxygen saturated 0.1 M HClO_4 at room temperature. Reprinted from ref 90 with permission of Elsevier, copyright (2011).

6.9.4 ORR Selectivity of Dealloyed PtCo_3 compared with Dealloyed PtCu_3 and pure Pt

RRDE measurements were performed in oxygen saturated 0.1 M HClO_4 to establish the percentage of the hydrogen peroxide production and the number of transfer electrons during oxygen reduction reaction on the highly catalytically active surface of dealloyed PtCo_3 (800°C/7h) and PtCu_3 (800°C/7h) nanoparticles. Figure 50 shows the polarization curves at various rotating

speeds, the Koutecki-Levich plot and the collected ring current of H_2O_2 oxidation obtained during the LSV measurements of dealloyed PtCo_3 (800°C/7h) and PtCu_3 (800°C/7h) electrocatalysts at 1600 rpm. The LSV experiment of the disk electrode prepared with a thin catalyst film shows nearly a well-defined diffusion limiting current (0.2 – 0.6 V/RHE) followed by a mixed kinetic control regime between 0.65 – 0.8 V/RHE. Finally, from about 0.80 V/RHE the reaction rate is only kinetic controlled based on the independence of the rotating speeds. It is clearly observed, that the simultaneously recorded ring current (i_{ring}) (at 1600 rpm) for the oxidation of the formed H_2O_2 is only a small fraction of the disk current (i_{disk}) in all potential regimes. The ring current decreased gradually during the anodical sweep of the disk electrode for dealloyed PtCo_3 (800°C/7h) and PtCu_3 (800°C/7h) and was close to zero at the kinetic regime. It evidences that ORR proceeds exclusively through a four electron reduction pathway for dealloyed PtCo_3 and PtCu_3 catalysts. Here, the ring measurements of peroxide oxidation were recorded by different rotating speeds and were independent from the measured speed range. The influence of the H_2O_2 production on the bare, highly polished and cleaned glassy carbon electrode is to neglect in our experiments.

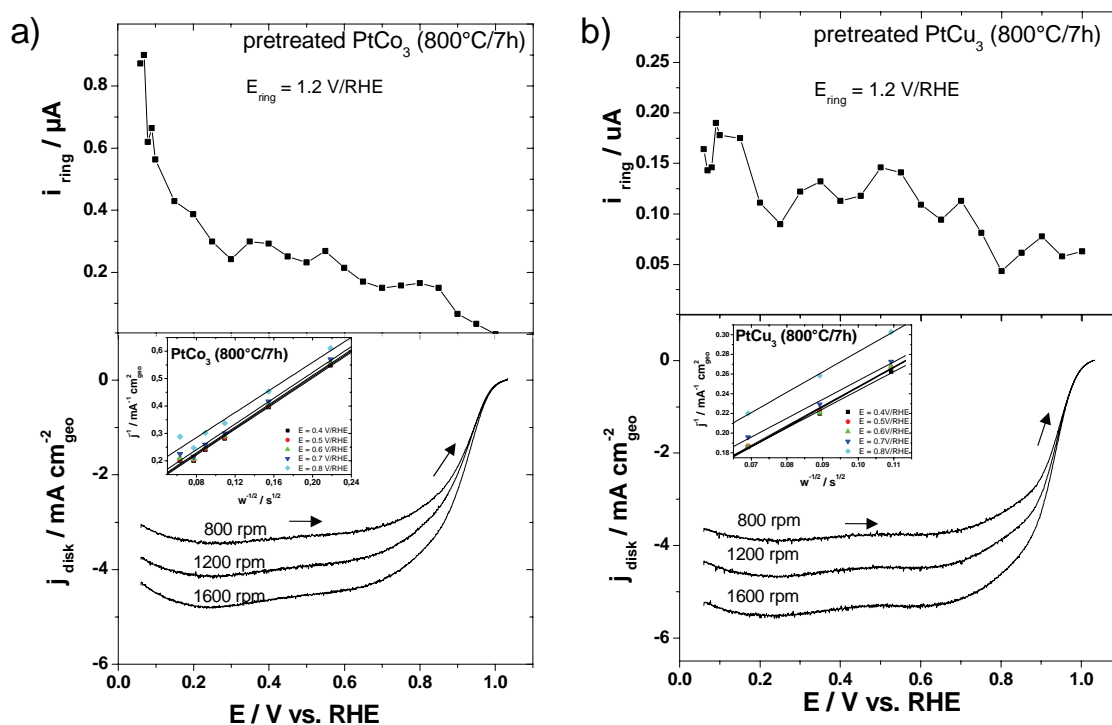


Figure 50 RRDE measurements of the oxygen reduction reaction for dealloyed a) PtCo₃ and b) PtCu₃ catalysts. Insert: Koutecky-Levich plots of dealloyed PtCo₃ (800°C/7h) and PtCu₃ (800°C/7h) at various electrode potentials. Linear sweep voltammetry were conducted anodically from 0.06 – 1.05 V/RHE with 5 mV s^{-1} in oxygenated 0.1 M HClO₄ at room temperature. Simultaneously recorded ring current at 1600 rpm for a ring potential of $E_{ring} = 1.20$ V/RHE. Reprinted from ref 90 with permission of Elsevier, copyright (2011).

Figure 51 presents the hydrogen peroxide production with the disk potential during the oxygen reduction for dealloyed PtCo₃ (800°C/7h) and PtCu₃ (800°C/7h) and compared to that for pure 28.2 wt. % Pt/HSAC. The peroxide production was calculated from the data in Figure 50 at 1600 rpm with $N = 0.22 \pm 0.01$. The platinum loading for PtCo₃ and PtCu₃ catalysts was around $11 \mu\text{g cm}_{geo}^{-2}$ and for Pt/HSAC it was $15 \mu\text{g cm}_{geo}^{-2}$. It is noted, that the peroxide fraction is below 0.5 % up to 0.20 V/RHE, indicating, that the reduction of O₂ runs exclusively via a direct four electron step in the voltage range relevant to the fuel cell cathodes. The RRDE study reveals that the peroxide production decreases continuously with higher disk potential for dealloyed Pt-Co and Pt-

Cu. The highest values of peroxide are in the H_{upd} regime between 0.06 and 0.30 V/RHE. The enhancement of peroxide formation in the H_{upd} regime is due to co-adsorption of H_{upd} and oxygen. The peroxide production of dealloyed PtCo_3 (800°C/7h) is slightly higher than that for dealloyed PtCu_3 (800°C/7h) with similar Pt loading. We suggest that the enhanced H_2O_2 production during the ORR is associated with the particle size effect. Durand et al.¹⁴⁹⁻¹⁵¹, Boudart et al.¹⁵² and Hwang et al.¹⁵³ reported that the degree of surface coverage by oxygenated species increases with the decrease of the particle size. Here, the particle size of 2.2 nm for PtCo_3 (800°C/7h) is smaller than that (3.6 nm) for PtCu_3 (800°C/7h). It is evident, that the H_2O_2 production increases, when the particle size decreases. The commercial 28.2 wt. % Pt/HSAC exhibits the lowest H_2O_2 production due to the high Pt loading. Thus, the peroxide production increases with decreasing platinum loading. This observation is an agreement with the reports from Inaba et al.¹⁵⁴ and Bonakdarpour et al.¹⁵⁵. Considering the influence of the support material, the high surface area carbon (HSAC), however, plays an important role for H_2O_2 production. The oxygen reduction on carbon only occurs at low potentials and leads to an increasing formation of H_2O_2 species. Shown in Figure 51, the untreated pure HSAC with a loading of around $51.0 \mu\text{g cm}_{\text{geo}}^{-2}$ exhibits a H_2O_2 production of above 10 % in a voltage range of 0.06 and 0.25 V/RHE. The change in H_2O_2 activity of HSAC was not tested after the thermal annealing.

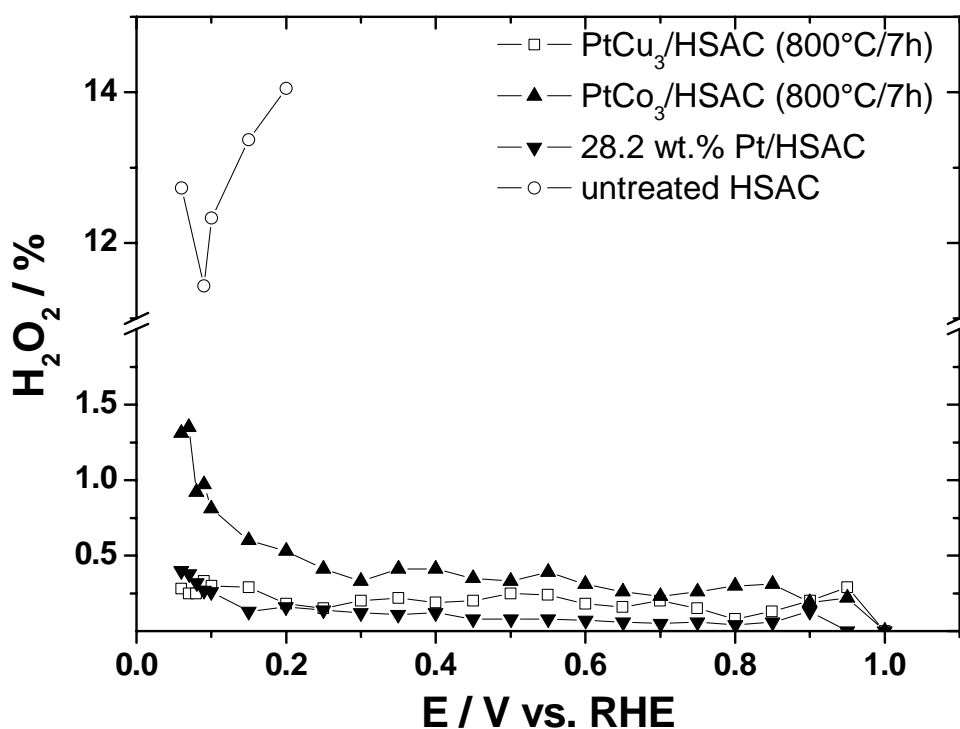


Figure 51 Hydrogen peroxide production with the disk potential during the O_2 reduction on dealloyed $PtCo_3/HSAC$ ($800^\circ C/7h$) with Pt loading of $11.4 \mu g cm_{geo}^{-2}$, pretreated $PtCu_3/HSAC$ ($800^\circ C/7h$) with Pt loading of $11.4 \mu g cm_{geo}^{-2}$, untreated 28.2 wt. % Pt/HSAC with Pt loading of $14.6 \mu g cm_{geo}^{-2}$ and untreated pure HSAC with carbon loading of $51.0 \mu g cm_{geo}^{-2}$ in oxygen saturated 0.1 M $HClO_4$ at room temperature. Calculated from the data in Figure 50 (at 1600 rpm) using the eq. (5) with $N = 0.22 \pm 0.01$. Reprinted from ref 90 with permission of Elsevier, copyright (2011).

Nevertheless, we assumed that the effects of carbon on H_2O_2 production are stronger at the low elevated potentials than the particle size effect and the Pt loading effect. We pointed out, that the H_2O_2 production for dealloyed $PtCo_3$ ($800^\circ C/7h$), $PtCu_3$ ($800^\circ C/7h$) and pure Pt nanoparticle catalysts is negligible based on the very low peroxide production during the ORR. It revealed that the direct four electron transfer is the main mechanism for oxygen reduction on dealloyed $PtCo_3$, $PtCu_3$ and Pt nanoparticle electrocatalysts in acidic media.

In Figure 50, the Koutecki-Levich plots for dealloyed PtCo₃ (800°C/7h) and PtCu₃ (800°C/7h) reveal a proportional dependence of the limiting current on the square root of the rotation rate in oxygen saturated 0.1 M HClO₄ at room temperature. The plot of 1/j vs. $\omega^{-1/2}$ is linear and the fits run nearly parallel at various electrode potentials, indicating a similar slope. The intercepts of 1/j axis at $1/\omega^{1/2} = 0$ gives the magnitude of the absolute kinetic current for that process in the absence of any mass transfer effects. From the slope of Koutecki-Levich plots, so-called “B factor”, it can be calculated the number of transfer electrons in the reduction of oxygen molecule and proved with the theoretical value for a four electron pathway. The Koutecki-Levich equation is described as follows

$$1/j = 1/j_{kin} + 1/j_{dif} = 1/j_{kin} + 1/(B \cdot \sqrt{\omega}) \quad (\text{eq 15})$$

$$B = 0.62 \cdot n \cdot F \cdot D(\text{O}_2)^{2/3} \cdot \nu^{-1/6} \cdot c(\text{O}_2) \quad (\text{eq 16})$$

where j_{kin} is the kinetic current density, j_{dif} is the diffusion-limiting current density through the solution boundary layer, B is a constant, ω is the rotation rate and F is Faraday constant ($F = 96485 \text{ C mol}^{-1}$). The theoretical value for B is calculated for four electron reduction process using published data for the oxygen diffusivity ($D(\text{O}_2) = 1.93 \times 10^{-5} \text{ cm}^2 \text{ s}^{-1}$)¹⁵⁶, the kinematic viscosity of the electrolyte ($\nu = 1.009 \times 10^{-2} \text{ cm}^2 \text{ s}^{-1}$)¹⁵⁶ and O₂ solubility ($c(\text{O}_2) = 1.26 \times 10^{-3} \text{ mol l}^{-1}$)¹⁵⁷. The experimental values for dealloyed PtCo₃ ($B = 0.429 \pm 0.005 \text{ mA cm}_{geo}^{-2} \text{ s}^{1/2}$) (divergence of 8 %) and for dealloyed PtCu₃ ($B = 0.494 \pm 0.007 \text{ mA cm}_{geo}^{-2} \text{ s}^{1/2}$) (divergence of 6 %) are in good agreement with the theoretical value of $B = 0.467 \text{ mA cm}_{geo}^{-2} \text{ s}^{1/2}$ for a four electron reduction.

6.9.5 Summary

This work has shown the effects of annealing conditions on the structure, the resulting electrochemical dealloying characteristic and the resulting ORR activities for PtCo₃ alloy nanoparticle catalysts. The PtCo₃ alloy nanoparticle precursor electrocatalysts were synthesized and annealed at 650 °C, 800 °C and 900 °C for 7 hours to drive the Pt-Co alloy formation and the particle growth. The Pt-Co alloy structures prepared by various annealing temperatures were correlated with the particle size, the ECSA, the mass and surface area specific activities for ORR. We concluded, that

- The overall chemical composition established by EDS is close to the Pt:Co atomic ratio of 1:3. The Rietveld refinement results correlated with the Vegard's rule, in contrast, revealed that the main component of Pt-Co alloys, is the disordered fcc crystal phase (Fm3m) as Pt₅₀Co₅₀ with a small particle size (2 - 3 nm).
- The increase of the annealing temperature only causes a particle growth and very low additional insertion of Co atoms in the existing fcc Pt lattice for alloy formation.
- The dealloyed PtCo₃ catalyst, annealed at 800°C for 7 hours shows the most favorable balance between mass and specific ORR activity with a crystallite size of 2.2 ± 0.1 nm compared to the dealloyed PtCo₃ (650°C/7h) and PtCo₃ (900°C/7h). The PtCo₃ (800°C/7h) catalyst exhibits 3 times higher in terms of mass activity and 4 - 5 times higher in terms of specific activity after the voltammetric activation by dealloying than 28.2 wt. % Pt/HSAC.
- The increasing activity improvement can be related to the uniformity of Pt-Co crystal phase.
- The hydrogen peroxide production is very low for dealloyed PtCo₃ (800°C/7h). The reduction of oxygen for PtCo₃ processes via four electron transfer established by RRDE and RDE experiments.

7 Size-dependent Morphology of Dealloyed Bimetallic Catalysts: Linking the Nano to the Macro Scale

Reprinted from ref 158 with permission of American Chemical Society, copyright (2012). <http://dx.doi.org/10.1021/ja2088162>

Chemical dealloying of Pt binary alloy precursors has emerged as a novel and important preparation process for highly active fuel cell catalysts. Dealloying is a selective (electro)chemical leaching of a less noble metal M from a M rich Pt alloy precursor material and has been a familiar subject of macroscale corrosion technology for decades. The atomic processes occurring during the dealloying of nanoscale materials, however, are virtually unexplored and hence poorly understood. Here, we have investigated how the morphology and intraparticle composition depend on the particle size of dealloyed Pt-Co and Pt-Cu alloy nanoparticle precursor catalysts. To examine the size – morphology – composition relation, we used a combination of high resolution scanning transmission electron microscopy (STEM), transmission electron microscopy (TEM), electron energy loss (EEL) spectroscopy, energy-dispersive X-ray spectroscopy (EDS), and surface sensitive cycling voltammetry. Our results indicate the existence of three distinctly different size-dependent morphology regimes in dealloyed Pt-Co and Pt-Cu particle ensembles: (i) The arrangement of Pt shell surrounding a single alloy core (“*single core-shell nanoparticles*”) is exclusively formed by dealloying of particles below a characteristic particle diameter $d_{\text{multiple cores}}$ of 10 - 15 nm. (ii) Above $d_{\text{multiple cores}}$, non-porous bimetallic core-shell particles dominate and show structures with irregular shaped multiple Co/Cu rich cores (“*multiple cores-shell nanoparticles*”). (iii) Above the second characteristic diameter d_{pores} of about 30 nm, the dealloyed Pt-Co and Pt-Cu particles start to show surface pits and nanoscale pores next to multiple Co/Cu rich cores. This structure prevails up to macroscopic bulk-like dealloyed particles with diameter of more than 100 nm. The size – morphology – composition relationships link the nano to the macro scale and provide an insight into the existing material gap of dealloyed nanoparticles and highly porous bulk-like bimetallic particles in corrosion science.

7.1 Introduction

In our previous work on dealloyed Pt bimetallic alloy fuel cell electrocatalysts, we focused on nanoparticles that exhibited a so-called “single core-shell structure” consisting of a near-concentric arrangement of a Pt rich shell and a Pt poor alloy rich particle core. This structure is characterized by a monotone drop of the non noble metal towards the particle surface. We found single core-shell particles of a few nanometers diameter as an important morphological basic type in dealloyed bimetallic nanoparticle ensembles. The morphology and contribution of larger dealloyed particles; yet, with their higher intrinsic catalytic activity^{7, 133, 148} have remained unclear to date. Previous studies have reported on at least one other structural type of bimetallic nanoparticles after acid and/or electrochemical treatment using microscopic and spectroscopic techniques.^{12, 15, 23, 24, 37, 159, 160} However, until now, no particular emphasis was given how the size of dealloyed bimetallic particles is linked with their intraparticle structure and composition on an atomic scale. A detailed understanding of the size – structure – morphology relationships of the bimetallic particles spanning from the nano to the macro scale is important for the rational design of improved electrocatalysts.

In this report, we have identified the basic dealloyed morphological and compositional structures in dealloyed bimetallic nanoparticles as a function of their size. In particular, we have examined the morphology and composition of dealloyed Pt-Co and Pt-Cu nanoparticle electrocatalysts using microscopic, spectroscopic and surface sensitive techniques, such as cyclic voltammetry, high-resolution aberration-corrected high-angle annular dark field scanning transmission electron microscopy (STEM-HAADF), transmission electron microscopy (TEM), electron energy loss (EEL) spectroscopy, and energy-dispersive X-ray spectroscopy (EDS). Our results of both dealloyed Pt-Co and Pt-Cu nanoparticle catalysts indicate the existence of three different size regimes associated with characteristic structural morphologies and compositions. The three size regimes involve two different characteristic particle diameters, where features of multiple cores and pores emerge. The goal of this work is to link the observed particle structures at the nano scale to those found

Size-dependent Morphology of Dealloyed Bimetallic Catalysts: Linking the Nano to the Macro Scale

at the macro scale, bridging the materials gap between dealloyed nanoparticles and macroscopic highly porous bulk-like bimetallic particles in corrosion science.

7.2 Formation of Platinum-enriched Particle Shell by Dealloying

Figure 52a and b compare the current-voltage characteristics (cyclic voltammograms, CVs) of the Pt alloy precursor electrocatalysts supported on HSAC before (dashed) and after (solid line) the electrochemical dealloying procedure. The Pt-Cu and Pt-Co exist largely as substitutional disordered cubic alloys.^{75, 90, 130} After dealloying, both alloy catalysts exhibit the characteristic CV features of a pure platinum surface, including the broad underpotential hydrogen deposition/stripping peaks (red areas) and the irreversible peak couple indicating Pt surface oxygenates (blue areas). Strong differences are evident in the initial (dashed) CVs of the two Pt alloy precursors. Unlike Pt-Co, the Pt-Cu precursor shows no signs of anodic hydrogen stripping on the first scan, implying complete surface segregation of Cu consistent with DFT theoretical predictions.^{57, 98} In addition, copper dealloyed in two distinct faradic current peaks are consistent with Cu bulk dissolution (Cu-Cu bond breaking, Figure 52a (1)) and, more anodically, with the dissolution of underpotentially deposited Cu surface atoms (Cu-Pt bond breaking, Figure 52a (2))⁹⁸. Due to the presence of Co on the surface of Pt alloy particles, Co atoms only dissolve in a broad single voltammetric peak (1), shown in Figure 52b. Measurements of the electrocatalytic oxygen reduction (ORR) activity show a 3 – 4 fold benefit for the dealloyed Pt-Co and a 4 – 5 fold benefit for the dealloyed Pt-Cu nanoparticle electrocatalyst compared with the benchmark Pt nanoparticle catalyst.^{75, 90, 91, 130}

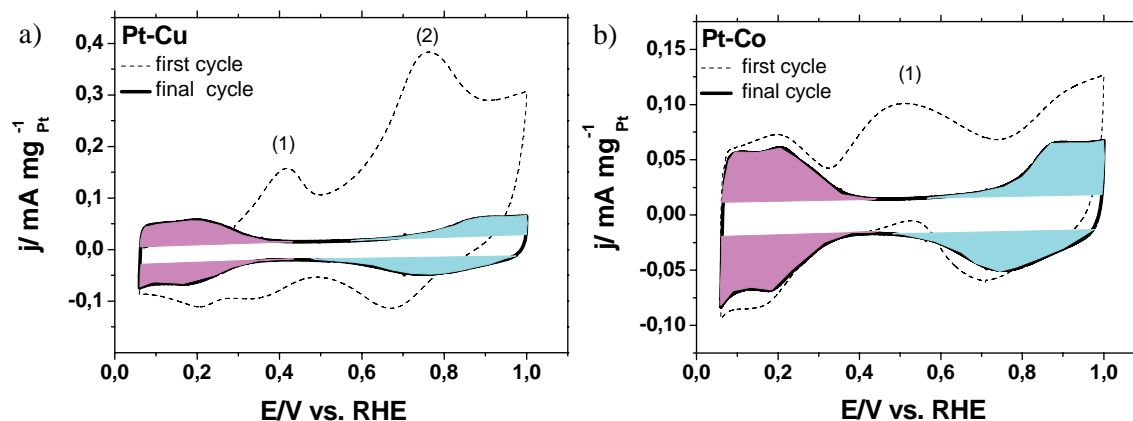


Figure 52 CV profiles of (a) Pt-Cu and (b) Pt-Co alloy nanoparticle electrocatalysts before (dashed) and after (solid line) the electrochemical dealloying process. The broad hydrogen ad/desorption regime and redox peak couple of Pt (hydr-)oxide are indicated by red and blue areas. (a) Positions (1) and (2) signify the surface dissolution of pure bulk Cu and underpotentially deposited Cu. (b) Position (1) indicates the surface dissolution of underpotentially deposited Co from a Pt alloy particle surface. Reprinted from ref ¹⁵⁸ with permission of American Chemical Society, copyright (2012).

7.3 Particle Morphology and Chemical Composition before and after Dealloying

Energy-dispersive X-ray spectroscopy (EDS) revealed that the overall chemical compositions of Pt-Co and Pt-Cu catalysts changed clearly from $\text{Pt}_{37\pm 2}\text{Co}_{63\pm 2}$ to $\text{Pt}_{80\pm 2}\text{Co}_{20\pm 2}$ and from $\text{Pt}_{35\pm 2}\text{Cu}_{65\pm 2}$ to $\text{Pt}_{65\pm 2}\text{Cu}_{35\pm 2}$ after dealloying. The losses of Co and Cu are in agreement with the observed faradic dissolution peaks in the cyclic voltammetric experiments. Note, the dealloying process did not result in completely dealloyed particles. Indeed, a significant content of cobalt/copper is found inside the catalytically active nanoparticles. Furthermore, the final CV profiles for Pt-Co and Pt-Cu indicate an almost complete covering of Pt atoms on the particle surface after the dealloying process.

To establish the relationships between particle size as well as the morphological and compositional structure of individual dealloyed bimetallic particles, we used HAADF-STEM and EEL spectroscopy techniques. The image intensity of an atom column is roughly proportional to $Z^{1.6}$ for sufficiently thin objects. Platinum and cobalt/copper reveal a significant difference in the atomic number: $Z = 78$ for Pt, $Z = 27$ for Co and $Z = 29$ for Cu which results in a distinct image contrast between Pt- and Co/Cu rich specimen regions.

Figure 53 displays HAADF overview images for Pt-Co and Pt-Cu alloy particles before and after dealloying. The well-alloyed Pt-M precursors show a uniform contrast distribution with the highest intensity in the center of the particles. These contrast features reveal spherical shapes of the individual particles and a homogeneous chemical composition (see Figure 53a and c). Bright contrast occurs where particles overlap along the optical axis. However, in their dealloyed structure configuration (see Figure 53b and d), the particle ensemble exhibits a variety of complex contrast patterns, indicating changes in particle morphology and intraparticle chemical composition. For instance, some selected particles with non-trivial contrast patterns are denoted by white arrows in Figure 53b and d.

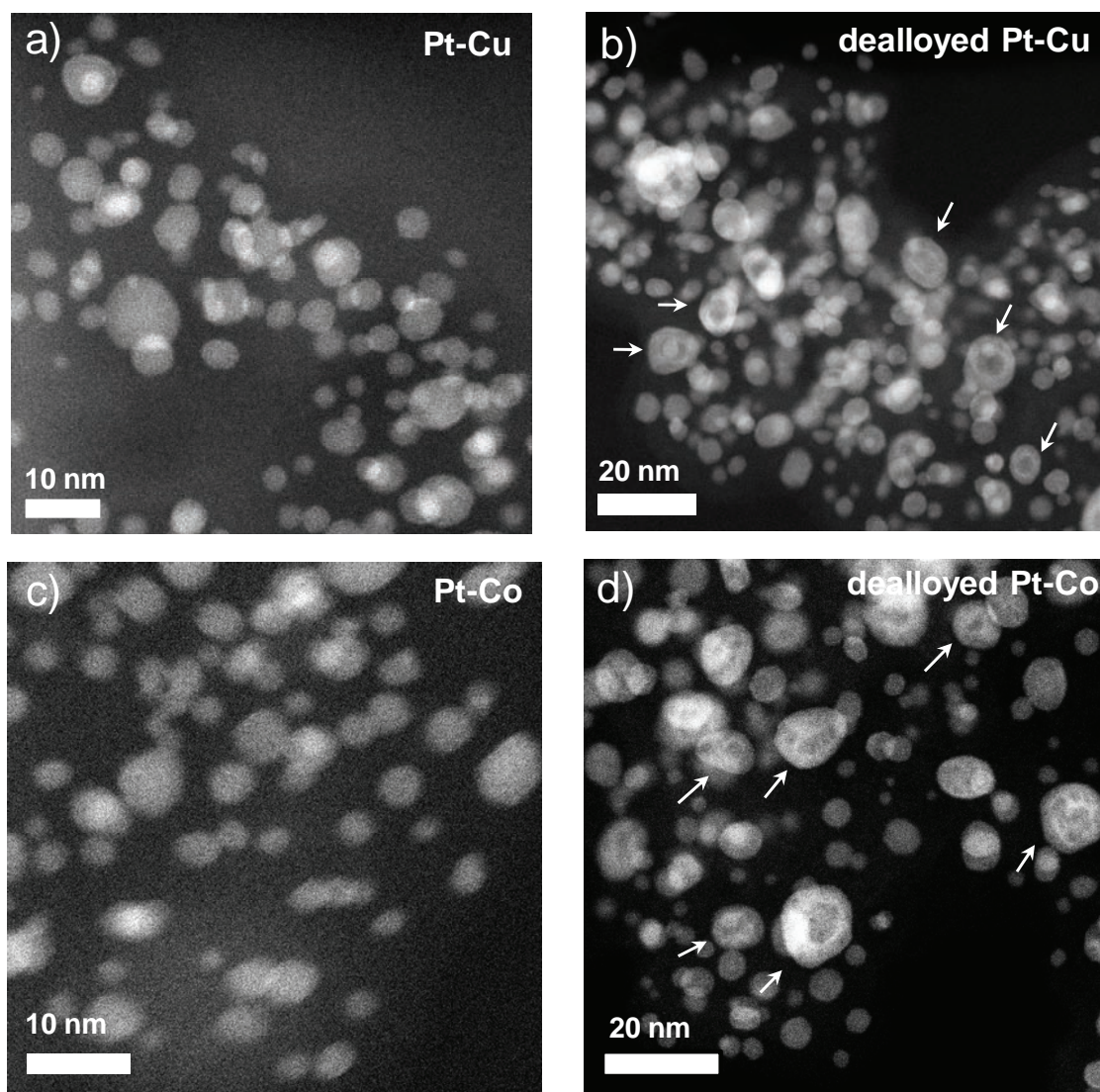


Figure 53 HAADF overview micrographs of Pt-Cu and Pt-Co particle ensembles; (a), (c) before and (b), (d) after dealloying. The white arrows exemplarily denote particles with non-trivial contrast features. Reprinted from ref ¹⁵⁸ with permission of American Chemical Society, copyright (2012).

Without more detailed analysis or comparison to calculated HAADF intensity profiles, these contrast variations may be due to the changes in thickness or composition or a combination of both. Most importantly for our discussion, however, is the question, if and how the intraparticle intensity variations are correlated with the size of the dealloyed particles; a question that has remained unaddressed to date.

7.4 Principle Nanoscale Particle Morphologies and Structures and their Size Dependence

7.4.1 “Single Core-Shell Nanoparticles” – Dealloyed Pt-Co and Pt-Cu Nanoparticles below 5 nm Diameter

We start with an analysis of the dealloyed particle morphologies in the smallest size regime of ≤ 5 nm. Figure 54 shows HAADF images for individual Pt-Co and Pt-Cu nanoparticles with a mean size of 3 - 4 nm. Lattice fringes are clearly resolved in each image. The dealloyed particles exhibit a spot in the center with darker shading than the outer part. This contrast feature is also reflected in the HAADF intensity line profiles (insets in Figure 54), which were taken with a line width of 0.4 nm. It shows a steep increase of the intensity at the edges of the particle, and a slight dip (upper left and right profile) or a flat plateau (lower left profile) at the center. To explain this observed course of the intensity profile, we recall that under Z-contrast conditions the image intensity of Pt ($Z = 78$) is much higher than that of Co ($Z = 27$) and Cu ($Z = 29$). Strictly spherical particle morphologies rule out thickness variations as source of the central dip of the contrast patterns. Hence, the observed contrast features must be related to the variation of the chemical composition in the center of the particles, suggesting a single Co/Cu rich particle core and a Pt rich shell.

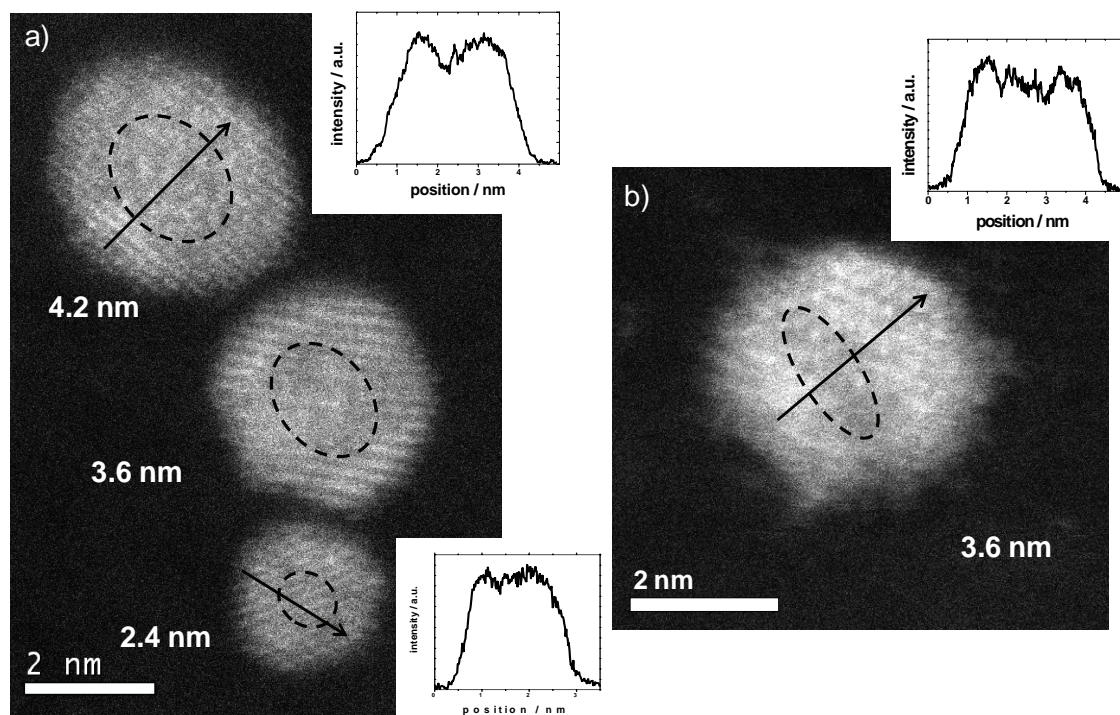


Figure 54 a) HAADF micrograph of individual dealloyed Pt-Cu nanoparticles up to 5 nm with their according HAADF intensity line profiles; b) HAADF micrograph of a dealloyed Pt-Co nanoparticle at 3.6 nm with the according intensity line profile. The black arrows signify the scan direction of the intensity profiles and the dashed lines indicate the dark shaded particle regions. Reprinted from ref ¹⁵⁸ with permission of American Chemical Society, copyright (2012).

To corroborate our conclusion, we calculated a HAADF intensity profile of a single core-shell nanoparticle formed by dealloying of a precursor alloy particle (see Figure 55a). Figure 55b shows the calculated HAADF intensity profile for a spherical core-shell nanoparticle consisting of a ~ 3.5 nm M rich alloy core and a ~ 0.8 nm pure Pt shell with a sharp compositional transition between core and shell (solid line). A more continuous compositional transition between core and shell would lead to a smoother HAADF intensity profile without pronounced spikes at the core-shell interface (dashed lines). This predicted line profile is in good agreement with the experimental results and reveals a core-shell structure for this size regime. The HAADF intensity maxima of the various core-shell particles at 3 - 4 nm showed a mean Pt shell thickness

of around 0.8 and 1.2 nm. Although the nanoparticles in the size regime below 5 nm appear to be basically spherical, slight deviations from an ideal centrosymmetric structure are found. Figure 54b for example shows a slightly elongated and off-center dark spot (dashed lines), which indicates an ellipsoidal core and a variable shell thickness around it. Nanopores or hollows were not observed in dealloyed Pt-Co and Pt-Cu nanoparticles of this size range. This is likely due to the high surface energy of voids of this size and the rapid annihilation process of vacancies by highly mobile low-coordinated Pt surface atoms, as discussed in more detail later.

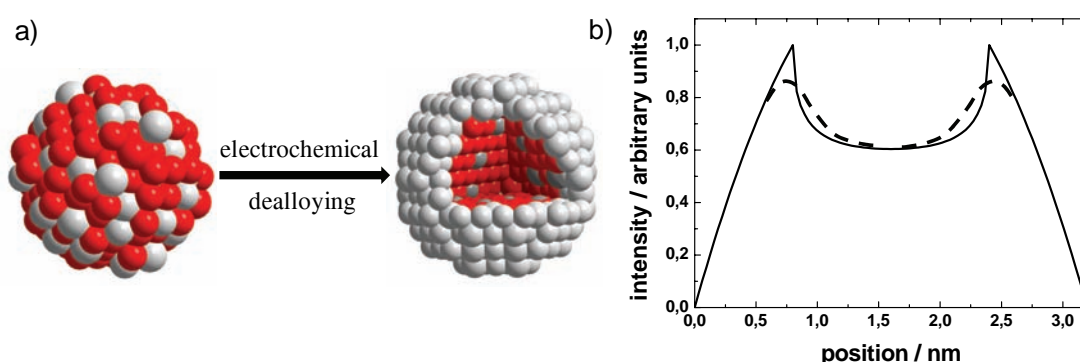


Figure 55 a) Illustration of the formation of core-shell bimetallic nanoparticle by electrochemical dealloying. Red and light grey spheres denote Cu atoms and Pt atoms, respectively. b) Simulated HAADF intensity profiles of a core-shell Pt-Co nanoparticle at ~ 3.5 nm with Pt shell thickness of ~ 0.8 nm. Solid line in the HAADF intensity profile denotes a sharp compositional transition between the core and shell, while dashed lines indicate a smoother profile with more continuous compositional transition at the core-shell interface. Reprinted from ref ¹⁵⁸ with permission of American Chemical Society, copyright (2012).

7.4.2 “Multiple Cores-Shell Nanoparticles” – Dealloyed Pt-Co and Pt-Cu Particles up to 20 nm Diameters

The particle morphology and intraparticle composition of dealloyed Pt-Co and Pt-Cu within the size range up to 20 nm are distinctly different from the simple core-shell structure.

Figure 56 shows a collection of HAADF micrographs for representative dealloyed Pt-Co particles between 8 and 15 nm. Lattice fringes are clearly resolved. Inside of the particles, the HAADF micrographs display contrast features which are more complex than simply dark shading in the center and bright shading in the outermost parts. As guide to the eye, these contrast features are outlined by black dashed lines in Figure 56. The frequently appearing particle motifs will now be discussed in detail considering the spectroscopic established composition profiles for Pt and Co using EEL spectroscopy (see Figure 57), respectively. The concentration profiles of the EEL spectroscopy line scans from the Pt $M_{4,5}$ (2155-2400 eV) and Co L_3 (770-785 eV) edges are shown in black and red. The EEL signals are normalized concerning the scattering cross section of the elements. The normalized intensity can be correlated with the projected thickness of the respective element. Error bars, which were calculated according to standard deviation of the EEL data within the limit of integration in addition to the mismatch of the background fit curves, indicate a good signal to noise ratio of the compositional measurements.

Figure 56a shows a HAADF micrograph of a dealloyed particle at 8 nm with a dark shaded region in the center (denoted with black dashed lines) and bright outermost edge, indicating the formation of single core-shell structure. The particle and its core, however, are not perfectly round and exhibit slightly irregular shape. The particle seems to be broken at the upper right side.

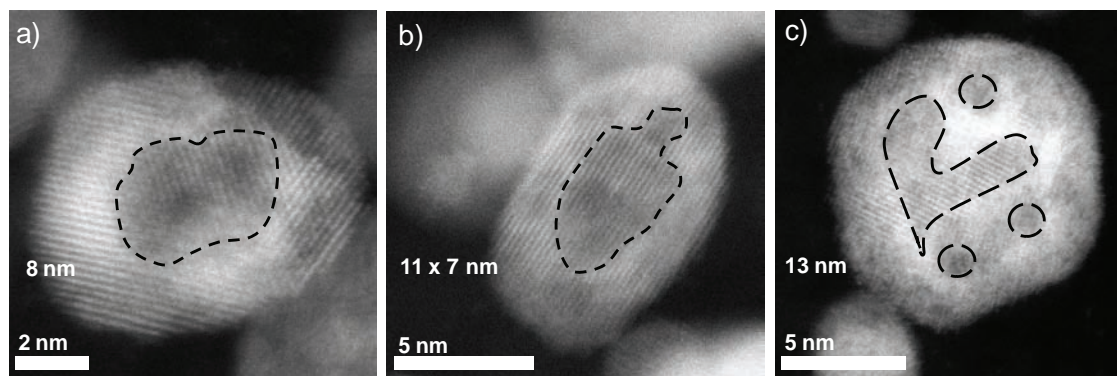


Figure 56 HAADF micrographs of individual dealloyed Pt-Co particles with various diameters of 8 - 15 nm. As guide to the eye, these contrast features are outlined by black dashed lines. Reprinted from ref ¹⁵⁸ with permission of American Chemical Society, copyright (2012).

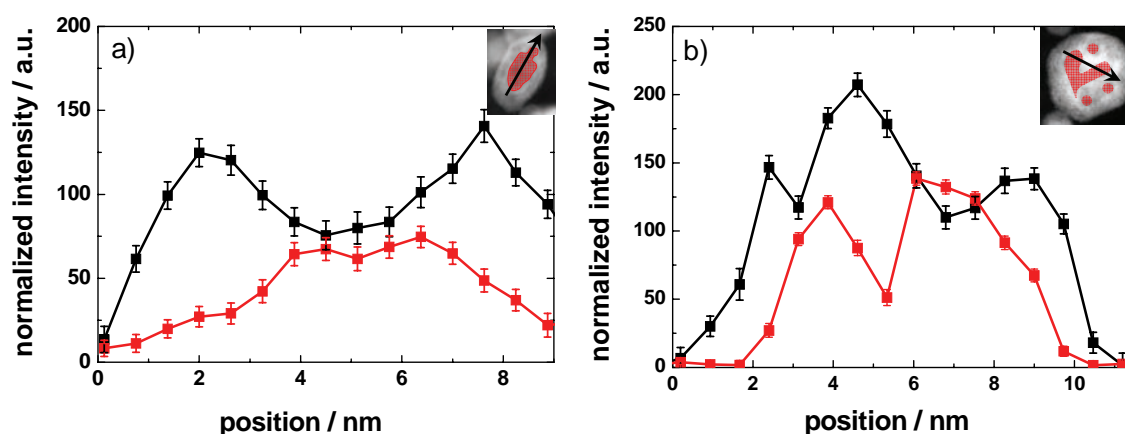


Figure 57 EEL line scan profiles for Pt (black) and Co (red) concentration in dealloyed Pt-Co nanoparticles at (a) 11 nm and (b) 13 nm. Insert: The direction of the line scan is indicated with a black arrow. The red area highlights the contrast features in the HAADF micrograph. Reprinted from ref ¹⁵⁸ with permission of American Chemical Society, copyright (2012).

In Figure 56b, an ellipsoidal particle with a dimension of 11 x 7 nm exhibits a dark shaded, elongated core of 3 x 5 nm (denoted with black dashed lines). The corresponding EEL line scans for Pt and Co across this particle are shown in Figure 57a. At the upper left side, the particle is overlapped with other particles and therefore the Co and Pt EEL signal do not drop to zero. Along the

EEL scan, the Pt signal increases rapidly on the edges and reaches its maxima at 2.0 and 7.5 nm. In the center of the particle, the Pt signal shows clearly a minimum at 4.5 nm. The Co signal is almost zero at the edge and exhibits broad maxima in a range of 4 and 6.5 nm which relates to the dark shaded, ellipsoidal core in the HAADF image.

Figure 56c shows a HAADF micrograph of an almost spherical particle at 13 nm with an irregular core structure (indicated with black dashed lines). Along the EEL spectroscopy line scan shown in Figure 57b, two Co rich core regions at 4 and 6 nm are crossed which display dark contrasts in the HAADF micrograph. The Co concentration is zero below the particle surface. The Pt EEL signal exhibits three distinct maxima at 2.2, 4.5 and 8.5 nm. The Pt maxima agree excellently with the bright regions of the particle in the HAADF micrograph.

Our microstructural and compositional study suggests that particles in this size regime possess a complex Co rich core structure, which even may split into multiple separate core regions. Irregular shaped dark regions near the particle center directly correlated with Co rich regions (cores); while dark shaded spots (indicated by dashed lines in Figure 56c) near the particle surface evidence Co rich regions of few nanometers diameter (*“Co satellite cores”*).

Dealloyed Pt-Cu particles show also morphological and compositional complexation, that are very similar to the observed structure for Pt-Co particles at similar size, for instance, multiple cores with irregular shape. Figure 58 displays a representative HAADF micrograph of four near spherical Pt-Cu particles with 11, 14, 15, and 22 nm diameters. Round dark regions of 5 - 6 nm diameter in the center are surrounded by bright outer particle shells. These contrast features indicate that copper is predominately located in the center, while platinum constitutes the outer shell. Our results suggest that Pt-Cu particles up to 15 nm diameter form a single core-shell structure, while particles with diameter greater than 20 nm show multiple irregular dark shaded regions (see Figure 58). The multiple dark shaded regions of about 3 - 4 nm represent the local enrichment of copper. The Cu rich regions form multiple cores inside the particle.

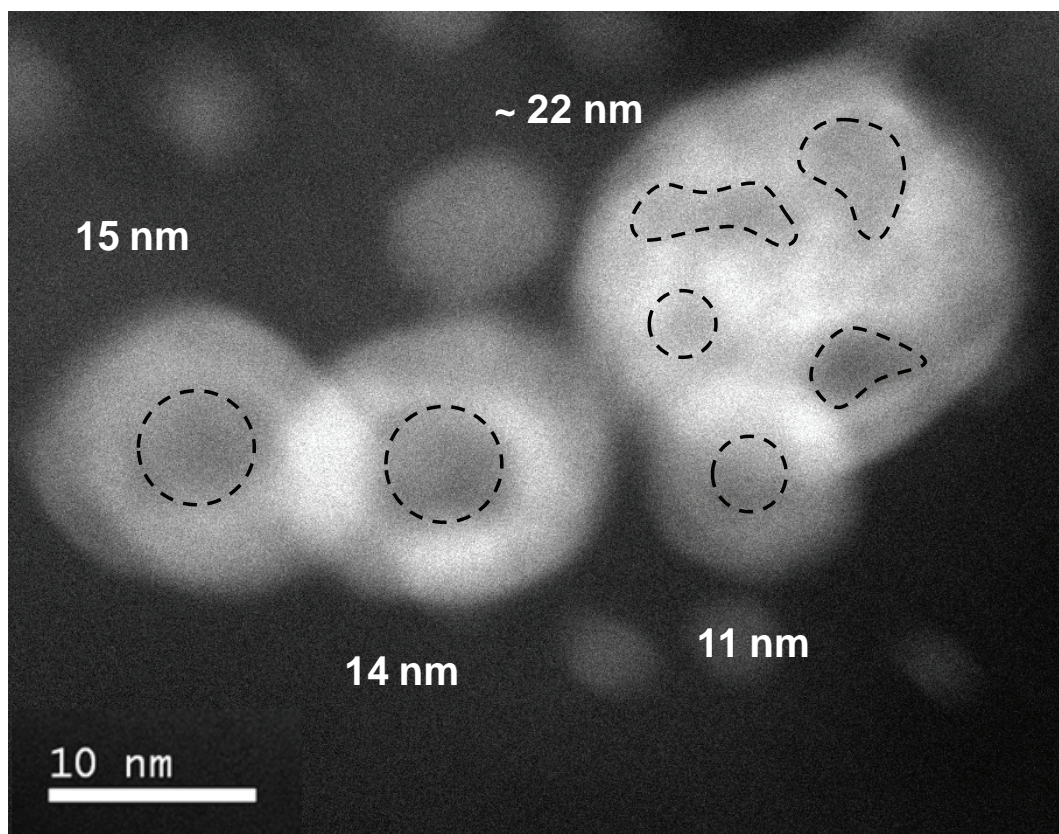


Figure 58 HAADF micrograph of individual dealloyed Pt-Cu particles in a size range of 10 - 22 nm. As guide to the eye, the black dashed lines in the HAADF image denotes the dark shaded regions. Reprinted from ref ¹⁵⁸ with permission of American Chemical Society, copyright (2012).

To summarize the analysis in the size regime up to 20 nm, we have identified a characteristic particle size, referred to as $d_{\text{multiple cores}}$, of 10 - 15 nm that separates a single core-shell arrangement from complex multiple cores-shell structure. The characteristic particle diameter highlights a distinct morphological and compositional structure change of the dealloyed particles. Above $d_{\text{multiple cores}}$, dealloyed bimetallic particles generally exhibit dominantly multiple less noble metal rich cores with irregular and/or ellipsoidal shape.

7.4.3 “Nanoporous Multiple Cores-Shell Particles” – Dealloyed Pt-Co and Pt-Cu Particles up to 100 nm Diameter

Figure 59a shows a representative HAADF image of an individual dealloyed Pt-Cu particle with 43 nm diameter which shows a large irregularly shaped dark region of around 20 nm in the center, bright outermost edges and multiple dark spots close to the particle surface. In contrast to the smaller size regimes, the particle exhibits irregular dark areas directly bordering at the surface (denoted with dashed black lines in Figure 59a). Since Cu rich regions on the surface rapidly dissolve under the chosen cycling conditions, these contrast features provide clearly evidence for corrosive pits and the formation of nanopores. The intensity variations in the dealloyed Pt-Cu particle are related to the presence of both multiple Cu rich cores and nanopores. A similar structure was also found for Pt-Co particles in a size range of 40 to 70 nm. Here, Figure 59b shows a dealloyed Pt-Co particle with some surface pits (outlined with dashed black lines).

To support our conclusion, a tilt series of HAADF micrographs was acquired which represents a three-dimensional tomographic structure picture. Our tomographic study reveals a complex three-dimensional inner structure with elongated channels like dark areas and a number of pits on its particle surface. In addition, Figure 60 shows TEM micrographs and overall chemical compositions established by EDS for various dealloyed Pt bimetallic particles in a size range between 30 and 200 nm. The EDS results of single Pt-Co particles show a final Co concentration of around 10 - 18 at. % after dealloying, whereas the residual Cu concentration of the Pt-Cu particles is around 34 at. %. These results are in excellent agreement with the overall chemical compositions of Pt-Cu and Pt-Co particle ensembles. It is noted, that the Co concentration loss for Pt-Co particle catalysts is higher than that for Pt-Cu due to the dissolution potentials and the oxygen adsorbate-induced surface segregation.^{13, 142} Nevertheless, it evidences that the large particles are not completely dealloyed after the electrochemical process.

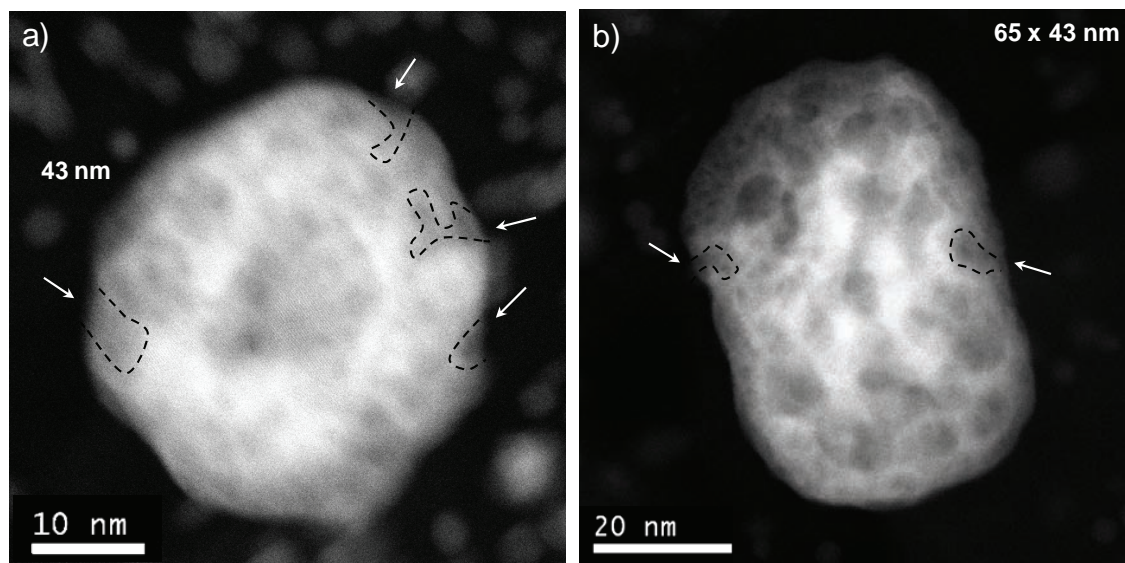


Figure 59 HAADF micrographs of dealloyed (a) Pt-Cu and (b) Pt-Co particles with diameters larger than 40 nm. As guide to the eye, the white arrows and black dashed lines denote the surface pits (nanopores) on the particle surface. Reprinted from ref ¹⁵⁸ with permission of American Chemical Society, copyright (2012).

Approaching macroscale dimensions, bulk dealloying behavior is more noticeable for particles in a size range above 100 nm. Figure 61 shows a dealloyed Pt-Cu particle at 100 x 150 nm with clearly visible pores and ligament structure. The formed nanopores are in the order of ~3 nm diameter and penetrate clearly the entire particle. TEM micrographs of particles at similar geometric size with the corresponding EDS results are also shown in Figure 60. The single particles of around 100 nm contained still a Co concentration of around 17 at. %, while the residual Cu concentration by comparable size was around 36 at. %. Surprisingly, this value is similar to the final chemical composition of the 30 - 70 nm particles that show a much smaller surface-to-volume ratio. Hence, bulk-like porous bimetallic particles above 100 nm diameter exhibit a much higher rate of Co/Cu loss than smaller particles under similar dealloying conditions. This is rationalized considering the much larger increase in the interfacial area of large particles during porosity evolution.

Importantly, the observed size of the nanopores in the particle of Figure 61 and similar particles was about 3 nm. At particle diameters above 30 - 40 nm,

Size-dependent Morphology of Dealloyed Bimetallic Catalysts: Linking the Nano to the Macro Scale

this value appeared to be a material-characteristic value and is in excellent agreement with pore sizes of nanoporous platinum obtained by acid leaching of $\text{Pt}_{25}\text{Cu}_{75}$ alloy films at room temperature.^{161, 162}

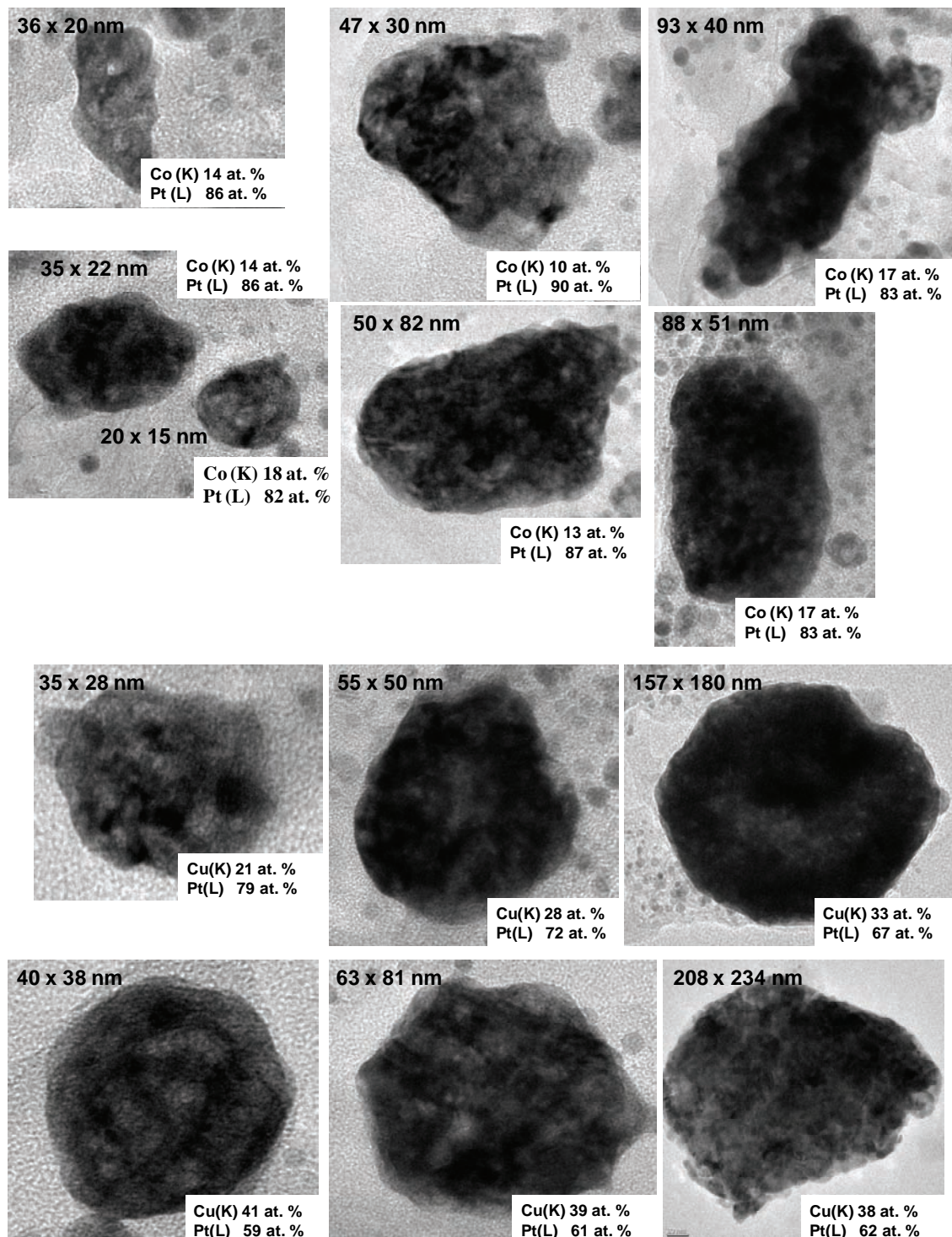


Figure 60 TEM images and EDS measurements of single dealloyed Pt-Cu and Pt-Co particles larger than 30 nm diameter after dealloying. Reprinted from ref ¹⁵⁸ with permission of American Chemical Society, copyright (2012).

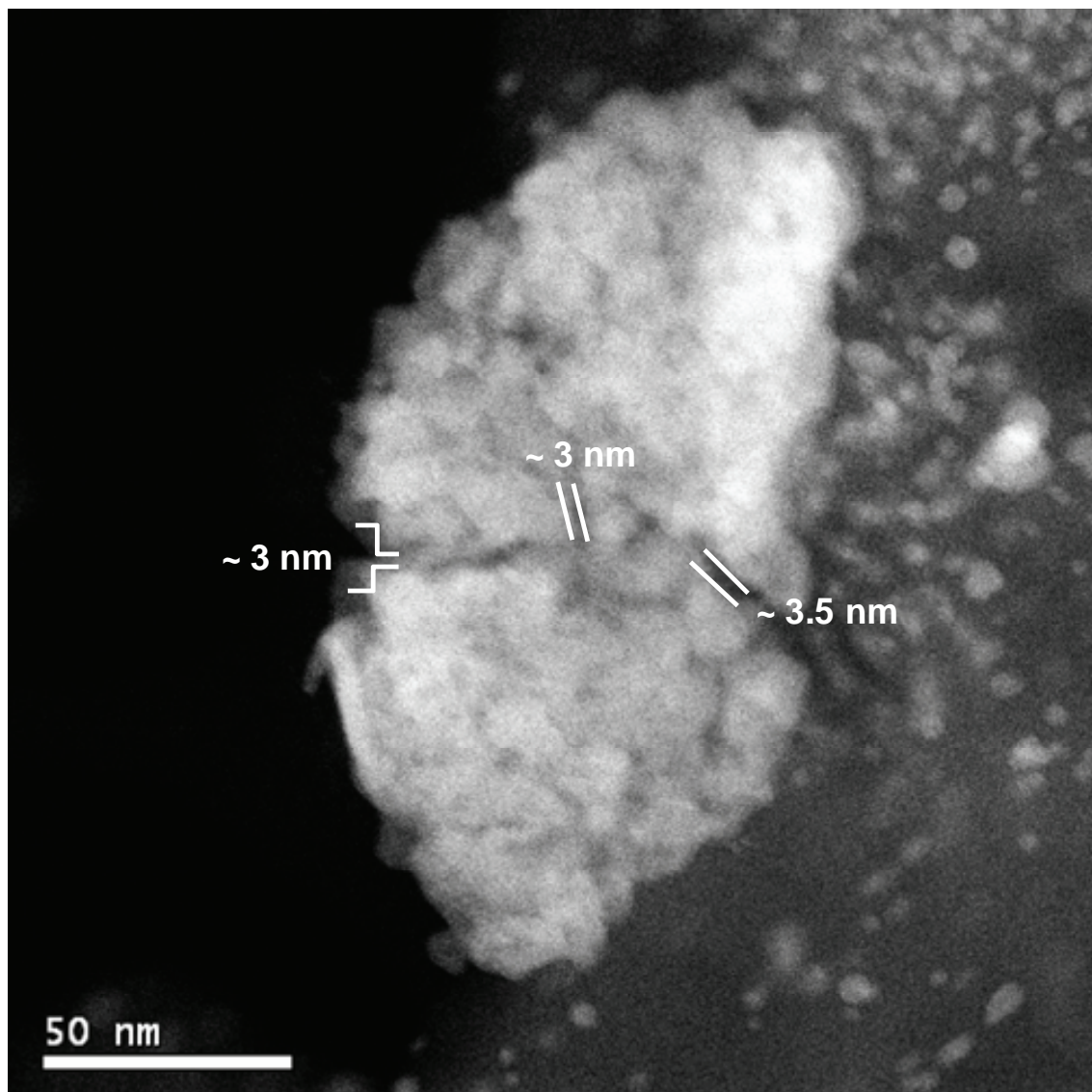


Figure 61 HAADF micrograph of dealloyed Pt-Cu particle at 100 x 150 nm with a clearly visible porous structure. The pores are on the order of 3 nm. Reprinted from ref ¹⁵⁸ with permission of American Chemical Society, copyright (2012).

To summarize our observation in the size regime of up to 100 nm size, we have uncovered the existence of a novel class of particle morphologies characterized by the presence of particle involving surfaces pits and pores of characteristic length scale coexisting with irregularly shaped multiple Co/Cu rich cores.

7.5 Discussions

7.5.1 Size-dependent Morphology and Chemical Composition of Dealloyed Pt-Co and Pt-Cu Particles

Based on our present microscopic and spectroscopic results, Figure 62 illustrates a detailed size – morphology – composition relation for dealloyed Pt-Cu and Pt-Co particle electrocatalysts in a size range of 3 - 100 nm. Unlike most other works, this study focuses on the dominant morphological classes of particle electrocatalysts in their most active dealloyed state. The catalysts were intentionally not treated with accelerated degradation protocols, yet were prepared and left in their dealloyed activated state.^{20, 81, 90, 95, 96, 163-165}

Obviously, the dealloyed Pt bimetallic particle morphology exhibits a strong size effect. The Pt shell of the dealloyed particles appears to scale with the particle size, i.e. large particles tend to exhibit a thicker Pt-enriched shell region after comparable dealloying time. This indicates that, for larger particles, the dealloying proceeds rapidly into larger depth. Our results suggest the existence of three different size/morphology regimes of dealloyed Pt-Co and Pt-Cu catalysts: With increasing size, a structural regime characterized exclusively by single core-shell structures give way to one involving multiple-core bimetallic structures. At even larger sizes, surface-pits and nanopores coexisting with multiple cores are formed. These size/morphological regimes are separated by two characteristic particle diameters, $d_{\text{multiple cores}}$ and d_{pores} .

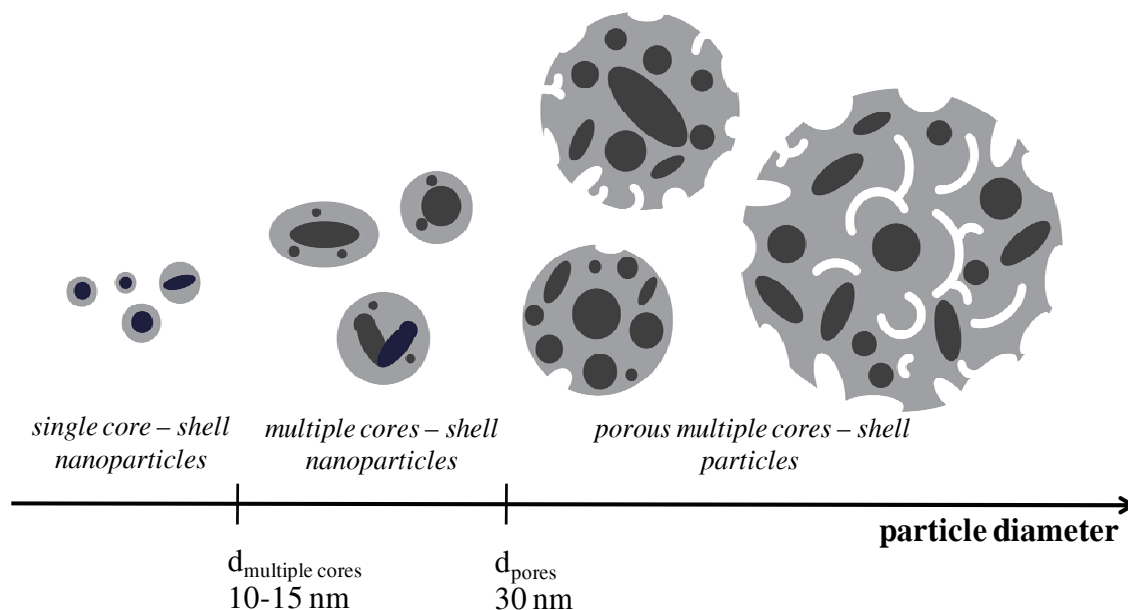


Figure 62 Illustration of the evolution in size-dependent morphology and composition of dealloyed Pt-Cu and Pt-Co particle electrocatalysts. Reprinted from ref ¹⁵⁸ with permission of American Chemical Society, copyright (2012).

The values of $d_{\text{multiple cores}}$ and d_{pores} represent the approximate lower particle size boundaries, where Cu/Co rich multiple cores and nanopores/voids were observed to exist, respectively. They are manifestations of nanoscale effects. The kinetic and thermodynamic aspects affecting the particle structure formation as a function of particle size can be described in a consistent picture as follows:

In Pt alloys with Cu/Co content above the parting limit, Cu/Co atoms are dissolved rapidly from the particle surface by electrochemical dealloying, because the upper potential limit of 1.0 V/RHE during the applied voltage cycling is far more positive than the critical dealloying potential^{117, 162}. At the macro scale, dealloying of bulk binary alloys results in the evolution of porosity with a characteristic pore size. The formation of porosity is thereby controlled kinetically by the interplay of the rates of electrochemical dissolution and surface diffusion^{114, 166}. For instance, Pugh et al. reported that dealloying of macroscopic Pt-Cu alloys leads to characteristic 3 nm pore diameter^{161, 162} based on the slow surface diffusion coefficient of Pt. Due to the macroscopic size, thermodynamic interfacial energy barriers can generally be neglected. The

detailed mechanisms leading up to porosity in macroscopic binary alloys were thoroughly analyzed by Erlebacher et al., who reported a detailed model for porosity evolution highlighting the role of electrochemical dissolution and surface diffusion.^{114, 167}

At the nanoscale, both kinetic and thermodynamic factors significantly affect the particle structure formation process. First, we will discuss the existence conditions for multiple Cu/Co rich particle cores. Our data suggests that Cu/Co rich cores are only stable above a size of 3 nm. This can be rationalized based on thermodynamic interfacial energy arguments prohibiting cores with smaller diameters. To accommodate two or more of these cores, the Pt particle shell has to be at least 3 nm thick, requiring an (ideal hard sphere-based) minimum particle size to about 10 nm. This is in good agreement with our experimentally observed lower value of the characteristic particle diameter for multiple cores, $d_{\text{multiple cores}}$.

Now, we address the observed existence conditions for porosity. Voids and pores exhibit a characteristic length scale of about 3 nm, but they were, under our conditions, only observed in particles with diameters above $d_{\text{pores}} = 30 - 40$ nm. Based on this vastly different dimensions, thermodynamic interfacial energy arguments now fail to account for the absence of porosity suggesting rather a largely kinetically controlled pore formation mechanism such as the Rayleigh surface instability¹⁶⁶.

Rayleigh instabilities are surface diffusion-driven processes and refer to the growth of randomly formed surface pits with their high vacancy density into bulk pores and, upon channel pinching into closed voids. Important for our discussion here is the fact that a successful Rayleigh surface instability requires the correct balance between the surface diffusivity of low-coordinated Pt atoms inside the surface pit and the Pt atoms around the pit. Pt atoms inside the pits tend to diffuse to the edges to raise their coordination. This favors the growth of the pit deeper into the particle bulk. If the surface diffusion rate of surface Pt atoms around the pit is sufficiently large, however, pits cannot grow and rather heal out resulting in the disappearance of the initial pits. Voids then become impossible. We hypothesize that the balance between the surface diffusivities of Pt surface atoms inside pits and around pits allow for the formation of voids

near the characteristic particle diameter d_{pores} , because surface atoms of large particles exhibit higher mean coordination numbers and hence lower diffusivities.

We mention in passing that recent work on void formation in particles has highlighted the role of the Kirkendall interdiffusion effect. This effect is based on bulk diffusivity differences at a bimetallic interface and involves vacancy supersaturation followed by vacancy condensation into voids on the fast diffuser side of the interface.¹⁶⁸⁻¹⁷² Examples of Kirkendall effects in nanoscale objects at elevated temperatures were reported by Henkes et al.¹⁷³ and Yin et al.¹⁷⁴. Considering the ambient temperatures of these studies combined with the relatively large distance a diffusing metal atom would have to overcome to reach the particle surface, we assume to exclude Kirkendall effect to explain our observations.

The two characteristic particle diameters $d_{\text{multiple cores}}$ and d_{pores} delineate three distinct size ranges with characteristic morphologies as follows:

(i) *“single core-shell nanoparticles”*: Single core-shell nanoparticles are exclusively formed by dealloying of particles below $d_{\text{multiple cores}} = 10 - 15$ nm. The voltammetric cycling in acidic electrolyte leads to an electrochemical rapid dissolution of Co/Cu from the particle surface. This structure is characterized by a monotone drop of Co/Cu towards the particle surface. The thickness of Pt-enriched shell is around 0.8 and 1.2 nm for this size range. Due to the stronger depletion of Co by electrochemical dealloying, the Pt-enriched particle shell for Pt-Co is slightly thicker than that of Pt-Cu particles. Based on our earlier discussion nanopores or hollows are not observed in the dealloyed Pt-Cu and Pt-Co catalysts of this particle size range due to thermodynamic and kinetic arguments. We emphasized that these dealloyed bimetallic nanoparticles exist in their dealloyed most active state and do not represent a stable thermodynamic final state.

(ii) *“multiple cores-shell nanoparticles”*: Non porous particles with irregular and/or ellipsoidal shaped multiple Co/Cu rich cores are prevailing above $d_{\text{multiple cores}} = 10 - 15$ nm and below $d_{\text{pores}} = 30 - 40$ nm. Our data suggests a slight

metal-dependent difference in $d_{\text{multiple cores}}$ and d_{pores} between Pt-Cu and Pt-Co particles. This can be explained by the distinct dissolution potential, surface segregation and surface diffusion behavior of Cu and Co in the presence of adsorbed oxygen species.^{13, 142} Based on our earlier discussion, fast annihilation of pit vacancies by highly mobile Pt surface atoms and decrease of surface energy suppresses the formation of voids and pores. The subsurface regions with high Cu/Co concentration are undercut on the side by dealloyed regions and results in the formation of Co/Cu rich satellite cores.

(iii) “*porous multiple cores-shell particles*”: Dealloyed bimetallic particles above d_{pores} exhibit multiple cores and various degrees of porosity ranging from surface pits to bulk nanopores and voids. Despite the decreasing surface-volume ratio large particles reveal smaller residual composition of Co/Cu and thus a faster dealloying behavior compared to smaller particles. The pit formation and porosity become more and more distinct with increasing particle size presumably based on increasing surface-controlled solid-state Rayleigh instabilities.¹⁶⁶

In summary, morphology and composition of dealloyed Pt bimetallics are strongly determined by their initial particle size. We note that some of the observed size-dependent morphological and compositional structures in Pt-Cu and Pt-Co particle catalysts do not necessarily represent a stable thermodynamic final state, rather they could be the catalytically most active, yet transient stages along a structural and compositional trajectory. However, we also emphasize that slight variations in initial alloy composition would not qualitatively alter the observed morphologies. Also values of $d_{\text{multiple cores}}$ and d_{pores} may slightly vary for different alloys.

7.6 Summary

We have uncovered how particle size affects the morphology and chemical composition of electrochemically dealloyed Pt-Co and Pt-Cu electrocatalysts. We have established in detail the size – morphology relationships of the bimetallic catalysts in their most active dealloyed state. The morphological structure and intraparticle composition of the particles correlate strongly with their size. Thereby, the interfacial energies and the size dependent diffusion rates of Pt are playing a key controlling role. After dealloying the overall compositions were slightly dependent on size for larger particles, where pores had emerged. This indicates a strong coupling of pore formation and rate of dealloying. Based on our high-resolution microscopic and spectroscopic results, we concluded the existence of three distinctly different size/morphology regimes of dealloyed active Pt-Co and Pt-Cu catalysts.

- “*single core-shell nanoparticle*”: The single core-shell structure is exclusively formed by dealloying up to a characteristic particle size ($d_{\text{multiple cores}} = 10 - 15$ nm).
- “*multiple cores-shell nanoparticles*”: Multiple Co/Cu rich cores with irregular and/or ellipsoid shape become prevalent in non-porous dealloyed particles above this characteristic particle diameter $d_{\text{multiple cores}}$. The formation of multiple cores is caused by the thermodynamic interfacial energy arguments and the inhomogeneous distribution of diffusing Pt surface atoms, where subsurface regions with high Cu/Co concentration are protected against further dealloying.
- Pores and voids of a material-characteristic length scale of roughly 3 nm observed in Pt binary alloys at the macro scale cannot be formed at particles below 20 nm due to the thermodynamic and kinetically aspects.
- “*porous multiple cores-shell particles*”: With increasing particle size the formation of pores becomes prevalent. Above the characteristic particle diameter of 30 nm, Pt-Co and Pt-Cu exhibit clearly surface pits (nanopores) and multiple cores inside the particles. Surface pores indicate the degree of porosity. Above 100 nm, the macroscopic bulk-like particles show a significant Co/Cu concentration and nanoporous structures on order of 3 nm

pore diameter after dealloying. Despite the decreasing surface-volume ratio with increasing particle size, the large particles are leached off stronger and therefore form increased pores and ligaments structures. The formation of porosity is thereby controlled kinetically by the interplay of the rates of electrochemical dissolution and surface diffusion.

Our results link morphological insight into dealloyed Pt-Co and Pt-Cu particles at the nanoscale to macroscopic corrosion phenomena, filling the material gap between core-shell nanoparticles and highly porous bulk-like particles. The identified size – morphology – composition relationships are likely to be of general importance in understanding the dealloying of other Pt bimetallics.

8 Atomic-scale Structural and Element-Compositional Characterization of Dealloyed Pt-Co Core-Shell Nanoparticles

An atomic-scale structural and element-compositional investigation of a Pt-Co core-shell nanoparticle fuel cell catalyst reveals unusual self-organized compositional subsurface finestructure. The combined scanning transmission electron microscopy (STEM) and electron energy loss (EEL) spectroscopy study uncovers new self-organized compositional motifs, such as off-center Co “satellite cores” and compositional depth profiles consisting of alternating layers with Co-depletion and Co-enrichment. Local sub-surface metal enrichments control surface lattice strain and help sustain high catalytic performance. The study exposes the conventional two-layer core-shell concept as an insufficient structural description for catalytically active dealloyed bimetallic nanoparticles. Backed up by model prediction, the mechanistic origin of the complex near surface structures is rationalized by interplay of selective Co dissolution, Pt surface diffusion, and an inverse Kirkendall effect of Co atoms, involving vacancy surface ejection coupled with atomic-range uphill Co diffusion. While present in other Pt bimetallics, as well, the particle fine structure is of general importance for the understanding and design of active bimetallic nanoparticle catalysts.

8.1 Introduction

Beyond M rich Pt-M bimetallic nanoparticles, it has now been established that, upon contact with acid electrolytes, virtually all Pt bimetallic catalysts enrich in Pt across the first few atomic layers leaving the interior close to the initial composition¹⁷⁵. Such a simple two-layer “core-shell” structure motif has emerged as the most frequently discussed feature of active bimetallic electrocatalysts. The concentration of the less noble metal M is assumed to drop monotonic from the core region to the particle surface based on rapid chemical or electrochemical dissolution near the surface. The core-shell interface is considered a steep drop in the concentration of M across few atomic layers below the surface. However, to date, no study has ever experimentally measured or confirmed this tacit two-layer assumption on the metal composition profile. We therefore set out to provide an accurate experimental atomic-scale description of dealloyed bimetallic core-shell structures and developed and derived a deeper understanding of their formation mechanisms and impact on surface catalytic activity. This structural insight will enable a more rational design of improved active bimetallic catalysts.

This work challenges the conventional description of single core-shell bimetallic nanoparticles and offers, to our knowledge, one of the most accurate descriptions of the atomic-scale intraparticle compositional structure of dealloyed core-shell catalysts. What sets this study apart from previous investigations of electrocatalysts^{15, 23, 109, 176} is the level of detail in which the cross-sectional microstructure and chemical composition is analyzed at the atomic-scale, using aberration-corrected high angle annular dark field (HAADF) scanning transmission electron microscopy (STEM) and electron energy loss (EEL) spectroscopy. We reveal the existence of novel nanostructural motifs, such as core-shell structures consisting of Co rich center cores with additional off-center Co rich satellite cores; we also found evidence for non-monotonic compositional Co profiles across the catalyst particle; both findings bear critical implications on the surface catalytic activity of the particles. Consistent with earlier experiments and computational predictions on dealloying in bimetallic systems, a mechanistic origin for the observed structures is proposed.

We chose Pt-Co bimetallic alloy nanoparticle electrocatalysts^{21, 90} for our microscopic fine structure investigations. Chemically and electrochemically dealloyed Pt-Co bimetallic alloy nanoparticle electrocatalysts are the most frequently studied and most deployed alternative to Pt for hydrogen fuel cell cathodes.^{15, 176} Well-alloyed single-phase carbon-supported Pt₂₅Co₇₅ precursor particles were electrochemically dealloyed, that is Co atoms were leached⁹⁰, by cycling the electrode potential between 0.06 and 1.0 V/ RHE^{16, 81, 93} for 200 cycles. This protocol is known to result in a catalytically activated particle ensemble for the electroreduction of oxygen close to its catalytic activity maximum.^{90, 130} Hence, unlike earlier studies^{15, 130} with their focus on alloy particle degradation after long-term testing, our study provides direct insight in the microstructure of the catalyst near its most active state.

8.2 Compositional Particle Depth Profiles of Dealloyed Self-organized Pt-Co Core-shell Nanoparticles

Figure 63 a – c shows representative high-resolution aberration-corrected HAADF electron micrographs of three selected dealloyed Pt-Co nanoparticles in the size range of 8 – 15 nm. Particles of this size show high structural stability^{89, 133, 148, 177} and constitute the catalytically active fraction of a dealloyed fuel cell electrocatalyst (see Figure 53). HAADF microscopy provides ‘Zcontrast’ conditions, i.e. the image intensity is proportional to $Z^{1.6}$ to $Z^{1.8}$, where Z is the atomic number. Pt ($Z = 78$) shows a bright contrast, whereas Co rich regions ($Z = 27$) display a dark contrast. Inside the particle in Figure 63a, a slightly off-center oval region of about 6.5 x 7.5 nm has darker contrast than portions of the shell resembling the two-layer single core shell arrangement as previously reported in dealloyed Pt bimetallic nanoparticles with 2 – 8 nm¹⁶. Particles in Figure 63 a-c, however, reveal more complex intensity variations across the particle interior, e.g. a number of dark spots of about 1.5 nm diameter at the upper left, lower, and lower right parts of the particle shell in Figure 63a. HAADF images provide an integrated intensity over the respective elements; chemical and thickness-related contrast interferes which may lead to ambiguous structural results and hampers a direct interpretation in terms of compositional maps. EEL analysis separates the chemical elements and provides reliable atomic-scale compositional information.

We performed experimental EEL line scans across the nanoparticles of Figure 63 a-c to probe their detailed local composition in Pt and Co. The scans are presented in Figure 64 a-e as core loss intensity profiles across the dealloyed particles from the Pt $M_{4,5}$ and Co L_3 edges in black and red, respectively. A vertical EEL line scan through the particle of Figure 63a is illustrated in Figure 63d (arrow ‘1’) and presented in Figure 64a. It shows a steep increase of the Pt signal at the edges (0 – 4 nm and 11.5 – 14 nm) and a clearly defined minimum at the center of the dealloyed particle at 8 nm. In between, two maxima in the Pt signal are discernible at 4 and 11.5 nm. Meanwhile, the Co signal peaks in the center of the particle at 8 nm drops off

toward the edges of the particle. A smaller local maximum was observed at 2.5 nm, clearly corresponding to a dark spot at the bottom of the dealloyed nanoparticle (Figure 63a and red in Figure 63d). Such small Co rich “satellite cores” within the Pt rich shell are a frequently recurring structural motif.

The data reveals an asymmetric Pt signal with maximum concentration at 4 and 10 nm; this specific EEL intensity profile is consistent with an off-center core in the HAADF micrograph (Figure 63a). The corresponding Co signal shows a Co rich core at around 8 nm, and exhibits a satellite core at 3 nm corresponding to the dark feature at the upper left of the micrograph. A comparison of the EEL data and the respective HAADF micrograph (Figure 63a) confirms that the circular dark shading at the particle center, as well as smaller additional dark areas at the bottom and upper left of the particle, represent Co rich cores. As dark areas in the HAADF micrograph are always associated to a distinct local increase in the Co concentration by EEL analysis, we found no evidence for voids, hollow spaces or porosity. Similar complex morphological features were also observed in dealloyed Pt-Cu nanoparticles (see chapter 7 Size-dependent Morphology of Dealloyed Bimetallic Catalysts: Linking the Nano to the Macro Scale). These features are clearly the result of electrochemical treatment, because initial non-dealloyed particles show perfect compositional homogeneity without any local metal-enriched regions (see Figure 53).

Figure 63b and c show representative examples of dealloyed Pt-Co nanoparticles with yet another type of complex self-organized core-shell structure. Scanned along arrow ‘1’ (see Figure 63e), the Co EEL signal (Figure 64c) shows a sharp peak between 4 and 7 nm emanating from a Co plateau with shoulders between the positions 3 and 9 nm (red arrows in Figure 64c). Scanned along arrow ‘2’ (Figure 64d), a broad central Co peak is visible with narrow shoulders, again between 3 and 9 nm (red arrows in Figure 64d). The Co EEL maxima point to an elliptical core region in the center of the nanoparticle (see red area in Figure 63e) in line with the dark shadow of Figure 63b.

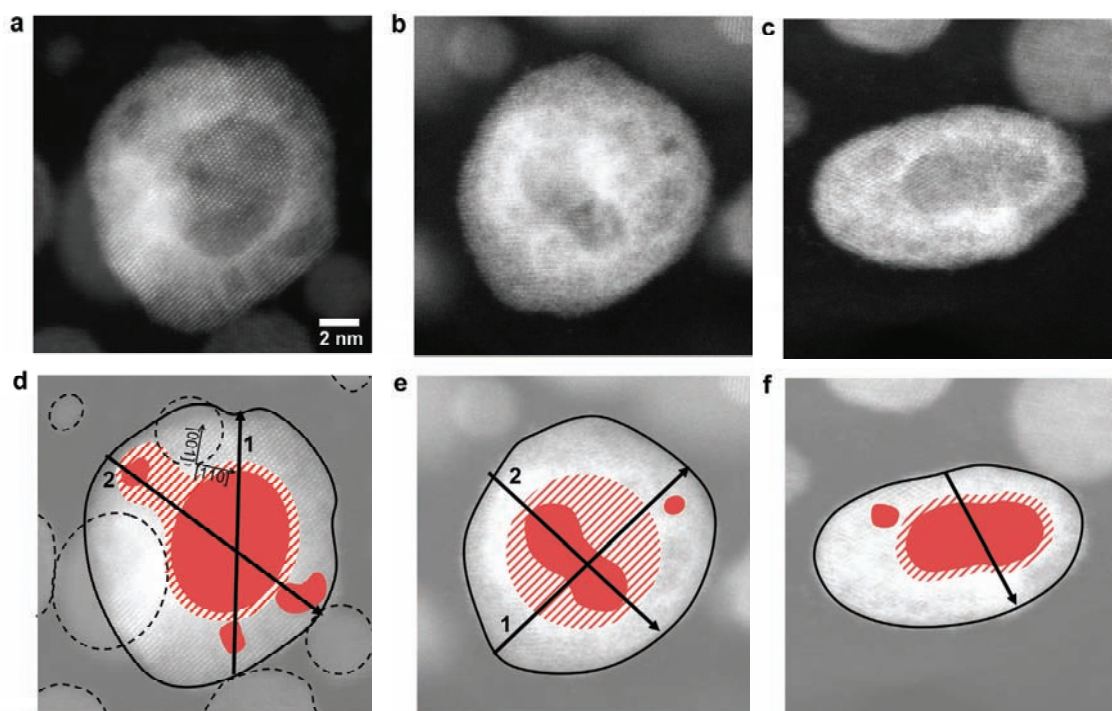


Figure 63 a, b, c) Atomic-scale resolution HAADF electron micrographs providing 'Z-contrast' conditions of three dealloyed Pt-Co bimetallic nanoparticle electrocatalysts. a) At the upper part of this nanoparticle, individual atomic columns are resolved. It is oriented along a (-110) zone axis of the face-centered-cubic structure. As guide to the eye, d, e and f highlight contrast features (hatched and red areas) of the corresponding micrograph. Black lines indicate the outlines of the nanoparticles and red areas signify Co-enriched dark shaded regions in the HAADF micrographs. Hatched red areas represent regions which show weak or no significant shading in the HAADF micrographs but clear Co signal in the EEL analysis. Dashed lines represent neighboring particles which are not in focus (d). Black arrows indicate the traces and direction of EEL line scans given in Figure 64.

Atomic-scale Structural and Element-Compositional Characterization of Dealloyed Pt-Co Core-Shell Nanoparticles

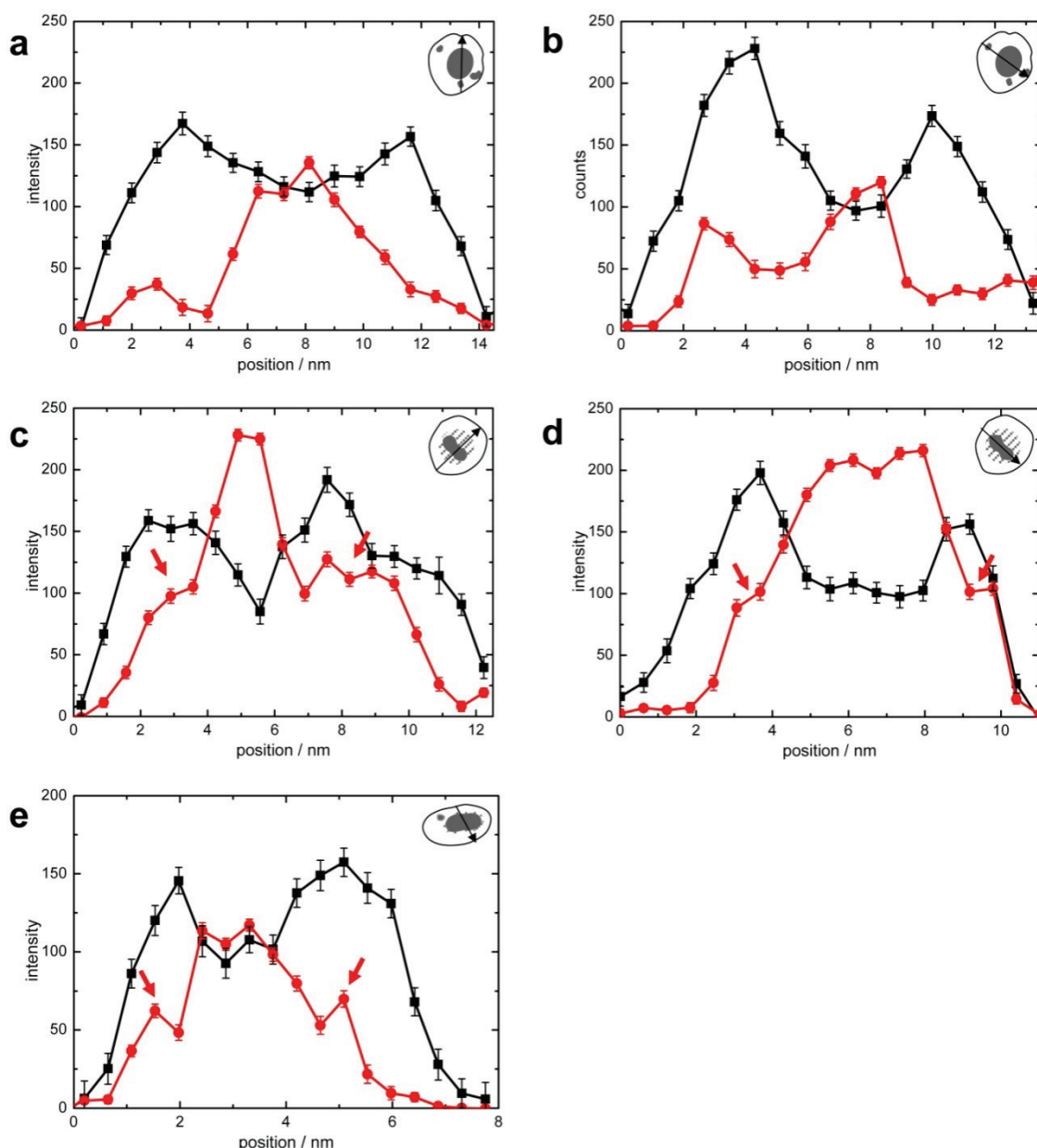


Figure 64 EEL intensity profiles across the dealloyed particles for Pt (black squares) and Co (red circles), respectively. The EEL profiles are normalized with the elemental scattering factor and hence represent thickness projected compositions. Insets on the top right depict sketches of the morphology and contrast features of the individual particles investigated. Black arrows across the sketches indicate the traces of the individual EEL line scans. Red arrows highlight shoulder/plateau and maxima features of the Co signal.

Pronounced shoulder-like features of the Co EEL scan are also observed in the ellipsoidal dealloyed Pt-Co particle shown in Figure 63c. Its dark core has an elongated shape and is displaced from the center of the particle. The EEL scan (direction in Figure 63f and data in Figure 64e) reveals a Co concentration maximum at 3 nm that coincides with a local minimum in the Pt concentration. Importantly, the Co core is now enclosed by symmetric Co maxima at 1.5 and 5 nm (red arrows in Figure 64e). This observation suggests the existence of two 2-3 atomic-layer thick adjacent bimetallic shells just below the outer Pt shell, the inner showing a compositional minimum in Co, the outer a Co maximum (see Figure 65).

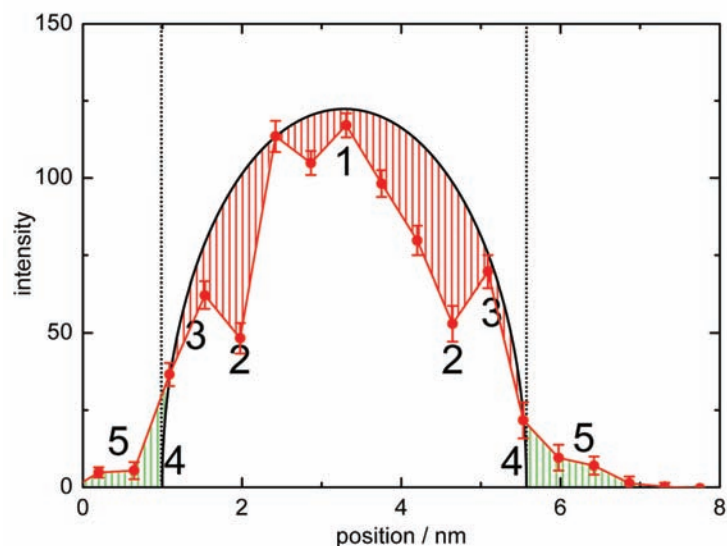


Figure 65 Co EEL scan of the particle in Figure 63c in comparison with the curve of an ideal ellipsoidal (or spherical) core with 4.6 nm diameter and a constant Co composition which shows no variation over the diameter of the core. The experimental curve has two local minima (2) within the core of the particle and clearly discriminates from the ideal curve (hatched area). The minima indicate a local depletion of Co. Outwards at the positions 3, the Co composition increases again and match the ideal curve of the ellipsoidal core of the particle. Outside of the core, i.e. in the shell region, the Co-composition decreases continuously. This observation suggests the existence of two 2 – 3 atoms thick adjacent bimetallic spherical shells just below the outer Pt shell, the inner showing a compositional minimum in Co, the outer a Co maximum.

The unusual EEL Co intensity features evidence a compositional profile across the nanoparticle that is more complex and hence inconsistent with a simple two-layer core-shell structure. A structural model with two-shells, a Co rich inner shell and an outer Pt shell, and an elliptical Co rich core does indeed yield EEL profiles with shoulder-like features. However, upon closer inspection even the two-shell model is insufficient to explain the experimental Co shoulders. Finally a multi-layer model structure was identified that accurately describes the experimentally observed features. It is based on a multi-layer/multi-shell profile with adjacent Co depletion and enrichment zones as shown in Figure 66.

The analysis in Figure 66a points out the connection between the EEL intensity profile and the radial composition profile and demonstrates that shoulder features in the EEL signal indicate a structure with adjacent shells of an inner depletion and outer enrichment of Co just below the outer Pt rich shell. Here, the accurate Co compositional profile across the nanoparticles was extracted from the experimental EEL data. The measured EEL intensities represent a line integral across different shells of the particle. The connection between the actual Co composition profile and the EEL intensity is mathematically given by the Abel transform¹⁷⁸. We applied the Abel transform to an averaged Co EEL intensity (red curve) in Figure 66a and extracted the corresponding radial Co composition profile (blue curve). It shows the presence of a very pronounced drop of the Co composition within the core to about 30 % of the composition at the center (2) and a subsequent increase of Co to about 55 % at the core/shell interface (3).

The formation of Co rich satellite cores a few atomic layers below the particle surface combined with the existence of adjacent bimetallic spherical shells with a minimum and maximum in the Co composition has important implications on the strain distribution across the nanoparticle surface and thus on the resulting catalytic activity. Based on Vegard's rule, Co rich regions exhibit smaller cubic lattice constants compared to Pt rich regions. Since geometric strain is a long-range effects^{16, 28, 179, 180} extending across up to 16 atomic Pt layers¹⁶, the Co maxima just below the Pt rich shells stabilize or even enhance the compressive surface strain and lower the chemisorption energy of

Atomic-scale Structural and Element-Compositional Characterization of Dealloyed Pt-Co Core-Shell Nanoparticles

adsorbates^{25, 28, 180-182}, this is beneficial for the intrinsic electrocatalytic activity of ORR^{27, 183-185} and helps offset some of the Pt mass based activity loss due to the larger particle size¹³⁸. Similarly, the Co rich satellite cores help maintain compressive strain in nearby surface sections and plausibly account for the sustained high catalytic activity of particles with a size of up to 20 nm.

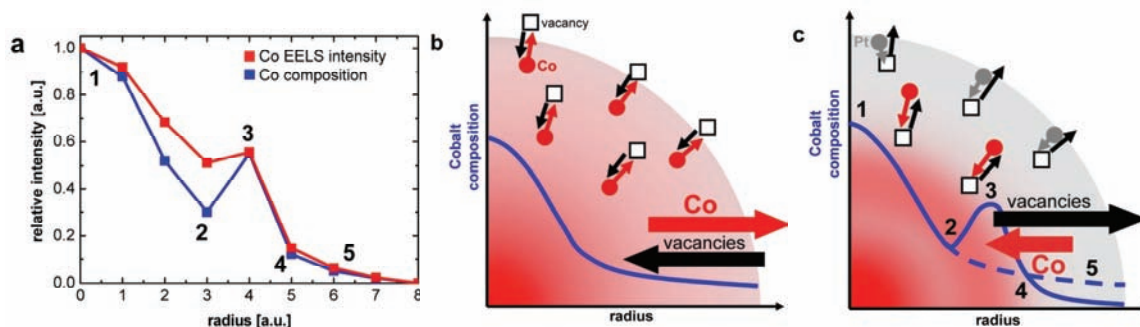


Figure 66 a) Extraction of the actual atomic-scale Co composition within a specific shell (blue) from a representative Co EEL intensity profile (red). Shoulders and slight minima in the EEL intensity profile (2) correspond to strong depletions in the local Co composition. (b) and (c): Illustration of the formation mechanism of the unusual compositional multi-shell nanoparticle structure. A quarter of a spherical cross section through a dealloyed Pt-Co particle with a Co rich core (red color near origin) and Pt rich shell (grey color) is shown as background in both Figures. (b) The blue solid line schematically shows an early-stage Co composition profile (Co concentration on vertical axis, and distance from particle center on x axis) with monotonic negative slope as a consequence of rapid initial surface dealloying, Co bulk downhill diffusion (red arrow), and associated vacancy injection into the particle (black arrow). Prohibitively high surface energies of nanoscale voids prevent aggregation of the injected vacancies. (c) Instead, Pt surface diffusion acts as a vacancy sink and causes vacancy back migration toward the particle surface (inverse Kirkendall effect) followed by subsequent vacancy ejection/annihilation at the surface. The migration of vacancies is coupled to an opposite uphill Co diffusion (red arrow) inducing a sharp Co drop-off at position 4. The resulting Co non-monotonic single-maximum compositional profile (dashed blue curve) is consistent with the experimentally observed compositional multi-layer structure involving adjacent Co maxima and minima.

The formation of off-center Co rich satellite cores near the surface of pore- and void-free dealloyed Pt rich nanoparticles, such as shown in Figure 63 and Figure 64, finds a plausible mechanistic origin in the interplay of i) rapid electrochemical Co surface dissolution, ii) terrace/step/kink vacancy formation, iii) followed by a much slower vacancy annihilation through Pt surface atom diffusion. Dealloying based on Co bulk diffusion across particle radii ($> 5\text{ nm}$) is unlikely due to low diffusion coefficients and bulk vacancy concentrations in the particle core. Erlebacher et al.¹¹⁴ showed that these processes control the formation of dealloyed porous metals from bimetallic alloys. Electrochemical dissolution of the less noble metal atoms creates terrace vacancies and low-coordinated mobile Pt surface atoms. The electric field, combined with surface adsorption of oxygenated (hydr)oxide species above 0.7 V/RHE ^{13, 186, 187}, promotes rapid Co segregation towards the surface, which causes terrace vacancies to be injected in the second and third subsurface layer, while more surface Co is dissolved. Simultaneously, low-coordinated Pt atoms diffuse toward step edges and induce inhomogeneous Pt distributions. This leads to Rayleigh surface instabilities¹⁶⁶ promoting the growth of stable channels and pores, thereby exposing more of the less noble component to (electro)chemical dissolution until all near-surface vacancies are annihilated by Pt surface diffusion. This mechanism explains the inhomogeneous loss of Co from nanoparticles below 20 nm diameter considered here, with one difference. Interfacial energies prevent the growth of terrace vacancies into stable pores and voids inside the nanoparticles. As a result, terrace vacancies and surface pits are eventually healed out by Pt surface diffusion, the particles remain non-porous. Bulk regions near surface sections with fewer terrace vacancies remain less affected by dealloying and this result in the observed Co rich satellite subsurface regions.

The formation of near-spherical compositional shells with Co enrichment adjacent to Co depletion again involves the combined processes of electrochemical surface Co dissolution and Pt surface diffusion^{114, 167, 188}, however, requires an additional element of short-range subsurface Co segregation as well; our proposed formation mechanism is illustrated in Figure 66b and c. Initially, potential cycling¹³ causes very rapid electric field-driven Co

dissolution from the surface and subsurface. Co removal is accompanied by equally rapid injection of lattice vacancies in the opposite direction, that is, towards the surface and subsurface. As discussed earlier, vacancies are unable to form stable voids inside the nanocrystals due to prohibitively high surface energies¹⁷⁰; instead, owing to Pt surface diffusion^{114, 188}, subsurface vacancies are gradually annihilated (Figure 66c). As predicted by Yu et al.¹⁸⁹, this outward flux of vacancies is associated with the diffusion of the faster diffusing component, here Co, in the opposite direction, that is, towards the center of the particle, and hence up-hill against the general radial Co concentration profile. This process is referred to in the literature as the “inverse Kirkendall effect”, because regular Kirkendall phenomena^{168, 169, 171, 172} – observed in bimetallic diffusion upon thermal annealing – have vacancies diffuse toward high concentrations of the fast diffuser, that is, here, the particle center. This kinetic segregation of Co is illustrated by the red arrows in Figure 66c; it continues as long as excess vacancies of the dealloying process are present the subsurface of the particle. In effect, the Co segregation results in a nonmonotonic Co profile (solid blue curve in Figure 66c) with a Co minimum and maximum consistent with the experimentally observed profiles.

The proposed formation mechanism involves Co diffusion only over very short distances of about 1 nm (according to the experimental EEL curves in Figure 64 c-e and, as schematically shown, from region 5 to region 3 in Figure 66c). It seems plausible, that this diffusion mechanism is considerably enhanced by the presence of subsurface excess vacancies injected during dealloying in comparison with diffusion with thermodynamic equilibrium vacancy concentration. Once the excess vacancies are annihilated, the micro structural state of the subsurface region becomes kinetically frozen. This conclusion is supported by the observation that the complex particle morphologies are stable during electron microscopy and do not show any microstructural or compositional changes even after some minutes of electron beam irradiation. Although the observed complex morphologies and compositional profiles do not necessarily represent thermodynamic final states, they are kinetically frozen metastable states.

8.3 Summary

In conclusion, we have uncovered the existence and discussed the impact on catalysis of the unusual compositional fine-structure of core-shell Pt bimetallic nanoparticle catalysts by STEM and EEL spectroscopy. Co-enriched nanoparticle cores are displaced from the center, are strongly ellipsoidal and are surrounded by self-organized Co rich satellite cores inside the Pt rich shell region. A detailed EEL compositional analysis revealed spherical 1 – 2 nm wide Co depletion and enrichment zones inconsistent with conventional models of dissolution and diffusion during the dealloying of bimetallics.^{114, 117, 166, 167, 188, 190} We rationalized the formation mechanism of the enrichment features through a combination of rapid selective Co surface electrodisolution and vacancy injection, followed by an inverse Kirkendall effect of outward vacancy annihilation associated with opposite very short-range Co segregation. Based on our results, the conventional simple two-layer description of bimetallic Pt nanoparticle electrocatalysts is insufficient in the 10 – 15 nm range.

Our results reflect how important a detailed knowledge of the compositional structure of bimetallic nanoparticles is for a thorough understanding of their surface electrocatalytic activity. Also, our insights suggest a practical design strategy to control and tune ORR activity of Pt core-shell nanoparticles in a size regime of about 10 – 15 nm. Particles of that size exhibit favorable stability^{89, 133, 148} yet possess shells with several nanometers in diameter, which limit the effective compressive strain¹⁶ in the particle surface and hence its activity. However, judicious formation of a Co-enriched spherical subsurface shell or, similarly, a subsurface Co satellite core by dealloying enhances the compressive lattice strain and catalytic activity of the Pt surface layer. The Co-enriched regions can be controlled by a careful choice of dissolution conditions of the less noble component, such as pH, dissolution time, or electrode potential.

9 Conclusions and Perspectives

9.1 Conclusions

This thesis has addressed in-situ studies of formation and particle growth, the structural and electrochemical characterization and oxygen reduction reaction (ORR) activities of dealloyed Pt-Cu and Pt-Co alloy nanoparticle electrocatalysts in acidic and alkaline media.

Dealloyed Pt bimetallic nanoparticles have emerged as one of the promising cathode catalyst concepts for the electroreduction of oxygen to meet and exceed the activity targets of the U.S. Department of Energy⁴¹. This family of catalysts is based on the core-shell nanostructure prepared by selective dissolution of the less noble metal and enrichment of Pt atoms on the particle surface (chapter 4). The improved reactivity of dealloyed core-shell nanoparticles is largely caused by compressive lattice strain in the Pt rich particle shell.

This catalyst concept was transferred and applied to the Pt-Co and Pt-Cu alloy systems in acidic and alkaline media. In the conclusion of this work a better understanding of the relation of structure, composition and reactivity is achieved and provide a rational design of novel core-shell cathode fuel cell electrocatalysts with improved ORR performance. Critical material characteristics as well as experimental parameters for an enhanced ORR activity were: (i) the degree of alloying and crystallinity, particle size and composition during thermal annealing, (ii) the effects of electrolyte and pH on the electrochemical dealloying behavior and (iii) their dominant morphological and compositional structures of dealloyed Pt alloys in their most catalytically active state. Also, the size – morphology – composition relationships of dealloyed Pt alloys have been established to link here the nano to the macro scale and provide an insight into the existing material gap of dealloyed nanoparticles and highly porous bulk-like bimetallic particles in corrosion science.

Synthesis of Pt Alloy Nanoparticle Precursor Catalysts (chapter 3): The electrocatalytic activity is critically sensitive to the structure, composition and particle size of bimetallic nanoparticles. Atomic-scale insight into the formation kinetics, the compositional and structural stability of nanoscale alloys are of great importance for the synthesis of functional bimetallic nanomaterials. This work has addressed this issue and used in-situ HT-XRD as a powerful technique to clarify the influences of the annealing temperature and time on the alloy formation process and particle growth dynamics. In particular, based on the lattice parameter – composition relations of the Pt-Cu nanoparticle system established by the temperature-corrected Vegard's law over a wide temperature range, this study provides practical synthetic guidelines toward to obtain disordered fcc highly dispersed PtCu₃ alloy electrocatalysts with desired size. It was found, that the maximum annealing temperature controls the composition of the disordered fcc Pt-Cu alloy phase. The annealing time, in contrast, controls the particle size of the resulting alloy. Thus, the annealing times can substantially be shortened without compromising composition for fcc Pt-M alloys.

Electrochemical Dealloying Behavior and ORR Activity (chapter 5 and 6): Pt bimetallic nanoparticles serve as precursor materials to form highly active fuel cell electrocatalysts by electrochemical surface dealloying of less noble metal. The electrochemical dealloying behavior and ORR activities of various Pt-Co and Pt-Cu alloy nanoparticle electrocatalysts were examined in different electrolyte solutions and pH values.

Unlike for Pt-Cu system, a strong surface enrichment of stable Co atoms is uncovered in Pt-Co alloy nanoparticles. This is explained by an adsorption of oxygen surface species which causes Co surface segregation and surface atom rearrangements during voltage cycling in 0.1 M KOH. Voltage cycling in 0.1 M HClO₄, in contrast, leads to the electrochemical dissolution of Co and the enrichment of Pt atoms on the particle surface (Pt-enriched shell - alloy core structure). After the voltage cycling in 0.1 M KOH the mass activities increase according: PtCo₃ < PtCo < Pt₃Co. The pretreated Pt₃Co catalyst shows 2 – 3 times higher j_{mass} than the benchmark pure Pt. In contrast, after voltage cycling

in 0.1 M HClO₄ the Pt mass based activities increase in the following trend: PtCo < Pt₃Co < PtCo₃. The pretreated PtCo₃ catalyst exhibits clearly 3 fold increase in j_{mass} compared to pure Pt due to the formation of the core-shell structure. However, the PtCo₃ core-shell nanoparticles show an outstanding ORR mass activity for alkaline PEM fuel cells, an increase by 4 times compared to pure Pt/C.

Pt-Cu alloy nanoparticles show also differences in their electrochemical behavior and resulting ORR activities in 0.1 M HClO₄ and 0.1 M KOH electrolyte solutions. The voltage cycling in 0.1 M KOH initiates the formation of Cu oxide surface species and subsequently the dissolution/deposition of Cu. The gradual loss of copper atoms due to the formation of soluble Cu species is traced by the changes in chemical composition established by EDS. In contrast, the voltage cycling in 0.1 M HClO₄ causes a strong surface dissolution of Cu and therefore the enrichment of Pt on the particle surface. After voltage cycling in 0.1 M KOH the Pt mass based activities increase according: PtCu₃ < PtCu < Pt₃Cu. Here, the pretreated Pt₃Cu catalyst is slightly less active for ORR than commercial pure Pt. Unlike the results in alkaline media, after the voltage cycling in 0.1 M HClO₄ the Pt mass based activities increase in the following trend: Pt₃Cu < PtCu < PtCu₃. The Pt mass based activity for dealloyed PtCu₃ catalyst increases by 3 – 4 times compared to the benchmark pure Pt. The activated PtCu₃ core-shell nanoparticle catalyst exhibits also 3 – 4 fold increase in j_{mass} in 0.1 M KOH than the benchmark pure Pt.

The main conclusion of these chapters is that measurements of the electrocatalytic ORR activity show a 3 – 4 fold benefit for the dealloyed PtCu₃ and PtCo₃ core-shell nanoparticle electrocatalysts in acidic as well as in alkaline media compared with the benchmark Pt nanoparticle catalyst. The core-shell structure only forms in acidic media due to the formation of stable less noble metal oxide species in alkaline solution.

High-resolution Morphological and Compositional Structure of Highly Active Self-organized Dealloyed Pt Bimetallic (chapter 7 and 8): Due to the significant activity enhancement, this work clarified the atomic process occurring during the electrochemical dealloying of nanoscale materials and showed size-dependent morphology – intraparticle composition relationship for the dealloyed PtCu₃ and PtCo₃ particle catalysts in their most active state. The existence of three distinctly different size-dependent morphology regimes in dealloyed Pt-Co and Pt-Cu particle ensembles is uncovered: With increasing size, a structural regime characterized exclusively by single core-shell structures give way to one involving multiple-core bimetallic structures. At even larger sizes, surface-pits and nanopores coexisting with multiple cores are formed. These size/morphological regimes are separated by two characteristic particle diameters, $d_{\text{multiple cores}}$ and d_{pores} . This observed size-dependent morphological structures can be explained by kinetic and thermodynamic aspects.

Interestingly, based on the atomic-scale structural and compositional investigations, Pt-Co core-shell nanoparticle catalyst in a size range of 10 and 20 nm reveal an unusual self-organized compositional structure with a depth profile of Co-depletion and Co-enrichment and the presence of less noble rich satellite cores located near the Pt-enriched surface. These observed features of spherical 1 – 2 nm wide Co-depletion and Co-enrichment zones can be explained by interplay of selective Co dissolution and Pt surface diffusion and an inverse Kirkendall effect of Co atoms.

This thesis provides a rational design of fuel cell nanocatalysts with improved surface catalytic properties for acidic and alkaline PEMFCs.

9.2 Perspectives

Practical MEA Implementation. The enhanced ORR activities of dealloyed Pt-Cu and Pt-Co catalysts were established by RDE technique. RDE is a suitable technique for catalyst screening and to obtain first details about the catalyst stability. The next step is the transfer from RDE to MEA without loss of activity. The replication and maintenance of ORR activities are currently great challenges. After a positive evaluation of the catalysts in a MEA as single fuel cell the next step is to study the long-term stability in a real fuel cell stack under operating conditions. Until now the long-term durability requirement of fuel cell electrocatalysts has not been met with performance losses of less than 40% (electrochemical surface area) of beginning-of-life activities for over 5000 h⁴¹.

Compositional Stability. The improved ORR activity is controlled on the thickness of the Pt-enriched particle shell. Above a shell thickness of a few nanometers, the surface layer would act like pure Pt.

The instability of the transition-metal alloy constituent in Pt alloy nanoparticles under operating fuel cell conditions is an important critical issue. The leaching of internal less noble metal from the alloy particle core results in an increasing Pt-enriched particle shell and a decreasing ORR performance. Therefore, the alloy core should be compositional stable and keep the reduced Pt-Pt distance on the surface. Further atomic arrangement types to protect the alloy core are segregation-induced Pt skin and acid treated Pt skeleton.

The dealloyed Pt bimetallic core-shell concept can be extended and evaluated for further Pt-M alloys. Pt alloys with 4d elements reveal a stronger enhancement of activity compared to Pt alloys with 5d metals due to the increased lattice mismatch. However, DFT-based calculation about the stability of a Pt monolayer on 5d metals as a core show a higher durability compared with those of 4d metals.¹⁹¹ According to the theoretical predictions, the improved long-term stability is experimentally observed for Pt-Pd or Pt-Au core-shell nanoparticles.^{23, 192}

Large Particles with Enhanced Activity. The detailed knowledge of the accurate compositional particle depth profile and dominant morphological structure provide a practical catalyst concept for the preparation of highly active and stable Pt alloy core-shell nanoparticles in a size regime of about 10 – 15 nm. Particles in this range show clearly improved durability^{89, 133, 148} yet possess a low mass activity due to the shell thickness of several nanometers and relatively reduced compressive strain in the Pt surface. Based on the high-resolution microscopic and spectroscopic results, the Pt shell of the dealloyed particles appears to scale with the particle size, i.e. large particles tend to a large Pt-enriched shell region. This indicates that dealloying proceeds into extensive depths in larger bimetallic particles.

However, the features of the Co-depletion and Co-enrichment and the less noble metal rich satellite cores located near the Pt-enriched surface were uncovered in dealloyed nanoparticles of 10 – 15 nm. The formation of Cu/Co rich satellite cores and Cu/Co-enriched spherical subsurface shell inside Pt shells are likely to increase and maintain compressive lattice surface strain in the adjacent region of the Pt surface. Increased locale active reaction centers generate on the Pt rich surface directly under Co rich satellite cores. The Co-enriched regions can be controlled by a careful choice of dissolution conditions of the less noble component, such as pH, dissolution time, or electrode potential. For more insight of the highly complex structure a high-resolution electron tomography is required.

Theoretical Calculations. The compressive lattice strain in the Pt-enriched shell for dealloyed PtCo₃ catalyst which is likely responsible for the significantly improved ORR activity is to determine and compare with dealloyed PtCu₃ catalyst. DFT calculations are required to prove the geometric effect. A DFT-based description of the surface dynamics of core-shell nanoarchitecture will also provide new insights of the catalytic ORR activity. Additional work is necessary to clarify the surface oxidation behavior of Pt alloys.

10 Appendices

10.1 List of Chemicals

acetone (Sigma Aldrich, 99.5+%, A.C.S. reagent; 179124-2.5l)

4 vol%/ 96 vol% hydrogen/argon, AirLiquide, quality 5.0

1 vol%/ 99 vol% oxygen/nitrogen, AirLiquide, quality 5.0

Nafion solution, 5 wt. % (Sigma-Aldrich, 274704-25ml)

2-propanol (Sigma-Aldrich, 99.5+%, A.C.S. reagent, #19076-4)

70% redistilled HClO₄ (Sigma Aldrich, #311421)

hydrogen, AirLiquide, quality 5.0

oxygen, AirLiquide, quality 5.0

nitrogen, AirLiquide, quality 5.0

28.2 wt. % Pt/HSAC (part no. TEC10E30E, supplied by TKK, Japan)

Cu(NO₃)₂ • 2.5 H₂O (Sigma Aldrich, #467855)

Co(NO₃)₂ • 6 H₂O (Alfa Aesar, #010694)

potassium hydroxide, pellets, 99,99% (Sigma-Aldrich, # 306568-100g)

10.2 Criteria of Fit for XRD Profiles

Table 14 Criteria of fit using TOPAS. The observed and calculated data at data point are denoted with $Y_{o,m}$ and $Y_{c,m}$, respectively. M is the number of data points and P the number of parameters. w_m the weighting given to data point m which for counting statistics is given by $w_m = 1/\sigma(Y_{o,m})^2$ where $\sigma(Y_{o,m})$ is the error in $Y_{o,m}$ and $I_{o,k}$ and $I_{c,k}$ the “observed” and calculated intensities of the k^{th} reflection.

Criteria of fit	Definition
R – weighted pattern (R_{wp})	$R_{wp} = \sqrt{\frac{\sum w_m(Y_{o,m} - Y_{c,m})^2}{\sum w_m Y_{o,m}^2}}$
R – expected (R_{exp})	$R_{exp} = \sqrt{\frac{\sum M - P}{\sum w_m Y_{o,m}^2}}$
Goodness of fit (GOF)	$GOF = \chi^2 = \frac{R_{wp}}{R_{exp}} = \sqrt{\frac{\sum w_m(Y_{o,m} - Y_{c,m})^2}{M - P}}$

10.3 Abbreviations

Symbol	Acceptation
CV	cyclic voltammetry
DoE	U.S. Department of Energy
ECSA	electrochemical active surface area
EDS	energy-dispersive X-ray spectroscopy
EEL	electron energy loss
eq.	equation
fcc	face centered cubic
GC	glassy carbon
GIF	Gatan image filter
HAADF	high angle annular dark field
hcd	high current density
HR-TEM	high resolution transmission electron microscopy
HR-STEM	high resolution scanning transmission electron microscopy
HSAC	high surface area carbon
HT	heat treated
HT-XRD	high temperature X-ray diffraction
H _{upd}	underpotentially deposited hydrogen
lcd	low current density
LSV	linear sweep voltammetry
M, Me	metal
MEA	membrane electrode assembly
MMS	mercury-mercury sulfate electrode
ORR	oxygen reduction reaction
PDF	reference powder diffraction patterns
PEMFC	proton exchange membrane fuel cell
PSD	position sensitive LynxEye detector
Q _{ad/de}	charge of the hydrogen adsorption and desorption
RDE	rotating disk electrode
RRDE	rotating ring disk electrode
RHE	reversible hydrogen electrode
STEM	scanning transmission electron microscopy
STEM-HAADF	high angle annular dark field scanning transmission electron microscopy
TEM	transmission electron microscopy
XRD	X-ray diffraction

Appendices

Symbol	Acceptation	Unit
α	symmetry factor	--
a	lattice parameter	Å
at.	atomic	%
B	Tafel slope	mV dec^{-1}
B	Koutecky – Levich slope	$\text{mA cm}^{-2}_{\text{geo.}} \text{ s}^{1/2}$
β	crystallite size (Scherrer)	nm
$c(\text{O}_2)$	oxygen solubility	mol l^{-1}
$D(\text{O}_2)$	oxygen diffusivity	$\text{cm}^2 \text{ s}^{-1}$
d_i	diameter	nm
$d_{\text{multiple cores}}$	characteristic particle diameters of multiple cores	nm
d_{pores}	characteristic particle diameters of pores	nm
E	voltage	V
ECSA	platinum electrochemical active surface area	$\text{m}^2 \text{ g}_{\text{Pt}}^{-1}$
ε_{β}	crystallite size(Scherrer)	nm
ε_{ω}	crystallite size(integral breath methode)	nm
F	Faraday constant	C mol^{-1}
f	intensity	a.u.
f_m	intensity at the maxium	a.u.
ΔG	Gibbs free energy	kJ mol^{-1}
GOF	goodness-of-fit	--
i_{disk}	disk current	mA
i_{disk}	ring current	μA
j	current density	$\text{mA cm}^{-2}_{\text{geo.}}$
j_0	exchange current density	mA cm^{-2}
j_D	current density	mA cm^{-2}
j_{dif}	diffusion limiting current density	$\text{mA cm}^{-2}_{\text{geo.}}$
j_{kin}	kinetic limiting current density	$\text{mA cm}^{-2}_{\text{geo.}}$
j_{mass}	platinum mass based activity	$\text{A mg}^{-1}_{\text{Pt}}$
j_{specific}	platinum surface area specific based activity	$\mu\text{A cm}^{-2}_{\text{Pt}}$
K_{ω}	shape factor (Scherrer)	--
m	mass	g
N	collection efficiency	--
n	number of transferred electrons	--
n_i	number of particles	--
$n(t)$	molar flux rate	mol s^{-1}
η	overpotential	V
ν	kinematic viscosity	$\text{cm}^2 \text{ s}^{-1}$
θ_{ad}	coverage of adsorbed species	
Θ	Bragg angle	°

Appendices

R	ideal gas constant	$\text{J mol}^{-1} \text{K}^{-1}$
R_{exp}	R-expected	--
R_{wp}	R-weighted pattern	--
T	temperature	$^{\circ}\text{C}$ or K
V	volume	L
Vol.	volume	%
ω	half width in angle	$^{\circ}$
ω	rotating rate	U min^{-1}
wt.	weight	%
λ	X-ray wavelength	nm
X	conversion	%
x	molar fraction	--

11 References

1. Spendelow, J. S.; Wieckowski, A., Electrocatalysis of oxygen reduction and small alcohol oxidation in alkaline media. *Physical Chemistry Chemical Physics* **2007**, 9, (21), 2654-2675.
2. Bidault, F.; Brett, D. J. L.; Middleton, P. H.; Brandon, N. P., Review of gas diffusion cathodes for alkaline fuel cells. *Journal of Power Sources* **2009**, 187, (1), 39-48.
3. Antolini, E.; Gonzalez, E. R., Alkaline direct alcohol fuel cells. *Journal of Power Sources* **2010**, 195, (11), 3431-3450.
4. McLean, G. F.; Niet, T.; Prince-Richard, S.; Djilali, N., An assessment of alkaline fuel cell technology. *International Journal of Hydrogen Energy* **2002**, 27, (5), 507-526.
5. Kinoshita, K., *Electrochemical Oxygen Technology*. Wiley: New York, 1992; p 448.
6. Bianchini, C., *Small Fuel Cells for Portable Applications* **2006**, (7th ed; The Knowledge Press. Inc.: Brookline, MA), 227.
7. Gasteiger, H. A.; Markovic, N. M., CHEMISTRY: Just a Dream--or Future Reality? *Science* **2009**, 324, (5923), 48-49.
8. Toda, T.; Igarashi, H.; Uchida, H.; Watanabe, M., Enhancement of Electroreduction of oxygen on Pt Alloys with Fe, Ni and Co. *J. Electrochem. Soc.* **1999**, 146, 3751.
9. Stamenkovic, V. R.; Fowler, B.; Mun, B. S.; Wang, G.; Ross, P. N.; Lucas, C. A.; Markovic, N. M., Improved Oxygen Reduction Activity on Pt₃Ni(111) via Increased Surface Site Availability *Science* **2007**, 315, 493.
10. Stamenkovic, V. R.; Mun, B. S.; Arenz, M.; Mayrhofer, K. J. J.; Lucas, C. A.; Wang, G.; Ross, P. N.; Markovic, N. M., Trends in electrocatalysis on extended and nanoscale Pt-bimetallic alloy surfaces. *Nature Materials* **2007**, 6, (3), 241-247.
11. Wang, J. X.; Inada, H.; Wu, L.; Zhu, Y.; Choi, Y. M.; Liu, P.; Zhou, W.-P.; Adzic, R. R., Oxygen Reduction on well defined Core-Shell Nanocatalysts: particle Size, Facet and Pt Shell Thickness Effects. *Journal of the American Chemical Society* **2009**, 131, 17298-17302.
12. Wang, C.; Chi, M.; Li, D.; Strmcnik, D.; van der Vliet, D.; Wang, G.; Komanicky, V.; Chang, K.-C.; Paulikas, A. P.; Tripkovic, D.; Pearson, J.; More, K. L.; Markovic, N. M.; Stamenkovic, V. R., Design and Synthesis of Bimetallic Electrocatalyst with Multilayered Pt-Skin Surfaces. *Journal of the American Chemical Society* **2011**, 133, (36), 14396-14403.
13. Mayrhofer, K. J. J.; Juhart, V.; Hartl, K.; Hanzlik, M.; Arenz, M., Adsorbate-Induced Surface Segregation for Core-Shell Nanocatalysts. *Angewandte Chemie International Edition* **2009**, 48, (19), 3529-3531.
14. Chen, S.; Sheng, W.; Yabuuchi, N.; Ferreira, P. J.; Allard, L. F.; Shao-Horn, Y., Origin of Oxygen Reduction Reaction Activity on "Pt₃Co" Nanoparticles: Atomically Resolved Chemical Compositions and Structures. *The Journal of Physical Chemistry C* **2008**, 113, (3), 1109-1125.
15. Chen, S.; Ferreira, P. J.; Sheng, W.; Yabuuchi, N.; Allard, L. F.; Shao-Horn, Y., Enhanced Activity for Oxygen Reduction Reaction on "Pt₃Co" Nanoparticles: Direct Evidence of Percolated and Sandwich-Segregation

Structures. *Journal of the American Chemical Society* **2008**, 130, (42), 13818-13819.

16. Strasser, P.; Koh, S.; Anniyev, T.; Greeley, J.; More, K.; Yu, C.; Liu, Z.; Kaya, S.; Nordlund, D.; Ogasawara, H.; Toney, M. F.; Nilsson, A., Lattice-strain control of the activity in dealloyed core-shell fuel cell catalysts. *Nature Chemistry* **2010**, 2, (6), 454-460.

17. Paulus, U. A.; Wokaun, A.; Scherer, G. G.; Schmidt, T. J.; Stamenkovic, V.; Radmilovic, V.; Markovic, N. M.; Ross, P. N., Oxygen Reduction on Carbon supported Pt-Ni and Pt-Co Alloy catalysts. *J. Phys. Chem. B* **2002**, 106, 4181-4191.

18. Watanabe, M.; Tsurumi, K.; Mizukami, T.; Nakamura, T.; Stonehart, P., Activity and Stability of Ordered and Disordered Co-Pt Alloys for Phosphoric-Acid Fuel-Cells. *Journal of the Electrochemical Society* **1994**, 141, (10), 2659-2668.

19. Greeley, J.; Stephens, I. E. L.; Bondarenko, A. S.; Johansson, T. P.; Hansen, H. A.; Jaramillo, T. F.; Rossmeisl, J.; Chorkendorff, I.; Norskov, J. K., Alloys of platinum and early transition metals as oxygen reduction electrocatalysts. *Nature Chemistry* **2009**, 1, (7), 552-556.

20. Koh, S.; Leisch, J.; Toney, M. F.; Strasser, P., Structure-Activity-Stability Relationships of Pt-Co Alloy Electrocatalysts in Gas-Diffusion Electrode Layers. *The Journal of Physical Chemistry C* **2007**, 111, (9), 3744-3752.

21. Koh, S.; Toney, M. F.; Strasser, P., Activity-stability relationships of ordered and disordered alloy phases of Pt₃Co electrocatalysts for the oxygen reduction reaction (ORR). *Electrochimica Acta* **2007**, 52, (8), 2765-2774.

22. Koh, S.; Yu, C.; Mani, P.; Srivastava, R.; Strasser, P., Activity of ordered and disordered Pt-Co alloy phases for the electroreduction of oxygen in catalysts with multiple coexisting phases. *Journal of Power Sources* **2007**, 172, 50-56.

23. Sasaki, K.; Naohara, H.; Cai, Y.; Choi, Y. M.; Liu, P.; Vukmirovic, M. B.; Wang, J. X.; Adzic, R. R., Core-Protected Platinum Monolayer Shell High-Stability Electrocatalysts for Fuel-Cell Cathodes. *Angewandte Chemie International Edition* **2010**, 49, (46), 8602-8607.

24. Chen, S.; Gasteiger, H. A.; Hayakawa, K.; Tada, T.; Shao-Horn, Y., Platinum-Alloy Cathode Catalyst Degradation in Proton Exchange Membrane Fuel Cells: Nanometer-Scale Compositional and Morphological Changes. *Journal of The Electrochemical Society* **2010**, 157, (1), A82-A97.

25. Kitchin, J. R.; Norskov, J. K.; Barteau, M. A.; Chen, J. G., Role of Strain and Ligand Effects in the Modification of the Electronic and Chemical Properties of Bimetallic Surfaces. *Physical Review Letters* **2004**, 93, (15), 156801.

26. Greeley, J.; Norskov, J. K.; Mavrikakis, M., Electronic Structure and Catalysis on Metal Surfaces. *Annual Review of Physical Chemistry* **2002**, 53, 319-348.

27. Nilsson, A.; Pettersson, L. G. M.; Hammer, B.; Bligaard, T.; Christensen, C. H.; Norskov, J. K., The electronic effect in heterogeneous catalysis. *Catal. Lett.* **2005**, 100, 111.

28. Mavrikakis, M.; Hammer, B.; Norskov, J. K., Effect of Strain on the reactivity of metal surfaces. *Phys. Rev. Lett.* **1998**, 81, (13), 2819-2822.

29. Hasché, F.; Oezaslan, M.; Strasser, P., Activity, Structure and Degradation of Dealloyed PtNi₃ Nanoparticle Electrocatalyst for the Oxygen

Reduction Reaction in PEMFC. *Journal of The Electrochemical Society* **2012**, 159, (1), B25-B34.

30. Strasser, P.; Oezaslan, M.; Hasché, F.; Koh, S.; Yu, C.; Srivastava, R., Nanoparticulate bimetallic core-shell catalysts for fuel cells. *Chemie Ingenieur Technik* **2008**, 80, (9), 1267.

31. Sao-Joao, S.; Giorgio, S.; Penisson, J. M.; Chapon, C.; Bourgeois, S.; Henry, C., structure and deformations of Pd-Ni Core-shell nanoparticles. *J. Phys. Chem. B* **2005**, 109, 342-347.

32. Soal, N. S.; Ebels, U.; Mohwald, H.; Giersig, M., Synthesis of Core-Shell PtCo Nanocrystals. *J. Phys. Chem. B* **2003**, 107, 7351-7454.

33. Giorgio, S.; Henry, C. R., Core-shell bimetallic particles, prepared by sequential impregnations. *Eur. Phys. J. Ap.* **2002**, 20, (1), 23-27.

34. Zhang, J.; Lima, F. H. B.; Shao, M. H.; Sasaki, K.; Wang, J. X.; Hanson, J.; Adzic, R. R., Platinum Monolayer on Nonnoble Metal - Noble Metal Core - Shell Nanoparticle Electrocatalysts for O₂ Reduction. *The Journal of Physical Chemistry B* **2005**, 109, (48), 22701-22704.

35. Mani, P.; Srivastava, S.; Strasser, P., Dealloyed Pt-Cu Core-Shell Nanoparticle Electrocatalysts for use in PEM Fuel Cell Cathodes. *Journal of the Physical Chemistry C* **2008**, 112, 2770-2778.

36. Wang, J. X.; Inada, H.; Wu, L.; Zhu, Y.; Choi, Y. M.; Liu, P.; Zhou, W.-P.; Adzic, R. R., Oxygen Reduction on well defined Core Shell Nanocatalysts: particle Size, Facet and Pt Shell Thickness Effects. *J. Am. Chem. Soc.* **2009**, 131, 17298-17302.

37. Wang, J. X.; Ma, C.; Choi, Y.; Su, D.; Zhu, Y.; Liu, P.; Si, R.; Vukmirovic, M. B.; Zhang, Y.; Adzic, R. R., Kirkendall Effect and Lattice Contraction in Nanocatalysts: A New Strategy to Enhance Sustainable Activity. *Journal of the American Chemical Society* **2011**, 133, (34), 13551-13557.

38. Adzic, R. R.; Zhang, J.; Sasaki, K.; Vukmirovic, M. B.; Shao, M.; Wang, J. X.; Nilekar, A. U.; Mavrikakis, M.; Valerio, J. A.; Uribe, F., Platinum Monolayer Fuel Cell Electrocatalysts. *Top. Catal.* **2007**, 46, 249-262.

39. Yang, R.; Leisch, J.; Strasser, P.; Toney, M. F., Structure of Dealloyed PtCu₃ Thin Films and Catalytic Activity for Oxygen Reduction. *Chemistry of Materials* **2010**, 22, (16), 4712-4720.

40. Yang, R.; Strasser, P.; Toney, M. F., Dealloying of Cu₃Pt (111) Studied by Surface X-ray Scattering. *The Journal of Physical Chemistry C* **2011**, 115, (18), 9074-9080.

41. Department_of_Energy; Motors, G. *Appendix D: Accelerated Test Protocols to demonstrate 5500 hr Catalyst Durability* 2006; p 46 www.doe.gov.

42. Spiegel, C. S., *Designing and Building Fuel Cells*. McGraw-Hill Professional: 2007.

43. O'Hayre, R.; Cha, S.-W.; Colella, W.; Prinz, F. B., *Fuel Cell Fundamentals*. Wiley: New York, 2006.

44. Prakash, J.; Tryk, D. A.; Aldred, W.; Yeager, E. B., Investigations of ruthenium pyrochlores as bifunctional oxygen electrodes. *Journal of Applied Electrochemistry* **1999**, 29, (12), 1463-1469.

45. Vante, N. A.; Tributsch, H., Energy conversion catalysis using semiconducting transition metal cluster compounds. *Nature* **1986**, 323, 431-432.

46. Cao, D.; Wieckowski, A.; Inukai, J.; Alonso-Vante, N., Oxygen Reduction Reaction on Ruthenium and Rhodium Nanoparticles Modified with Selenium and Sulfur. *Journal of The Electrochemical Society* **2006**, 153, (5), A869-A874.
47. Fournier, J.; Lalande, G.; Cote, R.; Guay, D.; Dodelet, J.-P., Activation of Various Fe-Based Precursors on Carbon Black and Graphite Supports to Obtain Catalysts for the Reduction of Oxygen in Fuel Cells. *Journal of the Electrochemical Society* **1997**, 144, (1), 218-226.
48. Gojkovic, S. L.; Gupta, S.; Savinell, R. F., Heat-treated iron(III) tetramethoxyphenyl porphyrin chloride supported on high-area carbon as an electrocatalyst for oxygen reduction: Part II. Kinetics of oxygen reduction. *Journal of Electroanalytical Chemistry* **1999**, 462, (1), 63-72.
49. Jaouen, F.; Dodelet, J.-P., Average turn-over frequency of O₂ electro-reduction for Fe/N/C and Co/N/C catalysts in PEFCs. *Electrochimica Acta* **2007**, 52, (19), 5975-5984.
50. Liu, R.; Wu, D.; Feng, X.; Müllen, K., Nitrogen-Doped Ordered Mesoporous Graphitic Arrays with High Electrocatalytic Activity for Oxygen Reduction. *Angewandte Chemie International Edition* **2010**, 49, (14), 2565-2569.
51. Yang, W.; Fellingner, T.-P.; Antonietti, M., Efficient Metal-Free Oxygen Reduction in Alkaline Medium on High-Surface-Area Mesoporous Nitrogen-Doped Carbons Made from Ionic Liquids and Nucleobases. *Journal of the American Chemical Society* **2010**, 133, (2), 206-209.
52. Bashyam, R.; Zelenay, P., A class of non-precious metal composite catalysts for fuel cells. *Nature* **2006**, 443, (7107), 63-66.
53. Gong, K.; Du, F.; Xia, Z.; Durstock, M.; Dai, L., Nitrogen-Doped Carbon Nanotube Arrays with High Electrocatalytic Activity for Oxygen Reduction. *Science* **2009**, 323, (5915), 760-764.
54. Maroun, F.; Ozanam, F.; Magnussen, O. M.; Behm, R. J., The Role of Atomic Ensembles in the Reactivity of Bimetallic Electrocatalysts. *Science* **2001**, 293, (5536), 1811-1814.
55. Watanabe, M.; Shibata, M.; Motoo, S., *J. Electroanal. Chem.* **1986**, 206, 197.
56. Chen, M.; Kumar, D.; Yi, C.-W.; Goodman, D. W., The Promotional Effect of Gold in Catalysis by Palladium-Gold. *Science* **2005**, 310, (5746), 291-293.
57. Hammer, B.; Norskov, J. K., Theoretical surface science and catalysis - calculations and concepts. In *Advances in Catalysis*, Academic Press: 2000; Vol. 45, pp 71-129.
58. Subramanian, P. R.; Laughlin, D. E., Cu-Pt (Copper-Platinum). In *Binary Alloy Phase Diagrams*, 2 ed.; Massalski, T. B., Ed. 1990; Vol. 2, pp 1460-1462
59. Pourbaix, M., *Atlas of Electrochemical Equilibria in Aqueous Solutions* Pergamon Press: Oxford, New York, 1966.
60. Alloy Phase Diagrams. In *ASM Handbook*, Baker, H.; Okamoto, H.; Henry, S. D.; Davidson, G. M.; Fleming, M. A.; Kacprzak, L.; Lampman, H., Eds. 1990; Vol. 3.
61. Hamann, C. H.; Hamnett, A.; Vielstich, W., *Electrochemistry*. Wiley-VCH: Weinheim, 2007.
62. Bard, A. J.; Faulkner, L. R., *Electrochemical Methods*. Wiley: New York, 1980.

63. Grgur, B. N.; Markovic, N. M.; Ross, P. N., Temperature-dependent oxygen electrochemistry on platinum low-index single crystal surfaces in acid solutions. *Can. J. Chem* **1997**, *75*, 1465-1471.
64. Damjanovic, A.; Sepa, D. B., An analysis of the pH dependence of enthalpies and Gibbs energies of activation for O₂ reduction at Pt electrodes in acid solutions. *Electrochimica Acta* **1990**, *35*, (7), 1157-1162.
65. Schmidt, T. J.; Paulus, U. A.; Gasteiger, H. A.; Behm, R. J., The oxygen reduction reaction on a Pt/carbon fuel cell catalyst in the presence of chloride anions. *Journal of Electroanalytical Chemistry* **2001**, *508*, 41-47.
66. Bett, J.; Lundquist, J.; Washington, E.; Stonehart, P., Platinum crystallite size considerations for electrocatalytic oxygen reduction-I. *Electrochimica Acta* **1973**, *18*, (5), 343-348.
67. Paulus, U. A.; Wokaun, A.; Scherer, G. G.; Schmidt, T. J.; Stamenkovic, V.; Markovic, N. M.; Ross, P. N., Oxygen reduction on high surface area Pt-based alloy catalysts in comparison to well defined smooth bulk alloy electrodes. *Electrochimica Acta* **2002**, *47*, (22-23), 3787-3798.
68. Schmidt, T. J.; Gasteiger, H. A., Rotating thin-film method for supported catalysts. In *Handbook of Fuel Cells - Fundamentals, Technology, and Applications*, Vielstich, W.; Lamm, A.; Gasteiger, H., Eds. Wiley: Chichester, 2003; Vol. 2, p 316 (Chapter 22).
69. Markovic, N. M.; Gasteiger, H. A.; Philip N. Ross, J., Oxygen Reduction on Platinum Low-Index Single-Crystal Surfaces in Sulfuric Acid Solution: Rotating Ring-Pt(hkl) Disk Studies. *J. Phys Chem* **1995**, *99*, (11), 3411-3415.
70. Albery, W. J.; Hitchman, M. L., Ring-Disc Electrodes. In Clarendon Press, Oxford: 1971.
71. Laue, M. v., *Z. Kristallogr.* **1926**, *64*, 115.
72. Scherrer, P., Bestimmung der Grösse und der inneren Struktur von Kolloidteilchen mittels Röntgenstrahlen. *Nachr. Ges. Wiss. Göttingen* **1918**, *26*, 98-100.
73. Langford, J. I.; Wilson, A. J. C., Scherrer after sixty years: A survey and some new results in the determination of crystallite size. *Journal of Applied Crystallography* **1978**, *11*, (2), 102-113.
74. Vegard, L., Die Konstitution der Mischkristalle und die Raumfüllung der Atome. *Zeitschrift fuer Physik* **1921**, *5*, 2-26.
75. Oezaslan, M.; Hasché, F.; Strasser, P., In Situ Observation of Bimetallic Alloy Nanoparticle Formation and Growth Using High-Temperature XRD. *Chemistry of Materials* **2011**, *23*, (8), 2159-2165.
76. Cebollada, A.; Farrow, R. F. C.; Toney, M. F., Structure and magnetic properties of chemically ordered magnetic binary alloys in thin film form. In *Magnetic Nanostructures*, Nalwa, H. S., Ed. American Scientific: Stevenson Ranch, 2002; pp 93-123.
77. Zhang, J.; Mo, Y.; Vukmirovic, M.; Klie, R.; Sasaki, K.; Adzic, R., Platinum Monolayer Electrocatalysts for O₂ Reduction: Pt Monolayer on Pd (111) and on Carbon-Supported Pd Nanoparticles. *J. Phys. Chem. B* **2004**, *108*, (2004), 10955-10964.
78. Stamenkovic, V. R.; Mun, B. S.; Mayrhofer, K. J. J.; Ross, P. N.; Markovic, N. M., Effect of Surface Composition on Electronic Structure, Stability, and Electrocatalytic Properties of Pt-Transition Metal Alloys: Pt-Skin versus Pt-Skeleton Surfaces. *J. Am. Chem. Soc.* **2006**, *128*, (27), 8702-8988.

79. Stamenkovic, V.; Moon, B. S.; Mayerhofer, K. J.; Ross, P. N.; Markovic, N.; Rossmeisl, J.; Greeley, J.; Norskov, J. K., Changing the activity of electrocatalysts for oxygen reduction by tuning the surface electronic structure. *Angew. Chem. Int. Ed.* **2006**, 45, 2897-2901.
80. Liu, Z.; Koh, S.; Yu, C.; Strasser, P., Synthesis, De-alloying, and ORR Electrocatalysis of PDDA-stabilized Cu-rich Pt alloy nanoparticles. *J. Electrochem. Soc.* **2007**, 154, (11), B1192-B1199.
81. Koh, S.; Strasser, P., Electrocatalysis on Bimetallic Surfaces: Modifying Catalytic Reactivity for Oxygen Reduction by Voltammetric Surface Dealloying. *Journal of the American Chemical Society* **2007**, 129, (42), 12624-12625.
82. Koh, S.; Hahn, N.; Yu, C.; Strasser, P., Effects of Composition and Annealing Conditions on Catalytic Activities of Dealloyed Pt-Cu Nanoparticle Electrocatalysts for PEMFC. *Journal of The Electrochemical Society* **2008**, 155, (12), B1281-B1288.
83. Schulenburg, H.; Müller, E.; Khelashvili, G.; Roser, T.; Bönnemann, H.; Wokaun, A.; Scherer, G. G., Heat-Treated PtCo₃ Nanoparticles as Oxygen Reduction Catalysts. *The Journal of Physical Chemistry C* **2009**, 113, (10), 4069-4077.
84. Lima, F. H. B.; de Castro, J. F. R.; Santos, L. G. R. A.; Ticianelli, E. A., Electrocatalysis of oxygen reduction on carbon-supported Pt-Co nanoparticles with low Pt content. *Journal of Power Sources* **2009**, 190, (2), 293-300.
85. Salgado, J. R. C.; Antolini, E.; Gonzalez, E. R., Structure and activity of carbon-supported Pt-Co electrocatalysts for oxygen reduction. *J. Phys. Chem. B* **2004**, 108, 17767-17774.
86. Koh, S.; Yu, C.; Mani, P.; Srivastava, R.; Strasser, P., Activity of ordered and disordered Pt-Co alloy phases for the electroreduction of oxygen in catalysts with multiple coexisting phases. *J. Power Sourc.* **2007**, 172, 50-56.
87. Watanabe, M.; Tsurumi, K.; Mizukami, T.; Nakamura, T.; Stonehart, P., Activity and Stability of Ordered and Disordered Co-Pt Alloys for Phosphoric-Acid Fuel-Cells. *J. Electrochem. Soc.* **1994**, 141, (10), 2659-2668.
88. Antolini, E.; Cardellini, F., Formation of carbon supported PtRu alloys: an XRD analysis. *Journal of Alloys and Compounds* **2001**, 315, (1-2), 118-122.
89. Hasché, F.; Oezaslan, M.; Strasser, P., Activity, stability and degradation of multi walled carbon nanotube (MWCNT) supported Pt fuel cell electrocatalysts. *Physical Chemistry Chemical Physics* **2010**, 12, (46), 15251-15258.
90. Oezaslan, M.; Strasser, P., Activity of dealloyed PtCo₃ and PtCu₃ nanoparticle electrocatalyst for oxygen reduction reaction in polymer electrolyte membrane fuel cell. *Journal of Power Sources* **2011**, 196, (12), 5240-5249.
91. Oezaslan, M.; Hasché, F.; Strasser, P., Structure-Activity Relationship of Dealloyed PtCo₃ and PtCu₃ Nanoparticle Electrocatalyst for Oxygen Reduction Reaction in PEMFC. *ECS Transactions* **2010**, 33, (1), 333-341.
92. Strasser, P., Dealloyed Core Shell Fuel Cell Electrocatalysts *Rev. Chem. Eng.* **2009**, 25, (4), 255-295.
93. Srivastava, R.; Mani, P.; Hahn, N.; Strasser, P., Efficient Oxygen Reduction Fuel Cell Electrocatalysis on Voltammetrically Dealloyed Pt-Cu-Co Nanoparticles. *Angewandte Chemie International Edition* **2007**, 46, (47), 8988-8991.

94. Mani, P.; Srivastava, R.; Strasser, P., Dealloyed binary PtM₃ (M= Cu, Co, Ni) and ternary PtNi₃M (M=Cu, Co, Fe, Cr) electrocatalysts for the oxygen reduction reaction: Performance in polymer electrolyte membrane fuel cells. *Journal of Power Sources* **2011**, 196, (2), 666-673.
95. Srivastava, R.; Mani, P.; Strasser, P., In situ voltammetric de-alloying of fuel cell catalyst electrode layer: A combined scanning electron microscope/electron probe micro-analysis study. *Journal of Power Sources* **2009**, 190, (1), 40-47.
96. Neyerlin, K. C.; Srivastava, R.; Yu, C.; Strasser, P., Electrochemical activity and stability of dealloyed Pt-Cu and Pt-Cu-Co electrocatalysts for the oxygen reduction reaction (ORR). *Journal of Power Sources* **2009**, 186, (2), 261-267.
97. Klimenkov, M.; Nepijko, S.; Kuhlbeck, H.; Bäumer, M.; Schlögl, R.; Freund, H. J., The structure of Pt-aggregates on a supported thin aluminum oxide film in comparison with unsupported alumina: a transmission electron microscopy study. *Surface Science* **1997**, 391, (1-3), 27-36.
98. Strasser, P.; Koh, S.; Greeley, J., Voltammetric surface dealloying of Pt bimetallic nanoparticles: an experimental and DFT computational analysis. *Physical Chemistry Chemical Physics* **2008**, 10, (25), 3670-3683.
99. Sinfelt, J. H., *Bimetallic Catalysts: Discoveries, Concepts, and Applications*. John Wiley & Sons: London, 1983.
100. Ross, P. N., The Science of electrocatalysis on bimetallic surfaces. In *Electrocatalysis*, Lipkowsky, J.; Ross, P. N., Eds. Wiley: New York, 1998; pp 43-74.
101. Markovic, N. M.; Schmidt, T. J.; Stamenkovic, V.; Ross, P. N., Oxygen Reduction Reaction on Pt and Pt Bimetallic Surfaces: A selective review. *Fuel Cells* **2001**, 1, 105.
102. Stamenkovic, V.; Grgur, B. N.; Ross, P. N.; Markovic, N. M., Oxygen Reduction Reaction on Pt and Pt-Bimetallic Electrodes Covered by CO. *Journal of The Electrochemical Society* **2005**, 152, (2), A277-A282.
103. Rodriguez, J. A.; Goodman, D. W., The Nature of the Metal-Metal Bond in Bimetallic Surfaces. *Science* **1992**, 257, (5072), 897-903.
104. Schuette, W. L.; Schweizer, A. E., Bifunctionality in Catalytic Cracking Catalysis. *Studies in Surface Science and Catalysis* **2001**, 134, 263-278.
105. Mukerjee, S.; Urian, R. C., Bifunctionality in Pt alloy nanocluster electrocatalysts for enhanced methanol oxidation and CO tolerance in PEM fuel cells: electrochemical and in situ synchrotron spectroscopy. *Electrochim. Acta* **2002**, 47, 3219-3231.
106. Roth, C.; Papworth, A. J.; Hussain, I.; Nichols, R. J.; Schiffrin, D. J., A Pt/Ru nanoparticulate system to study the bifunctional mechanism of electrocatalysis. *Journal of Electroanalytical Chemistry* **2005**, 581, 79-85.
107. Azzam, K. G.; Babich, I. V.; Seshan, K.; Leffert, L., A bifunctional catalyst for the single-stage water-gas shift reaction in fuel cell applications Part 2. Roles of the support and promoter on catalyst activity and stability. *Journal of Catalysis* **2007**, 251, 163-171.
108. Wang, C.; Chi, M.; Wang, G.; Vliet, D. v. d.; Li, D.; More, K.; Wang, H.-H.; Schlueter, J. A.; Nenad M. Markovic ; Stamenkovic, V. R., Correlation Between Surface Chemistry and Electrocatalytic Properties of Monodisperse Pt x Ni 1 - x Nanoparticles. *Adv. Func. Mat.* **2011**, 21, 147.

109. Wang, C.; van der Vliet, D.; More, K. L.; Zaluzec, N. J.; Peng, S.; Sun, S.; Daimon, H.; Wang, G.; Greeley, J.; Pearson, J.; Paulikas, A. P.; Karapetrov, G.; Strmcnik, D.; Markovic, N. M.; Stamenkovic, V. R., Multimetallic Au/FePt₃ Nanoparticles as Highly Durable Electrocatalyst. *Nano Letters* **2011**, 11, (3), 919-926.
110. Hunt, L. B., The True Story of Purple of Cassius. *Gold Bulletin* **1976**, 9, (4), 134-139.
111. Lechtman, H., Pre-Columbian surface metallurgy. *Scientific American* **1984**, 250, (6), 56-63154.
112. Raney, M., Method of producing finely-divided nickel. *United States Patent Office* **1927**, 1628190.
113. Snyder, J.; Fujita, T.; Chen, M. W.; Erlebacher, J., Oxygen reduction in nanoporous metal-ionic liquid composite electrocatalysts. *Nature Materials* **2010**, 9, (11), 904-907.
114. Erlebacher, J.; Aziz, M. J.; Karma, A.; Dimitrov, N.; Sieradzki, K., Evolution of nanoporosity in dealloying. *Nature* **2001**, 410, (6827), 450-453.
115. Newman, R. C.; Sieradzki, K., Metallic Corrosion. *Science* **1994**, 263, 1708-1709.
116. Corcoran, S. G., The Morphology of Alloy Corrosion. In *Critical Factors in Localized Corrosion III*, Kelley, R. G.; Frankel, G. S.; Natishan, P. M.; Newman, R. C., Eds. Electrochemical Society: Pennington, New Jersey, 2000; Vol. 98-17, pp 500 -507.
117. Rugolo, J.; Erlebacher, J.; Sieradzki, K., Length scales in alloy dissolution and measurement of absolute interfacial free energy. *Nature Materials* **2006**, 5, (12), 946-949.
118. Renner, F. U.; Stierle, A.; Dosch, H.; Kolb, D. M.; Lee, T. L.; Zegenhagen, J., Initial corrosion observed on the atomic scale. *Nature* **2006**, 439, (7077), 707-710.
119. Renner, F. U.; Stierle, A.; Dosch, H.; Kolb, D. M.; Lee, T. L.; Zegenhagen, J., In situ x-ray diffraction study of the initial dealloying and passivation of Cu₃ Au (111) during anodic dissolution. *Physical Review B* **2008**, 77, (23), 235433.
120. Renner, F. U.; Stierle, A.; Dosch, H.; Kolb, D. M.; Zegenhagen, J., The influence of chloride on the initial anodic dissolution of Cu₃Au(1 1 1). *Electrochem. Comm.* **2007**, 9, (7), 1639.
121. Dursun, A.; Pugh, D. V.; Corcoran, A. G., Probing the Dealloying Critical Potential. *J. Electrochem. Soc.* **2005**, 152, B65-B72.
122. Aziz, D.; Dylan, V. P.; Sean, G. C., A Steady-State Method for Determining the Dealloying Critical Potential. *Electrochemical and Solid-State Letters* **2003**, 6, (8), B32-B34.
123. Pareek, A.; Borodin, S.; Bashir, A.; Ankah, G. N.; Keil, P.; Eckstein, G. A.; Rohwerder, M.; Stratmann, M.; Gründer, Y.; Renner, F. U., Initiation and Inhibition of Dealloying of Single Crystalline Cu₃Au (111) Surfaces. *Journal of the American Chemical Society* **2011**, 133, (45), 18264-18271.
124. Strasser, P., Dealloyed Pt bimetallic electrocatalysts for oxygen reduction. In *Handbook of Fuel Cells:Advances in Electrocatalysis, Materials, Diagnostics and Durability*, Vielstich, W.; Gasteiger, H. A.; Yokokawa, H., Eds. John Wiley & Sons Ltd: Chichester, West Sussex, UK, 2009; Vol. Volumes 5 & 6, pp 30-47.

125. Koh, S.; Strasser, P., Dealloyed Pt Nanoparticle Fuel Cell Electrocatalysts: Stability and Aging Study of Catalyst Powders, Thin Films, and Inks. *Journal of The Electrochemical Society* **2010**, 157, (4), B585-B591.
126. Oezaslan, M.; Hasché, F.; Strasser, P., PtCu₃, PtCu and Pt₃Cu Alloy Nanoparticle Electrocatalysts for Oxygen Reduction Reaction in Alkaline and Acidic Media. *Journal of The Electrochemical Society* **2012**, 159, (4), B444-B454.
127. Oezaslan, M.; Hasché, F.; Strasser, P., Oxygen Electroreduction on Pt_xCo_{1-x} and Pt_xCu_{1-x} Alloy Nanoparticles for Basic and Acidic PEM Fuel Cell. *ECS Transactions* **2011**, 41, (1), 1659-1668.
128. Strmcnik, D.; van der Vliet, D. F.; Chang, K. C.; Komanicky, V.; Kodama, K.; You, H.; Stamenkovic, V. R.; Markovic, N. M., Effects of Li⁺, K⁺, and Ba²⁺ Cations on the ORR at Model and High Surface Area Pt and Au Surfaces in Alkaline Solutions. *The Journal of Physical Chemistry Letters* **2011**, 2, (21), 2733-2736.
129. Strmcnik, D.; Kodama, K.; van der Vliet, D.; Greeley, J.; Stamenkovic, V. R.; Markovic, N. M., The role of non-covalent interactions in electrocatalytic fuel-cell reactions on platinum. *Nat Chem* **2009**, 1, (6), 466-472.
130. Hasché, F.; Oezaslan, M.; Strasser, P., Activity, Stability, and Degradation Mechanisms of Dealloyed PtCu₃ and PtCo₃ Nanoparticle Fuel Cell Catalysts. *ChemCatChem* **2011**, 3, (11), 1805-1813.
131. Kadirgan, F.; Beden, B.; Lamy, C., Electrocatalytic oxidation of ethylene-glycol: Part II. Behaviour of platinum-ad-atom electrodes in alkaline medium. *Journal of Electroanalytical Chemistry and Interfacial Electrochemistry* **1983**, 143, (1-2), 135-152.
132. Salgado, J. R. C.; Antolini, E.; Gonzalez, E. R., Carbon supported Pt₇₀Co₃₀ electrocatalyst prepared by the formic acid method for the oxygen reduction reaction in polymer electrolyte fuel cells. *Journal of Power Sources* **2005**, 141, (1), 13-18.
133. Holby, E. F.; Sheng, W.; Shao-Horn, Y.; Morgan, D., Pt nanoparticle stability in PEM fuel cells: influence of particle size distribution and crossover hydrogen. *Energy & Environmental Science* **2009**, 2, (8), 865-871.
134. Mukerjee, S., Particle size and structural effects in platinum electrocatalysis. *J. Appl. Electrochem.* **1990**, 20, 537-548.
135. Loukrakpam, R.; Luo, J.; He, T.; Chen, Y.; Xu, Z.; Njoki, P. N.; Wanjala, B. N.; Fang, B.; Mott, D.; Yin, J.; Klar, J.; Powell, B.; Zhong, C.-J., Nanoengineered PtCo and PtNi Catalysts for Oxygen Reduction Reaction: An Assessment of the Structural and Electrocatalytic Properties. *The Journal of Physical Chemistry C* **2011**, 115, (5), 1682-1694.
136. Mayrhofer, K. J. J.; Strmcnik, D.; Blizanac, B. B.; Stamenkovic, V.; Arenz, M.; Markovic, N. M., Measurement of oxygen reduction activities via the rotating disc electrode method: From Pt model surfaces to carbon-supported high surface area catalysts. *Electrochimica Acta* **2008**, 53, (7), 3181-3188.
137. Nesselberger, M.; Ashton, S.; Meier, J. C.; Katsounaros, I.; Mayrhofer, K. J. J.; Arenz, M., The Particle Size Effect on the Oxygen Reduction Reaction Activity of Pt Catalysts: Influence of Electrolyte and Relation to Single Crystal Models. *Journal of the American Chemical Society* **2011**, 133, (43), 17428-17433.

138. Gasteiger, H. A.; Kocha, S. S.; Sompalli, B.; Wagner, F. T., Activity benchmarks and requirements for Pt, Pt-alloy, and non-Pt oxygen reduction catalysts for PEMFCs. *Applied Catalysis B: Environmental* **2005**, 56, (1-2), 9-35.
139. Paulus, U. A.; Schmidt, T. J.; Gasteiger, H. A.; Behm, R. J., Oxygen reduction on a high-surface area Pt/Vulcan carbon catalyst: a thin-film rotating ring-disk electrode study. *Journal of Electroanalytical Chemistry* **2001**, 495, (2), 134-145.
140. Oezaslan, M.; Hasché, F.; Strasser, P., Oxygen Electroreduction on PtCo₃, PtCo and Pt₃Co Alloy Nanoparticles for Alkaline and Acidic PEM Fuel Cells. *Journal of The Electrochemical Society* **2012**, 159, (4), B394-B405.
141. Duong, H. T.; Rigsby, M. A.; Zhou, W.-P.; Wieckowski, A., Oxygen Reduction Catalysis of the Pt₃Co Alloy in Alkaline and Acidic Media Studied by X-ray Photoelectron Spectroscopy and Electrochemical Methods. *The Journal of Physical Chemistry C* **2007**, 111, (36), 13460-13465.
142. Mayrhofer, K. J. J.; Hartl, K.; Juhart, V.; Arenz, M., Degradation of Carbon-Supported Pt Bimetallic Nanoparticles by Surface Segregation. *Journal of the American Chemical Society* **2009**, 131, (45), 16348-16349.
143. Stamenkovic, V.; Schmidt, T. J.; Ross, P. N.; Markovic, N. M., Surface Composition Effects in Electrocatalysis: Kinetics of Oxygen Reduction on Well-Defined Pt₃Ni and Pt₃Co Alloy Surfaces. *J. Phys. Chem. B* **2002**, 106, 11970-11979.
144. Wang, C.; Wang, G.; van der Vliet, D.; Chang, K.-C.; Markovic, N. M.; Stamenkovic, V. R., Monodisperse Pt₃Co nanoparticles as electrocatalyst: the effects of particle size and pretreatment on electrocatalytic reduction of oxygen. *Physical Chemistry Chemical Physics* **2010**, 12, (26), 6933-6939.
145. Wang, C.; van der Vliet, D.; Chang, K.-C.; You, H.; Strmcnik, D.; Schlueter, J. A.; Markovic, N. M.; Stamenkovic, V. R., Monodisperse Pt₃Co Nanoparticles as a Catalyst for the Oxygen Reduction Reaction: Size-Dependent Activity. *The Journal of Physical Chemistry C* **2009**, 113, (45), 19365-19368.
146. Lima, F. H. B.; Salgado, J. R. C.; Gonzalez, E. R.; Ticianelli, E. A., Electrocatalytic Properties of PtCo/C and PtNi/C alloys for the Oxygen Reduction Reaction in Alkaline Solution. *Journal of The Electrochemical Society* **2007**, 154, (4), A369-A375.
147. Lima, F. H. B.; Ticianelli, E. A., Oxygen electrocatalysis on ultra-thin porous coating rotating ring/disk platinum and platinum-cobalt electrodes in alkaline media. *Electrochimica Acta* **2004**, 49, (24), 4091-4099.
148. Shao-Horn, Y.; Sheng, W.; Chen, S.; Ferreira, P.; Holby, E.; Morgan, D., Instability of Supported Platinum Nanoparticles in Low-Temperature Fuel Cells. *Topics in Catalysis* **2007**, 46, (3), 285-305.
149. Kabbabi, A.; Gloaguen, F.; Andolfatto, F.; Durand, R., Particle size effect for oxygen reduction and methanol oxidation on Pt/C inside a proton exchange membrane. *Journal of Electroanalytical Chemistry* **1994**, 373, (1-2), 251-254.
150. Gamez, A.; Richard, D.; Gallezot, P.; Gloaguen, F.; Faure, R.; Durand, R., Oxygen reduction on well-defined platinum nanoparticles inside recast ionomer. *Electrochimica Acta* **1996**, 41, (2), 307-314.
151. Antoine, O.; Durand, R., RRDE study of oxygen reduction on Pt nanoparticles inside Nafion®: H₂O₂ production in PEMFC cathode conditions. *Journal of Applied Electrochemistry* **2000**, 30, (7), 839-844.

152. Hanson, F. V.; Boudart, M., The reaction between H₂ and O₂ over supported platinum catalysts. *Journal of Catalysis* **1978**, 53, (1), 56-67.
153. Tae Hwang, J.; Shik Chung, J., The morphological and surface properties and their relationship with oxygen reduction activity for platinum-iron electrocatalysts. *Electrochimica Acta* **1993**, 38, (18), 2715-2723.
154. Inaba, M.; Yamada, H.; Tokunaga, J.; Tasaka, A., Effect of Agglomeration of Pt/C Catalyst on Hydrogen Peroxide Formation. *Electrochemical and Solid-State Letters* **2004**, 7, (12), A474-A476.
155. Bonakdarpour, A.; Dahn, T. R.; Atanasoski, R. T.; Debe, M. K.; Dahn, J. R., H₂O₂ Release during Oxygen Reduction Reaction on Pt Nanoparticles. *Electrochemical and Solid-State Letters* **2008**, 11, (11), B208-B211.
156. Markovic, N. M.; Gasteiger, H. A.; Grgur, B. N.; Ross, P. N., Oxygen reduction reaction on pt(111): effects of bromide. *J. Electroanal. Chem.* **1999**, 467, 157-163.
157. *CRC Handbook of Chemistry and Physics*. 76th ed.; CRC Press: New York, 1996.
158. Oezaslan, M.; Heggen, M.; Strasser, P., Size-dependent morphology of dealloyed bimetallic catalysts: Linking the nano to the macro scale. *Journal of the American Chemical Society* **2012**, 134, (1), 514-524.
159. Dubau, L.; Durst, J.; Maillard, F.; Guétaz, L.; Chatenet, M.; André, J.; Rossinot, E., Further insights into the durability of Pt₃Co/C electrocatalysts: Formation of "hollow" Pt nanoparticles induced by the Kirkendall effect. *Electrochimica Acta* **2011**, 56, (28), 10658-10667.
160. Maillard, F.; Dubau, L.; Durst, J.; Chatenet, M.; André, J.; Rossinot, E., Durability of Pt₃Co/C nanoparticles in a proton-exchange membrane fuel cell: Direct evidence of bulk Co segregation to the surface. *Electrochemistry Communications* **2010**, 12, (9), 1161-1164.
161. Pugh, D. V.; Dursun, A.; Corcoran, S. G., Formation of nanoporous platinum by selective dissolution of Cu from Cu_{0.75}Pt_{0.25}. *J. Mater. Res.* **2003**, 18, 216.
162. Pugh, D. V.; Dursun, A.; Corcoran, S. G., Electrochemical and Morphological Characterization of Pt-Cu Dealloying. *Journal of The Electrochemical Society* **2005**, 152, (11), B455-B459.
163. Koh, S.; Hahn, N.; Yu, C.; Strasser, P., Effects of Annealing Conditions on Catalytic Activities of Pt-Cu Nanoparticle Electrocatalysts for PEM Fuel Cells. *ECS Transactions* **2008**, 16, (2), 1093-1104.
164. Liu, Z.; Yu, C.; Rusakova, I.; Huang, D.; Strasser, P., Synthesis of Pt₃Co Alloy Nanocatalyst via Reverse Micelle for Oxygen Reduction Reaction in PEMFCs. *Top. Catal.* **2008**, 49, 241-250.
165. Liu, Z.; Koh, S.; Yu, C.; Strasser, P., Synthesis, De-alloying, and ORR Electrocatalysis of PDDA-stabilized Cu-rich Pt alloy nanoparticles. *Journal of The Electrochemical Society* **2007**, 154, (11), B1192-B1199.
166. Erlebacher, J., Mechanism of Coarsening and Bubble Formation in High-Genus Nanoporous Metals. *Physical Review Letters* **2011**, 106, (22), 225504.
167. Erlebacher, J.; Seshadri, R., Hard Materials with Tunable Porosity. *Mrs Bulletin* **2009**, 34, 561-568.
168. Yin, Y.; Rioux, R. M.; Erdonmez, C. K.; Hughes, S.; Somorjai, G. A.; Alivisatos, A. P., Formation of Hollow Nanocrystals Through the Nanoscale Kirkendall Effect. *Science* **2004**, 304, (5671), 711-714.

169. Huang, H. C. W., Ring formation of Kirkendall voids in Pb-alloy thin-film diffusion couples. *APPLIED PHYSICS LETTERS* **1982**, 41, (8), 724-726.
170. Glodán, G.; Cserhádi, C.; Beszedá, I.; L. Beke, D., Production of hollow hemisphere shells by pure Kirkendall porosity formation in Au/Ag system. *APPLIED PHYSICS LETTERS* **2010**, 97, 113109(1-3).
171. Fan, H. J.; Gösele, U.; Zacharias, M., Formation of Nanotubes and Hollow Nanoparticles Based on Kirkendall and Diffusion Processes: A Review. *Small* **2007**, 3, (10), 1660-1671.
172. Aldinger, F., Controlled porosity by an extreme kirkendall effect. *Acta Metallurgica* **1974**, 22, (7), 923-928.
173. Henkes, A. E.; Vasquez, Y.; Schaak, R. E., Converting Metals into Phosphides: A General Strategy for the Synthesis of Metal Phosphide Nanocrystals. *Journal of the American Chemical Society* **2007**, 129, (7), 1896-1897.
174. Yin, Y.; Erdonmez, C. K.; Cabot, A.; Hughes, S.; Alivisatos, A. P., Colloidal Synthesis of Hollow Cobalt Sulfide Nanocrystals. *Advanced Functional Materials* **2006**, 16, (11), 1389-1399.
175. Toda, T.; Igarashi, H.; Uchida, H.; Watanabe, M., Enhancement of the Electroreduction of Oxygen on Pt Alloys with Fe, Ni, and Co. *Journal of The Electrochemical Society* **1999**, 146, (10), 3750-3756.
176. Chen, S.; Sheng, W.; Yabuuchi, N.; Ferreira, P. J.; Allard, L. F.; Shao-Horn, Y., Origin of Oxygen Reduction Reaction Activity on "Pt3Co" Nanoparticles: Atomically Resolved Chemical Compositions and Structures. *The Journal of Physical Chemistry C* **2009**, 113, (3), 1109-1125.
177. Ferreira, P. J.; O, G. J. I.; Shao-Horn, Y.; Morgan, D.; Makharia, R.; Kocha, S.; Gasteiger, H. A., Instability of Pt/C Electrocatalysts in Proton Exchange Membrane Fuel Cells. *Journal of The Electrochemical Society* **2005**, 152, (11), A2256-A2271.
178. Abel, N. H., Aufloesung einer mechanischen Aufgabe. *Journal für die reine und angewandte Mathematik* **1826**, 1826, (1), 153-157.
179. Schlapka, A.; Lischka, M.; Gro; szlig; A.; auml; sberger, U.; Jakob, P., Surface Strain versus Substrate Interaction in Heteroepitaxial Metal Layers: Pt on Ru(0001). *Physical Review Letters* **2003**, 91, (1), 016101.
180. Gsell, M.; Jakob, P.; Menzel, D., Effect of Substrate Strain on Adsorption. *Science* **1998**, 280, (5364), 717-720.
181. Grabow, L.; Xu, Y.; Mavrikakis, M., Lattice strain effects on CO oxidation on Pt(111). *Physical Chemistry Chemical Physics* **2006**, 8, (29), 3369-3374.
182. Kibler, L. A.; El-Aziz, A. M.; Hoyer, R.; Kolb, D. M., Tuning reaction rates by lateral strain in a palladium monolayer. *Angew. Chem. Int. Ed.* **2005**, 44, (14), 2080-2084.
183. Kitchin, J. R.; Nørskov, J. K.; Barteau, M. A.; Chen, J. G., Modification of the surface electronic and chemical properties of Pt(111) by subsurface 3d transition metals. *J. Chem. Phys.* **2004**, 120, (21), 10240-10246.
184. Nilsson, A.; Pettersson, L.; Norskov, J., *Chemical Bonding at Surfaces and Interfaces*. Elsevier Science: Amsterdam, 2008.
185. Norskov, J. K.; Rossmeisl, J.; Logadottir, A.; Lindqvist, L.; Kitchin, J. R.; Bligaard, T.; Jonsson, H., Origin of the Overpotential for Oxygen Reduction at a Fuel-Cell Cathode. *J. Phys. Chem. B* **2004**, 108, 17886-17892.

186. Stamenkovic, V.; Schmidt, T. J.; Ross, P. N.; Markovic, N. M., Surface segregation effects in electrocatalysis: kinetics of oxygen reduction reaction on polycrystalline Pt₃Ni alloy surfaces. *J. Electroanal. Chem* **2003**, 554, 191-199.
187. Ruban, A. V.; Skriver, H. L.; Nørskov, J. K., Surface segregation energies in transition-metal alloys. *Phys. Rev. B* **1999**, 59, (24), 15990-16000.
188. Erlebacher, J., An Atomistic Description of Dealloying. *J. Electrochem. Soc.* **2004**, 151, C614-C626.
189. Yu, H.-C.; Yeon, D.-H.; Li, X.; Thornton, K., Continuum simulations of the formation of Kirkendall-effect-induced hollow cylinders in a binary substitutional alloy. *Acta Materialia* **2009**, 57, (18), 5348-5360.
190. Sieradzki, K.; Dimitrov, N.; Movrin, D.; McCall, C.; Vasiljevic, N.; Erlebacher, J., The Dealloying Critical Potential. *Journal of The Electrochemical Society* **2002**, 149, (8), B370-B377.
191. Ramirez-Caballero, G. E.; Balbuena, P. B., Surface segregation of core atoms in core-shell structures. *Chemical Physics Letters* **2008**, 456, (1-3), 64-67.
192. Zhang, J.; Sasaki, K.; Sutter, E.; Adzic, R. R., Stabilization of Platinum Oxygen Reduction Electrocatalysts using Gold Clusters. *Science* **2007**, 315, 220-222.